Coherent Neutral Pion Photoproduction on ^{16}O and ^{208}Pb

Ruth Sanderson

Presented as a Thesis for the Degree of Doctor of Philosophy

Nuclear Physics Group
Department of Physics and Astronomy
University of Glasgow

October 2002

Abstract

Neutral pion photoproduction in nuclei has particular potential as a source of information on the matter distribution in nuclei but it also has important contributions to make in extending our knowledge of the pion-nucleus interaction and the medium modifications of the pion production process. This thesis presents the experimental study of coherent neutral pion photoproduction on ^{16}O and ^{208}Pb, performed using the tagged photon beam facility at MAMI-B, University of Mainz, and the TAPS photon spectrometer, a highly segmented detector array built to detect light mesons.

Total and differential cross sections were measured in the incident photon energy range 135-380 MeV, covering a wider angular range and with smaller statistical errors than previous measurements. The diffraction-like structure of the differential cross section due to the nuclear form factor was demonstrated. Comparisons were made with plane and distorted wave impulse approximation models and show the importance of including a description of the final state interaction in the theoretical predictions but suggest that the magnitude of the pion-nucleus interaction is underestimated in the DWIA. Comparison with the Δ resonance energy model suggests that the nuclear medium does affect the Δ properties but that modifications are needed to the parameterisation used.

An assessment of the A-dependence of the total coherent (γ, π^0) cross section was made using the measurements on ^{12}C and ^{40}Ca performed at the same time as the present experiment. This comparison reinforces the conclusion that there is medium modification of the Δ and also suggests that this modification may have an A-dependence.

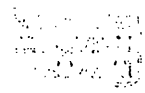

To: Donald Dyson and Tom Wheldon

Acknowledgements

Firstly, I would like to thank my supervisor, Prof. R. Owens, for all his help and guidance, particularly in the interpretation of the data. Thanks also to Cameron McGeorge for his many helpful comments on my work throughout my time in the Nuclear Physics Group.

I would like to thank the Institut für Kernphysik, Universtät Mainz, for providing the facilities for the experiment. I am indebted to all the members of the TAPS/A2 collaboration for all their hard work in setting up and running experiments, and their advice and guidance during the analysis. I owe particular thanks to Martin Kotulla and Marco Pfeiffer for always being quick to answer my questions about the analysis code. Special thanks to Lotte Fog, office-mate and fellow Glasgow TAPS student, for her help and support in everything, but mostly for her friendship.

I would like to thank my second supervisor, Ken Livingston, particularly for your help with all things computing. I owe my gratitude to every member of the Nuclear Physics Group, past and present, sorry not to mention you all by name but this thesis is long enough! However, I must mention Andreas with whom I've shared many a discussion on subjects as wide ranging as the delights of GEANT, and English versus German football; thanks to Dan for his support on the latter (you're OK for a Lancastrian), Scott for many things including saving me from being impaled by a light fitting, and a big, big thank you to Westley for my dinosaurs and much, much more.

I wish to thank the Engineering and Physical Sciences Research Council and the Nuclear Physics Group for providing financial support and travel expenses during my time as a student.

As always, I owe many thanks to my family, especially to Mum, Dad, and Neil for their continued support. Thanks to Sam and Kristen for the shopping sprees, thermal spas, and big slices of cake. As for Steven, words can't express what I owe you for keeping me sane the past year - thank you.

Finally, the two people to whom I dedicate this thesis: Donald Dyson, my beloved Grandfather, and Tom Wheldon, my mentor and dear friend; both were diagnosed with, and lost their fights against, cancer while I worked on this project.

Declaration

The data presented in this thesis were obtained in collaboration with colleagues from the Institut für Kernphysik, Universtät Mainz, II Physikalisches Institut, Giessen and the Nuclear Physics Group, Glasgow University as part of the TAPS/A2 collaboration. I participated fully in the preparation and execution of the experiment. The analysis of the experimental data is entirely my own work. This thesis was composed by myself.

Ruth Sanderson
October 2002

Contents

List of Figures

List of Tables

Chapter 1

Introduction

1.1 Introduction

It was only about 10 years after the discovery of the pion in the late 1940's [1] that neutral pion photoproduction was first proposed as a useful technique for nuclear size and shape determination [2–5]. However, progress in this field of study was very slow because the technology required has not been available until relatively recently and there has been a lack of overlap between the experimentally and theoretically accessible areas of the field.

In many early measurements the recoil nucleus was detected due to the technical problems involved in the direct detection of the pion. The π^0 decays predominantly into two photons in a time of the order of 10^{-16} seconds, and therefore must be detected via these decay products. Its momentum is then calculated from the measured momenta of the two photons. This requires a large segmented array of photon detectors and such detector systems have only become available in the past ten years. An alternative approach of detecting the π^0 with the simultaneous observation of the final nuclear system using an active target was used in the early 1980's in Bonn [6].

Neutral pion photoproduction in nuclei has particular potential as a source of information on the matter distribution in nuclei but it also has important contributions to make (i) in determining the amplitudes for the (γ, π^0) reaction on nucleons and (ii) in extending our knowledge of the π^0-nucleus interaction. These topics are introduced later in this section.

Neutral pion photoproduction can take place either coherently or incoherently. It is much easier to detect charged pions than neutral pions and hence charged pion photoproduction has received much greater attention [7–13]. However, charged pion photoproduction can only take place incoherently. Incoherent means that the final nucleus produced in the reaction is different from the initial nucleus whereas coherent means that the final nucleus is the same as the initial. So, incoherent can mean that,

as in the case of π^+ production, the nucleus is different because a proton was converted to a neutron, or as in the case of π^0 production, the nucleus makes a transition to an excited state. In coherent π^0 photoproduction the total production amplitude is the sum of the amplitudes on all nucleons resulting in a reaction cross section that scales with the square of the nuclear mass and is proportional to the matter form factor. The Fourier transform of this form factor is the matter density distribution as a function of radius. Hence the coherent reaction is an especially interesting process; it is one of the very few direct probes of the nuclear matter distribution. However to make use of this probe it is important to be able to separate the coherent process from the incoherent processes.

Most of the detailed studies of nuclear size and shape have used the elastic scattering of electrons [14] which determines the charge and magnetisation density of the nucleus and thus is more sensitive to the density distribution of the protons than to the zero-charged neutrons. Therefore, the study of the combined proton and neutron density using results from the coherent (γ, π^0) reaction will be of great interest. For light nuclei, this is expected to confirm what has been determined from electron scattering studies because the nuclear models have little flexibility to allow differences between the distributions of protons and neutrons. However, there is much more to be learned for heavy nuclei where the effective potential wells occupied by the neutrons and protons may be significantly different in shape. For example, measurement of the (γ, π^0) reaction in ^{208}Pb could demonstrate the presence of a neutron halo with the distribution of its 126 neutrons extending beyond that of its 82 protons. It is expected that any difference between the charge and matter distribution will be very small and therefore very accurate determination of the form factor from the (γ, π^0) reaction is needed. Such information will help the theoretical prediction of nucleon distributions in all nuclei.

The elementary amplitudes for the nucleon (γ, π^0) reaction have been established with reasonable accuracy from the analysis of nucleon data [15–19] but significant disagreements remain even for some of the more important multipoles. Some effects due to nucleon spins that are present in the reactions on protons and neutrons cancel out in nuclei in which the nucleon spins are paired off. Therefore, measurements of the reaction on suitable, closed shell nuclei can produce less ambiguous data than that for nucleon reactions. The effective (γ, π^0) amplitudes may also be modified in the nuclear medium. Indeed, a change in some amplitudes may be expected in nuclei; for example, the dominant M_{+1} amplitude comes from Δ excitation[1] even near threshold and the complex nature of the Δ-nucleus interaction is known to modify the propagation of the Δ in the nuclear environment [20–28] (for example, Pauli blocking

[1]The Δ is the first excited state of a nucleon.

and the coupling of the Δ to other channels alter the decay width of the resonance in a nuclear environment). Therefore the reaction on complex nuclei allows the study of the production, propagation, and decay of the Δ resonance in the nuclear medium.

The interaction of pions with nuclei has been mainly studied through elastic pion scattering, inelastic pion scattering, and pionic atoms[2] [30]. The pion-nuclear interaction can only be studied at one energy with pionic atoms. Pion scattering experiments are only possible for pion energies larger than around 30 MeV due to experimental difficulties stemming from the short distances the pions travel before decaying. Pion photoproduction in the region just above threshold allows the pion energy range to be extended all the way down to near zero.

In pion photoproduction the pions can, in principle, be produced anywhere in the nuclear interior as the photon can penetrate the whole nucleus essentially unattenuated. Hence information can be obtained on the π^0-nucleus attraction, or repulsion, and the nuclear absorption of π^0. The real part of the interaction produces a difference between the momentum of the π^0 when it is produced inside the nucleus and its final momentum outside the nucleus leading to an angular shift in the (γ, π^0) angular distribution. This is most obvious at the minima in the form factor and can be used to estimate the strength of the π^0-nucleus interaction [31]. Most of the previous information on the pion-nucleus interaction is from pion-induced reactions which take place in the nuclear surface [30].

1.1.1 Previous Measurements

There is relatively little data on either coherent or incoherent π^0 photoproduction from nuclei due to the required high duty factor source of monochromatic or tagged photons and the π^0 detector array both being large scale technical developments. Only with the commissioning of the high duty cycle, high intensity linear accelerators with tagged photon facilities, starting in the mid-seventies, and through recent advances in detection and data processing equipment, has it been possible to perform with sufficient accuracy pion photoproduction experiments where the contributions of the coherent process can be separated from the cross sections leading to excited nuclear bound states and to continuum states.

Several high duty factor electron accelerators at energies in the 100 MeV - 10 GeV range are now in operation around the world and most of these are equipped to produce high quality tagged photon beams with good energy resolution. Tagged photon beams allow the direct measurement of photonuclear cross sections thus avoiding the

[2] A pionic atom is a bound state where a π^-meson occupies an orbital about a nucleus much like that of an electron. These states may be thought of as atomic orbitals with pions instead of electrons, with modifications due to the pion's larger mass and its strong interaction with the nucleus [29].

various uncertainties and assumptions involved in the extraction of cross sections from the yield measurements performed with continuous Bremsstrahlung spectra [32, 33]. Monochromatic photon beams suitable for experiments such as photomeson production have also been produced using a technique involving the backscattering of a beam of laser photons from an electron beam circulating in a storage ring such as the Laser Electron Gamma Source (LEGS) at the National Synchrotron Light Source, Brookhaven, USA [34].

Neutral pions must be detected via their $\pi^0 \rightarrow 2\gamma$ decay so the technical difficulty is simply in assembling a sufficiently large array of individual photon detectors with energy and position resolution such that the two decay photons can be observed with high efficiency and the pion momentum reconstructed from the photon momenta. Only in the past few years have highly segmented arrays of inorganic scintillators suitable for this purpose become available.

Early Work

Despite the severe limitations of the available photon sources and detectors for the π^0 decay photons, many of the main qualitative features of the coherent (γ, π^0) process were established in the early experiments carried out in the 1950's.

The first observation of the production of neutral pions by high energy photons was made by Steinberger et al. at Berkeley in 1950 [35]. They used the 330 MeV x-ray beam of the Berkeley synchrotron to produce neutral pions from hydrogen, carbon, and beryllium and observed coincidences between the two π^0 decay photons for the first time. These photons were detected in two telescopes, each consisting of a veto scintillator to reject charged particles followed by a lead converter and two further scintillators in coincidence to detect the electron-positron pairs produced in the lead. Events were accepted if a photon was detected in each telescope. Aluminium absorbers were inserted between the last two crystals of one of the telescopes to measure the energy of the electrons produced in the lead converter. However at the energies studied the radiation losses are important so all that could be said about the energy of the decay photons was that their average energy was approximately 100 MeV. The properties of the photon coincidences were studied by measuring their rate as a function of the angle between the beam direction and the plane of the telescopes and as a function of the angle between the telescopes. They obtained the pion energy by assuming that the angle between the telescopes corresponded to a unique energy, that corresponding to the median decay gamma-ray opening angle given in equation 1.1, where E_π is the total pion energy and m_π is its rest energy. However, the angular resolution of the telescopes was insufficient to give more than a rough indication of the energy distribution.

$$\psi_{median} = \sin^{-1}\left(\frac{2m_\pi}{(3E_\pi^2 + m_\pi^2)^{\frac{1}{2}}}\right) \tag{1.1}$$

Over the following years, the group at Berkeley performed a series of experiments studying the yields of neutral pions from beryllium [36]. They observed that, as expected from the kinematics of π^0 decay, the minimum opening angle between the decay photons decreases with increasing π^0 energy (see section 2.4 and Appendix A.2.2), and obtained an angular distribution of π^0 photoproduction made at values of decay photon opening angle corresponding to an incident photon energy of 260 MeV. This showed the angular distribution for the photoproduction of neutral pions at a given photon energy to be strongly forward peaked.

Similar measurements were performed at MIT [37] on hydrogen and at Cornell University on hydrogen and deuterium [38, 39]. DeWire et al. studied the elastic (coherent) photoproduction of neutral pions from deuterium for incident photon energies of 250-300 MeV and π^0 mesons emitted at 90°-120° in the laboratory frame by detecting the recoil deuteron and one pion decay photon in coincidence [40] but no attempt was made to measure the angular and energy dependence of the cross section. The first measurement of coherent π^0 photoproduction on ^4He was made by Goldwasser et al. in 1954 [41]. Separation of the coherent process is possible for this nucleus because the threshold for π^0 production is 137 MeV but the threshold for incoherent production is some 20 MeV above this since ^4He has no excited nuclear states (threshold for $\gamma + ^4He \rightarrow \pi^0 + ^3H + p$ is 158 MeV; $\gamma + ^4He \rightarrow \pi^0 + ^3He + n$ is 159 MeV; $\gamma + ^4He \rightarrow \pi^0 + ^2H + ^2H$ is 162 MeV). Counting rates of photon pairs from ^4He were obtained at incident photon energies of 160 MeV, where the π^0 production is confined almost entirely to the coherent process, and at 190 MeV where both coherent and incoherent production processes are allowed. The coherent process was found to be still important at this higher energy.

The first measurement of the angular distribution and total cross section for ^4He was reported by deSaussure and Osborne of MIT the following year [42]. Measurements were performed as a function of center-of -mass angle for incident photon energies of 170-340 MeV by detecting the recoil nucleus rather than the π^0 decay photons. This allowed the separation of the coherent process because the ^3He nucleus produced in incoherent production along with a pion and a nucleon (reaction: $\gamma + ^4He \rightarrow \pi + ^3He +$ nucleon) was calculated to be of such a low energy that it would not reach the detection plates.

The earliest detailed work on coherent π^0 photoproduction on nuclei with $A > 4$ was carried out at the MIT synchrotron on ^{12}C, ^{40}Ca, and ^{208}Pb by Davidson in 1959 [3]. The first excited states of ^{12}C, ^{40}Ca, and ^{208}Pb are 4.4 MeV, 3.7 MeV,

and 2.6 MeV respectively and since the energy resolution of this data was 20 MeV it would have been contaminated with incoherent events. The cross section at large angles failed to show the expected diffraction structure, indicating that at least some of the cross section was incoherent. Unfortunately, this work was never published and the only information available on it is that in the paper of Saunders who compared his theoretical predictions with it [43] (see section 1.3).

Measurements of the coherent (γ, π^0) reaction were made on a wide range of nuclei by Schrack and a number of collaborators in the late 1950's and early 1960's [2, 4, 5]. The measurements used the photon beam from the 170 MeV electron synchrotron of the National Bureau of Standards (NBS), USA. Thus the energy region up to around 35 MeV above threshold was covered but no attempt was made to determine the energy of the incident photons. The total yield due to all available photon energies was measured. The two pion decay photons were detected in coincidence in a pair of detectors consisting of plastic scintillators that observed the electron-positron pairs produced from the decay photons in thin lead converters. This gave some information on the π^0 energy and an angular resolution not better than 20° (FWHM). However, clear signs of diffraction structure were observed in the π^0 angular distributions from three large A targets (Cu, Cd, and Pb) and the rms matter radii for 8 nuclei were obtained with accuracies of around 20 %.

Total (γ, π^0) Cross Section in the Threshold Region and its Photon Energy Dependence

Due to the complexity of the detector required to be capable of measuring the energy and angle of π^0 mesons, few measurements of the differential (γ, π^0) cross sections were made before 1990. However, it was possible to construct a large angular acceptance detector capable of identifying neutral pions without giving any energy or angle information. This allowed measurements of the total (γ, π^0) cross section to be made in the threshold region where the bulk of the cross section is expected to be coherent. Therefore, measurement of the π^0 energy that would be needed to separate the incoherent process could be dispensed with.

Argan et al. performed relative measurements of π^0 photoproduction yields on hydrogen, deuterium, ^3He and ^4He in the threshold region in 1980 [44]. Understanding of the experimental results was restricted by experimental aspects, particularly calculation of the detection efficiency, as well as theoretical difficulties - there were no satisfactory theoretical estimates of the cross sections for the four reactions measured. A more refined detection efficiency calculation was performed and a re-analysis of the data was reported the following year [45] with a better determination of the threshold elementary photoproduction amplitudes on nucleons. The data were re-analysed a

third time in 1988 [46] following improved measurements having been made on the proton by Mazzucato et al. [15].

In the early eighties, the Boston University group studied the gross features of photoproduction of π^0 mesons from targets of ^6Li, ^{12}C, ^{28}Si, ^{40}Ca, ^{nat}Cd, and ^{nat}Pb in the threshold region using the bremsstrahlung beam of the MIT Bates Linear Accelerator [47]. The two pion decay photons were detected by converting them in a thin lead foil and the resulting electron-positron pairs were detected in two plastic Čerenkov detectors. Four of these two-detector sub-systems were placed symmetrically on either side of the target producing a detector system with an efficiency relatively insensitive to the π^0 production angle except for the highest energies investigated. However, the number of data points for a single target was not adequate to unfold the yield curve to obtain a total cross section directly so experimental yields were compared with theoretical ones. The yields for all nuclei were seen to increase with energy at a rate faster than that predicted by simple coherent production which they suggested could be explained by incoherent contributions to the cross section where the nucleus was left in an excited state. Comparison of the yields from the range of nuclei measured indicated the production to scale as A^2 as was expected for coherent production where the elementary amplitudes of all nucleons add up coherently.

The first measurement of a total cross section for π^0 photoproduction in the threshold region with a tagged photon beam was reported by Jammes et al. [48] in 1989. The experiment utilised tagged in-flight positron annihilation monochromatic photons and an almost 4π Pb-glass π^0 detector. The data obtained for the $^4He(\gamma,\pi^0)$ reaction compared well with the Argan et al. data [46] in which bremsstrahlung yields were measured.

A series of total (γ,π^0) cross section measurements in the threshold region were made in the 1980's at Saclay [48–50] and Tomsk [51] on ^6Li, ^{12}C, and ^{40}Ca. The incoherent and quasi-free cross sections are both expected to be small in comparison with the coherent cross section in the first 10-20 MeV above threshold so these measurements could be done with relatively simple detectors that did not determine the energy of the detected π^0 meson. A typical set up was a box of Pb-glass Čerenkov detectors positioned closely around the target to detect the two π^0 decay photons in coincidence. The results confirmed the importance of the π^0-nucleus interaction and the need to carry out distorted wave calculations to explain the magnitude of the measured cross sections which were typically 20 % larger than the plane wave predictions (see section 1.3).

Differential Cross Section Measurements for ^4He

As stated previously, differential cross section measurements of the coherent (γ, π^0) process on ^4He do not require as high an energy resolution from the π^0 detector as measurements on other nuclei. It is also possible to carry out the measurement by detecting the recoil ^4He nucleus. For these reasons the initial progress with detailed studies of the differential cross section was largely confined to ^4He.

LeFrançois et al. obtained limited data on π^0 photoproduction in the Δ resonance region - measurements of back-angle differential cross sections only [52]. Measurements were obtained by detecting the recoil nucleus and this experiment, performed in 1970, gave believable cross sections at a few photon energies and pion angles.

Tieger et al. provided the first forward angle data for the reaction $^4He(\gamma, \pi^0)^4He$ in the Δ resonance region [53]. The π^0 was detected directly via its decay photons. The π^0 spectrometer employed consisted of two independent photon detectors, each consisting of two Pb-glass converter and multiwire proportional chamber arrays followed by total-absorption Pb-glass blocks. These made a precise ($\sim$4 mm) determination of the photon conversion points and a rough ($\sim$35 %) measure of the photon energies. Events were restricted to the symmetric two photon decay where the photon energies are roughly equal so the π^0 energy was determined primarily by the measured opening angle of the photons. The spectrometer energy resolution depended on E_π but was typically 9 MeV (FWHM) which allowed separation of the coherent process from the incoherent reactions of ^4He listed earlier. The production angle of the π^0 was determined with an uncertainty of $\pm 1.0°$. Differential cross sections were obtained for a limited number of laboratory angles (25°, 40°, 60°, 70°, and 80°) and were found to be in agreement with those of LeFrançois et al. [52]. A total cross section was obtained at $E_\gamma = 290$ MeV by integrating the measured angular distributions. However, because the data did not cover the whole angular range, an assumed shape for the angular distribution was used from the Δ-hole model of Koch and Moniz [24].

Anan'in et al. also measured the differential cross section for coherent (γ, π^0) production on ^4He in the Δ resonance region [54]. The recoil nucleus was detected in a helium streamer chamber in coincidence with one of the pion decay photons. The photon was detected in a Čerenkov γ-spectrometer of the total-absorption type located at an angle 41° to the bremsstrahlung beam. The gas of the streamer chamber was used as the target and as a medium in which the energy of the scattered nucleus was determined on the basis of range. They were unable to explain the experimental results quantitatively but qualitative agreement was obtained with the Δ-hole model of Koch and Moniz [24].

The reaction $^4He(\vec{\gamma}, \pi^0)^4He$ in the Δ resonance region was studied with the LEGS [34] tagged, polarised gamma ray beam by Bellini et al. [55]. The pion was

detected through its asymmetric decay in which one of the decay photons takes a large part of the pion's energy and the other low energy photon is emitted in the opposite hemisphere. The higher energy photon of the two pion decay photons was detected by a high resolution, cylindrical NaI(Tl) scintillator of 48 cm diameter by 48 cm deep. The lower energy photon was detected by eight NaI(Tl) bars $10 \times 10 \times 35\,\mathrm{cm}^3$ placed around the target with their axis parallel to the beam-line. Data were collected at six values of the pion angle (in the centre of mass frame) from 33° to 133° and divided into nine energy bins centred at incident photon energies from 206 to 322 MeV allowing differential cross sections to be compared with the data of LeFrançois et al. [52] and Tieger et al. [53], both of which were performed with bremsstrahlung beams. There was good agreement with both sets of previous experimental data.

Rambo et al. performed a similar experiment to that of Bellini et al. at the MAinz MIcrotron (MAMI) using the TAPS photon spectrometer and the Glasgow/Mainz tagged photon facility [56]. TAPS, a highly segmented array of BaF_2 crystals, is the best π^0 detector available in Europe at the present time (see section 2.4). The differential cross sections were measured over a larger range of photon energies (E_γ = 200-400 MeV) than Bellini et al. and covered all pion production angles. The high angular resolution of TAPS allowed the opening angle between the two decay photons to be used to separate the coherent from the incoherent π^0 photoproduction processes. For this purpose, use was made of the relation

$$\psi_{min} = 2\sin^{-1}\left(\frac{m_\pi}{E_\pi}\right) \tag{1.2}$$

between the minimum opening angle, ψ_{min}, that corresponds to the symmetric two photon decay and the π^0 energy, E_π, in the laboratory frame (see Appendix A.2.2). Since, as discussed earlier, all incoherently produced π^0 mesons from ^4He have at least 20 MeV less energy than those produced coherently for a given fixed incident photon energy, their opening angles, ψ, are shifted to distinctly higher values. This shift defines, via equation 1.2, a range of opening angles that only contains coherently produced π^0 mesons. The resulting differential cross sections were in general agreement with those of Bellini et al. [55] except for some deviations especially at the highest energies accessible in reference [55]. These extensive results were used to fix the parameterisation of the Δ-nucleus interaction in what is probably the best currently available theoretical treatment of the coherent (γ, π^0) reaction [57]. However, ^4He is such an "atypical" nucleon system that the chosen Δ-nucleus parameters may need revision if the model is to account for the present wider ranging data that will provide a more severe test of this model.

Differential Cross Section Measurements for A > 4 Nuclei

After the initial work of Davidson at MIT and Schrack at NBS, progress was very slow with most of the measurements performed on ^4He where, as described above, the lack of excited nuclear states enabled the separation of the coherent process from the incoherent processes even with the available poor energy resolution detectors. The next set of measurements on heavier nuclei was not performed until 1981 by Bellinghausen et al. The photon energy dependence of the (γ, π^0) cross section at pion angles below 10° was examined for ^4He, ^{nat}Li, and ^9Be [58], ^{12}C, ^{13}C, and ^{16}O [59] across the Δ-region. The bremsstrahlung beam of the 500 MeV Bonn synchrotron was used and the two decay photons of the π^0 were detected in a π^0 spectrometer consisting of two Pb-glass detectors with lead collimators and scintillation veto counters. The acceptance of the spectrometer was limited to small pion angles so that only the coherent π^0 production process would contribute because the momentum transfer was too small to excite the nucleus. A water target was used to investigate ^{16}O and in this case, the π^0 contribution from the proton was calculated and subtracted from the measured yield. Differential cross sections were obtained for ^{12}C and ^{16}O as a function of the incident photon energy scaled to a centre of mass pion angle of 10°. Measurements were also made with a ^{13}C target in order to investigate if the extra neutron compared to the ^{12}C target gave a measurable effect in the π^0 rate. The π^0 rates for the two carbon isotopes were compared and it was concluded that the coherent π^0 production on ^{13}C at small angles was very similar to that on ^{12}C.

In order to make detailed measurements of the coherent angular distribution, it is necessary not only to measure the pion direction but also the energies of the incident photons and the outgoing pions with a resolution of a few MeV. This energy information is needed to enable the separation of the coherent and incoherent yields that is required if the interesting detail of the angular distributions in the diffraction minima and at backward pion angles, where the incoherent process may dominate, is to be observed. This became possible with the advent of tagged photon facilities and the first such measurements were made by Arends et al. [6] using the tagged photon beam at the Bonn 500 MeV synchrotron. Measurements were performed of the (γ, π^0) reaction on ^{12}C covering the whole range of photon energies from threshold to 400 MeV. This work produced the first indications of the trends of the cross section with angle and energy. A scintillation counter was used as an active ^{12}C target in an attempt to separate coherent and incoherent π^0 production. The coherent differential cross section was strongly forward peaked whereas the cross section for incoherent production was rather flat with a slight decrease at forward angles. However, the π^0 detector employed (this consisted of a series of five cylindrical wire chambers covering a solid angle of nearly 4π: the first two acted as a charged particle veto, a lead converter

was positioned between chambers 2 and 3 and chambers 3-5 detected the resulting e^-e^+ pairs from the decay photons) did not have adequate π^0 energy resolution and coherent production could not be separated from transitions to excited bound states. Comparison with more recent results has shown that such incoherent processes make significant contributions to the measured yield in some kinematic regions. The apparent discrepancy found at backward pion emission angles between the result of the coherent Δ-hole model calculation of Koch and Moniz [24] and the experimental data was later found to vanish if incoherent contributions are added to the calculation.

Koch et al. performed two experiments in the threshold region on ^{12}C [60] and ^{40}Ca [31]. The tagged photon facility at Mainz was used, providing $E_\gamma = 158$-168 MeV, and the pion decay photons were detected using a segmented Pb-glass detector array with good photon position but poor photon energy resolution resulting in a pion energy resolution of around 9 MeV. This was not good enough to separate the coherent and the incoherent processes. An investigation of the $^{12}C(\gamma,\pi^0)$ reaction revealed the presence of incoherent contributions by examining the angular variation of the average emitted pion energy after an angle dependent correction for the nuclear recoil. The so-corrected pion energy was not constant as it should be for a coherent process but was decreased by 1-2 MeV for backward pion emission near threshold. This was a clear indication of excitation in the residual nucleus but the incoherent and coherent contributions could not be quantified. For ^{40}Ca, the variation in the pion decay photon opening angle with pion energy was used to obtain a separation of the coherent and incoherent processes. For a given pion energy the opening angle ψ between the two decay photons is distributed between a minimum value ψ_{min}, given by equation 1.2, and 180° with ψ_{min} being strongly favoured by phase space (Jacobian peak distribution). In incoherent pion production the energy of the emitted pion is reduced by the excitation energy of the nucleus, leading to

$$\psi_{min}^{\text{incoh}} > \psi_{min}^{\text{coh}} \tag{1.3}$$

Therefore, for example, the first excited state of ^{40}Ca is at 3.35 MeV so the minimum opening angle for incoherent production must be at least 4° larger than for coherent pion production. The typical excitation energy was said to be 8 MeV resulting in a difference in opening angle in the coherent and incoherent reactions of 9°. The opening angle resolution was 8°. A corresponding cut on the opening-angle distribution strongly selects coherent production but also results in a low efficiency in pion detection. However, there was good separation of the coherent events for ^{40}Ca and the resulting angular distribution demonstrated a clear diffraction minima for the first time. The magnitude of the cross section along with the shift in the position of the diffraction minima of the experimental data compared with plane wave

impulse approximation predictions (see section 1.3), confirmed the need to include the π^0-nucleus interaction in any theory of the process. The incoherent cross section was also determined by subtracting the obtained coherent cross section from the total cross section. The shape looked as expected, rather structureless with a much slower variation with pion angle than the coherent cross section.

Belousov et al. measured differential cross sections for the photoproduction of π^0 mesons on ^6Li, ^{12}C, ^{27}Al, ^{nat}Cu, and ^{nat}Cd as functions of incident photon energy in the Δ-region (E_γ = 300-450 MeV) at a mean pion centre of mass emission angle of 8.4°. The energy resolution of the π^0 meson ($\sim \pm 3.4\,\%$) was sufficient that the contribution of the incoherent process to the measured cross section was estimated at not more than $\sim 10\,\%$ allowing comparison of the measured cross sections with theoretical calculations of coherent production. The ^{12}C data gave cross sections considerably smaller than that of Bellinghausen et al. [59]. This was attributed to a large contribution from the inelastic process or to possible systematic errors in the determination of the pion detection efficiency in the latter's data. Belousov et al. concluded that there seemed to be an indication of a decrease of the width of the Δ resonance in photoproduction on account of its interaction with the nucleus and an indication of some increase of its mass. This contradicted the conclusions of Bellinghausen et al., which was attributed to the lack of data at incident photon energies above 400 MeV in reference [59].

Gothe et al. measured coherent π^0 photoproduction on ^{12}C and ^{13}C near the threshold region (used 170.1 MeV $\leq E_\gamma \leq$ 176.8 MeV) using the tagged photon facility at Mainz and produced absolute differential and integrated-over-angle cross sections [61]. The pion decay photons were detected in coincidence using the Giessen-Mainz π^0 spectrometer which consisted of two blocks, each comprising 8×11 Pb-glass modules, that could be adjusted in all three dimensions to optimise the π^0 detection efficiency and the angular resolution. The Pb-glass detectors had poor energy resolution (σ_π = 30.3 MeV) so event-by-event separation of the coherent π^0 production reaction was only possible by taking advantage of the good angular resolution ($\sigma_{\gamma\gamma} = 2.34°$) of the spectrometer. The data were restricted by setting the spectrometer to observe symmetrical pion decay into two photons. This reduced the energy resolution to σ_π = 2.91 MeV, allowing the suppression of the incoherent contributions to less than 0.6 % for ^{12}C and 1.1 % for ^{13}C. The integrated-over-angle cross sections extracted for ^{12}C showed the coherent cross section to be significantly smaller than the total cross section (obtained by accepting all pions whether they were produced coherently or incoherently) with the latter agreeing well with the results of previous experiments at lower energies where the coherent could not be separated [48, 50, 60]. Previously, the theoretical calculations of the coherent $^{12}C(\gamma,\pi^0)^{12}C$ cross section

could only be compared with total cross section measurements. Comparison with this data showed that the Distorted Wave Impulse Approximation (DWIA) calculations of Boffi et al. [62] and Chumbalov et al. [63] overestimated the measured coherent cross section in this energy region. The discrepancies were much stronger for ^{13}C where even the shape of the differential cross section was not reproduced. The ratio of the absolute coherent (γ, π^0) cross sections of ^{13}C to ^{12}C at forward angles agreed with the relative measurement of Bellinghausen et al. [59]. However, comparison of the total differential cross sections with the coherent ones revealed significant incoherent contributions at small pion angles for both targets which disagrees with the assumption of reference [59].

Schmitz obtained the first separation of the coherent and incoherent processes for ^{12}C in the Δ-region but only a small π^0 angular range ($\theta_\pi = 60 \pm 10°$) was measured [64]. The pion was detected through its asymmetric decay. The high energy photon was detected using large NaI crystals and an array of 61 BaF_2 detectors was used for the low energy decay photon. The pion energy resolution was 6-8 MeV (FWHM) which is better than that of Koch [60]. The coherent process was isolated over the whole Δ-region up to 430 MeV. In addition, the 4.4 MeV decay photons from the incoherent reaction populating the first excited state in ^{12}C were detected directly enabling the incoherent cross section to be determined. This measurement set the new standard for measurements in the Δ-region but because of the limited angular range it did not provide a strong test of the theoretical models.

Bergstrom et al. performed a series of measurements on ^{12}C [65], ^{2}H [66] and ^{6}Li [67] using the tagged photon facility at the Saskatchewan Accelerator Laboratory (SAL), Canada, in conjunction with the large acceptance calorimeter IGLOO [68]. All measurements were made within the region 25 MeV above threshold. The π^0 spectrometer IGLOO consists of a rectangular box of 68 Pb-glass detectors symmetrically arranged to define a hollow cave of dimensions $100 \times 40 \times 40$ cm. In this "closed" configuration the large geometric acceptance is exploited to perform total cross section measurements. Pion angular distribution measurements are performed by splitting IGLOO along a diagonal of the cave and retracting each L-shaped arm about 42 cm in order to enhance the angular resolution to the π^0 decay photons. The total cross section measurements for ^{12}C were in good agreement with previous results from Saclay [48, 50] and Mainz [60, 61]. However, the pion angular distributions were not unfolded from the intrinsic pion angular resolution of the π^0 spectrometer which was typically 25-35° (FWHM) but were analysed to obtain a measure of the incoherent (γ, π^0) transition strength to the 4.43 MeV (2^+) state. The ^{6}Li cross sections exceeded those of Glavanakov et al. [51] by as much as 50 % but the cross sections of the latter were determined by means of the bremsstrahlung-difference method while

the Bergstrom et al. measurements employed tagged photons. Bergstrom et al. took advantage of the cancellation of the spin-amplitudes in ^{12}C and extracted the elementary p-wave amplitude, $P_3^{(+)}$, from the ^{12}C data. The value obtained was in agreement with that of the free nucleon, i.e. there was no change of the basic amplitude when the reaction takes place in the nuclear medium.

The most recent measurements made on the (γ, π^0) reaction were from an experiment mainly intended to study $2\pi^0$ production. Krusche et al. performed measurements on ^{12}C, ^{40}Ca, ^{93}Nb, and ^{nat}Pb using the tagged photon facility at Mainz [69]. Incident photon energies throughout the Δ-region (E_γ = 200-400 MeV) were examined. The pion decay photons were detected using TAPS as it was at the time - 320 BaF_2 detectors as opposed to the current 522. Energy resolution deteriorates as pion energy increases so the separation of the coherent and incoherent processes becomes more difficult at high incident photon energies. However, separation was attempted by the "energy difference" analysis described by Rambo et al. for ^4He [56]. Contributions from breakup reactions were practically completely removed in this way but incoherent excitations to low-lying nuclear states were incompletely suppressed. A clear diffraction structure due to the nuclear form factor was seen for all targets and the approximate validity of the Plane Wave Impulse Approximation (PWIA) was demonstrated at the lowest incident photon energies around 220 MeV. Reasonable agreement was only obtained at higher energies with the Δ resonance model of Dreschel et al. [57] that takes the Δ-nucleus interaction into account. As stated earlier, the Δ-nucleus interaction parameterisation for this model was extracted from the ^4He data of Rambo et al.. Dreschel et al. suggested that the Δ-nucleus interaction saturates for ^4He. The data of Krusche et al. indicated that the Δ-nucleus interaction can be parameterised for heavy nuclei with the same potential parameters as for ^4He since the agreement between the model predictions and the data was very good for ^{12}C and ^{40}Ca and still reasonable for ^{nat}Pb.

1.1.2 Glasgow Experiment - Mainz 1999

In late 1999, a series of measurements of π^0 photoproduction were made at the tagged photon beam facility MAMI-B in Mainz, Germany on ^{12}C, ^{16}O, ^{40}Ca, and ^{208}Pb. The electron beam was used at a reduced energy of 405 MeV to obtain a photon energy resolution from the Glasgow Tagger of 1 MeV. The pions were detected via their decay photons using the detector array TAPS (originally a Two Arm Photon Spectrometer). The energy resolution of TAPS is good (pion energy resolution is about 3 MeV FWHM at incident photon energies around 200 MeV, [70, 71]) and a comparison between the incident photon energy and the total pion energy has been used successfully in an earlier experiment to separate the coherent and incoherent

processes as discussed in the previous section [69] (this method is described in detail in section 4.7.2). However, two large sodium iodide (NaI) detectors were introduced to attempt to detect the additional decay photons resulting from incoherent pion production when the nucleus returns to its ground state (the TAPS detector itself did not have a sufficient dynamic range to detect the nuclear decay photons at the same time as the high energy photons from the π^0 decay). It was hoped that this would aid the separation of the coherent process and maybe even enable the investigation of the incoherent processes. At the time of the experiment, TAPS consisted of 522 barium fluoride (BaF_2) crystals arranged to cover a wider pion angular range than that obtained by Krusche et al. [69] in order to facilitate the extraction of the total cross section.

The first results from ^{12}C and ^{40}Ca have been reported in a recent thesis [72]. The data presented here represents the first complete measurement of differential and integrated cross sections for ^{16}O and ^{208}Pb. Both are spin-zero nuclei for which both N and Z are magic numbers according to the shell model. Oxygen has been treated many times by theorists in their models [22,23,25,73–75] but there has been only one previous experimental measurement, performed by Bellinghausen et al. in 1982 [59] and that was made at only one pion centre of mass angle (see section 1.1.1). A pure ^{208}Pb target was purchased from ISOFLEX Isotopes, Moscow. As stated earlier, ^{208}Pb lead is potentially very interesting as it has a complete extra shell of neutrons and so could give new information on how the neutron distribution compares with that of the protons. The previous measurement was on natural lead [69] which is only 52.4 % ^{208}Pb and the other isotopes affect the resultant cross sections.

The range of nuclei studied should enable the A-dependence of the cross section to be determined. A more sophisticated analysis was performed on the ^{12}C and ^{40}Ca data from [72] for this A-dependence assessment.

Further details on the experimental set-up are given in chapter 2.

1.2 Neutral Pion Photoproduction

Yukawa proposed in 1935 that the strong force was carried by particles exchanged between nucleons [76]. These exchanged particles are called mesons and the lightest of the mesons, the π-meson or simply pion, is responsible for the major portion of the longer range (1.0 to 1.5 fm) part of the nucleon-nucleon potential. There must be three pions with charges of +1, 0 and -1 in order to satisfy all the varieties of the exchanges needed in the two-nucleon system. The pions have spin 0 and rest masses of 139.57 MeV (for $\pi^{\pm}$) and 134.98 MeV (for π^0) [77]. The single pion that is exchanged between two identical nucleons must be a π^0 but the neutron-proton interaction can

be carried by charged as well as neutral pions. Other mesons, including ρ and ω, contribute to the short-range nuclear interaction.

The pion is the lightest meson and as such it cannot decay into lighter strongly interacting particles by the strong interaction (characteristic lifetime 10^{-22} seconds). It must decay by the much slower electromagnetic or weak interaction and therefore with a much longer lifetime. The π^0 usually (branching ratio 98.798 %) decays electromagnetically into two gamma-rays in a time of the order of 10^{-16} seconds [77]. Thus it is detected via its decay products. Details on the detection of neutral pions in the present experiment are given in chapter 2.

1.2.1 Production on a nucleon

A photon incident on a nucleon couples to the nucleon electromagnetic current resulting in meson production if the photon energy is sufficiently high. The production of photomesons is dominated by the production of single pions and pion pairs for photon energies up to 1 GeV [30].

The main Feynman diagrams for single neutral pion photoproduction from a nucleon are shown in Figure 1.1. In the first two diagrams, (a) and (b), the photon interacts with the charge and the magnetic moment of the nucleon and the pion is "shaken off" after or before the absorption of the photon [78]. These two processes have different signs and almost cancel each other.

The mass of the Δ, which is involved in diagrams (c) and (d), is 1232 MeV which is around 300 MeV greater than the mass of both the proton and the neutron. In the process shown in Figure 1.1(d), the pion is emitted before the photon is absorbed which would require the intermediate Δ to be more than 400 MeV off its mass shell. Hence the contribution from this process is very small. The mass of the ω is 782 MeV which is much greater than the energy available in the experiment described here. Hence the contribution from the process illustrated in Figure 1.1(e) is also very small.

Therefore, the process shown in Figure 1.1(c) dominates at all incident photon energies except very close to the π^0 production threshold. This is because close to threshold there is not enough energy for the pion to have an orbital angular momentum but, for process (c), the pion must have an orbital angular momentum of $1\hbar$ as the Δ has spin $\frac{3}{2}$. Thus the contribution due to Figure 1.1(c) vanishes and the cross section is determined by the other processes shown in Figure 1.1.

1.2.2 Production on a nucleus

The elementary production operator for free nucleons is used as a starting point to describe nuclear pion photoproduction. Additionally, the modification of the produc-

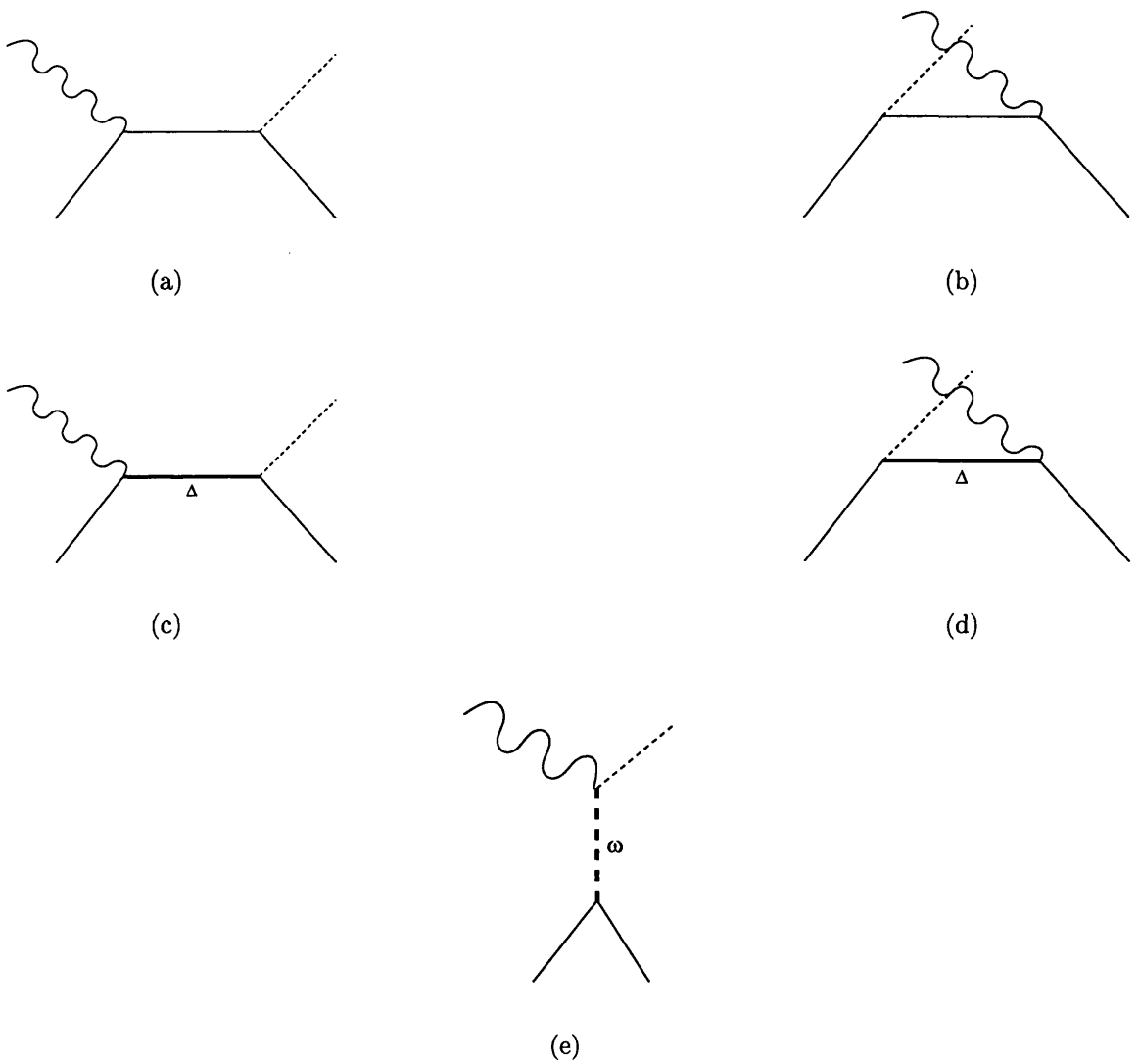

Figure 1.1: **The main Feynman diagrams contributing to neutral pion production on a nucleon:** (a) and (b) are the Born terms for single neutral pion photoproduction from a nucleon; (c)-(e) are the isobar and heavy meson diagrams for single neutral pion photoproduction from a nucleon. The production process is dominated by (c).

tion operator by the surrounding medium, the nuclear structure, and the interaction of the pion with the final nucleus have to be taken into account.

The characteristic features of nuclear pion photoproduction processes depend on the excitation energy of the residual nuclear system. The coherent reaction leaves the residual nucleus in its ground state with zero excitation. Pion production may also lead to discrete excited states of the residual nucleus. At higher excitation energy the nucleus can be excited to a continuum of particle unstable giant resonance states. At even higher excitation energy the pions are mainly produced on quasifree nucleons which are knocked out of the nucleus.

Coherent production of neutral pions is especially interesting as the coherent addition of the production amplitudes on all the nucleons provides a dramatic enhancement of the cross section for the ground state transition compared with the corresponding process for charged pions. For coherent pion production from even-even nuclei (0^+-ground state), angular momentum conservation implies that the neutral pion will be emitted as a p-wave ($l = 1$). Since parity is conserved, M1-photon absorption is dominant and this proceeds mainly via Δ-excitation apart from small Born term and ω-exchange contributions. A comparison of (γ, π^0) experiments on the proton and on complex nuclei can therefore shed light on the modification of the Δ in nuclear matter and on the final state interaction [60].

The cross section for a spin-zero nucleus with A nucleons can be written, neglecting π^0 final state interactions, as given in equation 1.4 (see section 1.3.1). This simple picture accounts quite well for the shape of the measured angular distributions. At small angles the shape of the differential cross sections is governed by the $\sin^2\theta$ term, at large angles and at high photon energy by the steep fall-off of the nuclear form factor ($F(q)$) with increasing momentum transfer (q). The form factors used in the theoretical models that will be compared with the experimental data presented here are shown as a function of q in Figure 1.2. These are based on the assumption that the matter distribution has the same shape as the charge distribution.

1.3 Theoretical Descriptions

The simplest theoretical description of pion photoproduction is that of the plane wave impulse approximation (PWIA). This assumes that the incident photon interacts only once and that there is no final state interaction (FSI) between the pion and the nucleus. The FSI was first taken into account by the distorted wave impulse approximation (DWIA). This theory treats the pion-nucleus attraction dynamically starting from the elementary pion-nucleon amplitude and uses a complex pion-nucleus optical potential to distort the outgoing wave.

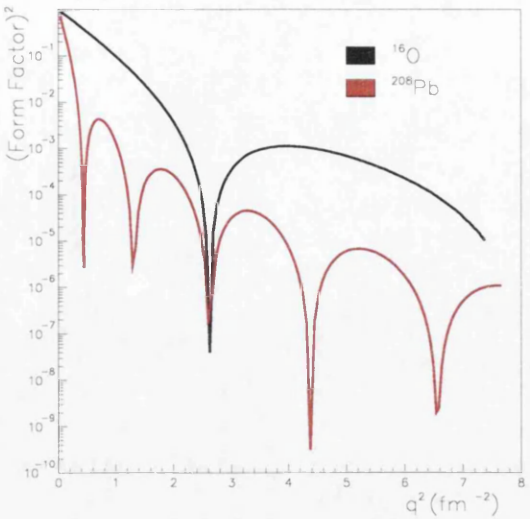

Figure 1.2: **The matter form factors:** The matter form factors used in the theoretical calculations of [79].

However, FSI is only one aspect of the medium effects due to the modification of the pion propagator in the nuclear medium. When the outgoing pion energy exceeds 100 MeV it becomes increasingly probable that its collisions with nucleons in the residual nucleus will result in Δ excitation and this can not be properly accounted for by an optical potential. The modification of the Δ resonance characteristics (width and position) inside the nucleus were first taken into account in the isobar doorway model (IDM) and the Δ-hole model. The latter takes the modifications of the Δ resonance properties into account by means of a Δ-nuclear potential constructed using explicit expressions for the contributions of the single particle states. The remaining part of the Δ-nuclear interaction was considered phenomenologically by a Δ spreading potential. Pauli blocking and Fermi-motion corrections were also included.

Recently the DWIA approach has been returned to and extended. Dreschel et al. [57, 80] have presented a calculation starting from their Unitary Isobar Model (UIM) for the elementary reaction and included a phenomenological parameterisation of the Δ self-energy. A relativistic non-local model including medium modifications, e.g. in the production operator of the Δ resonance, has been developed by Peters et al. [81].

Further details of these theoretical treatments of neutral pion photoproduction are given in the remainder of this section.

1.3.1 The Plane Wave Impulse Approximation

The PWIA is the simplest theoretical description of coherent pion photoproduction. Final state interactions of the photoproduced pion with the surrounding nucleons are neglected, i.e. the pion leaves the nucleus as a plane wave. The coherent cross section for spin-zero nuclei can be written, neglecting any FSI and medium effects as [57]

$$\frac{d\sigma_{PWIA}}{d\Omega}(E_\gamma, \theta_\pi) = \frac{s}{m_N^2} A^2 \frac{d\sigma_{NS}}{d\Omega}(E_\gamma^*, \theta_\pi^*) F^2(q_A) \tag{1.4}$$

where

E_γ	=	incident photon energy [MeV]
θ_π	=	pion polar angle in the photon – nucleus centre of mass system [radians]
A	=	atomic mass number
m_N	=	nucleon mass [MeV]
$F(q_A)$	=	nuclear matter form factor
q_A	=	momentum transfer [MeV/c]
s	=	square of the total energy of the photon – nucleon pair [MeV^2]
E_γ^*	=	photon energy in photon – nucleon centre of mass system [MeV]
θ_π^*	=	pion angle in photon – nucleon centre of mass system [radians]

The photon energy and pion angle in the photon-nucleon centre of mass system (E_γ^* and θ_π^*) are evaluated in the factorisation approximation from

$$\overrightarrow{P_N} = -\frac{A-1}{2A}\overrightarrow{q_A} \tag{1.5}$$

where the average momentum $\overrightarrow{P_N}$ of the nucleon follows from the momentum transfer $\overrightarrow{q_A}$ to the nucleus.

For a spin-zero nucleus all the spin-dependent terms in the elementary cross section cancel and only the spin-independent elementary cross section contributes. This is given by [57]

$$\frac{d\sigma_{NS}}{d\Omega}(E_\gamma^*, \theta_\pi^*) = \frac{1}{2}\frac{q^*}{k^*}\left|f_2(E_\gamma^*, \theta_\pi^*)\right|^2 \sin^2(\theta_\pi^*) \tag{1.6}$$

with the pion and photon momenta q^*, k^* in the photon-nucleon centre of mass system. The dominant process contributing to the spin-independent amplitude $f_2(E_\gamma^*, \theta_\pi^*)$ is the Δ excitation.

Chew et al. [82] used dispersion relations to obtain a general amplitude for photoproduction from nucleons. Even though a number of simplifying assumptions had to be made, the cross sections calculated with this amplitude (hereafter called the CGLN-amplitude) compared well with the available data on the reactions $\gamma + p \rightarrow \pi^+ + n$

and $\gamma + p \rightarrow \pi^0 + p$. In 1967 Berends et al. [83] used dispersion theory to predict the elementary pion photoproduction multipole amplitudes (hereafter called the BDW-amplitude), basically along the same lines as CGLN but carried out in much more detail. Applications to nuclear photoproduction were made by Devanathan and Ramachandran [84–87] to study charged and neutral pion production from deuterons and later from heavier nuclei. Their formalism was based on the impulse approximation using the CGLN-amplitude for the photoproduction operator, and harmonic oscillator wavefunctions for the nuclear states. Final state interactions (FSI) between the pion and the nucleus were not considered explicitly but simulated in a phenomenological way by the surface production model. In this model it is assumed that pions produced inside the nucleus are reabsorbed and therefore contributions to the cross section come only from the production of pions in the peripheral regions of the nucleus. For the first time transitions to discrete nuclear states were considered in detailed microscopic shell model calculations.

In the work presented here, comparisons with the PWIA theory were made using the CGLN-amplitude f_2 taken from a unitary isobar analysis of pion photoproduction and averaged over proton and neutron numbers [69, 80].

The characteristic features of the PWIA are that its magnitude is proportional to the square of the number of nucleons, and that the shape of the differential cross section is described by the square of the form factor and modulated by the $\sin^2(\theta^*_\pi)$ term. Krusche at al. have recently demonstrated the approximate validity of the PWIA for low incident photon energies [69]. At higher incident photon energies, PWIA does not describe the reaction well because significant final state interactions occur due to the strong interaction between the pion and the nucleus.

1.3.2 The Distorted Wave Impulse Approximation

The DWIA group of models aims at the study of the pion-nucleus interaction and the in-medium properties of the pion. The starting point is the elementary pion-nucleon amplitude and the FSI of the pion in the nuclear medium is taken into account but medium modifications of the resonance properties are neglected. The necessary nuclear structure information can be adopted directly from electron-scattering form factors. Early calculations took the FSI of the pion into account dynamically by a complex pion-nucleus optical potential which distorts the outgoing pion wave (changes its wavelength and introduces damping). The distorted wavefunction of the pion was obtained in position coordinate space by solving the Klein-Gordon equation with an optical potential for every partial wave that significantly contributes to the cross section.

The optical potential plays a crucial role since it takes care of the corrections

due to the interaction of the propagating particle with other nucleons in the nuclear medium, Pauli blocking, and binding energy effects. These are all essential for an off-shell extrapolation but are ignored in PWIA. In coherent (γ, π^0), the general shape of the angular distributions is mainly determined by the nuclear density distribution but the absolute size of the theoretical cross section depends sensitively on the optical parameters chosen. The pion optical potential of Stricker et al. [88, 89], where good fits to low-energy pion scattering on light nuclei were achieved, has been used by a number of authors [62, 73]. It has the basic form suggested by Kisslinger [90]:

$$V(r) = \frac{-2\pi}{\mu}\left[q(r) - \nabla\alpha(r)\cdot\nabla\right] \tag{1.7}$$

where $\mu = \frac{m_\pi m_T}{m_\pi + m_T}$ is the reduced mass of the pion with m_π and m_T the mass of the pion and the target respectively. The functions $q(r)$ and $\alpha(r)$ are proportional to the nuclear matter density $\rho(r)$ through a factor related to the pion-nucleon s- and p-wave scattering length respectively.

Saunders was the first to study the effect of the FSI between the pion and the residual nucleus explicitly using an optical model [43]. His calculations for coherent pion production from ^{12}C, ^{40}Ca and ^{208}Pb yielded results that were much lower than the experimental data available at the time [3] due to the lack of reliable pion-nucleus optical potentials. This was interpreted by some authors as the failure of the DWIA theory to explain the coherent π^0 production from nuclei and thereby stimulated other approaches to this problem, namely the isobar doorway model (IDM) and the Δ-hole model (see next section).

Girija et al. performed DWIA calculations on ^4He, ^{12}C, ^{16}O, and ^{40}Ca in 1983 and found good agreement with the available data [73]. Their calculations also compared numerically with other calculations using the IDM and the Δ-hole model implying that these calculations all include the medium effects on the production operator and the final state interactions to the same extent [30].

A large variety of results were produced as a result of different choices being made on how to use the free-nucleon amplitude in a nuclear environment and selection of the pion-nucleus optical potential [43, 62, 73, 75, 91]. More recent calculations have been carried out in momentum space [63, 92, 93] with the advantage that the Fermi motion of the nucleons inside the nucleus can be taken into account and that the distortion of the pion wavefunction can be related directly to the pion-nucleus interaction.

1.3.3 The Isobar Doorway Model and the Δ-hole Model

A different approach for a theoretical description of π^0-photoproduction from complex nuclei uses the fact that the dominant feature of intermediate energy photon-induced

reactions is the excitation of the Δ resonance. Subsequently, the phenomenological isobar-doorway model (IDM), which treats the isobars[3] as nuclear constituents, was employed for a study of the reaction in ^{12}C using the isobar-nuclear form factor obtained by fitting pion-nucleus elastic scattering data [94]. A dip in the angular distribution corresponding to the first diffractive minima of the pion-nucleus elastic scattering cross sections (around 50°) was found for an incident photon energy of about 250 MeV. This was a consequence of only having a single form factor parameterising the total amplitude. However, the IDM did give substantial cross sections for large angles as is seen in the experimental data. The model was refined by modifying the transition operator to account for many body effects [25]. This modification adopted the same method as that employed for the pion-nucleus optical potential [95] and also took into account the non-locality associated with the isobar propagation and recoil corrections. A fairly good fit was obtained to the then existing data for π^0 production from ^{12}C [3] and ^4He [96]. However, since the ^{12}C data is known to have been contaminated with contributions from incoherent processes, this agreement is not necessarily a sign of the success of the model.

Another theoretical approach similar to the IDM is the Δ-hole model. This studies the in-medium properties of the Δ resonance with special attention to the Δ and π dynamics but mostly without non-resonant contributions in the elementary production process [22–24, 27, 74]. It has been used mainly in the Δ resonance region with considerable success [23, 24].

The DWIA assumes that the pion is produced on one nucleon and describes the effect of the other nucleons as a mean field in which the pion propagation takes place. It assumes that the properties of the Δ particle that takes part in the production process are the same as those of a free Δ particle so that the elementary amplitude is unaffected by the nuclear medium.

The basic hypothesis of the Δ-hole model is that the Δ is a nuclear quasi-particle which can be treated as a separate nuclear species on an equal footing with the nucleon, i.e. the Δ particle interacts strongly with the other nucleons inside the nucleus. Modifications of the properties of the Δ (change in the mass and width of the Δ resonance) are taken into account using a complex potential to parameterise the interaction of the Δ-hole (the Δ and the missing nucleon) with the nucleus. The result is a reduced cross section compared with the PWIA calculation, which has been shown to compare favourably with experiment in the Δ resonance region [24].

In the Δ-hole formalism of Koch and Moniz [24], the Δ-hole Hamiltonian ($H_{\Delta h}$) incorporates the Δ propagation effects through the kinetic energy operator (K_Δ) and the binding effects through the potential (V_Δ) and hole energy (H_{A-1}) in the

[3]Isobars are excited nucleon states of isospin $I = \frac{1}{2}(N^*)$ and $I = \frac{3}{2}(\Delta)$.

Δ-Hamiltonian (H_Δ):

$$H_{\Delta h} = \gamma(E)H_\Delta + \delta W + W_\pi + V_{sp} \tag{1.8}$$

where

$$H_\Delta = K_\Delta + V_\Delta + H_{A-1} \tag{1.9}$$

Pauli blocking of the Δ decay in the nuclear medium is given by δW. This produces a substantial reduction in the free Δ width in nuclei, because the intermediate decay will be partly blocked by the nucleons in occupied states, and shifts the resonance up in energy. The term W_π describes the intermediate pion propagation in the presence of the nuclear ground state and corresponds to multiple scattering or, equivalently, to iteration of the optical potential in pion-nucleus scattering. Taken together, these terms constitute the full first order optical potential, including binding, recoil, and exchange effects and are evaluated microscopically in the space of the Δ-hole configurations. In contrast V_{sp}, the spreading potential, is a phenomenological term that represents coupling to multi-hole intermediate channels, and in particular to states reached by pion absorption via the mechanism $\pi NN \rightarrow \Delta N \rightarrow NN$. It is taken to be a complex (optical) potential for the Δ proportional to the local density. Although V_{sp} itself is energy independent, its effect on the photoproduction amplitude has a strong energy dependence. For example, it increases damping of the pion wavefunction far from the resonance and decreases it near the resonance.

Oset and Weise developed a microscopic approach for the calculations of the Δ-nuclear interaction [22]. Medium effects were considered in terms of the Δ self-energy in the nuclear medium calculated using a microscopic many-body framework. The Δ self-energy contained Pauli corrections resulting from the partial blocking of the Δ-decay into occupied nucleon states, absorption corrections that take into account the coupling of the Δ-hole states to the 2p-2h continuum (the main channel for π-absorption) and other rescattering corrections (reflection terms: where the π from the Δ-decay is allowed to rescatter resonantly from the nucleus). Carrasco et al. suggested a less sophisticated approach based on the local density approximation [27] that was able to separate contributions of the quasielastic, two-, and three-body pion absorption processes. Both these models were quite successful in describing pion photoproduction on heavy nuclei.

Takaki et al. extended the Δ-hole approach to incoherent π^0 photoproduction where the nucleus is excited to a discrete state [26]. The nuclear production amplitude was considered in two parts:

$$T^{\gamma\pi^0} = T_{NR} + T_\Delta \tag{1.10}$$

where T_{NR} is the non-resonant production part containing background terms and T_Δ

is the Δ-part of the the amplitude. The former was treated in the DWIA and the latter was calculated in the Δ-hole formalism. The data of Arends et al. [6] was compared with the coherent calculation and with the calculation of the coherent plus contributions from the three lowest ^{12}C states. The coherent alone did not describe the data: the calculated cross section was too low in the peak area and dropped off faster with increasing θ_π. The incoherent cross sections, mainly from the 2^+ and 3^- states, gave a large contribution at larger angles, where the transition form factor peaks. Due to the transverse nature of the photon coupling, the elementary pion-photoproduction amplitude is proportional $\sin\theta_\pi$. Therefore, π^0 photoproduction is favoured at larger angles where, however, the coherent form factor is much smaller. The incoherent form factor grows with increasing θ_π, hence the $\sin\theta_\pi$ helps to enhance the incoherent photoproduction cross section. The combined coherent and incoherent cross section gave a better description of the experimental data.

1.3.4 The Δ Resonance Energy Model

The most recent development in the theoretical description of neutral pion photoproduction on nuclei is the Δ resonance energy model (DREN) of Dreschel et al. [57,80].

The DWIA gives a good description of the neutral pion photoproduction process for photon energies close to threshold but the optical potential that represents the propagation of the π^0 is not enough in the resonance region. It is necessary to put in explicitly that as the pion propagates it changes from being a pion by combining with a nucleon to form a Δ. The IDM and Δ-hole models consider the Δ-nucleus interaction and have the advantage that they provide a clear visual picture of the production, propagation and the decay of the Δ within the nucleus. However, they are greatly restricted to the energy region where the isobar contribution dominates.

The DREN model uses the DWIA approach and extends it to include the medium modification of the Δ resonance properties via a parameterisation of the Δ self-energy which modifies the effective mass of the Δ. This offers the possibility of a model that describes pion production at all photon energies.

The Δ self-energy was fitted using data from the $^4He(\gamma,\pi^0)^4He$ reaction [56,57] and this single parameterisation is assumed to be suitable for calculations on all nuclei. Dreschel et al. have compared their prediction with available $^{12}C(\gamma,\pi^0)^{12}C$ data [6,64] which suggests that the Δ-nucleus interaction has already saturated for ^4He leading to the conclusion that this assumption is valid. This has been confirmed by recent measurements by Krusche et al. in the resonance region on ^{12}C, ^{40}Ca, ^{93}Nb, and ^{nat}Pb [69] where this theoretical model gave the best agreement with the data.

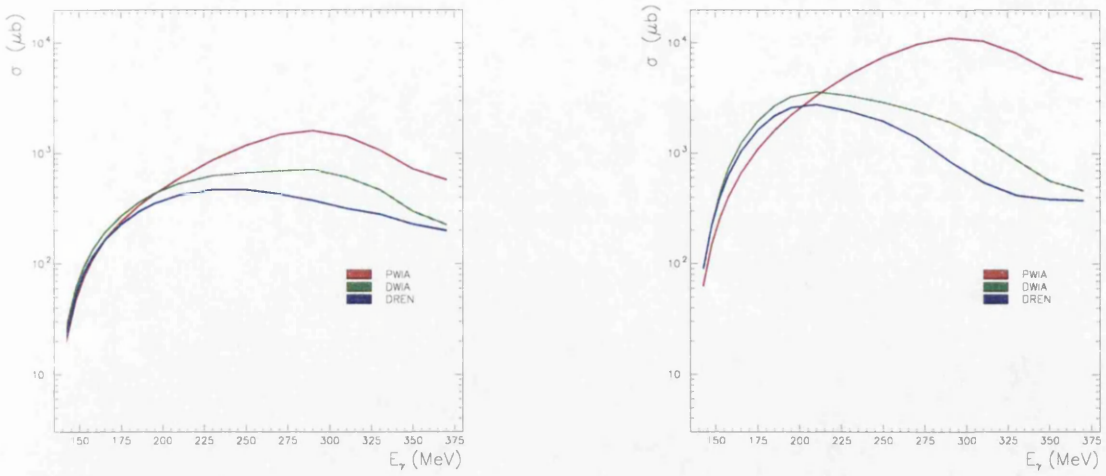

(a) ^{16}O (b) ^{208}Pb

Figure 1.3: **Theoretical calculations of σ:** (a) ^{16}O, (b) ^{208}Pb; from [79].

1.3.5 Overall Trends of the Theoretical Predictions by Kamalov

The recent calculations by Kamalov [79] are by far the most comprehensive available giving the basic PWIA result and the effects of pion distortion (DWIA) and the Δ-nucleus interaction (DREN) for four nuclei, ^{12}C, ^{16}O, ^{40}Ca, and ^{208}Pb spanning the periodic table.

Figure 1.3 shows the $^{16}O(\gamma,\pi^0)^{16}O$ cross section and the $^{208}Pb(\gamma,\pi^0)^{208}Pb$ cross section, the red plot is for the PWIA calculation, the green is for the DWIA calculation, and the blue is for the DREN calculation, all from [79].

Pion wave distortion from rescattering modifies the total PWIA cross section in an energy-dependent manner. The cross sections obtained with the DWIA are higher than the cross sections obtained with the PWIA for incident photon energies up to about 195 MeV for ^{16}O and up to about 215 MeV for ^{208}Pb, due to the attractive p-wave pion-nucleus interaction, but then decrease at higher incident photon energy due to absorption of the pion. The behaviour of the dispersive and the absorptive parts are caused primarily by the same mechanism: Δ resonance formation in the nucleus [91]. The mechanism behind the attractive real part of the DWIA optical potential is the scattering of the pion from a single nucleon and this is dramatically increased in the Δ resonance region. The absorptive imaginary part however is the result of several mechanisms such as nucleon knock-out, excitation of nuclear states, and two-nucleon processes. At very low E_γ some of the absorptive channels are not yet available resulting in a small imaginary part of the potential which allows the

attractive real part to enhance the coherent cross section. As E_γ increases, specifically in the Δ resonance region, a larger number of absorptive channels become available leading to a large dampening of the cross section. Although the attractive part also increases around the Δ resonance region, this increase is more than compensated by the absorptive part, which greatly reduces the probability for the pion to interact elastically with the nucleus. At any specific E_γ, the reduction in the cross section is larger for ^{208}Pb than for ^{16}O because it is a bigger nucleus.

The cross sections obtained with the DWIA are higher than the cross sections obtained with the DREN at all incident photon energies but the difference is less pronounced up to 180 MeV for both nuclei, corresponding to pion energies up to about 50 MeV. In this region, the interaction between the pion and the nucleus is not very strong and can be accounted for adequately by treating it as a mean field in which the motion of the pion can be calculated. For pion energies above this the interaction is too strong and this approximation is no longer valid. The Δ which is created must be introduced specifically into the calculation. The reduction in the cross section produced by the addition of the medium modification of the Δ resonance properties has a strong E_γ-dependence and this reduction has its maximum at the peak of the Δ resonance after which the difference between the DWIA and DREN calculations decreases again.

The peak in the cross section gives information on the Δ resonance. The PWIA gives the same Δ resonance shape as that obtained from pion production on nucleons. The shape remains the same for all nuclei and the magnitude simply scales proportional to A^2. Figure 1.4 shows the total cross sections for the DWIA and DREN calculations for coherent pion photoproduction on ^{12}C, ^{16}O, ^{40}Ca and ^{208}Pb. The DWIA gives the same peak position as the PWIA but a reduced strength. However, the E_γ-dependent pion absorption in the DWIA is stronger with increasing nuclear size and this for ^{208}Pb, and to a lesser extent for ^{40}Ca, appears to shift the peak position of the total cross section. The DREN does shift the peak position, i.e. there is medium modification of the Δ, but the large pion absorption dominates everything for ^{208}Pb (and for ^{40}Ca) resulting in a maximum in the cross section that is no longer at the peak of the "shifted" resonance.

The situation for the angular distributions is, in general, more complicated than for the total cross section since pion distortion modifies the interference between the competing partial waves which alters the angular dependence of the differential cross sections, although the overall shape is still determined by the form factor. Figure 1.5 shows a comparison of the theoretical differential cross sections, again for the $^{16}O(\gamma,\pi^0)^{16}O$ reaction and the $^{208}Pb(\gamma,\pi^0)^{208}Pb$ reaction, for incident photon energies of 200 MeV and 350 MeV. The PWIA result is proportional to the Fourier transform

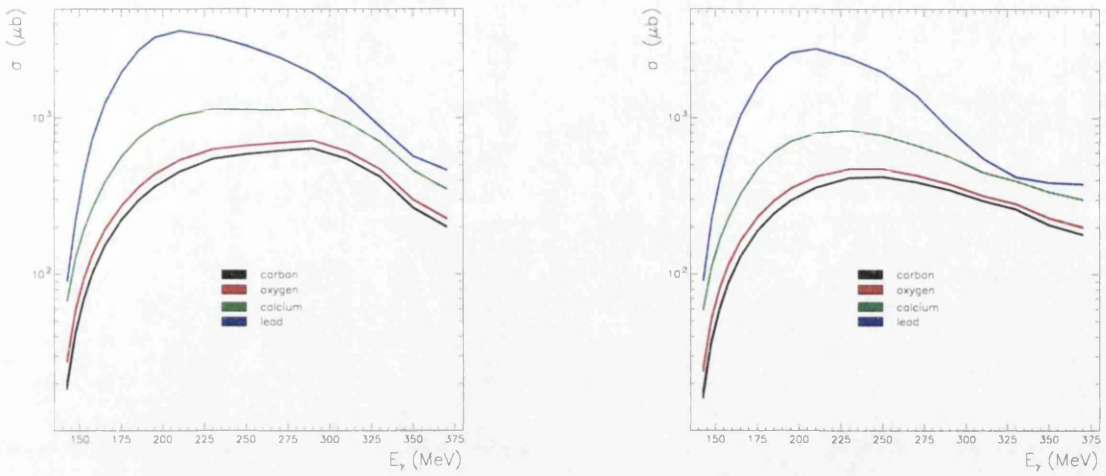

(a) DWIA (b) DREN

Figure 1.4: **Theoretical calculations of σ for ^{12}C, ^{16}O, ^{40}Ca and ^{208}Pb:** (a) DWIA calculation, (b) DREN calculation; from [79].

of the nuclear density with its characteristic diffraction pattern. The rapid decrease of the calculated coherent cross section is caused by the ground-state form factor.

For the DWIA, the real part of the optical potential causes a bending (refraction) of the pion paths as they leave the nucleus. Therefore, each E_γ, θ_π combination can no longer be associated with a unique q (momentum transfer) resulting in the smearing out of the minima of the cross sections for this model compared with the PWIA. This angular smearing also means that the cross section is transferred from low q (where the cross section is large) to high q (where it is small) and so the relative heights of the second, third, etc. maxima in the cross section are bigger in the DWIA than in the PWIA.

The maxima and minima for the DWIA calculation shift towards smaller pion lab angles with increasing incident photon energy because the pion-nucleus potential is attractive. This attractive potential means, in general, that the momentum transfer, q, calculated from the reaction kinematics is less than the "true" momentum transfer, $q\prime$, at the instant the reaction takes place and so the features of the cross section determined by the form factor (which depends on $q\prime$) appear at lower E_γ and/or θ_π than that calculated from the reaction kinematics. This general result is reversed if $p_\pi < p_\gamma \cos\theta_\pi$[4], where p_π, p_γ and θ_π are the pion momentum, incident photon momentum, and pion angle respectively in the centre of mass frame. This is possible for small θ_π at E_γ close to threshold where p_π is small. This effect is demonstrated in Figure

[4]The general case is $p_\pi > p_\gamma \cos\theta_\pi$.

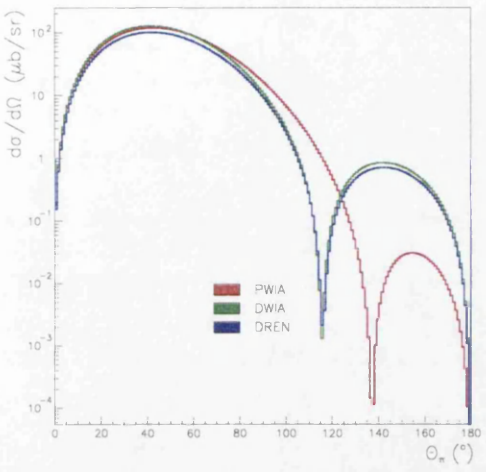

(a) ^{16}O

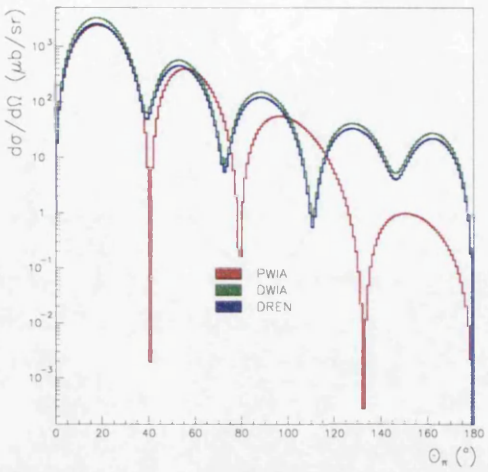

(b) ^{208}Pb

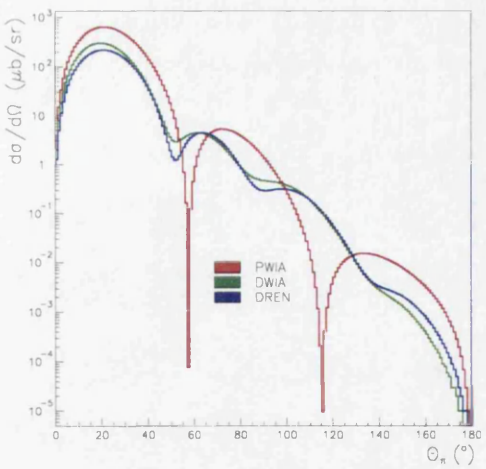

(c) ^{16}O

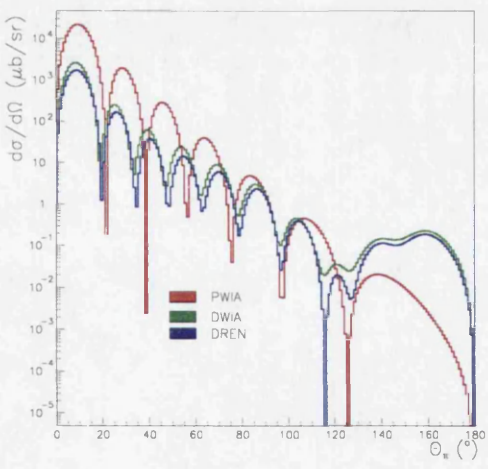

(d) ^{208}Pb

Figure 1.5: **Theoretical differential cross sections** for ^{16}O (a & c) and ^{208}Pb (b & d) at incident photon energies of 200 MeV (a & b) and 350 MeV (c & d) from [79]

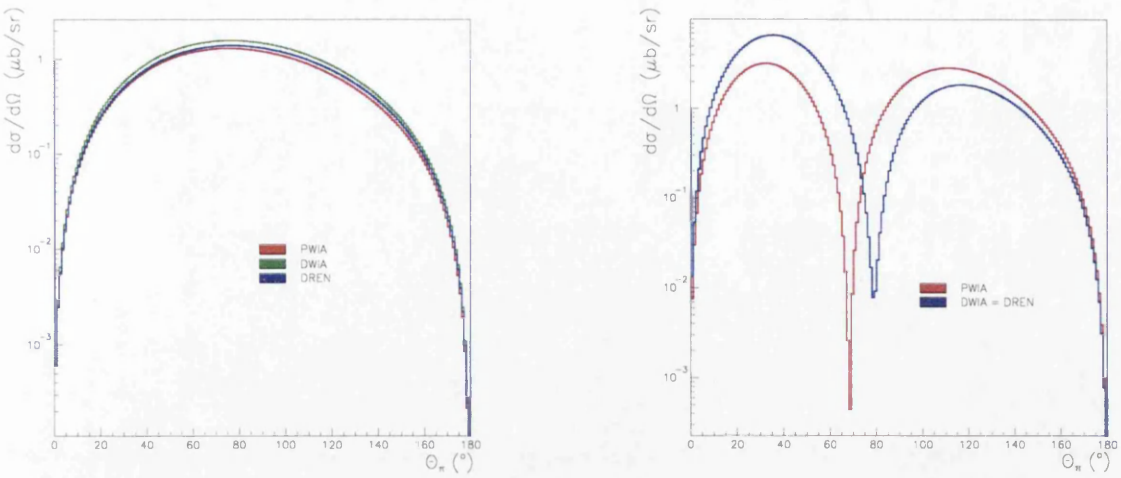

(a) ^{16}O (b) ^{208}Pb

Figure 1.6: **Theoretical differential cross sections near threshold:** At low incident photon energies the diffractive behaviour disappears for ^{16}O and is reduced for ^{208}Pb. The calculations of [79] are shown for $E_\gamma = 140\,\text{MeV}$.

1.6(b) which shows the calculated differential cross sections for the $^{208}Pb(\gamma,\pi^0)^{208}Pb$ reaction close to threshold; the minimum of the DWIA calculation is at a larger value of θ_π than that of the PWIA.

With decreasing incident photon energies, the diffractive behaviour disappears because the range of the recoil momentum of the nucleus gets smaller and does not allow appreciable variations of the nuclear form factor to be explored. The angular distribution is therefore dominated by the $\sin^2\theta_\pi$ behaviour due to the transition operator, with the maximum shifted forwards by the form factor. This effect is demonstrated in Figure 1.6(a) which shows the calculated differential cross sections for the $^{16}O(\gamma,\pi^0)^{16}O$ reaction close to threshold.

The cross sections at all incident photon energies for ^{208}Pb are larger and show more, well defined diffraction minima than those for ^{16}O. This is a consequence of the larger nuclear size of ^{208}Pb, since both the maxima and the minima of the nuclear form factor occur at a momentum transfer which is inversely proportional to the nuclear radius, i.e. scales with $A^{-\frac{1}{3}}$ (see Figure 1.2).

The effect of the Δ-nucleus interaction on the angular distribution is minor. At low incident photon energies the interaction between the pion and the nucleus is not very strong resulting in no difference between the DWIA and DREN calculations for ^{208}Pb close to threshold.

The most recent measurements made on coherent neutral pion photoproduction indicated that the DREN model provides the best description of this process [69].

Comparison with the present data which cover a wider pion angular range than that obtained by Krusche et al. [69] and extend the range of incident photon energies down to threshold will provide a further test of this model.

Chapter 2

Experimental Details

2.1 Introduction

Since the lifetime of a π^0 meson is short (10^{-16} seconds) it is detected by the observation of the two photons produced in 98.8% of decays [77]. The measured energies and directions of the two photons are then used to calculate the energy and direction of the π^0 that produced them. The accuracy with which the π^0 energy and direction are known depends upon the accuracy with which the photon detector determines the photon momenta.

The work described in this thesis was performed at the electron microtron MAMI (MAinz MIcrotron) of the Institüt für Kernphysik, University of Mainz, Germany. The Glasgow photon tagging spectrometer was used together with the high resolution photon spectrometer TAPS as shown in Figure 2.1. The setting up and operation of the experiment was performed by members of the TAPS/A2 collaboration that included members of the Nuclear Physics groups of the Universities of Glasgow, Giessen, Mainz, Saskatchewan, Edinburgh, and the Massachussets Institute for Technology.

The MAMI accelerator was set to produce a 405 MeV 100 % duty cycle electron beam that was steered to a thin nickel radiator producing bremsstrahlung photons. The Glasgow photon tagging system, consisted of a dipole magnet and a 352 channel focal plane detector for the detection of the residual electrons. The photon beam was collimated on exit from the radiator and induced photonuclear reactions in a target placed downstream from the collimator. Decay photons from π^0-photoproduction were detected in the large segmented barium fluoride detector array, TAPS, arranged in blocks in the horizontal plane around the target position. A large sodium iodide detector was positioned above and a second one below the target to attempt to identify characteristic decay photons from incoherent processes.

2.2 The Mainz Microtron - MAMI

The Mainz Microtron MAMI is a cascade of three normal conducting microtrons (RTM1, RTM2, and RTM3) with a 3.5 MeV injector linear accelerator (linac) and is shown in Figure 2.1. The first two stages were successfully operated as MAMI-A until 1987, providing electron beams in the range 14-187 MeV. The third stage became operational in 1990 and increases the electron beam from 180 MeV to 855 MeV in 15 MeV steps. The three stages are named MAMI-B and offer a 100 % duty cycle, low emittance and high stability continuous electron beam, with a resolution of 60 keV at currents up to about 100 μA [97].

A racetrack microtron consists of a linac situated between two uniform field bending magnets which recirculate the electrons through the accelerating section. In the linac, the electrons are accelerated by the axial electric component of a standing wave in a series of standing wave cavities for which a set of phase locked klystrons generate the radio frequency (RF) power. In each turn, the electrons pass through the same accelerating section situated between the magnets. There are a total of 14 turns in the first stage, RTM1, after which the electrons are accelerated to 14 MeV. The electrons then enter stage two, RTM2, where they are accelerated through 51 turns to reach an energy of 180 MeV. In the third and final stage, RTM3, the electrons are accelerated through 90 turns to reach an energy of 855 MeV. At the last chosen turn an extractor magnet deflects the beam into the beam handling system which subsequently guides it to the bremsstrahlung radiator.

For each microtron, the radius of the orbit of the electron in the magnetic field of the dipoles increases as its energy increases with each recirculation. Thus each return path is spatially separated. Higher energy electrons have a larger orbit to circulate than those of lower energy. The difference in the path lengths is arranged to be an integer number of RF wavelengths to ensure all the electrons are sent into the accelerator in phase.

Racetrack microtrons have an important feature - inherent phase correction. If an electron becomes displaced from the resonant energy an automatic re-adjustment takes place. Electrons of energies that are too high travel in an orbit of greater radius and so take slightly longer to arrive back at the accelerating field. As a result, they are slightly out of phase with respect to the accelerating field and hence are not accelerated by as much as the electrons of the correct energy. Similarly electrons of energies that are too low are over-accelerated on subsequent passes through the accelerating section. This feed-back mechanism, together with the energy loss due to synchrotron radiation suffered by all electrons, is responsible for compressing the energy spread of the MAMI-B final beam to $\Delta E \sim 60\,\text{keV}$ FWHM. It also results in a very low emittance beam (i.e. spot size and divergence).

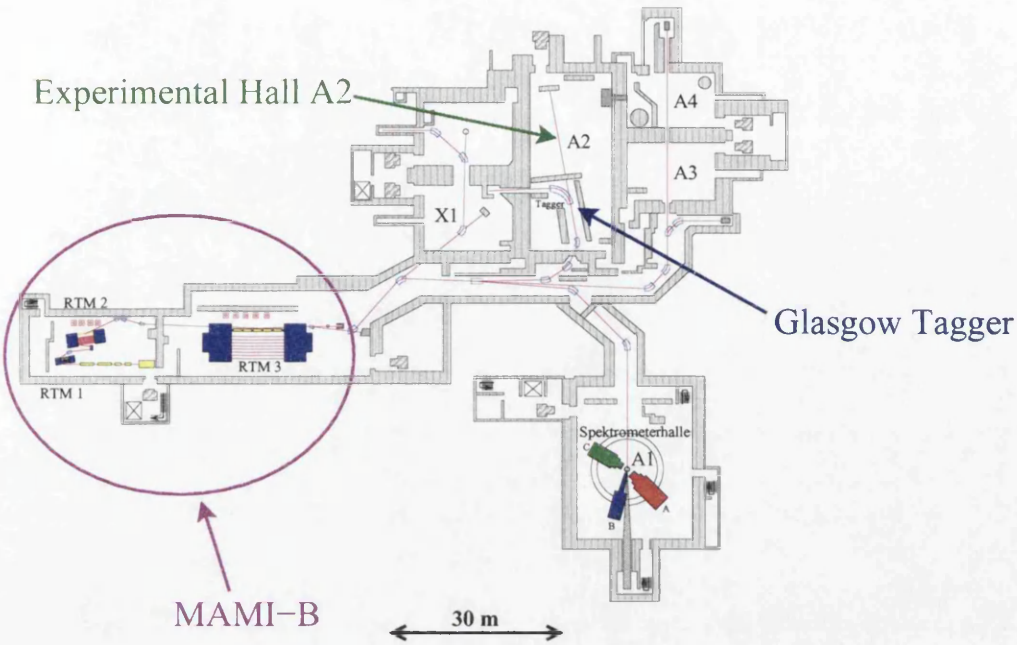

(a) The Mainz experimental facility.

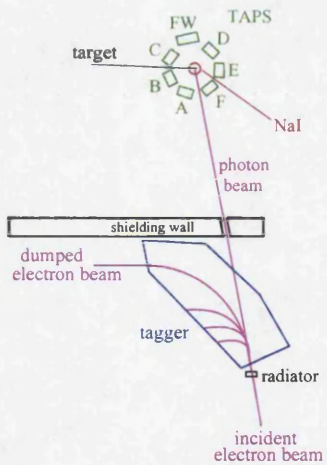

(b) Schematic of the tagger and the TAPS set-up (not to scale).

Figure 2.1: **The Mainz experimental facility:** (a) The Mainz Microtron MAMI-B serves a number of experimental halls. (b) The work described here was carried out in Hall A2 that houses the Glasgow photon tagging spectrometer. [Figure 2.1(b) courtesy of [72]]

After its extraction from RTM3, the beam is transported through various dipole steering and quadrupole focusing elements to the A2 hall tagged photon facility.

2.3 The Glasgow Tagging Spectrometer

The quality of experimental photonuclear results has improved over the last 15 years due in large part to the application of the tagging technique in order to obtain "monochromatic" photons. The use of this coincidence technique has become possible due to the advent of high duty-factor, continuous electron beams. Full advantage of this technique could not be taken with the previously available $\leq 0.1\,\%$ duty factor pulsed electron beams as they produced a $1000\times$ poorer real to random coincidence ratio than is now obtained.

The monochromatic electron beam from MAMI-B is focused on to and passes through a thin nickel radiator. The electrons radiate by the bremsstrahlung process producing a continuous photon energy spectrum up to a maximum energy equal to the kinetic energy of the incident electrons. The resulting photon beam passes through a collimator into the experimental hall (A2 in Figure 2.1) where it is incident on a target inducing photonuclear reactions. Electrons with a known incoming energy of E_0 can be scattered with a range of energies E_e following the bremsstrahlung process. So the energy of the photon that passes into the hall, E_γ, can be determined, if the energy of the scattered electron, E_e, is measured since

$$E_\gamma = E_0 - E_e \tag{2.1}$$

At Mainz, the tagging is performed by the detection of the post-bremsstrahlung electron in the detector ladder of a wide band magnetic spectrometer built by Glasgow University [32,33]. The tagger consists of a large magnet used to focus the scattered electrons onto a focal plane detector, Figure 2.2, at a position which depends on their energy. Hence the energy of the photon can be deduced. The photon can be identified by demanding that there is a time coincidence between a tagger detector in the focal plane and the photoreaction-product detectors near the target position.

The photon tagger focal plane detector consists of 353 overlapping scintillators. Each element comprises a scintillator/lightguide assembly attached to a photomultiplier tube. The 2 mm thick NE 111 plastic scintillators form an array with a half-width overlap between adjacent detectors. The overlap is used as "real" scattered electrons interact with adjacent detectors and the required coincidence reduces background. At the full MAMI-B electron energy of 855 MeV, the tagger has an energy resolution of about 2 MeV per channel and a coincidence resolving time of about 1 ns. For the experiment described here, MAMI-B was used with a reduced energy electron

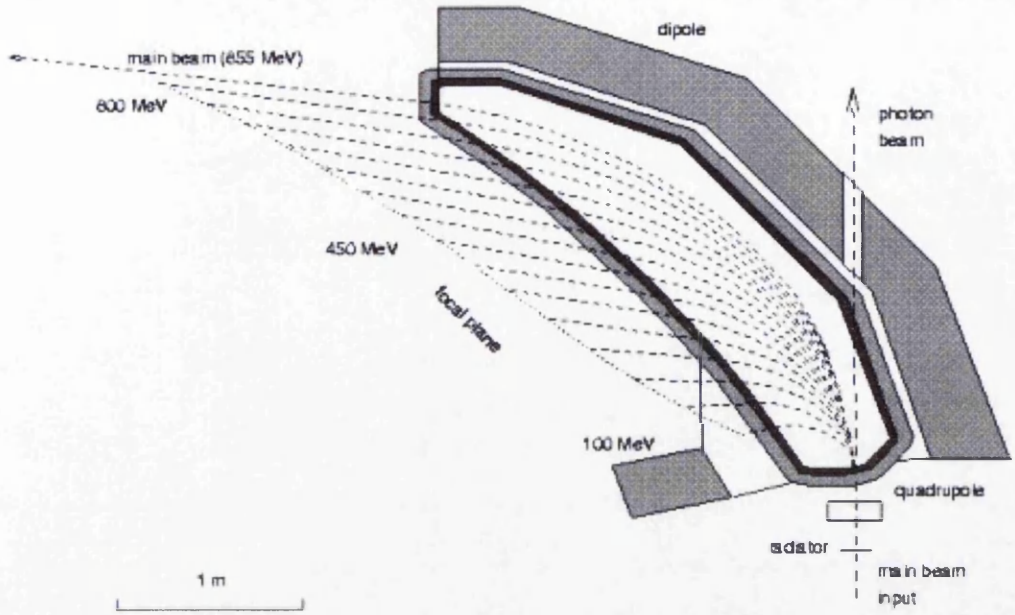

Figure 2.2: **The Glasgow Tagger:** Tagging is performed by the detection of the post-bremsstrahlung electron in the detector ladder of a wide band magnetic spectrometer.

beam of 405 MeV. This gives a photon energy resolution from the tagger of 1 MeV, a higher upper limit to the photon rate per MeV, and removes the unwanted events in the detectors that would be produced by higher energy photons in the tagged beam. This setting produced tagged photons in the energy range 90 to 375 MeV as shown in Figure 2.3.

The photon flux produced by the bremsstrahlung process varies approximately as E_γ^{-1} for most of the energy spectrum. Therefore the rate of photons at low energies is much higher than the rate at high energies as is clearly demonstrated in Figure 2.3. The maximum rate that a single detector in the tagger can take is 2 MHz, set to preserve the phototube lifetime. Also, the real to random ratio is poor at high rates. Therefore the lowest photon energy channels in the focal plane were turned off as they would not give useful information and would limit the performance of the channels that do give useful information. The lowest used E_γ was chosen to be 30 MeV below the pion photoproduction threshold. This gave a 30 MeV region which could be used to check some of the background contributions to the pion yield in the experiment.

2.3.1 Photon Beam Collimation and Tagging Efficiency

The photon beam on exit from the spectrometer was collimated by aligned lead cylinders with an axial hole of 5 mm diameter, positioned 2.5 m downstream of the radiator. This produces a narrow beam of photons of diameter 1.5 cm at the target but clearly not all the photons pass through the collimator. A 'tagging efficiency' measurement

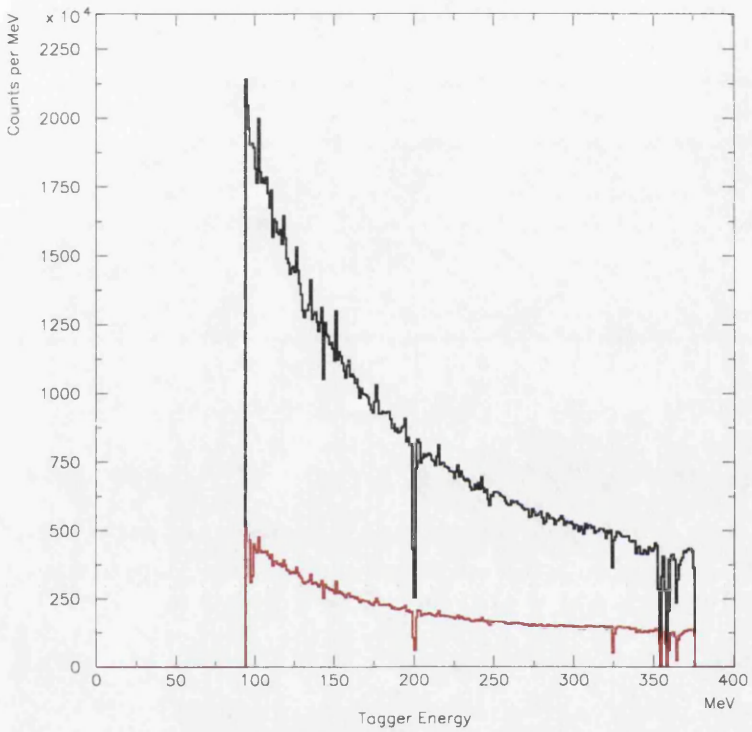

Figure 2.3: **Tagged photon energy distribution:** The black plot is for the ^{208}Pb data and the red is for ^{16}O. Data was taken for ^{208}Pb for almost three times as many hours as for ^{16}O, hence the difference in counts. However both demonstrate the same shape, the approximate E^{-1} shape obtained for photons produced from the bremsstrahlung process. The dips correspond to tagger channels that were "dead" or "died" sometime during the run. There are channel to channel variations of a few per cent due to mechanical variations in the overlap width of the tagger scintillators.

is performed to measure how many photons do pass through. This compares the measured photon flux with the electron rate in the tagger. For this purpose a lead-glass detector is moved into the path of the photon beam to detect the photons that are not stopped by the collimator. The photon beam is reduced by a factor of 5×10^4 since the lead-glass detector can not operate at the photon flux used for data-taking. The lead-glass detects photons by measuring the Čerenkov radiation produced. It is $\sim 100\,\%$ efficient as it has a thickness equivalent to 30 radiation lengths. The tagging efficiency is defined as

$$\epsilon_{tagg} = \frac{N_\gamma}{N_e} \tag{2.2}$$

where N_γ is the number of tagged photons that pass through the collimator and N_e is the number of electrons detected in the focal plane. It is measured in practice as

$$\epsilon_{tagg}(i) = \frac{N_{coin}(i)}{N_e(i)} \tag{2.3}$$

where $N_{coin}(i)$ is the number of coincidences between the lead-glass photon detector and the ith focal plane channel, and $N_e(i)$ is the number of electrons detected in that channel.

An ion chamber in the beam line is used to obtain an on-line indication of the tagging efficiency. The ratio of the current detected in the ion chamber to the rate of electrons counted in the tagger focal plane detector is proportional to the tagging efficiency. This was continuously monitored as it indicates any changes in the electron beam position or direction that would affect the tagging efficiency. Complete tagging efficiency measurements were made at least once a day throughout the beam time. More details on these measurements are given in section 4.2.

2.4 The Two Arm Photon Spectrometer (TAPS)

The TAPS spectrometer [98] was designed to detect high energy photons ($E_\gamma \leq 1$ GeV) which enables the reconstruction of neutral mesons such as π^0- and η-mesons because these decay predominantly into two or more photons. The reconstruction of the meson energy and mass require the simultaneous measurement of the point of impact and the energy of both photons, hence a modular setup is used.

A π^0 in the centre of mass frame decaying into two gamma-rays emits them in opposite directions but when this is seen from the lab system in which it has a total energy E_π, then the opening angle between the two gamma-rays varies between ψ_{min} (see Appendix A.2) and 180°. The opening angle distribution is strongly peaked at ψ_{min}, the value of which decreases with increasing pion energy; both these effects

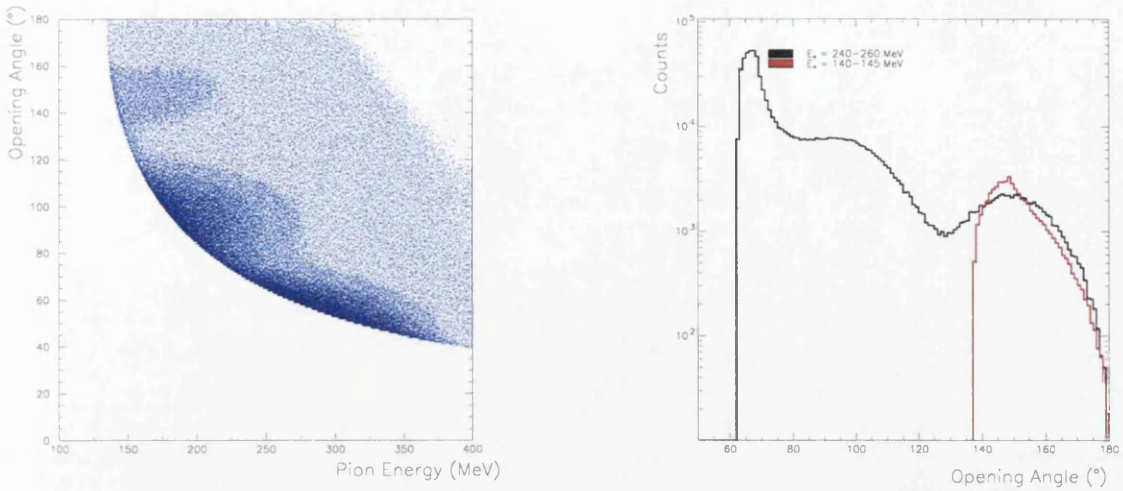

(a) (b)

Figure 2.4: **Effect of pion energy on opening angle between its two decay photons.**

Table 2.1: **Summary of the TAPS setup.**

Block	A	B	C	FW	D	E	F
r (cm)	55.5	55.2	55.6	68.8	55.6	55.1	55.4
θ (°)	152.4	103.0	54.0	0.2	-54.1	-103.8	-152.6

are clearly illustrated in Figure 2.4 which shows the distribution of opening angles observed in the present experiment and its dependence on the pion energy. Further details on pion kinematics are given in Appendix A.

The TAPS detector came into operation in 1990. Initially called the two arm photon spectrometer (and hence the acronym TAPS) as it comprised 320 individual BaF_2 scintillation detectors arranged on two arms [99], it has since increased in size such that at the time of the present experiment, TAPS consisted of 522 identical modules. These were assembled into 6 blocks (labelled A-F) of 64 elements (Figure 2.5) and a larger forward wall consisting of 138 elements, positioned in air around the target. The setup is shown in Figure 2.6 and summarised in Table 2.1, where r is the distance from the geometric centre of the front face of the block to the centre of the target and θ is the angle from the beam direction. The employment of a layout in which the detectors are placed fairly uniformly around a horizontal circle centred on the target produces: (a) a reasonably smooth variation of the detection efficiency with pion energy despite the rapid variation of the opening angle distribution of the photons; (b) a rise in detection efficiency at forward and backward angles which partially compensates for the drop in solid angle at these angles.

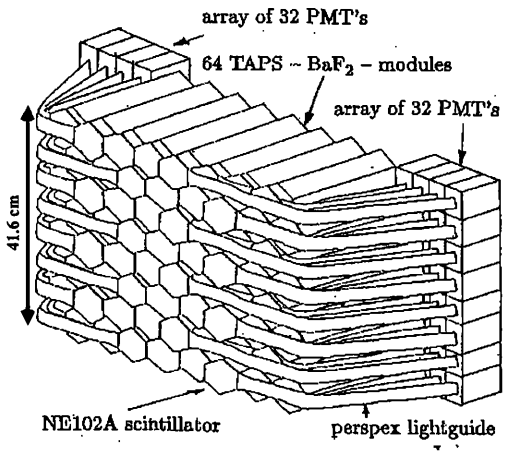

Figure 2.5: **A TAPS Block:** A standard TAPS block consists of 64 BaF_2 detector modules and 64 plastic (NE 102A) veto detectors.

Each detector module consists of two elements, Figure 2.7. The first is a BaF_2 scintillation crystal of length 250 mm (corresponding to more than 12 radiation lengths) and an hexagonal section with inner radius of 29.5 mm (corresponding to 87% of the Molière radius[1]). The crystals are wrapped with PTFE to act as a UV-reflector and an additional layer of aluminium foil to exclude light and are coupled optically to the quartz window of a photomultiplier tube with high viscosity grease [101]. The last 25 mm length of the crystal has a cylindrical section to fit the quartz-window of the photomultiplier and allows for magnetic shielding. The second element of the module is a 5 mm thick plastic scintillator (NE 102A) veto detector of identical granularity mounted in front of the BaF_2 crystal for on-line charged particle discrimination. These veto detectors are read-out individually by lightguides and photomultipliers.

The discovery of the fast component in the scintillation light of BaF_2 in the early 1980's [102] prompted several studies into its use as a detector for gamma rays [103–105]. Time resolution is excellent, approaching 80 ps full width half maximum (FWHM) for small crystals [102] and 400 ps FWHM for large crystals [106]. The scintillator has a relatively high density (4.89 g/cm^3) which combined with the high atomic number of barium (56) give BaF_2 good detection efficiency for gamma rays (radiation length $X_0 = 2.05\,\text{cm}$). The scintillation light output of BaF_2 has two wavelength components: the first component is at 220 nm (decay time 600 ps) and the second is at 315 nm (decay time 620 ns) [105]. The presence of two components in the scintillation light output enables charged particles to be distinguished from gamma rays via pulse shape analysis (see section 4.4.1). For these reasons BaF_2 was selected as the scintillation material for TAPS [99].

[1] A characteristic constant of a material describing its electromagnetic interaction properties.

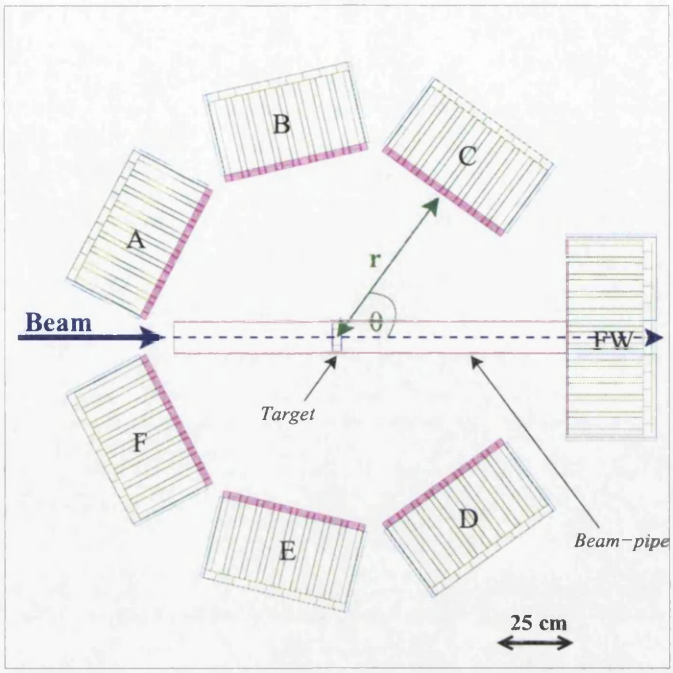

(a) Standard TAPS setup viewed from above.

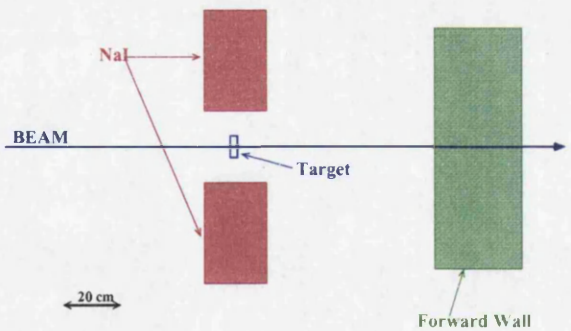

(b) Setup viewed from the side.

Figure 2.6: **Standard TAPS setup:** (a) The standard TAPS setup of 6 blocks of 64 BaF_2 elements (labelled A-F) with a larger forward wall (FW) viewed from above. The forward wall has a hole in the middle to allow the passage of the beam. This picture was produced using the visualisation capabilities of GEANT3 [100]: Green represents the BaF_2 detectors and magenta represents the plastic scintillation veto detectors. (b) Side-on view. In addition to the standard TAPS setup, two large NaI detectors were positioned one above and one below the target, TAPS is absent in this picture with the exception of the FW.

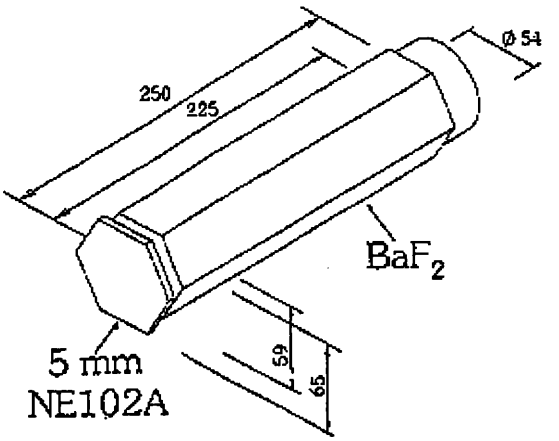

Figure 2.7: **A TAPS Detector Module:** TAPS consists of 522 identical modules made up of two elements - a 250 mm long BaF_2 scintillation crystal and a 5 mm thick NE102A plastic scintillator.

The response of TAPS to monochromatic photons with energies between 45 and 790 MeV was investigated by Gabler et al. [70,71] and the rms energy resolution (σ) for central impact of a collimated photon beam was found to be

$$\frac{\sigma}{E_\gamma} = 0.59\% \times E_\gamma^{-\frac{1}{2}} + 1.9\% \tag{2.4}$$

where the photon energy, E_γ, is given in GeV. The spatial resolution of the point of impact was found to be $\Delta x = 2\,\text{cm}$ (FWHM) at the highest energies corresponding to 30 % of the diameter of an individual module. The position resolution depends strongly on the number of detectors that respond and at lower energies (< 300 MeV) it is determined largely by the granularity of the detector system [107].

2.5 Sodium Iodide Detectors

Neutral pion photoproduction can take place either coherently or incoherently. As discussed in section 1.1, the coherent process is the primary interest of the present investigation and therefore the coherent events need to be separated from the incoherent events. In the incoherent process the residual nucleus is left in an excited state. The excited nucleus decays back to its ground state and from some excited states this is via gamma ray emission. Two large, cylindrical, sodium iodide (NaI) crystals were used in addition to the TAPS setup in an attempt to detect these additional decay gamma rays and thus identify incoherent events.

The NaI detectors were positioned one above and one below the target at a distance of about 11.7 cm as shown in Figure 2.6(b). The choice of position is discussed in

Table 2.2: **Properties of the NaI detectors.**

Manufacturer	Bicron	Harshaw
Model No.	9.37414/73	5-2117
Length (cm)	33.97	35.00
Diameter (cm)	24.76	25.50
Distance from Target (cm)	11.88	11.48
Solid Angle (steradians)	1.94	2.07
Dynamic Range (MeV)	0 - 23.19	0 - 23.51

section 3.5. The properties of the crystals are summarised in Table 2.2. One crystal was manufactured by Bicron and the other by Harshaw. Each was housed in an aluminium casing and optically coupled to seven photomultiplier tubes.

2.6 Targets

As a closed shell nucleus, ^{16}O is an interesting target to study coherent pion photoproduction on (see section 1.1) and many theorists have performed calculations for it [22, 23, 25, 73–75]. However there has been only one previous experimental measurement, performed by Bellinghausen et al. in 1982 [59]. Oxygen is readily available in the form of water (isotope composition is ^{16}O, ^{17}O, and ^{18}O with abundances of 99.757%, 0.038%, and 0.205 % respectively [108]) but the contribution to the yield from pions produced from the hydrogen must be removed. Bellinghausen et al. simulated the coherent pion production from hydrogen and subtracted this from their data. For a given incident photon energy and pion lab angle the energy of a pion produced from hydrogen is smaller than the energy of a pion produced coherently from oxygen since the lighter recoil nucleus takes a larger proportion of the energy. Calculations were performed to evaluate the difference (ΔE_π) in the energies of the pions produced coherently from these two nuclei for a few incident photon energies and a sample of the results are given in Table 2.3. The value of ΔE_π increases with increasing incident photon energy but the pion energy resolution decreases. However at any given E_γ, the energy resolution is less than half the value of ΔE_π (see section 3.4.1) and thus the kinematics of the reactions on the two nuclei can be used to separate the oxygen-produced pions.

A simple water target which is shown in Figure 2.8 was constructed from perspex with a thin (0.06 mm) Melinex window through which the beam was incident on the water. Data were also taken on an empty target to allow correction for any π^0 production processes taking place on the support structure.

Lead-208 is also a closed-shell nucleus. It is additionally interesting as it contains a complete extra shell of neutrons and may give additional information on how the

Table 2.3: **Comparison of the energy of a pion produced from hydrogen with that produced coherently from oxygen.**

E_γ [MeV]	θ_π [°]	E_π (^{1}H(γ,π^0)^{1}H) [MeV]	E_π (^{16}O(γ,π^0)^{16}O) [MeV]	ΔE_π [MeV]
175.0	15.0	157.72	174.83	17.11
175.0	165.0	157.55	172.55	15.00
195.0	60.0	172.11	194.05	21.95
210.0	60.0	182.67	208.87	26.20

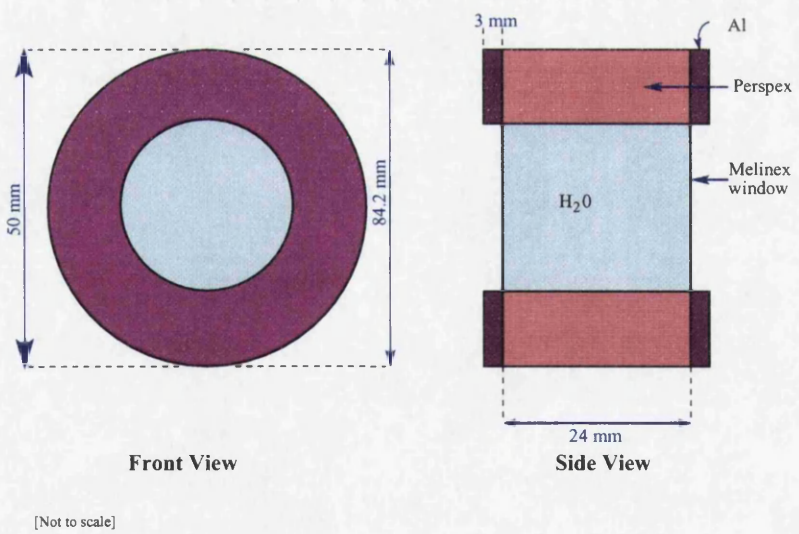

Figure 2.8: **Water Target.**

Table 2.4: **Target Data.**

Target	Thickness (mm)	Atomic Mass ($\frac{m_a}{u}$)	Surface Density ($g\,cm^{-2}$)	Beam time (hrs)
^{16}O	24.00 ± 0.01	15.9994	2.695	69
^{208}Pb	0.52 ± 0.01	207.977	0.8369	169

distribution of the neutrons compares with that of the protons. However, natural lead is only 52.4 % ^{208}Pb (isotope composition is ^{204}Pb, ^{206}Pb, ^{207}Pb, and ^{208}Pb with abundances of 1.4 %, 24.1 %, 22.1 % and 52.4 % respectively) [108]. Lead is a large, high atomic number atom and therefore the incidence of atomic processes that contribute to the background of any pion photoproduction experiment is greater than for lighter nuclei. A pure ^{208}Pb target was purchased from ISOFLEX Isotopes, Moscow. A summary of the targets is given in Table 2.4. Both targets were placed in an evacuated beam-pipe, made of 5 mm thick clear plastic, at the geometrical centre of TAPS to an accuracy of 2 mm.

The water target thickness corresponded to approximately $\frac{1}{10}$ of a radiation length so that neither the angular resolution of TAPS nor the quality of the tagged beam are degraded. The lead target was less than $\frac{1}{10}$ of a radiation length. Positioning it at 45° to the beam increased the effective thickness by $\sqrt{2}$.

2.7 Electronics

2.7.1 Tagger Read-out

The tagger read-out hardware comprises three linked bus systems; VME-bus, CAMAC, and FASTBUS. Each of the 352 channels has its own scaler and TDC in high density FASTBUS crates. An ECL logic pulse is produced by an electron hit in the focal plane which is sent to be recorded in TDCs and pattern units and also to a free running scaler. A photoreaction product is signalled by a coincidence between an electron in the tagging spectrometer and a trigger from TAPS. This is tested for by a logic pulse derived from an OR output of all 352 tagger channels. If this coincidence condition is satisfied, the TDC is read - the time is needed to determine whether or not a real coincidence has occurred between TAPS and the electron or if it was a random coincidence.

The tagger electronics are controlled by a VME processor which is itself controlled by the VME processor in the data acquisition system of TAPS.

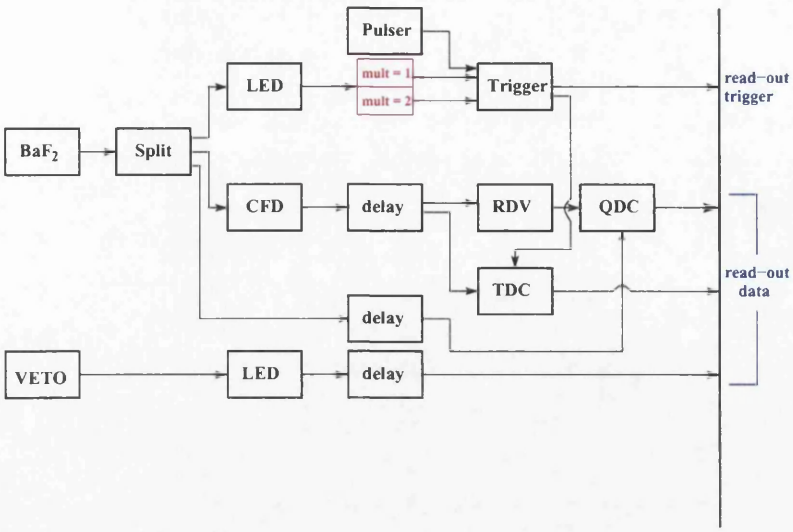

Figure 2.9: **TAPS read-out.**

2.7.2 TAPS Read-out

A simplified diagram of the TAPS read-out is given in Figure 2.9. Photons produce scintillation light in the BaF_2 detectors which is transformed into an electrical pulse by the photomultiplier tube. The size of the pulse is proportional to the amount of energy deposited in the detector. The signals from each TAPS detector element are passed through a signal-splitter (Split) producing three outputs. One output goes direct via a 500 ns delay to two charge to digital converters (QDC). The second output is fed into a constant fraction discriminator (CFD) and used to get accurate timing information about when the BaF_2 element had been triggered. The threshold for the CFD was set to be between 0.5 and 1.0 MeV. The CFD output was fed into a variable delay unit from which there were two outputs. One was fed into the time to digital converter (TDC) to get timing information from the detector and the other was fed into an RDV (Retard Durée Variable) module. This provided gates for the two QDC's, one short (50 ns) and one long (2 μs) to enable use to be made of the two decay components of BaF_2 scintillation. A variable delay box was used so that it could be set to ensure that the QDC signal read-out was aligned with the RDV generated gates and the TDC. The third output was fed into a leading edge discriminator (LED) which was used for the trigger. The LED threshold was set to 10 MeV.

The output from a veto is fed into an LED. The vetoes were calibrated by colleagues at the University of Giessen and the veto threshold was set to be between the "noise" and the "minimum ionising peak" of the energy deposition spectrum [109]. The veto is said to have "fired" if the resulting logical output signal is above this threshold and this was recorded by feeding the LED outputs to a pattern unit.

For the data taking there were three triggers for the read-out:

1. LED multiplicity of two, that is events were only accepted and recorded if there were LED signals from at least two separate TAPS blocks,

2. LED multiplicity one: done for diagnostic purposes and this trigger was scaled down by a factor of 100,

3. a pulser to provide a continuous monitor of the QDC pedestal.

A single trigger of LED multiplicity one was used for the cosmic ray calibration runs (see sections 3.2 and 4.3.1).

The TAPS electronics are controlled by a VME processor. The data acquisition was run on E6/7 CPUs. There were "slave" processors: one readout TAPS blocks A-D, and F, another controlled writing the data to tape (20 GB DLT tapes), while a third distributed the data to an on-line analysis. These were controlled by the "master" processor that also readout TAPS block E and the Forward Wall.

2.7.3 NaI Read-out

Each sodium iodide crystal was optically coupled to seven photomultiplier tubes. The signals from each tube were summed (the high voltages were used to align their relative gains) and this was fed into a QDC and a TDC. When there was a LED multiplicity two trigger in TAPS (see previous section), the QDC and TDC for both NaIs were read.

2.8 Analysis Code

The data analysis and display software written in the 'C' language contained routines for monitoring the detectors and allowed a detailed overview of progress during the experiment. This analysis software, the Analysis Support Library (ASL), was provided by colleagues from the University of Giessen where it has been developed over many years [110]. The same basic analysis software was used for both on-line and off-line analysis. The on-line analysis involved looking at raw QDC and TDC data along with some derived spectra, e.g. invariant mass, using preliminary calibrations. These basic spectra were provided as part of the standard off-line analysis. The complete analysis was performed by adding the required specific spectra, e.g. pion energy difference cut on incident photon energy and pion lab angle (see chapter 4).

Chapter 3

GEANT Simulations

3.1 Introduction

The TAPS detector array consists of 522 BaF_2 elements in a complex geometry and the response to any one high energy photon involves several of these elements. For any given π^0 direction and energy the π^0 decay photons have a range of angles and energies. Therefore to determine the response of TAPS to neutral pions it is essential to carry out simulations of the π^0 decay and subsequent detection of the decay photons.

GEANT is a system of detector description and simulation tools that help physicists design and optimise detectors, develop and test reconstruction and analysis programs, and interpret experimental data. It was devised in CERN in 1974 when it was just a bare framework that initially emphasised tracking of a few particles per event through relatively simple detectors. The system has been developed over the years and we are currently using version 3.21.

The GEANT program simulates the passage of elementary particles through matter. The principle applications of GEANT in High Energy Physics are:

1. the transport of particles through an experimental setup for the simulation of detector response;

2. the graphical representation of the setup and of the particle trajectories.

The GEANT system allows you to:

- Describe an experimental setup by a structure of geometrical volumes;

- Accept events simulated by Monte Carlo generators;

- Transport particles through the various regions of the setup, taking into account geometrical volume boundaries and physical effects according to the nature of the particles themselves, their interactions with matter and magnetic fields;

- Record particle trajectories and the response of the detectors;
- Visualise the detectors and the particle trajectories

Colleagues at the University of Giessen, Germany, already had a working GEANT simulation program for TAPS. This was modified to perform various simulations for a number of investigations the details of which follow. For the analysis of both experimental data and simulated events the same analysis routines could be used thus allowing comparisons and cross-checks.

In the course of obtaining experience with the TAPS GEANT simulation program, an incorrect modification of the basic TAPS code was discovered. This modification, whose origin could not be traced by colleagues in Giessen, resulted in energy below a user-set threshold being discarded at the end of tracks of neutral particles. For example, as much as 12 MeV of the initial energy of a 200 MeV photon could be lost in this way. This error was corrected before routine use was made of GEANT, although as a consequence it was not possible to use the results of any of the earlier investigations done by the TAPS group because all of these had been done with the incorrect code.

3.2 Cosmic Ray Calibrations

Cosmic rays are used to obtain a 'relative' energy calibration for each of the 522 BaF_2 detector modules in TAPS on the assumption that they deposit the same average energy in all the TAPS elements independent of their position in the array (the procedure is described in section 4.3.1). Cosmic rays consist of high energy muons (both μ^- and μ^+ are present in almost equal probabilities). The muon flux at sea level has a mean energy of 2 GeV and a differential spectrum falling as E^{-2}, steepening smoothly to $E^{-3.6}$ above a few TeV. The angular distribution is $\cos^2\theta$, changing to $\sec\theta$ at energies above a few TeV, where θ is the zenith angle at production [77]. We carried out a simulation to check the constancy of the average energy deposition. Two possible effects might be

1. change in $\frac{dE}{dx}$ because E changes along the muon path,
2. some of the energy deposited in any one detector might be due to particles that were produced by the muon in previous detectors that it passed through.

A simple indicator is the difference in the average energy deposited in a top row detector compared with the energy deposited in a bottom row detector. This difference will give an indication of the magnitude of residual calibration differences after the cosmic calibration has been carried out.

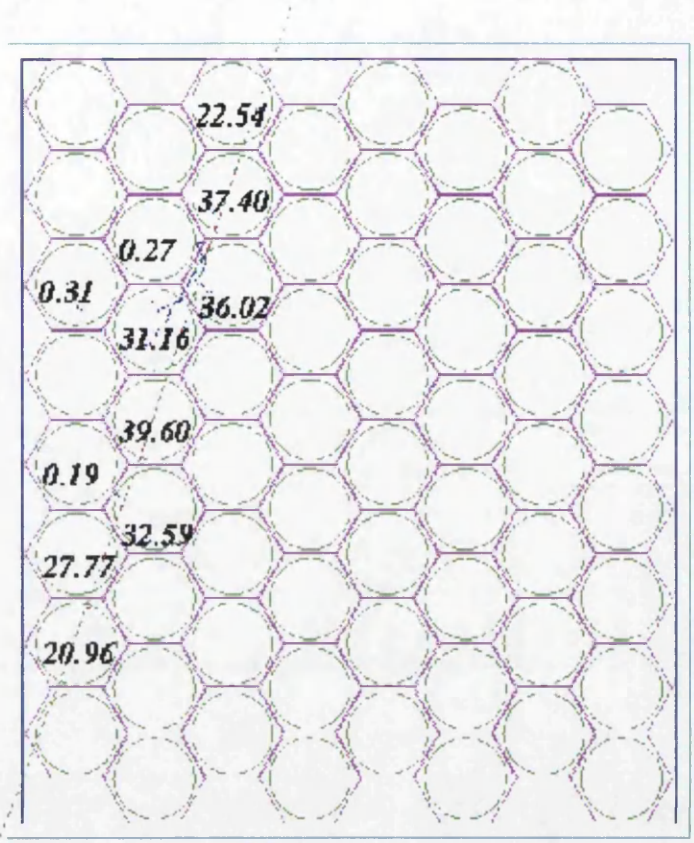

Figure 3.1: **Example of a cosmic ray track:** Here is an example of a cosmic muon (green track; again blue tracks are photons and red tracks correspond to electrons and positrons). The numbers correspond to the energy deposition (in MeV) in that detector.

A GEANT simulation was performed with muons incident on a single TAPS block. To investigate the effect only those events that produced signals in both a top row detector and a bottom row detector were accepted. To reduce computing time the muons were limited to originate from a plane the same size as the block and 2 cm above it. The direction in which they were travelling was chosen according to their known $\cos^2\theta$ distribution [77]. A μ^- or a μ^+ was chosen randomly with a 50:50 probability. An example of a typical cosmic ray track through a TAPS block is shown in Figure 3.1. One million events were simulated for two muon energies, 2 GeV and 5 GeV, which sample the range of energies present in the real muon spectrum [77]. The cosmic ray spectrum and angular distribution in the experimental hall, which is 9 m below ground level, will both be altered by absorption in the thick shielding roof but this was not modelled. The resulting data were analysed and, for each muon

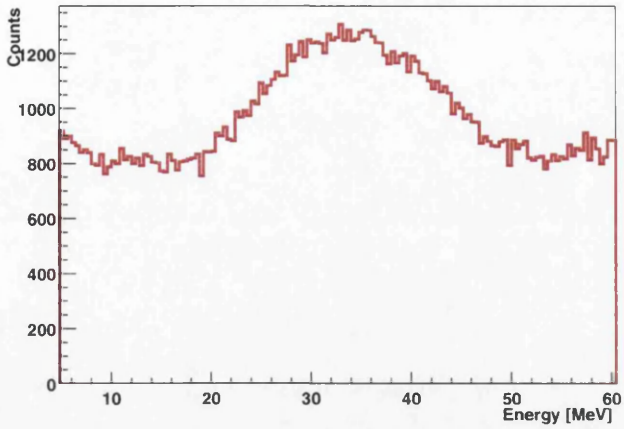

Figure 3.2: **A simulated TAPS cosmic ray energy deposition spectrum:** The energy deposition resulting from 2 GeV muons.

Table 3.1: **Peak positions for energy spectra to investigate the effect of muon energy and path through a TAPS block.**

Detectors	Peak Position (MeV) 2GeV	5GeV
Det 60 (top)	39.87	40.22
Det 5 (bottom)	39.50	40.49
Average for top row	39.87±0.42	41.03±0.41
Average for bottom row	39.58±0.38	40.99±0.23

energy, the peak positions of the energy spectra for detectors in the top row were compared with the peak positions of the energy spectra for detectors in the bottom row by fitting a Gaussian function to each. The energy deposited by muons has a Landau distribution with a well-defined peak as seen in Figure 3.2 which shows a typical energy deposition spectra for a detector in a TAPS block from a simulation of 2 GeV cosmic muons.

The difference in the energy deposited between a detector in the top row and one in the bottom row is not significant, of the order of 1 %, as shown in Table 3.1. Thus it was concluded that cosmic rays provide satisfactory relative calibrations. A difference of 4 % was observed between the peak energy values for 2 and 5 GeV indicating that cosmics can not be used for absolute calibrations unless the cosmic ray energy distribution is known accurately (and it is not for the A2 experimental hall). There has been some debate as to what energy to use as the peak position with values between 37 and 40 MeV used at one time or another [110, 111]. However, since the cosmic ray measurements are only used for relative alignment of the TAPS detectors and the absolute calibration is determined from a reconstruction of the π^0 mass (see section 4.5), the value chosen is not particularly important. For the work presented

here, the peak position was set at 38 MeV.

3.3 Light Collection Correction

One possible reason for the inability to obtain an absolute calibration based on the cosmic ray measurements is the neglect of scintillation light collection losses in previous analyses of TAPS data. Since it may also affect the linearity of the photon energy dependence in the TAPS response to photons, it was decided to investigate the light collection process in more detail. GEANT3 simulates the passage of elementary particles through matter but only to quite a basic level. It does not model the scintillation process itself or the processes involved in the collection of the photons emitted by the scintillator and their conversion into photo-electrons at the cathode of the photomultiplier [112]. Scintillation photons generated inside a detector travel by complicated paths to the photocathode, often undergoing multiple reflections in the process. During the collection process, photons may be lost due to absorption at the surface or in the scintillator itself [113]. For energy deposited at some particular point in the scintillator, the anode pulse is proportional to the energy deposited. However, the proportionality constant will, in general, vary from one point in the scintillator to another due to different fractions of the light being lost by absorption. To simulate the overall loss of light from a shower generated by a high energy incident photon, it is necessary to determine the loss as a function of position throughout the detector. This information was obtained experimentally using a collimated ^{22}Na source.

As described in section 2.4, the TAPS BaF_2 detector components consist of a 250 mm long hexagonally shaped BaF_2-crystals (see Figure 2.7). Positrons from the ^{22}Na source decays are annihilated producing back-to-back 511 keV photons. The experimental setup is shown in Figure 3.3.

Two TAPS detector elements were used to detect the 511 keV decay photons from the ^{22}Na source: the anode pulse from one element (the sample) was measured when a photon was detected in the other (the trigger). Energy spectra were collected for various source positions along the length of the sample detector and the peak channel in the energy spectrum for each entry position was recorded. An approximately exponential relationship was expected between the peak channel number and the distance along the detector, namely

$$I = I_0 \mathrm{e}^{-\lambda d} \tag{3.1}$$

where I_0 is the initial intensity of radiation and I is the intensity after passing through thickness d of material of absorption coefficient λ. However, the graph of ln (Peak Channel) versus distance, shown in Figure 3.4, is not a straight line but

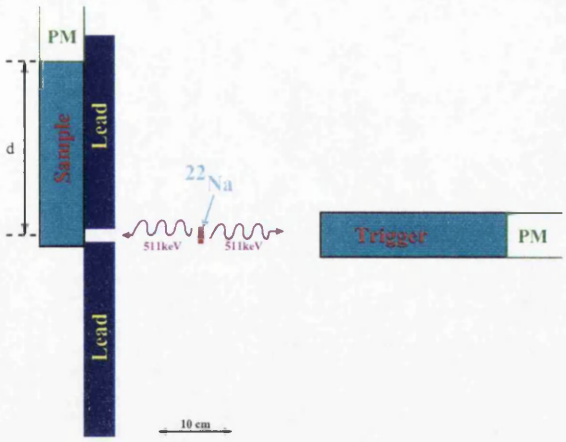

Figure 3.3: **Experimental setup for light collection measurement:** Two TAPS detector elements were used to measure light collection using a ^{22}Na source.

shows a more complicated behaviour. This could be due to the two wavelength components in the scintillation light output from BaF_2 [103], which may have different absorption lengths, or to the contribution of light reflected from the end of the BaF_2 scintillator back towards the photomultiplier tube. The results were fitted with the expression

$$I = I_0 \mathrm{e}^{-\alpha d - \beta d^2} \tag{3.2}$$

where d is the distance from the photomultiplier end of the BaF_2 detector as shown in Figure 3.3. The values obtained were $\alpha = -0.0122\,\mathrm{cm}^{-1}$ and $\beta = 0.0004\,\mathrm{cm}^{-2}$.

This information was used to add a light collection correction to the GEANT3 code. The light collection effect is present in the real detector system, so if the simulation is to correctly model this it should be included. In GEANT3 a particle is *tracked* through a geometry of objects by calculating a set of points in a seven-dimensional space $(x, y, z, t, p_x, p_y, p_z)$ specifying the position, time, and momentum which is called the trajectory of the particle. This is achieved by integrating the equations of motion over successive steps from one trajectory point to the next and applying corrections for the presence of matter. A detailed description of the kinematics of the particle would require the trajectory point to be calculated every time a component of the momentum changed. This is not possible as it would result in an enormously large number of points being calculated. Processes like the loss of energy due to bremsstrahlung and ionisation are essentially continuous so an arbitrary distinction is made between discrete and continuous processes, controlled by a set of thresholds which can be set by the user. Thus a particle trajectory is a set of points at which a discrete process has happened. The tracking package contains a subprogram which performs the tracking for all particles in the current event and for the secondary products which

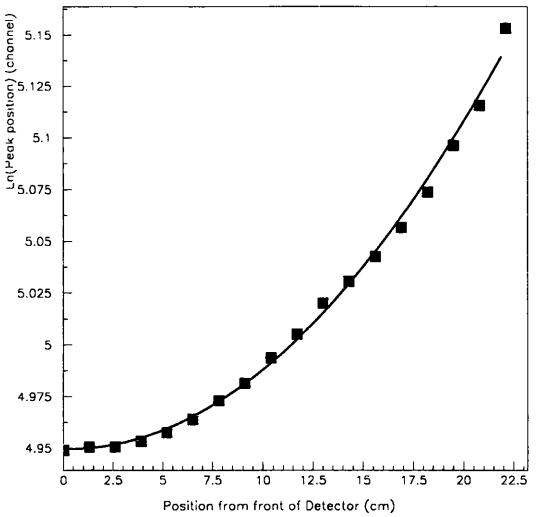

Figure 3.4: **Results from Na-22 source:** A polynomial order 2 gives a good fit to the data points.

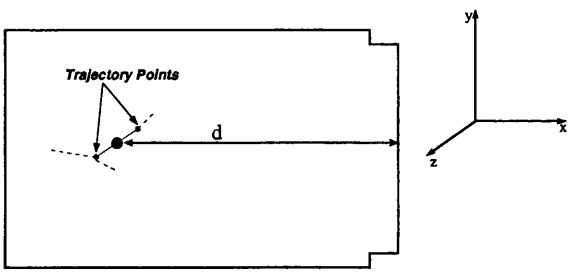

Figure 3.5: **Light Collection Correction Coordinate System:** GEANT3 gives each interaction an x, y, and z coordinate. Any change in the y and z was ignored as it was the distance from the photocathode at which the scintillation light was produced that was of interest. Thus the parameter d was introduced.

they generate, plus some tools for storing the space point coordinates computed along the corresponding trajectories [100].

As discussed above, the amount of light that reaches the photocathode depends on how far away from it the light is produced. This will determine how much of the deposited energy is "detected". The important distance is how far along the length of the detector the light is produced, the value of d. It was assumed that the light collection did not vary significantly over the cross section of the detector at a fixed value of d. The energy lost by the particle for each tracking step was reduced according to the distance from the photocathode with

$$E = E_0 e^{-\alpha d - \beta d^2} \tag{3.3}$$

where E_0 is the uncorrected energy deposition at that step, E is the light collection

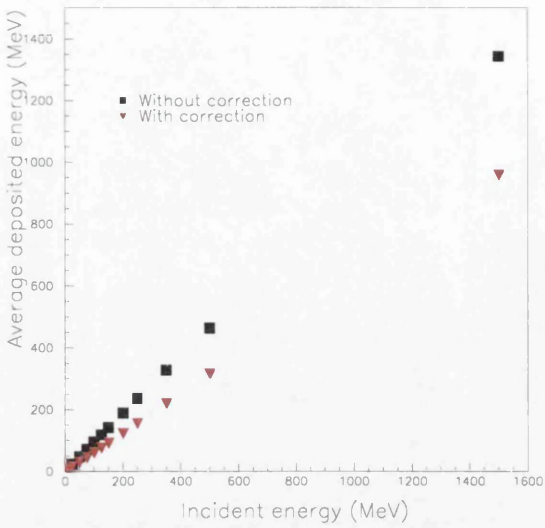

Figure 3.6: **Graph to show the effect of light collection correction:** Comparison of average energy deposited in a single TAPS block for GEANT3 simulations with and without light collection correction.

corrected energy - the "detected" energy , d is the distance from the photocathode of the centre of the path at that step as shown in Figure 3.5, and α and β have the same values as in equation 3.2.

Appendix B gives details of how the distance from the point of interaction to the photocathode was determined for each detector element in order to implement this correction into the simulations.

For a range of energies from 10 to 1500 MeV simulations were performed where 10,000 photons were fired into the centre of a TAPS block both with and without the light collection correction in the code. The average simulated detected energy in the block was calculated for each algorithm. The effect of the light collection correction is shown in Figure 3.6.

Shower collection (fraction of incident energy deposited in the block with the uncorrected algorithm) and light collection (fraction of the deposited energy that is "detected" when the correction is applied) were also calculated and their dependence on the incident photon energy is shown in Figure 3.7. The size of the electromagnetic shower resulting from the photon increases with its energy and therefore the probability of some of the shower escaping the block and not being detected increases and is illustrated in Figure 3.8. This results in a decrease of 3 % in shower collection when the incident photon energy increases from 10 MeV to 1500 MeV. However, as the energy of the photon increases, the average depth of the shower in the detector also increases and so the resulting scintillation light is produced nearer to the photocathode. Hence light collection is found to increase by 10 % over the same range of

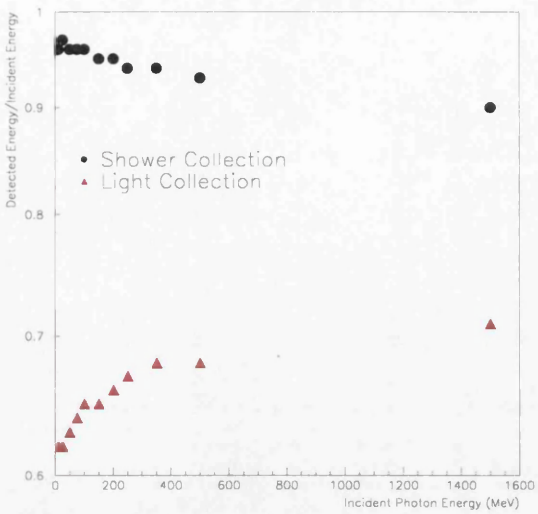

Figure 3.7: **Effect of incident photon energy on shower and light collection.**

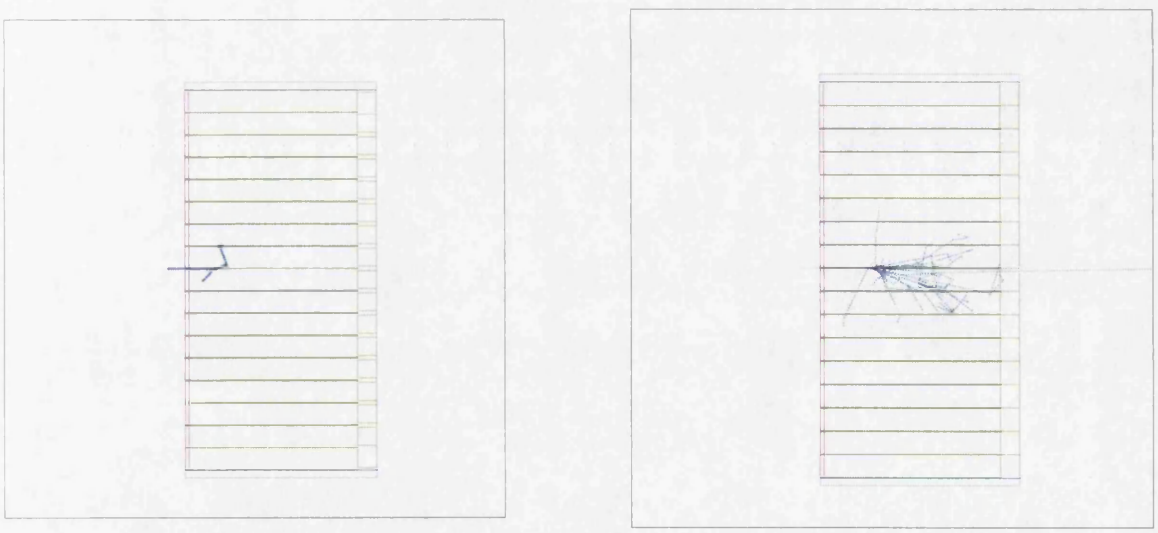

(a) 10 MeV photon

(b) 200 MeV photon

Figure 3.8: **Effect of photon energy on the size of the electromagnetic shower produced in TAPS:** The size of the shower produced in TAPS increases with incident photon energy as does the probability of part of that shower escaping the block as can be seen in these examples of (a) a 10 MeV photon and (b) a 200 MeV photon incident on a TAPS block as viewed from the side. Photons are represented by blue tracks and charged particles by red tracks. The incident photon enters the block from the left.

incident photon energies. The shower collection effect was clearly already included in the existing simulation but the light collection effect was not and in fact was found to be the larger effect of the two. Therefore the light collection correction algorithm was used in all subsequent simulations for the present experiment.

3.4 Detection Efficiency

As TAPS is not a 4π detector and its component detectors are non-uniformly positioned, the efficiency with which it detects neutral pions varies strongly with both pion energy and angle. A significant fraction of the pion decay photons was not incident on any part of TAPS. The opening angle distribution of the two pion decay photons is strongly correlated with the pion energy (see Appendix A.2). The pion decay photons were detected in separate TAPS blocks as described in section 2.7.2. Pions whose decay photons had an opening angle for which TAPS provided little solid angle were unlikely to be detected.

GEANT3 simulations were performed for pions with discrete energies (range E_π = 135-380 MeV) and lab angles (θ_π = 0-180°). The pions were generated inside the target and the decay photon interactions with the target and beam-pipe were simulated along with the interaction with the TAPS detector system itself. The resultant particles were tracked until their energy was less than 1 MeV after which it was assumed that they were absorbed by the material. The simulated data sets were analysed using the same analysis with the same cuts (except timing cuts - see below) as were applied to the experimental data. For ^{16}O, 100,000 pions were simulated for each energy and angle combination and the detection efficiency was determined for each by simply comparing the number of simulated pions generated and detected. Cross sections were to be produced in bins of incident photon energy and pion lab angle (see section 4.8). Therefore, pion energy was converted to incident photon energy assuming coherent production (see Appendix A.4) and the efficiency values for discrete incident photon energies and pion lab angles were converted into efficiencies for the bins to be used for the cross sections. The variation in detection efficiency with pion angle is given in Figure 3.9(a). For ^{208}Pb, 500,000 pions were simulated for each energy and angle combination and the detection efficiency was determined in the same way as for ^{16}O. The variation in detection efficiency with pion angle is given in Figure 3.9(b). The statistical error associated with the detection efficiencies is discussed in section 4.8.1. Simulating a greater number of pions for each pion energy and angle combination would have decreased this error but it would also have increased the computing time significantly. For example, the ^{208}Pb simulation took around 2 weeks to perform but the ^{16}O simulations took only a couple of days. As the contribution to the error in

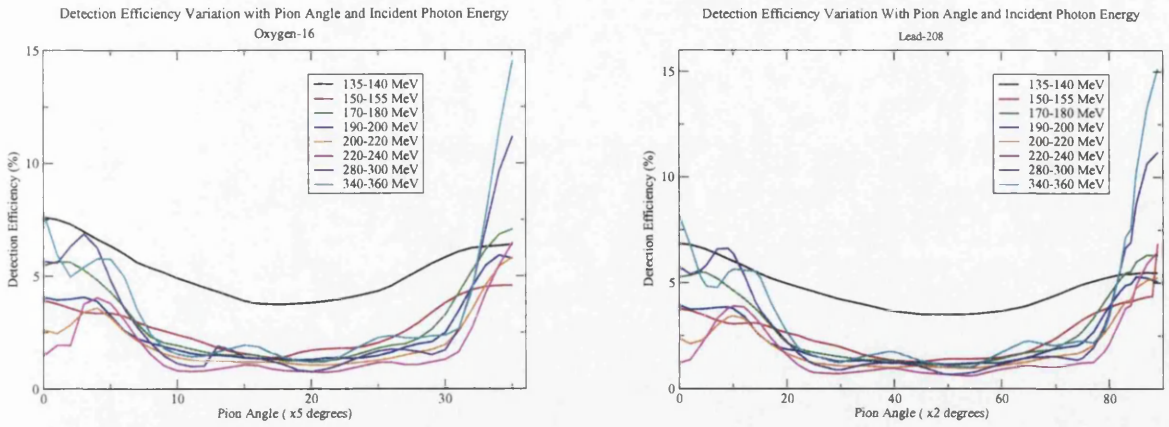

(a) ^{16}O (b) ^{208}Pb

Figure 3.9: **TAPS detection efficiency as a function of pion lab angle for various pion energies:** The difference between targets is small and the general trends match.

the cross section due to the uncertainty in the detection efficiency was comparable to the contribution from the estimate of the number of coherent events (see section 4.7.2), simulations of a greater number of pions was not carried out.

The GEANT3 simulation did not provide information about the timing of the TAPS signals and therefore the calculated efficiency did not allow for the reduction produced by the cuts applied to the time spectra. Therefore, separate corrections were made for this (see section 4.8).

3.4.1 Pion Energy and Angle Resolution

Since simulations of pions with discrete energies and angles were performed for the calculation of detection efficiency, these could also be used to determine how well the TAPS analysis reconstructs the pion energy and angle in the laboratory frame by simply comparing what was simulated with what the analysis software reconstructs. Examples of this comparison are given in Table 3.2 and shown in Figure 3.10. The pion energy resolution is affected slightly by pion angle but the main effect is the deterioration with increasing pion energy as a result of increasing shower losses. The pion angular resolution is reasonably steady at fixed pion energy whatever the angle but it improves with increasing pion energy.

The effect of the TAPS geometry combined with the effect of the pion energy on the opening angle between its decay photons is also evident in the results. The reconstructed pion angle is always close to the correct value whatever the pion energy. However, there are a few pion energy and angle combinations that give reconstructed pion energies significantly below the true value. These correspond to pions with a

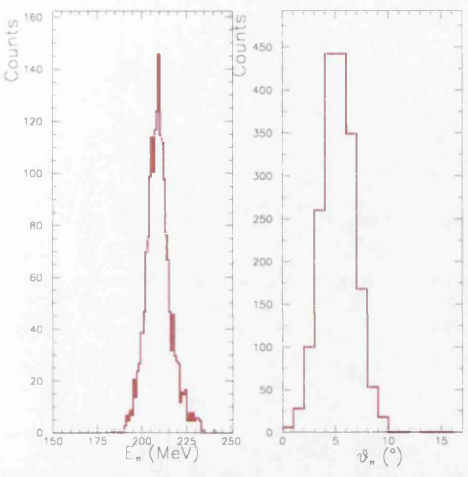

(a) $E_\pi = 210MeV; \theta_\pi = 5°$

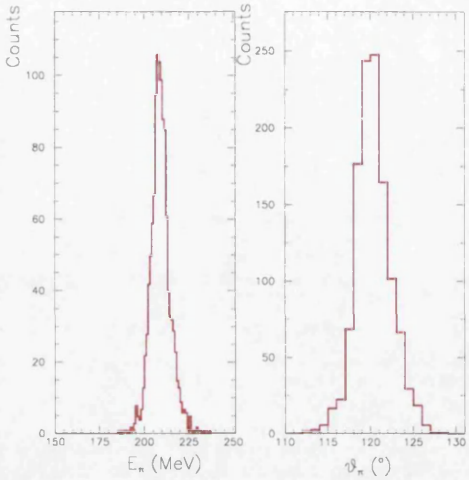

(b) $E_\pi = 210MeV; \theta_\pi = 120°$

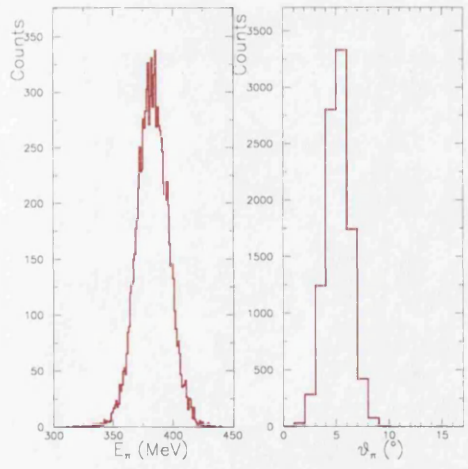

(c) $E_\pi = 380MeV; \theta_\pi = 5°$

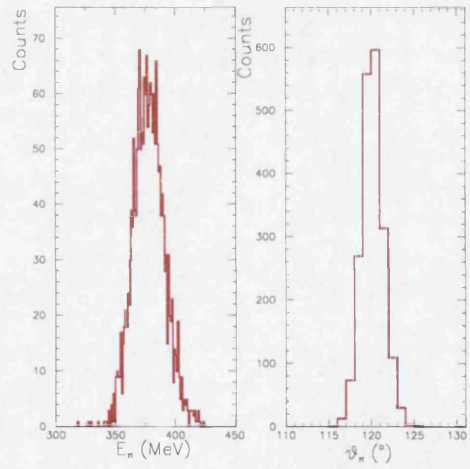

(d) $E_\pi = 380MeV; \theta_\pi = 120°$

Figure 3.10: **Reconstructed pion energy and angle:** Increasing the pion energy results in poorer pion energy resolution but improved pion angular resolution.

Table 3.2: **Comparison of simulated and reconstructed pion energy and angle.** (Reconstructed values quoted are the peak positions of the particular spectrum)

Simulated		**Reconstructed**			
E_π **(MeV)**	$\theta_\pi(°)$	E_π **(MeV)**	**FWHM (MeV)**	$\theta_\pi(°)$	**FWHM (°)**
145	**10**	144.50	3.0	10.43	6.96
	35	144.53	3.0	34.42	8.01
	45	144.47	3.0	44.34	7.97
210	**5**	208.45	13.01	5.25	4.03
	60	209.22	8.99	60.17	4.02
	120	208.50	11.05	120.08	4.02
	175	209.51	13.01	175.06	4.01
295	**5**	291.96	19.96	5.08	4.01
	60	297.06	18.92	60.34	2.99
	120	297.39	18.01	120.21	2.99
	175	296.07	18.01	175.12	2.05
380	**5**	380.84	29.11	5.28	3.03
	60	380.25	25.94	59.98	4.02
	120	377.19	25.95	120.04	2.99
	175	374.11	25.04	175.02	1.96

minimum opening angle between their decay photons that for certain θ_π values results in one, or even both, the photons being directed toward a gap between blocks. For example, the minimum opening angle for a pion with 295 MeV is $\sim 55°$ which means that for such a pion with $\theta_\pi = 5°$, its decay photons will most likely have directions with one toward the gap between block C and the forward wall and the other toward the gap between block D and the forward wall (see Figure 2.6). Most decay photon pairs have an opening angle close to the minimum (see section 2.4) so those that are detected will be incident at the edges of blocks and therefore suffer significant shower losses, hence the low value of reconstructed pion energy. The reconstructed pion angle in this particular example has a wider FWHM than those for other pion angles at the same energy for the same reason.

3.5 Positioning the NaI Detectors

As discussed in section 2.5, two NaI detectors were positioned one above and one below the target to attempt to detect the decay photons from incoherent π^0 photoproduction. In order to detect as many of these photons as possible the crystals should be positioned close to the target for maximum solid angle coverage. However, the exact positioning must take into account the proximity of the TAPS blocks. The sodium iodide crystals must not be in the line of sight of any block to the target so as not to interfere with the detection of the pion decay photons. Therefore the closest

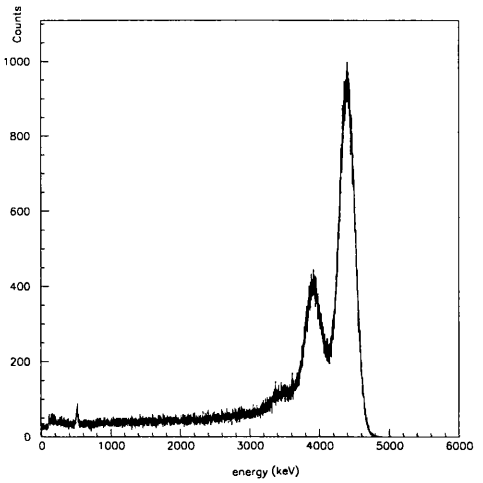

Figure 3.11: **Typical energy deposition spectrum for a NaI:** From a simulation with the NaI positioned 13.5 cm from the centre of the ^{12}C target. Photon energy = 4.4 MeV.

they could be to the target was 9 cm. The decay photons from the excited nucleus in the incoherent process could clip the corners of the NaI crystal and as a result only deposit a fraction of their energy thus adding to the background in the energy spectra. Collimating the crystals would remove these events from the spectra. A number of simulations were performed to investigate if this was worthwhile and to calculate the optimum distance of the detectors from the target.

A typical NaI energy deposition spectrum for 4.4 MeV photons is shown in Figure 3.11. The most prominent feature is the full energy peak with a slightly smaller first escape peak 511 keV below it. A collimator would only be of use if it increased the ratio of events in the full energy peak to events in the background without a significant drop in efficiency. Simulations were performed of photons from within a target fired into a single NaI at a range of positions, with and without a collimator. The photons were generated from a point at the centre of the target with random trajectories within a cone of diameter equal to that of the NaI. This ensured that all photons generated would strike the NaI and therefore reduced computing time. Two sizes of collimator were investigated: 16 and 18 cm diameter, both centred on the NaI detector. For each simulation the peak:background ratio was calculated. Comparison of these indicated that a detector at 13.5 cm from the target with no collimator compared favourably with a detector at 9 cm with a collimator (see Table 3.3). The photon energies chosen were typical of the decay photon energies in the (γ, π^0) experiment (the first excited state of ^{12}C is 4.4 MeV and the first excited state of ^{208}Pb is 2.6 MeV). Increasing the target to detector distance to 13.5 cm actually increased the number of counts in the peak region by a factor of 1.5 (comparing 13.5 cm with no collimator to 9 cm with

Table 3.3: **Positioning the NaI detector 13.5 cm from the ^{12}C target with no collimator gives a comparable peak to background ratio to positioning it at 9 cm with a collimator.**

	Peak:Background	
Source Position/Collimator	**1.25 MeV**	**4.4 MeV**
9 cm, no coll	2.06	0.86
9 cm, coll diameter=16 cm	2.81	1.07
9 cm, coll diameter=18 cm	2.48	0.97
13.5 cm, no coll	2.79	1.09
13.5 cm, coll diameter=16 cm	4.36	1.55
13.5 cm, coll diameter=18 cm	3.82	1.40

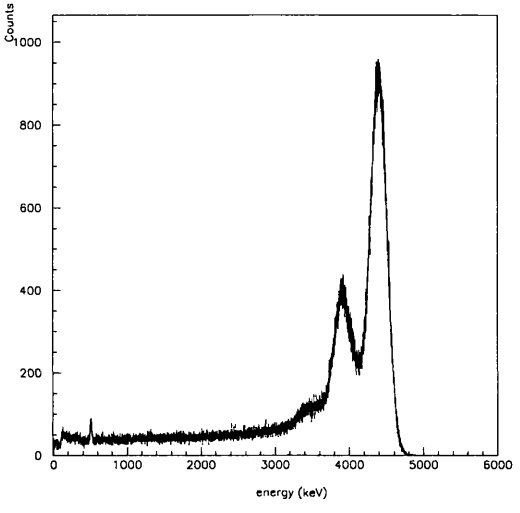

Figure 3.12: **Energy deposition spectrum for NaI:** A simulation of photons of energy 4.4 MeV fired into a NaI from within the carbon target. The NaI was 11.5 cm from the centre of the target.

collimator). The number of counts in the background also increased but by a lesser factor of 1.3 resulting in cleaner spectra.

In the experiment the NaI detectors were positioned 11.5 cm from the target (distance from centre of target to front face of crystal) as this was out of the line of sight of the TAPS blocks and provided a compromise between cleaner spectra and solid angle coverage (see Figure 3.12).

3.6 Summary

A series of GEANT3 simulations were performed and have been described in this section.

It was verified that cosmic ray muons could be used to obtain a relative calibration

of TAPS. Details of this calibration procedure are in section 4.3.1.

Measurements were made of the light collection in a TAPS detector module and this effect was included in the GEANT code and used in the simulations performed to obtain the detection efficiency of TAPS for neutral pions. Detection efficiency simulations were performed for each target. The resulting detection efficiencies were used in the calculation of the cross sections (see section 4.8).

Finally, simulations were performed to investigate the optimum positioning of the NaI blocks used to try to identify the additional decay photons from the incoherent (γ, π^0) process. No collimator was necessary and the experiment was performed with each NaI at 11.5 cm from the target (see section 2.5 and 4.9).

Chapter 4

Data Analysis

4.1 Introduction

This section describes the steps in the analysis required to get to the cross sections for ^{16}O and ^{208}Pb and is summarised as follows:

The energy deposited in the detectors was read out by charge to digital converters (QDC's) which output in channels. Therefore a translation from QDC channel number to energy (in MeV) was needed, an energy calibration. The energy signals from TAPS were recorded in two QDC's, one with a narrow (50 ns) and one with a wide (2 μs) logic signal as a gate. Each of these signals required separate energy calibrations. Energy calibrations were also carried out for the two NaI detectors using radioactive sources.

Time signals from the TAPS elements and the tagger were read out by time to digital converters (TDC's) which also output in channel numbers. Translation from channel number to time (in ns) was performed by a colleague at the University of Giessen [109]. The TDC outputs from the tagger and the TDC outputs from the TAPS elements were aligned and changes in the alignment during the data runs were identified.

The two decay components of the BaF_2 scintillation were used after the energy calibrations were completed to separate the photons from heavier particles like mesons and baryons. The wide and narrow gate energy signals were compared and pulse shape analysis (PSA) cuts were determined for every TAPS element to exclude heavier particles. The veto detector outputs were also examined and the selection criteria for which TAPS elements would be classed as constituting part of a cluster was determined.

The photon cluster energy was reconstructed and a method for reconstructing the position of the cluster was chosen. A correction was then applied to this position reconstruction method to correct an identified systematic error.

Cuts on the timing and reconstructed pion mass were applied to the data to select

pions. The "pion energy difference" of the pion was reconstructed and as a result the use of the veto detectors was reconsidered. The coherent part of the cross section was determined from fits made to the pion energy difference distributions. For the ^{16}O data part of the incoherent contribution was also determined from fits made to the pion energy difference distributions.

The data from the NaI detectors were investigated.

The tagging efficiency measurements performed during the data taking run were investigated and corrections for the presence of the target in the photon beam and background in the tagger following beam optimisations were made. Finally, the detection efficiencies described in section 3.4 were implemented and the cross sections and their associated errors were calculated.

4.2 Tagging Efficiency

The energy and flux of the bremsstrahlung photons which produced the (γ, π^0) reactions were determined, as explained in section 2.3, by the photon tagging technique. The fractional number of photons that pass through the collimator was measured during the experimental run usually at a frequency of once a day. The tagging efficiency measurement process was described in section 2.3.1.

In a tagging efficiency measurement, N_γ photons pass through the collimator and N_c are intercepted. The number of electrons detected in the focal plane is

$$N_e = N_c + N_\gamma \tag{4.1}$$

The tagging efficiency is

$$\epsilon_{tagg} = \frac{N_\gamma}{N_e} = \frac{N_\gamma}{N_c + N_\gamma} \tag{4.2}$$

N_c and N_γ are uncorrelated so their statistical errors σ_{N_c}, σ_{N_γ} are $\sqrt{N_c}$ and $\sqrt{N_\gamma}$ respectively. Hence the statistical error in the tagging efficiency is given by

$$\frac{\sigma_{\epsilon_{tagg}}}{\epsilon_{tagg}} = \sqrt{\frac{N_e - N_\gamma}{N_\gamma N_e}} \tag{4.3}$$

A first analysis of the tagging efficiency measurements identified a number of tagger channels that sometimes worked and sometimes did not. Most of these were concentrated in the first 30 channels of the focal plane detector so these channels were excluded when polynomial order 2 fits were performed on all tagging efficiency measurements to determine the variation of the efficiency with channel number. The shapes of the efficiency plots and the fit parameters obtained from the different mea-

surements were compared and details of this follow.

4.2.1 Effect of Target

Tagging efficiency measurements are normally performed with the target removed from the beam. Unfortunately in the TAPS setup this could not be done by remote control. Removing our targets involved bringing the vacuum up to air. After removing the target it was necessary to pump back down to vacuum, perform the tagging efficiency measurement and then do the whole thing in reverse to get back to running conditions. This was not only time consuming but would possibly introduce error in the repositioning of the targets and change the beam conditions. Therefore it was decided to perform most of the tagging efficiency measurements with the target in place. When the targets were changed an additional measurement was performed with no target in position. These measurements showed how the target affected the tagging efficiency measurement. Figure 4.1 shows a tagging efficiency measurement with (a) ^{12}C, (b) with ^{208}Pb and (c) with no target. The measurement with no target has a small fall-off in tagging efficiency at high tagger channels (corresponding to low incident photon energies) due to the divergence of the photon beam. In measurements with the target present, the beam interacts with the target and this effect is more pronounced at low energies resulting in an increased fall-off. However no significant difference between targets was observed. Hence a correction for the presence of the target was required but it was found that the same correction could be used for all targets.

The data from tagging efficiency measurements with no target were summed, as were the data from all the measurements made with targets in position, to improve the statistics in order to evaluate the general trend. As discussed, initially a polynomial order 2 function was fitted to all the tagging efficiency measurements. A number of functions were investigated to find which provided the best representation of the variation of tagging efficiency with tagger channel. As a result it was found that a polynomial order 3 function provided the best fit to the no target measurements but a polynomial order 6 function provided the best fit to the target in measurements. Therefore, a polynomial order 3 function was fitted to both sets of summed data and additionally a polynomial order 6 function was fitted to the target in data. There was no significant difference between target-in and target-out measurements up to tagger channel 100 so the target-in fit was used for this region. Correction for the presence of the target was only required for higher tagger channels.

Thus the fit determined from the summed data was applied to each tagging efficiency measurement:

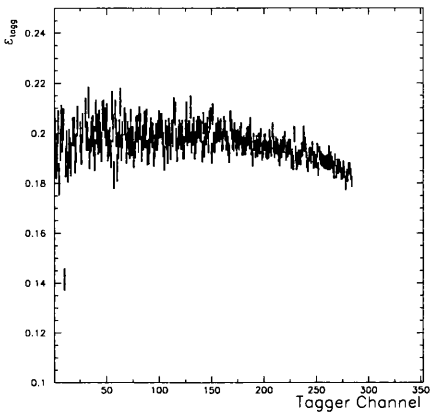

(a) ^{12}C

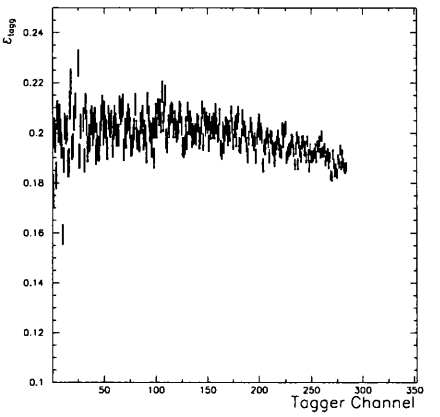

(b) ^{208}Pb

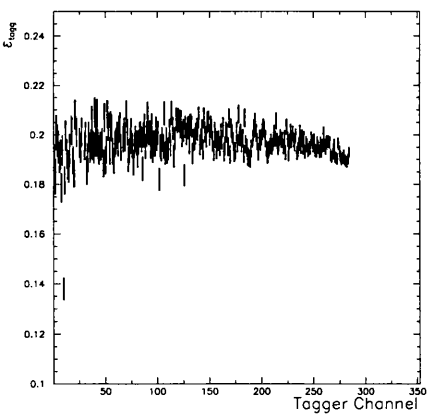

(c) No Target

Figure 4.1: **Effect of target on tagging efficiency:** The presence of any target clearly affects the shape of the tagging efficiency particularly at high tagger channels (compare figure (a) and (b) with (c)). However, variation between targets is small as can be seen by comparing (a) ^{12}C with (b) ^{208}Pb.

$$\epsilon_{tagg} = \begin{cases} Tf(x) & if\, x < 100 \\ T\frac{1}{g(100)}f(x)g(x) & if\, x \geq 100 \end{cases} \tag{4.4}$$

where

$$\begin{aligned} f(x) &= \text{fit of sum of target in runs} \\ &= 1 + 0.003x - 0.0799 \times 10^{-3}x^2 + 0.9787 \times 10^{-6}x^3 - 5.955 \times 10^{-9}x^4 \\ &\quad +1.741 \times 10^{-11}x^5 - 1.965 \times 10^{-14}x^6 \qquad (4.5) \\ g(x) &= \frac{\text{fit of target out runs}}{\text{fit of target in runs}} \\ &= 0.9639 + 0.0004x - 2 \times 10^{-6}x^2 + 5 \times 10^{-9}x^3 \qquad (4.6) \\ \frac{1}{g(100)} &= \text{normalisation factor} \\ &= 0.9889 \qquad (4.7) \end{aligned}$$

The values for T, the tagging efficiency in channel $x = 0$, in equation 4.4 were typically 0.18-0.20.

4.2.2 Effect of Background in the Tagger

On the first look through all the tagging efficiencies an "oddity" was noted in one measurement performed just after a beam optimisation. The efficiency was significantly lower at low tagger channels than in other measurements and is shown in Figure 4.2. These tagger channels are those located nearest to the beam-pipe.

The "odd" tagging efficiency consisted of two data files and when these were analysed separately it was much more pronounced in the first file as shown in Figure 4.3. This suggested that there was some background in the tagger scalers due perhaps to the beam hitting the collimator or beam pipe during the optimisation and producing some form of radioactivity in them.

As a result of this observation, measurements on the tagger scalers were performed in Mainz in December 1999. They were observed with no beam, i.e. background only, before and after an optimisation. This showed there to be an effect of about 2 % increasing to 5-10 % after an optimisation resulting in a background correction of:

$$B_{corr} = \frac{N_{BTS}}{N_{\epsilon TS}} \times \frac{t_\epsilon}{t_B} \tag{4.8}$$

where

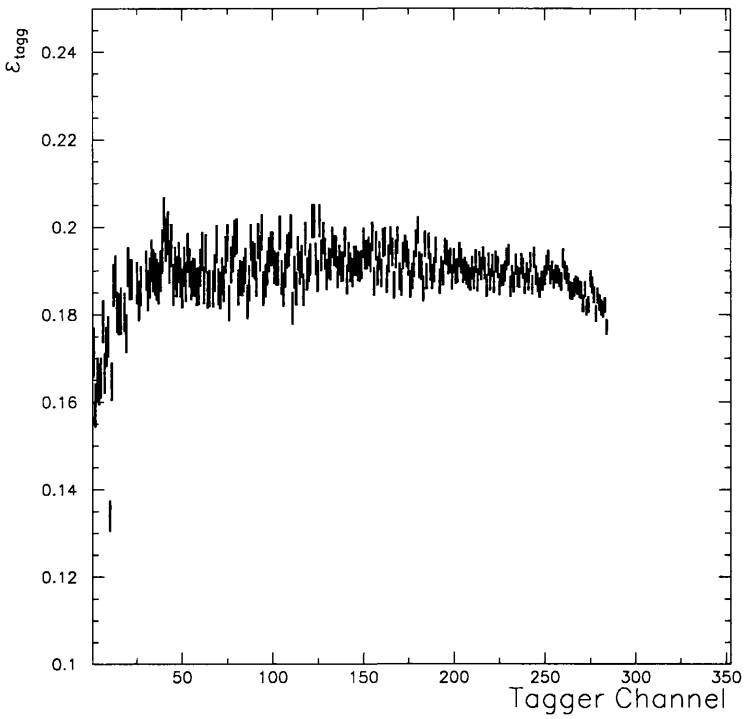

Figure 4.2: **Tagging efficiency performed shortly after beam optimisation:** The efficiency is significantly lower at low tagger channels than usual, see Figure 4.1.

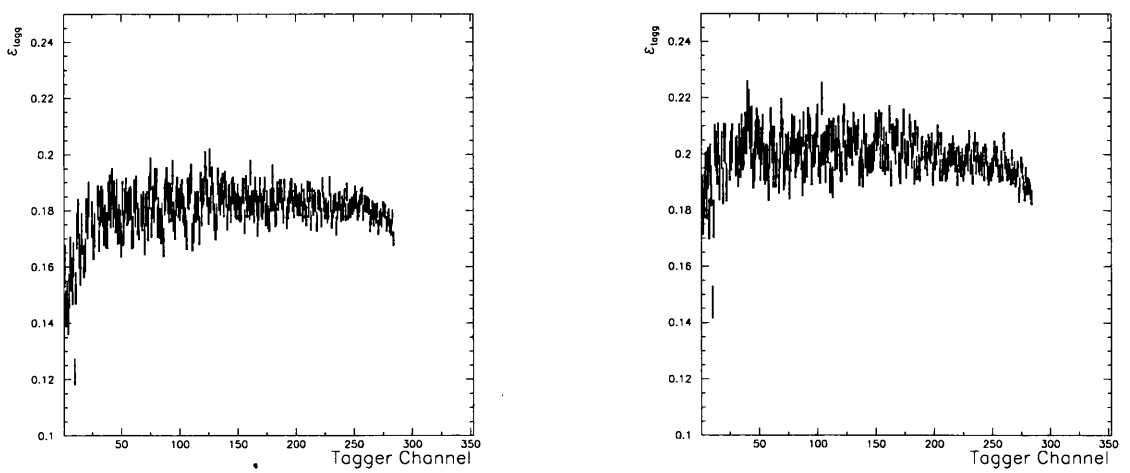

(a) First file

(b) Second file

Figure 4.3: **Tagging Efficiency performed just after beam optimisation:** (a) the first file of data clearly shows the decrease in efficiency at low tagger channels; (b) the efficiency is starting to increase back to the normal level.

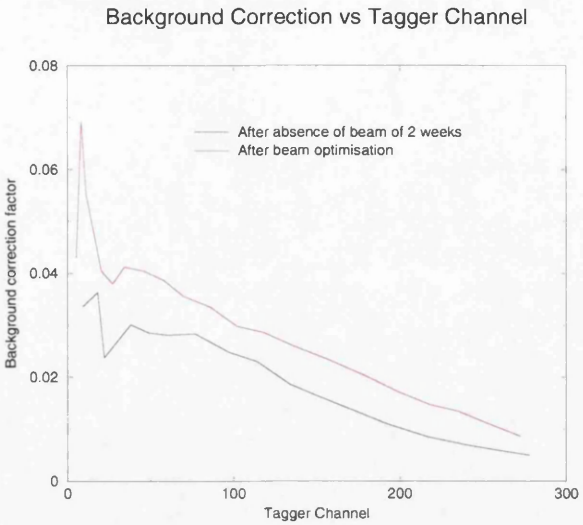

Figure 4.4: **Background correction.**

N_{BTS} = number of counts from the tagger scaler for background measurement
$N_{\epsilon TS}$ = number of counts from the tagger scalers for efficiency measurement
t_ϵ = duration of efficiency measurement [60 min]
t_B = duration of background measurement [10 min]

Figure 4.4 gives the plot of background correction versus tagger channel and this correction was applied to all tagging efficiency measurements (i.e., $\epsilon_{tagg} = \epsilon_{tagg}(1 + B_{corr})$). The measurement made very shortly after a beam optimisation that first identified this problem was discarded.

A total of 18 tagging efficiency measurements were performed during the experiment and as stated in the previous section, these gave values of T ranging from 0.18 to 0.20. Therefore, 18 calibration files were produced, each containing values for the tagging efficiency for each tagger channel. The file for a particular tagging efficiency measurement was used for all the data taken between that measurement and the next.

4.3 Calibrations

4.3.1 Energy Calibrations

Energy calibration of the TAPS detectors, that is the translation from channels to MeV, can be carried out in a number of ways: using radioactive sources, firing the tagged photon beam straight into the TAPS detector elements, or detection of cosmic radiation. Cosmic rays have been the standard method of performing energy calibrations in TAPS for a number of years but the photon energy equivalent to the peak

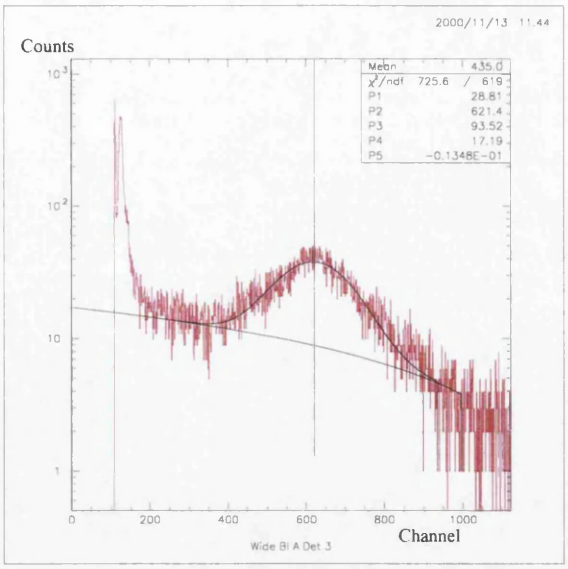

Figure 4.5: **A TAPS cosmic ray energy deposition spectrum:** The peak is fitted with a Gaussian distribution on a linear background. The pedestal is the sharp peak furthest to the left hand side of the spectrum. [Figure courtesy of [72]]

position of the cosmic energy deposition spectrum is not well known [71, 110, 111]. However, it is accepted that wherever the peak is it should be at the same energy for all the TAPS elements as was verified in section 3.2. Therefore, the cosmic rays were used for a 'relative' energy calibration.

A typical TAPS cosmic ray energy deposition spectrum is shown in Figure 4.5. Cosmic ray calibration runs were performed before and after each data taking period by triggering the data acquisition on a single hit in any TAPS element with a minimum energy of 10 MeV. A calibration was produced for each TAPS element using the channel numbers of the pedestal (the channel number corresponding to zero energy deposition) and the peak channel. The pedestal was determined by eye. The cosmic peak position was determined by fitting a Gaussian peak on a linear background as shown in Figure 4.5. The energy of the peak position in the cosmic energy deposition spectrum was taken to be 38 MeV. An absolute calibration was obtained by applying a multiplication factor of 1.05 to the cluster energies to shift the peak of the reconstructed pion mass to its accepted value (see section 4.5).

A pulser was used during the data runs to trigger the read-out of all elements when no energy was deposited. This was used to monitor changes in the pedestals during the data runs and some were found to drift over a period of several days by up to 10 channels. Sudden jumps of typically 10 channels were also seen [72].

The gain of the TAPS detector elements also varied. This was most serious in the forward wall (FW). The gain changes in the elements in blocks A-F were random and less than 3 %. The greatest gain changes were seen in the elements in the FW close

to the beam-line: the gains of those immediately adjacent to the beam-pipe decreased by about 10 % during a data-taking period [72]. This change was probably due to the factor of 10 higher count rate in those FW elements ($\sim$ 80 kHz) compared with other detector elements elsewhere in TAPS. At the start of the second data-taking period the gains of those elements that had decreased considerably during the first data-taking period had returned to their original values. Similar changes in gain were seen in the second data-taking period [72].

The pedestal values could be tracked throughout the data-taking runs but the gain values could only be determined from the cosmic calibration runs performed before and after each data-taking period. Four energy calibration files were produced for each of the two data-taking periods with some pedestal values changing for each new calibration file. The first and last calibration files used the initial and final gain values respectively. An average of the initial and final gain values were used for the two calibration files used in the middle of each data-taking period.

4.3.2 Time Calibrations

The translation from TDC channel number to time (in ns) was performed by a colleague at the University of Giessen using cable delays of varying lengths [109].

Alignment offsets for the TDC's in TAPS and the tagger were determined and changes in the alignment during the data taking runs were identified and suitable new offsets were produced.

First, the TDC outputs for the tagger channels were aligned with each other. This was performed using the tagging efficiency runs where the photon beam was fired into a large Pb-glass detector at a very low intensity ($\sim$ 0.07 pA) so that the TDC spectrum was dominated by the prompt peak, as described in section 2.3.1. The difference in time between the pulses in each tagger channel and the Pb-glass detector were used to align the tagger TDC spectra and shift the peak of the distribution to centre on 0 ns. The tagger TDC is started by the detection of an electron in the tagger detector ladder and stopped by the TAPS trigger, so

$$\text{Tagger TDC} = \text{trigger} - \text{electron} \tag{4.9}$$

If all the tagger TDC outputs are aligned with each other, the TAPS TDC spectra can be aligned using information from the data-taking runs by examining the difference between the time signals from each individual TAPS element and the time of the OR signal from all the tagger channels. This is because the TAPS TDC is started by the TAPS trigger and stopped by the CFD of the TAPS element, so

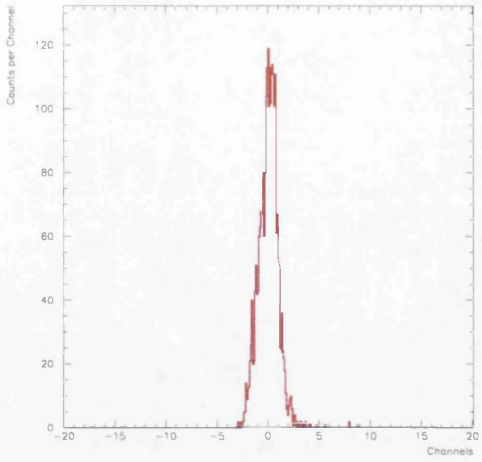

(a) After alignment

Figure 4.6: **Tagger TDC alignment:** The spectrum of time difference between the signal from the tagger channel and the signal from the Pb-glass detector for tagger channel 175 after alignment. The FWHM of the peak is 2.0 ns.

$$\text{TAPS TDC} = \text{TAPS element} - \text{trigger} \tag{4.10}$$

Thus adding equations 4.9 and 4.10 gives

$$\begin{aligned} \text{TAPS TDC} + \text{Tagger TDC} &= \text{TAPS element} - \text{electron} \\ &= \text{Alignment offset} \end{aligned} \tag{4.11}$$

For each tagging efficiency measurement, a Gaussian peak was fitted to each tagger channel TDC spectrum (there were 284 such spectra for each tagging efficiency measurement since 284 of the available tagger channels were used in this experiment). The fitted peak positions were used to correct the tagger channel offsets. An example of a time difference spectrum for a single tagger TDC after alignment is given in Figure 4.6.

To carry out the TAPS TDC alignment, for each TAPS element a Gaussian peak was fitted to the spectrum of difference in time between the signal from that element and the OR signal from all the (aligned) tagger channels (a typical time difference distribution after alignment is given in Figure 4.7). Again, the fitted peak position was used to correct the offset. The TAPS TDC alignment was repeated a number of times until all the time spectra had peaks centred on 0 ns.

Alignments were checked for all the tagging efficiency measurements and for all the experimental data. The spectra for both the tagger and for TAPS showed both

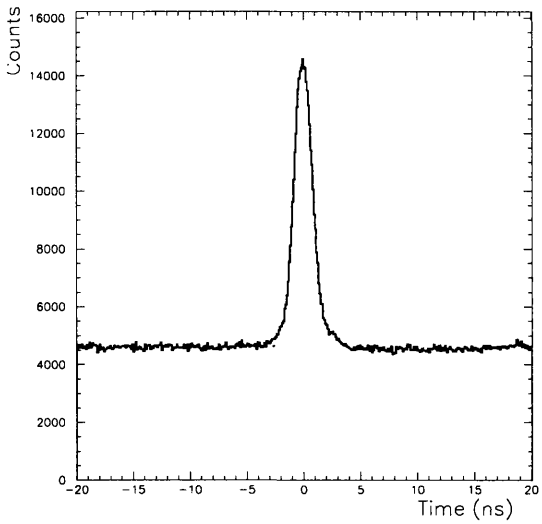

Figure 4.7: **TAPS TDC alignment:** A typical spectrum of the distribution of the difference in time between the signal from an individual TAPS element and the OR signal from all tagger channels after alignment (FWHM=2.6 ns).

gradual changes in peak positions and sudden jumps of up to several ns during the data-taking periods. As a result three time calibration files were made for the tagger and twelve calibration files were made for TAPS to account for these changes.

The time peaks in the TAPS TDC spectra are broadened to some extent by the charged particles present in addition to photons amongst the detected particles. The time alignment for TAPS was therefore repeated following the pulse shape analysis (see section 4.4.1), to get more accurate alignment values for photons following the exclusion of mesons and baryons. This second time alignment required corrections of typically less than 1 % of the alignment value.

4.4 Identification of Photons

When a photon is incident on a TAPS detector module, an electromagnetic shower is formed and this often propagates through several detector modules. As in previous TAPS experiment analyses, modules that fired simultaneously were grouped into clusters [71,110]. A cluster consists of a central element (the module with the greatest energy deposition) and neighbours (the remaining cluster members) which must share a common boundary with another cluster member. A cluster was only accepted by the analysis if the total energy deposited in its members was greater than 15 MeV and the central element had a minimum of 10 MeV deposited in it. The threshold for the cluster and that for its central element were set to discard low energy photons produced in the target by other processes, e.g. atomic processes in the target.

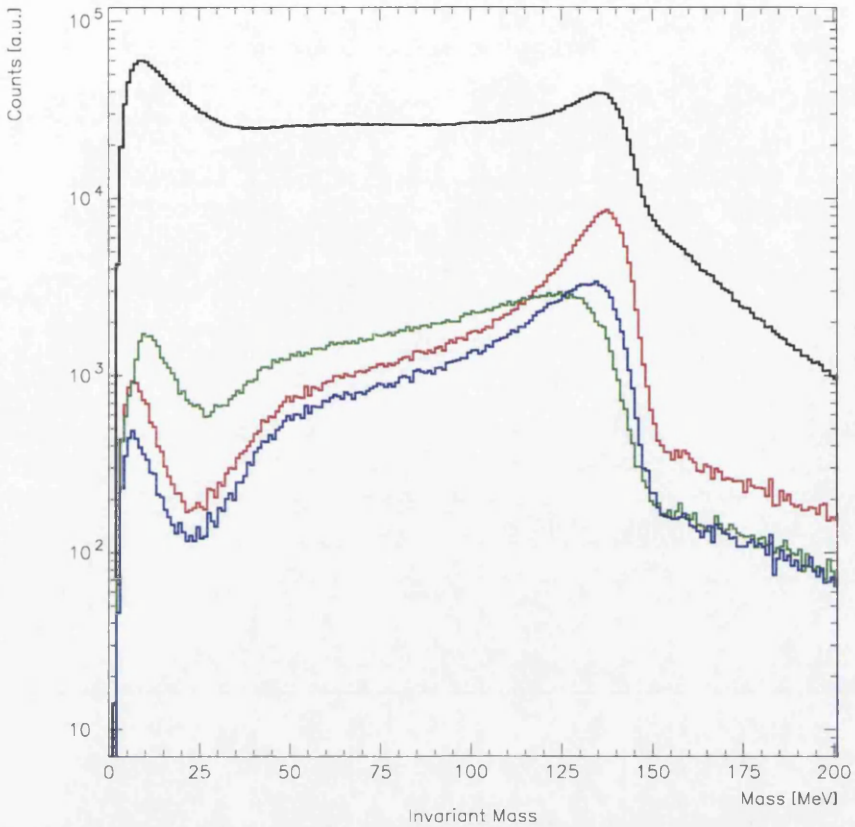

Figure 4.8: **Effect of edge detectors as central cluster elements on the pion mass (^{12}C data):** The black plot is the pion mass for the case where all TAPS detector elements are allowed to be a central cluster element and the red is for the case where only non-edge detectors are allowed to be a central cluster element. The plot in green is the worst case scenario where both pion decay photons produced a cluster whose central element was an edge detector, the blue plot is the intermediate case where one photon produced a cluster centred on an edge detector and the other produced a cluster centred on a non-edge detector.

The threshold for the neighbouring elements was kept low, at the 1 MeV hardware threshold of the CFDs (see section 2.7.2), for accurate determination of the cluster energy.

Detector modules located at the edge of a TAPS block (edge detectors) were not used as central elements but could be neighbour elements in clusters. This improved the energy resolution because in most cases a significant part of the shower spreads to neighbouring elements so not all the photon energy will be detected if the neighbouring elements are missing. This is clearly demonstrated in Figure 4.8 which shows the effect on the reconstructed pion mass spectrum of different cluster conditions for the ^{12}C data. The spectrum in black is the reconstructed pion mass (see section 4.5) where all TAPS detector modules can be a central cluster element. The spectrum in red

is the pion mass where only non-edge detectors can be the central element. Edge detectors constitute 44 % of TAPS so preventing these detectors from being central cluster elements reduced the number of accepted events by $\sim$ 70 % but significantly improved the energy resolution (the FWHM of pion mass peak reduced from 21.1 MeV to 14.0 MeV). The plot in green is the worst case scenario where both pion decay photons produced a cluster whose central element was an edge detector, the blue plot is the intermediate case where one photon produced a cluster centred on an edge detector and the other produced a cluster centred on a non-edge detector. The position resolution is also better for the retained events [72].

The clusters formed in TAPS do not all result from interactions of decay photons from a π^0, e.g. protons and neutrons can be knocked out of the target and hit TAPS. The identification and discrimination of neutral and charged particles can be achieved using the intrinsic properties of BaF_2 in combination with a fast plastic scintillator. The short decay time and high light output of BaF_2 allow time resolutions better than $\sigma = 85$ ps even for the large TAPS modules [101]. Therefore, particle identification can be performed based on a time-of-flight (TOF) technique.

The shape of the BaF_2 scintillation pulse is extremely sensitive to the nature of the impinging particle [101] and so pulse-shape analysis can be used to exclude mesons and baryons.

4.4.1 Pulse-Shape Analysis

As discussed in section 2.4, the scintillation output from BaF_2 consists of a fast component which makes up about 15 % of the total light output and a slow component which makes up the remainder. The relative contribution of the fast BaF_2 scintillation component to the total light output is smaller for particles with high rates of energy loss. As described in section 2.7.2, each TAPS element output was fed into two QDC's, one with a narrow (50 ns) gate and one with a wide (2 μs) gate. A plot of the narrow gate versus the wide gate QDC output is effectively a plot of the fast component versus the slow component and Figure 4.9 illustrates the typical TAPS response. The lower ridge is the response to protons and neutrons which could be removed with a cut on this spectrum. The upper ridge contains the response from photons but will be contaminated with pions which produce a ridge lying between the photons and protons. A better separation of particles can be obtained by the more sophisticated PSA described below.

Each event in the plot of narrow gate energy versus wide gate energy can be described by polar coordinates as illustrated in Figure 4.9, where:

$$\alpha = \arctan\left(\frac{E_{narrow}}{E_{wide}}\right) \tag{4.12}$$

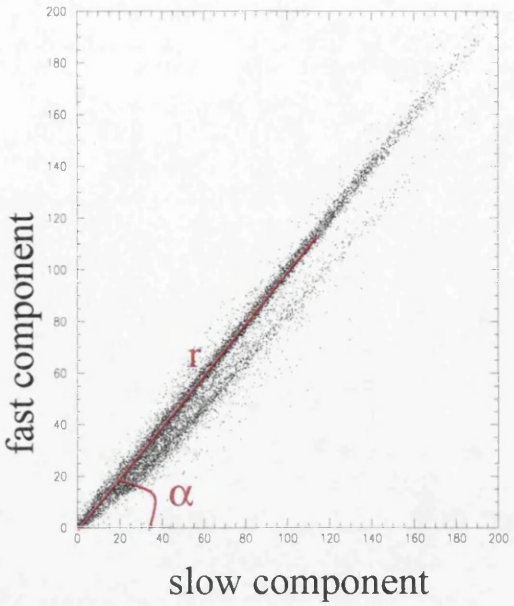

Figure 4.9: **Pulse Shape Analysis:** Plot of the narrow gate energy versus the wide gate energy. [Figure courtesy of [72]]

$$r = \sqrt{E_{narrow}^2 + E_{wide}^2} \tag{4.13}$$

The energy calibrations performed for the wide and narrow gates as described in section 4.3.1 result in $\alpha \approx 45°$ for photons and electrons. Heavier particles have smaller values of α. This difference was used to separate light and heavy particles. For each TAPS detector element a plot of r versus α was produced, a typical example is given in Figure 4.10. The photons form a ridge at $\alpha \approx 45°$ and protons appear in a banana shape at lower α. Charged pions are visible between the photon and proton ridges.

The (α, r) plot was sliced into twelve bins of r and projected onto the α-axis as illustrated in Figure 4.11. Each projection was fitted with a Gaussian around the photon peak at $\alpha \approx 45°$. A cut, defined as the distance 3σ below the peak value (where σ is the width of the fitted Gaussian), was applied in each element bin to remove heavy particles from the analysis. Events to the left of the cut were discarded. The cut is shown by the white dashed line in Figure 4.10.

The photon ridge, clearly visible to the right of the white dashed line in Figure 4.10, was found to bend towards low α at low r values. This was probably because the pedestals of the narrow gate energy spectra were overestimated. The photon ridge was also found to bend towards either lower or higher α at high values of r, depending on whether the narrow or wide gate signal saturated at the lower channel number [72]. Thus PSA was only used for particles with energies between 10 and 150 MeV in order

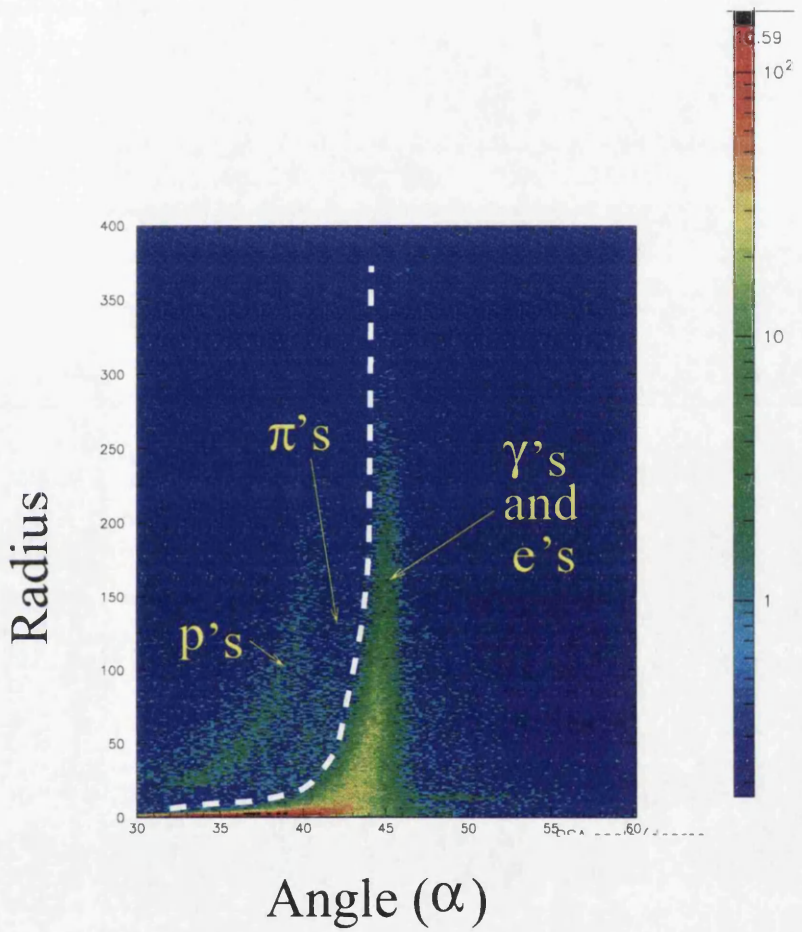

Figure 4.10: **PSA radius versus PSA angle for one TAPS element:** Photons, pions, and protons have clearly identifiable regions. The cut shown by the white dashed line was used for particles with energies between 10 and 150 MeV. [Figure courtesy of [72]]

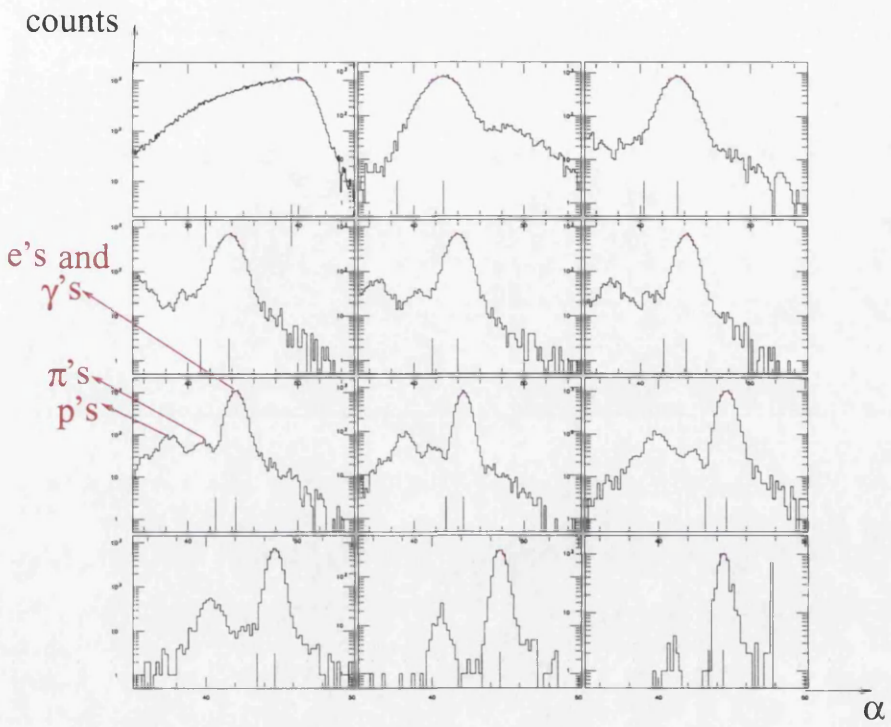

Figure 4.11: **PSA** (α, r) **plot sliced into twelve bins of** r **and projected onto the** α**-axis:** Plots are in bins of increasing r. Plots are in bins of increasing r. The r bins range from 0-10 MeV in the top left hand plot to 237.5-380 MeV in the bottom right. For low values of r, particles cannot be identified: for intermediate values of r, particles can be separated into (photons and electrons), (pions) and (protons). For high values of r, the separation between photons and electrons, and heavier particles is possible for some TAPS elements (like the one shown) but not all. The vertical lines under each spectrum mark the fitted peak position (right-hand line) and the 3σ cut-off (left-hand line). [Figure courtesy of [72]]

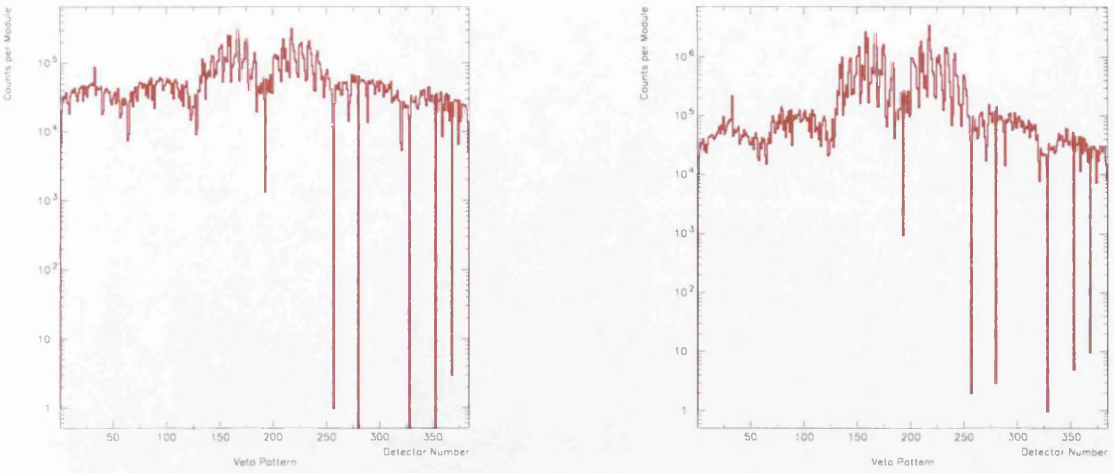

(a) ^{16}O (b) ^{208}Pb

Figure 4.12: **Veto detector pattern for blocks A-F:** A systematic trend is seen in groups of 8 detectors and from the top of a block down to the bottom (see text).

to avoid the regions where the photon ridge may bend. No PSA was carried out on particles outside this region as separation could not be performed reliably.

4.4.2 Veto Detectors

As described in section 2.4, each TAPS element is provided with a 5 mm thick plastic scintillator veto detector of identical granularity mounted in front of the BaF_2 crystal for on-line charged particle discrimination. The output from a veto detector was fed into an LED (see section 2.7.2) and the outputs from all the veto LED's are read out by a pattern unit. Therefore there was no information about the energy deposition in these detectors. The threshold for each veto should be set at the same energy to ensure a constant efficiency for identifying charged particles for all the veto detectors. Colleagues from Giessen attempted this with radioactive sources [109].

The veto pattern spectra for the ^{16}O and ^{208}Pb data are shown in Figures 4.12 and 4.13. The veto detectors were numbered from 1 to 522 with numbers 1-64 mounted on block A, 65-128 on block B, and similarly for blocks C to F. The veto detectors numbered 385-522 were mounted on the FW. The spectra for both targets show that the highest number of counts are in the veto detectors mounted on the FW and on blocks C and D since the distribution of the charged particles is forward peaked. There is a systematic variation in the number of counts every 8 detectors. This is because the veto detectors were numbered in horizontal rows of 8 such that a row consisted of detectors numbered 1-8, 9-16 etc. For any given row one end is at a more forward

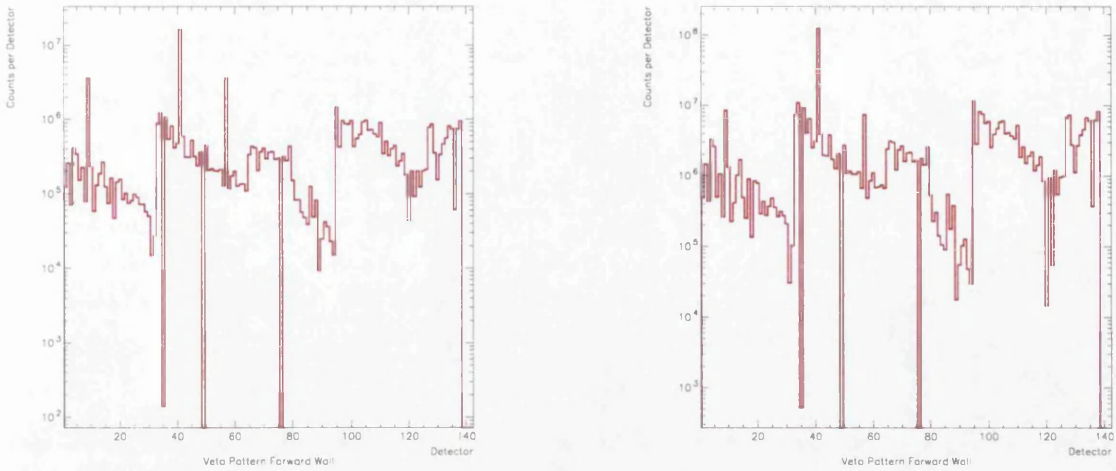

(a) ^{16}O (b) ^{208}Pb

Figure 4.13: **Veto detector pattern for the FW:** The numbering system is not straightforward for this block but generally those detectors with a high number of counts are those located in the centre.

angle than the other. There is also a systematic trend in counts from the top row of a block to the bottom row: the number of counts increase and then decrease again. This is because the top and bottom rows are further from the target than those in the middle and therefore cover a smaller solid angle. The numbering system for the veto detectors in the FW is not straightforward but generally the detectors with the high number of counts were those in the centre of the block.

Some veto detectors did not give any signals. These were exclusively mounted on the TAPS detectors in the edges of detector assemblies [72]. Faulty electronic modules and cabling resulted in some veto detectors with very high count rates. These were also all located in the edges of detector assemblies.

The use of the veto detectors in the experiment presented here is discussed in section 4.7.1.

4.5 Photon Energy Correction

If two photons detected in TAPS are produced in the target by the decay of a neutral meson, the mass of that meson can be obtained from the energies, E_1 and E_2 of the photons and the opening angle, Ψ, between them (see Appendix 4.4) by:

$$m_{meson}c^2 = \sqrt{2E_1E_2(1-\cos\Psi)} \tag{4.14}$$

Table 4.1: **Variation of the pion mass peak position with pion decay photon energy.**

E_1 [MeV]	Reconstructed Pion Mass Peak Position [MeV]									
	E_2 [MeV]									
	20	40	60	80	100	120	140	160	180	200
200	131.0	131.6	129.1	128.9	129.9	130.8	131.3	131.9	133.1	135.8

Many simultaneous hits of photons were registered in the experiment and those combinations that originate from pion decay must be identified. Thus for every photon pair combination the mass given by equation 4.14 is calculated and a spectrum is produced. Pions are selected by accepting values of mass within an appropriate window. The resolution of the mass peak depends on the angular and energy resolution of the spectrometer:

$$\frac{\Delta m}{m} = \left[\left(\frac{\Delta E_1}{2E_1}\right)^2 + \left(\frac{\Delta E_2}{2E_2}\right)^2 + \left(\frac{\Delta \Psi}{2\tan\Psi}\right)^2\right]^{\frac{1}{2}} \tag{4.15}$$

The resolution of the pion mass peak was improved by not allowing edge detectors to be central cluster elements as discussed in section 4.4. In the present measurement, the mass resolution is principally determined by the energy resolution of the detector except for photon pairs with small opening angles from pions with total energy above $\sim$ 250 MeV. However, the mass resolution did not vary rapidly with pion energy or photon opening angle and the overall value was $\sim$ 16 MeV FWHM.

The mass of the pion is known to be 134.98 MeV [77]. Therefore the pion mass obtained using all pairs of photons whose clusters met the cluster conditions should peak at 134.98 MeV. However, as the energy calibration carried out using cosmic rays was only a 'relative' calibration, an additional correction to the cluster energies was required to obtain the peak in the correct position.

Since light collection and shower collection effects in the TAPS detectors are known to depend on the photon energy (see section 3.3), an energy dependent correction for the cluster energies was looked for. Therefore, mass spectra were produced for various combinations of decay photon energies and examples are shown in Figure 4.14. The peak position, m_{obs}, was determined for each decay photon energy combination spectrum. The values of m_{obs} obtained varied from 129.0 MeV to 135.8 MeV and a sample of the results are given in Table 4.1. The TAPS trigger was set such that the two pion decay photons had to be detected in different TAPS blocks (see section 2.7.2). The large values of m_{obs} occurred at combinations of decay photon energies corresponding to opening angles of $\sim$ 69° where the photons would be detected in neighbouring blocks. As is clear from equation 4.14, the pion mass is affected by the reconstructed opening angle as well as the two photon energies and this observation indicated that the angular affect was not negligible. Pion mass spectra were produced

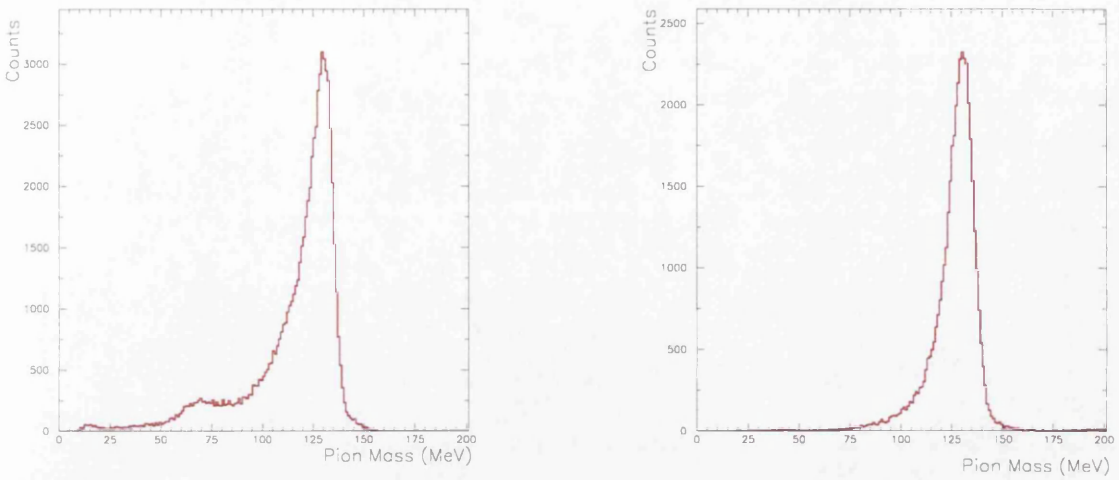

(a) (b)

Figure 4.14: **Effect of the pion decay photon energy on the reconstructed pion mass:** pion mass spectra using decay photons with energies E_1 and E_2 as follows - (a) $70 < E_1 < 90$ MeV and $50 < E_2 < 70$ MeV; (b) $190 < E_1 < 210$ MeV and $50 < E_2 < 70$ MeV.

Table 4.2: **Variation of pion mass peak position with block combinations.**

	m_{obs} [MeV]					
Block	**B**	**C**	**FW**	**D**	**E**	**F**
A	131.1	131.0	131.2	131.9	131.7	131.1
B		131.1	131.1	131.6	132.1	131.7
C			128.7	131.0	131.8	131.9
FW				128.6	131.9	131.0
D					132.7	131.7
E						131.0

for each possible combination of TAPS blocks. Again, for each spectrum the value of m_{obs} was obtained and it was found to depend on how far apart the blocks were. The results are given in Table 4.2, neighbouring block combinations are highlighted in red. The spectra for block C with the forward wall and block D with the forward wall had particularly low values of m_{obs}. This could be because on average these block combinations see photons with higher energies than other combinations and therefore it is a photon energy effect (only high energy pions give a small enough opening angle for the decay photons to be detected in neighbouring blocks, Appendix A.2.2, and then the decay will be symmetric such that both photons have similar energies). However, no acceptable energy dependent correction could be found. Therefore, a correction of 5 % was applied to increase the photon energies and move the pion mass, taking all combinations of photon energy, block etc., to $\sim$ 135 MeV. The possible effect due to

the reconstruction of the decay photon opening angle is discussed in the next section.

4.6 Position Reconstruction

TAPS is a modular setup chosen to obtain good energy resolution together with good angular resolution. The best energy resolution is obtained by summing all modules that contain parts of the electromagnetic shower. A position resolution better than the size of the detectors can be obtained by calculating the weighted centre of gravity of the electromagnetic shower, which at the energies used in the present experiment is not confined to a single BaF_2 module.

The algorithm used recently to reconstruct the entry position, (x, y), of a photon on the surface of a TAPS block was a centre of gravity algorithm but with a logarithmic weight [114]. The reconstructed x position of the photon, X_{calc}, is expressed as a weighted sum of the x positions of the cluster elements, x_i, (with similar expressions for Y_{calc}):

$$X_{calc} = \frac{\sum_i w_i x_i}{\sum_i w_i} \tag{4.16}$$

with:

$$w_i = \max\left\{0, \left[ln\left(\frac{E_i}{E_T}\right) + W\right]\right\} \tag{4.17}$$

where the energy deposited in each cluster element, E_i, is summed to obtain E_T, the total energy of the cluster. The parameter W is a dimensionless free parameter, that influences the position resolution and essentially decides the minimum energy deposit used in the reconstruction. It has usually been set so that the threshold used in the calculation matched the detector hardware threshold. The logarithmic weights w_i are introduced in order to suppress the weight of the central module and to enhance the weight of the surrounding modules and hence reduce the "pull" towards the centre of the central module. This method has been compared favourably with simulations [107].

All the reconstruction methods give an estimate of the (x, y) coordinates of the centre of the electromagnetic shower which occurs at a distance d from the front face of the TAPS block and increases with photon energy as given in equation 4.18 [115].

$$d = 2.05\,\text{cm}\left(\log\frac{E_\gamma}{12\ \text{MeV}}\right) + 1.2\,\text{cm} \tag{4.18}$$

For photons that do not hit the surface of a TAPS block at normal incidence, i.e. oblique incidence, a correction must be made to (X_{calc}, Y_{calc}) to obtain the entry position on the surface of the TAPS block. The corrected position coordinates,

(X_{corr}, Y_{corr}), are obtained through equation 4.19.

$$X_{corr} = X_{calc}\left(1 - \frac{d}{\sqrt{l^2 + X_{calc}^2 + Y_{calc}^2} + d}\right) \tag{4.19}$$

where l is the distance from the target to the centre of the front face of the TAPS block. The expression for Y_{corr} is similar.

4.6.1 Investigation of Methods to Improve Position Reconstruction

The separation of coherent and incoherent π^0 photoproduction processes requires as good a position resolution as possible and so a colleague investigated methods of improving the position reconstruction [72].

A number of different position reconstruction algorithms were investigated. All used the centre of gravity algorithm but used different expressions for the weight, w_i. The simplest weight is a linear weight given by:

$$w_{i_{lin}} = \frac{E_i}{E_T} \tag{4.20}$$

This tends to "pull" the reconstructed position towards the centre of the central module as large weights are given to elements with large energy deposition.

The logarithmic method was described in the previous section and, as discussed, was introduced to reduce the "pull" towards the centre of the central module. The lower the value of W, the lower the minimum energy deposit used in the reconstruction and thus potentially more members of a cluster will contribute. Values of W of 3.5 and 8.0 were investigated along with 5.0 which is the value that has been used in the past [70, 110].

New methods of position reconstruction were proposed and investigated. One such method was the "power" method, where the energy depositions were weighted with a power function:

$$w_{i_{power}} = \left(\frac{E_i}{E_T}\right)^P \tag{4.21}$$

Values of P from 0.1 to 0.9 were chosen to give elements with small energy depositions relatively large weights compared with the linear method, again to suppress the "pull" towards the centre of the central module.

Another method ignored the central cluster member and used only the ring of 6 elements around it - the "frac6" method The y position is reconstructed as:

$$Y_{calc_{frac6}} = c_{y_1}\left(F_2 + 0.5\left(F_1 + F_3\right)\right) + y_1 \tag{4.22}$$

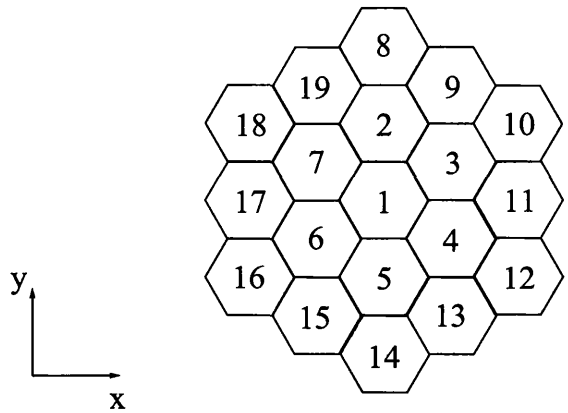

Figure 4.15: **Numbering used in the frac6 reconstruction method.** [Figure courtesy of [72]]

where

$$F_1 = \left(\frac{(E_6 + E_7 + E_2) - (E_3 + E_4 + E_5)}{\sum_{i=2}^{7} E_i} \right) \tag{4.23}$$

$$F_2 = \left(\frac{(E_7 + E_2 + E_3) - (E_4 + E_5 + E_6)}{\sum_{i=2}^{7} E_i} \right) \tag{4.24}$$

$$F_3 = \left(\frac{(E_2 + E_3 + E_4) - (E_5 + E_6 + E_7)}{\sum_{i=2}^{7} E_i} \right) \tag{4.25}$$

The y position of the central element is y_1, c_{y_1} is a constant, and the factor of 0.5 comes from projecting the unit vectors along the non-vertical axes of symmetry onto the vertical (y) direction. The parameter E_i is the energy deposition in detector element i (see Figure 4.15 for the numbering of the elements for this position algorithm). Further details on these reconstruction algorithms are given in [72].

For these methods to be tested, a series of simulations were performed using GEANT v3.21 [100] where photons of various energies were fired into a single element in a TAPS block. For each energy, a number of different points of entry were simulated both for direct and oblique incidence. The reconstruction algorithm was performed on the resulting simulated data and then the calculated position could be compared with the known position.

The distribution of reconstructed positions for the different methods is shown in Figure 4.16(a) for 100 MeV photons incident normally at the centre of a TAPS element. The average reconstructed position for various entry points is shown in Figure 4.16(b). The linear method and the logarithmic method with small values of W reconstruct the entry points of photons incident at the centre and at the edge of the element correctly but tend to "pull" the entry point towards the centre for those incident at positions in between. This is because the element with the greatest energy deposition

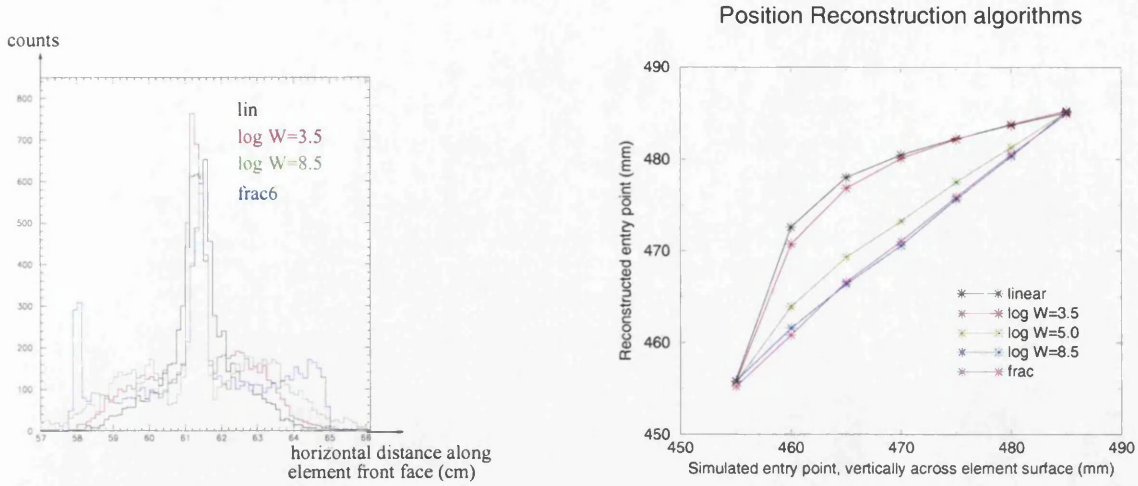

(a) (b)

Figure 4.16: **Comparison of position reconstruction algorithms using simulated data:** (a) Distribution of reconstructed positions for 100 MeV photons incident normally on the centre of a TAPS element - the edges of the element are at 58 and 65 cm. (b) The average reconstructed position versus simulated entry position - the centre of the element is at 455 mm and the vertical edge is at 485 mm. [Figures courtesy of [72]]

is assigned a very large weight compared with elements with smaller values of energy deposition. The power method with high values of P give results similar to those from the linear method.

The fractional methods and the power methods with low values of P, averaged over many events, tend to reconstruct the true position on average, but had a large uncertainty.

The position reconstruction algorithms were investigated further with real data by comparing the pion mass distributions resulting from each. The power and linear methods produced considerably worse pion reconstructed mass resolution than the logarithmic methods and so were discarded. Of the remaining logarithmic methods, setting $W = 3.5$ produced a slightly better pion mass resolution [72]. Modifying the reconstruction process to only use the central cluster element and its 6 neighbours resulted in improvement in the pion mass resolution. The logarithmic method with $W = 5.0$ when used with this modification provided the best resolution and, therefore, this method was used in the analysis.

4.6.2 Correction to the Reconstructed x and y Positions

As discussed in section 4.5, because the energy calibration carried out using cosmic ray measurements was only a relative calibration (see section 4.3.1), attempts were made

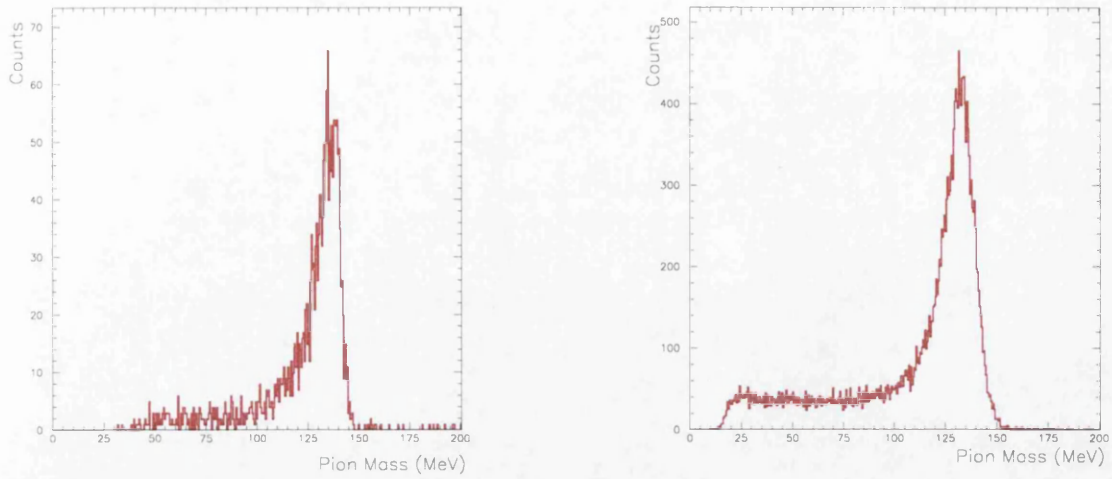

(a) D37 with block B

(b) D37 with the FW

Figure 4.17: **Pion mass energy calibration correction:** Spectra of pion mass for each central cluster detector in combination with all detectors from a TAPS block were produced. (a) Spectrum for pions reconstructed from photons with one cluster centred on detector 37 in Block D and the other cluster anywhere in block B. Peak position = 136.1 MeV; (b) Spectrum for pions reconstructed from photons with one cluster centred on detector 37 in Block D and the other cluster anywhere in the forward wall. Peak position = 132.4 MeV.

to correct the photon cluster energies such that the reconstructed pion mass spectrum had a peak at $\sim$ 135 MeV. However, no photon energy dependent correction could be found and the investigations performed indicated that there was a non-negligible effect from the reconstructed decay photon opening angle.

Using data from the same TAPS running period, M. Kotulla [116] determined photon energy correction factors for every single detector to make the pion mass peak appear at 135 MeV. Larger correction factors were needed for detectors away from the centre of a TAPS block because clusters centred on these were more likely to lose significant parts of the shower. This method was investigated for the present data. Pion mass spectra were produced for each central cluster detector taken with any detector from another whole block, e.g. detector D37 with any detector from block B, or from the FW. These are shown in Figure 4.17. Block D and the forward wall are neighbouring blocks at forward angles and so, for the energies studied here, detect mainly high energy pions with symmetric break-ups into two photons. The opening angle is such that if one photon strikes the centre of block D (detector 37 used as an example in Figure 4.17 is in the centre), the other will most likely strike towards the edge of the forward wall away from block D. Therefore, the cluster from the forward wall is likely to lose a significant portion of the shower. Thus the resulting pion mass

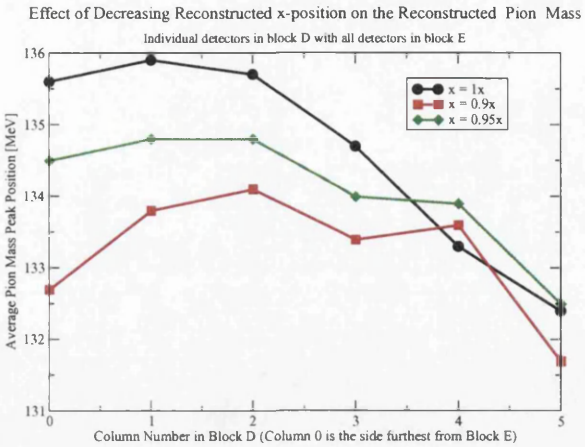

Figure 4.18: **Effect of decreasing the reconstructed x-position on the pion mass peak:** Decreasing the reconstructed x-position by 10 % decreased the variation in pion mass peak position across a block.

spectrum has a larger tail (Figure 4.17(b)) than that from photons in D37 and block B (Figure 4.17(a)) which are positioned almost opposite each other (see Figure 2.6). The difference in the position of the pion mass peaks is perhaps more significant. The pion mass peak position for D37 with the FW is $\sim$ 4 MeV below that for D37 with block B. A small reconstructed pion mass is obtained if either of the two photon energies (or both) are too small or the reconstructed photon opening angle is too small. It is possible that there is some combination of these effects.

Each TAPS block except the forward wall can be considered as 8 columns of 8 detectors (see Figure 2.5). The average mass peak position for each column, $\overline{m_{obs}}$, was calculated for each block combination. As reported by Kotulla, differences in $\overline{m_{obs}}$ were observed for the columns across a block [116]. However, these effects were larger when the photons were detected in neighbouring blocks. Again, this indicated a reconstructed opening angle effect as was suspected from the earlier investigations described in section 4.5. This effect was not reported by Kotulla as he only looked at mass spectra for individual central cluster detectors with all other detectors.

For blocks other than the forward wall, $\overline{m_{obs}}$ increased with opening angle implying that the reconstructed photon angle away from the centre of the block was too large. Decreasing the reconstructed x-position decreased the variation across a block as shown in Figure 4.18. If the reconstructed x-position required to be decreased then it follows that the reconstructed y-position should also be decreased as the x and y coverage of the TAPS blocks is similar. Therefore, the same factor used to decrease the reconstructed x-position was used to decrease the reconstructed y-position.

The forward wall is a factor 1.4 taller than it is wide. Decreasing the reconstructed y-position decreased the variation across the forward wall but decreasing its reconstructed x-position increased the variation. Therefore, the following corrections were

Table 4.3: **Variation of pion mass peak position with block combinations after position correction.** (Values of m_{obs} are larger than those in the corresponding Table 4.2 because the 5 % photon energy correction has been applied).

Block	m_{obs} [MeV]					
	B	C	FW	D	E	F
A	132.2	135.7	135.3	136.1	135.9	132.7
B		132.7	135.1	135.9	136.6	136.0
C			131.5	135.4	136.3	136.3
FW				132.0	136.5	135.4
D					134.5	136.0
E						131.8

Table 4.4: **Comparison variation of pion mass peak position with block combinations for real and simulated data.**

Block Combinations	Real Data		Simulated Data	
	$\overline{m_{obs}}$	σ_n	$\overline{m_{obs}}$	σ_n
Neighbours	132.5	0.9	132.1	0.2
Next but one	135.8	0.5	134.9	0.4
Next but two	135.8	0.4	136.0	0.3

applied:

$$\text{TAPS blocks A} - \text{F} \begin{cases} X_{calc}^{corr} = 0.9 X_{calc} \\ Y_{calc}^{corr} = 0.9 Y_{calc} \end{cases} \tag{4.26}$$

$$\text{Forward Wall} \begin{cases} X_{calc}^{corr} = 1.0 X_{calc} \\ Y_{calc}^{corr} = 0.95 Y_{calc} \end{cases} \tag{4.27}$$

These corrections decreased the variation in the pion mass peak position for the block to block combinations reported in section 4.5. The results are given in Table 4.3, neighbouring block combinations are highlighted in red. The peak positions for neighbouring blocks are still lower than other block combinations but block C with FW and block D with FW no longer give peak positions lower than those for other neighbouring blocks (although block D with block E is now a little higher than the other neighbouring block combinations). However, the trend for the pion mass peak position to decrease the closer the blocks are to each other compares well with that seen for simulated data as is shown in Table 4.4. Therefore, the corrections of equations 4.26 and 4.27 were used in the analysis.

4.7 Selection of Pions

Neutral pions are identified initially by the coincident detection of their two decay photons. Events where only one photon triggered a response in TAPS were rejected.

However, since some of the photons detected by TAPS will not originate from the decay of a π^0 but come from a number of sources including atomic processes in the target, it is also necessary to reconstruct the mass of the mesons.

If a photon came from a pion decay then the aligned time difference between its detection in TAPS and the detection of the electron in the tagger (corresponding to the incident photon that caused the photonuclear reaction) will be close to zero. The spectrum of the time difference between the tagger and the TAPS trigger is shown in Figure 4.19 and shows a coincidence peak around 0 ns on a flat background. This background is due to random coincidences between TAPS and the tagger. To select prompt coincidences only events with a time difference between the tagging electron and the TAPS trigger (T_{TT}) from -2.0 ns to $+3.0$ ns were accepted. The distribution of T_{TT} is slightly asymmetric, probably due to the time signals from TAPS and the tagger drifting during the data run. The random background in the T_{TT} acceptance region was subtracted by selecting regions on both sides of the peak that correspond to random background events only. Figure 4.19(a) illustrates the regions used and Figure 4.19(b) and (c) shows the T_{TT} distribution for ^{16}O and ^{208}Pb respectively. The chosen background regions had a width 6 times that for the acceptance region so these events were given a weight of $-\frac{1}{6}$ in the calculation of the cross section.

The reliability of this random background subtraction in the tagger was investigated by producing the differential cross section for π^0 production for the region just below threshold (the $130 < E_\gamma < 135$ MeV region). Figure 4.20 shows how this compares with the differential cross section just above threshold (see section 4.8 for details of the differential cross section calculation). On average, this cross section should be zero since the incident photon energy is below the π^0 production threshold. The average value is actually 0.008 μb and this small yield is probably due to insufficient subtraction of random background events in the distribution of time difference between TAPS and the tagger (see Figure 4.19). However, the cross section below threshold is negligible compared with other errors in the present result: it is less than $\frac{1}{10}$ of the cross section in the threshold region and less than $\frac{1}{1000}$ of the cross section in the highest energy region. Therefore the cross sections for $135 < E_\gamma < 380$ MeV were not corrected for this.

If two photons detected in TAPS both came from the same pion decay then the time between their detection in TAPS will be small. Therefore only events with detection time differences from -1.8 ns to +1.8 ns were accepted. Figure 4.21 shows this distribution to be sharp for both ^{16}O (FWHM = 700 ps) and ^{208}Pb (FWHM = 550 ps). It was estimated that only 0.1 % of pions were lost with this cut.

The reconstructed pion mass spectra for ^{16}O and ^{208}Pb are shown in Figures 4.22(a) and (b) respectively. The finite resolution of TAPS smears out the distribution of the

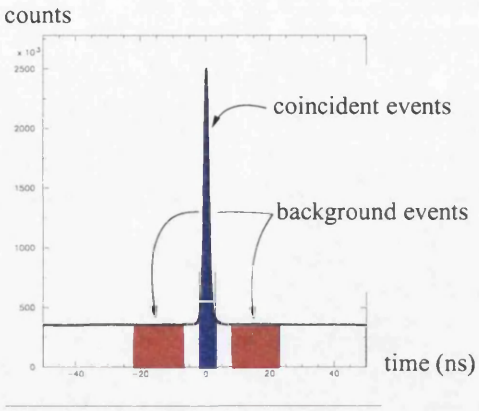

(a) Peak and Background regions

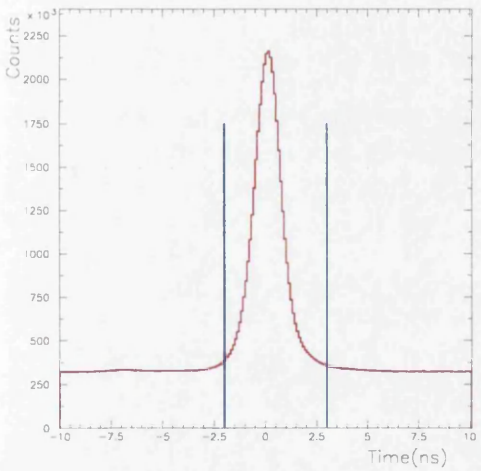

(b) ^{16}O

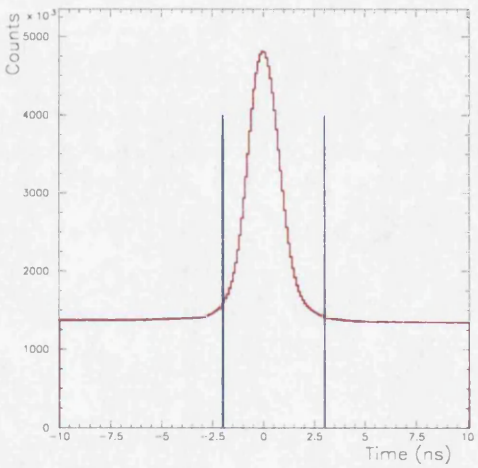

(c) ^{208}Pb

Figure 4.19: **Time difference between the tagging electron and the TAPS trigger:** Events were accepted if the difference was between -2.0 ns and $+3.0$ ns (as indicated by the blue lines in (b) and (c)) and background regions were used to subtract random coincidences from the prompt region. (a) illustrates the regions used; (b) distribution for ^{16}O (FWHM = 1.7 ns); (c) distribution for ^{208}Pb (FWHM = 2.4 ns).

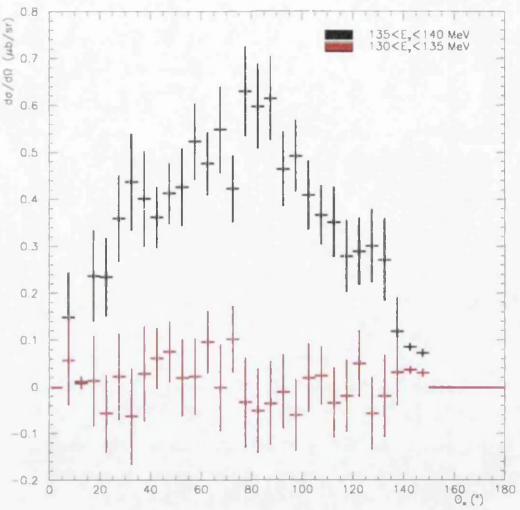

Figure 4.20: **The below threshold differential π^0 production cross section for ^{16}O:** The below threshold cross section, $130 < E_\gamma < 135$ MeV, (red) is negligible compared with the just above threshold, $135 < E_\gamma < 140$ MeV, (black) cross section.

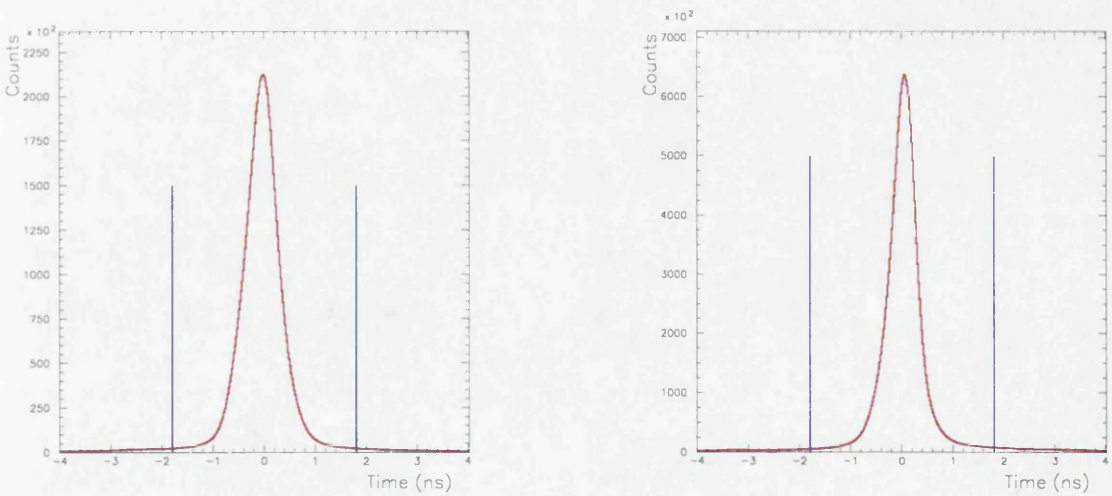

(a) ^{16}O (b) ^{208}Pb

Figure 4.21: **Time difference between the two pion decay photons:** A cut from -1.8 ns to +1.8 ns was made as indicated by the blue vertical lines.

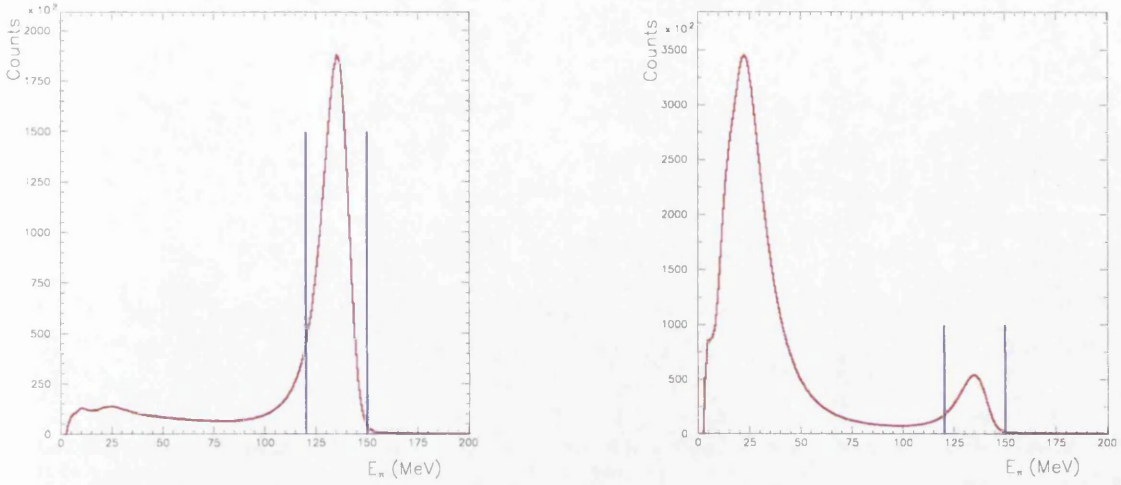

(a) ^{16}O (b) ^{208}Pb

Figure 4.22: **Reconstructed pion mass:** A cut from 120-150 MeV was applied to the pion mass as indicated by the vertical blue lines.

reconstructed pion mass, widening the peak at 135 MeV. The FWHM of the pion mass spectrum is 15.5 MeV for ^{16}O and 17.0 MeV for ^{208}Pb. Part of the electromagnetic shower produced in TAPS by the photons can escape the detectors resulting in an energy deposition lower than the photon energy and hence a low reconstructed pion mass. This produces the slower fall-off on the low mass side of the peak. However, a significant number of photon pairs reconstruct a mass well below the known pion mass. This is due principally to pair production in the target which results in a bump at 25 MeV [117]. This bump is far more noticeable in the ^{208}Pb data and indeed dominates the spectrum, Figure 4.22(b). This is because ^{208}Pb is a much larger nucleus than ^{16}O and its larger electric field gives rise to more pair production.

Photon pairs that produced a pion mass outside the region 120-150 MeV were rejected. No correction for pions lost by this cut was necessary because this was already accounted for in obtaining the detection efficiencies since the same cut was applied to the simulated data.

As discussed in section 2.6, the water target construction resulted in the beam passing through thin (0.06 mm) Melinex windows as well as the water. Therefore, data were taken on the empty target to allow correction for any processes taking place on the support structure. Data were taken on the empty target for 4 hours 45 minutes. The reconstructed pion mass plot for this data compared with that for the full target data is shown in Figure 4.23 and clearly shows that some pions were produced in the support structure. The yield from the empty target was investigated and compared with that from the full target. Figure 4.24 shows differential cross

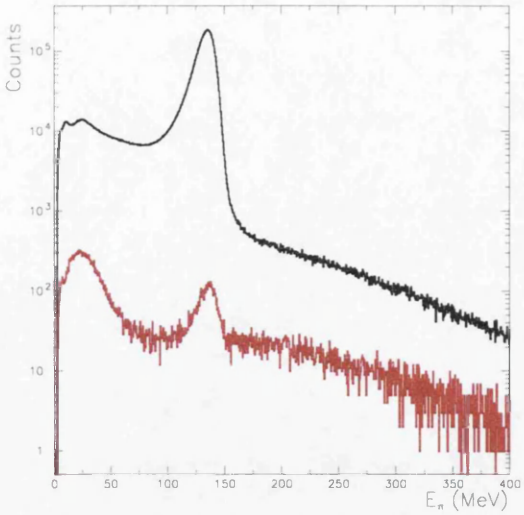

Figure 4.23: **Comparison of the reconstructed pion mass spectra from full (black) and empty (red) water target data:** A pion peak at 135 MeV is clearly visible in the empty water target data although background dominates more than in the data with the full target.

sections for E_γ = 135-140 MeV and E_γ = 200-220 MeV full and empty water target data. The differential cross section from the empty water target is very small: zero close to threshold and less than $\frac{1}{100000}$ of that from the full target at higher incident photon energies. Therefore no correction for this was performed.

Data were also taken for 4 hours and 50 minutes on the empty ^{208}Pb target holder to check that the ^{208}Pb data were not contaminated with pions produced in the support structure. Figure 4.25 shows the reconstructed pion mass spectra for the ^{208}Pb data and the empty target data. There are clearly no pions in the empty target data so no correction was needed.

4.7.1 Use of the Veto Detectors

The veto detectors were discussed in section 4.4.2. In the experiment, the main source of charged particles is pair production by the photon beam and the pion decay photons, which takes place mainly in the target and the beam-pipe. Investigations were performed to decide whether to use the veto information in the analysis.

At least two clusters from separate TAPS blocks had to be present to start the trigger (see section 2.7.2). Electrons or positrons resulting from pair production that are incident on a TAPS element could be discarded by rejecting clusters whose central element veto detector gave a signal. However, combining a cluster created from a pair production process with a cluster made by a pion decay photon, or two clusters from the electron-positron pair, would probably reconstruct a pion mass very different

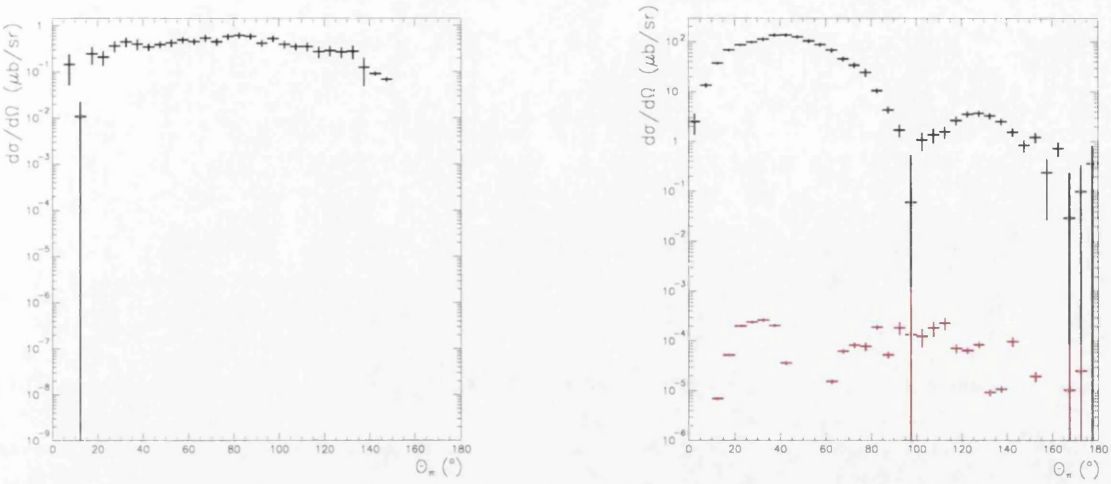

(a) $135 < E_\gamma < 140$ MeV (b) $200 < E_\gamma < 220$ MeV

Figure 4.24: **Differential cross sections for full (black) and empty (red) water target data:** (a) Close to threshold there is no yield from the support structure; (b) At higher incident photon energies the yield from the support structure is still negligible,

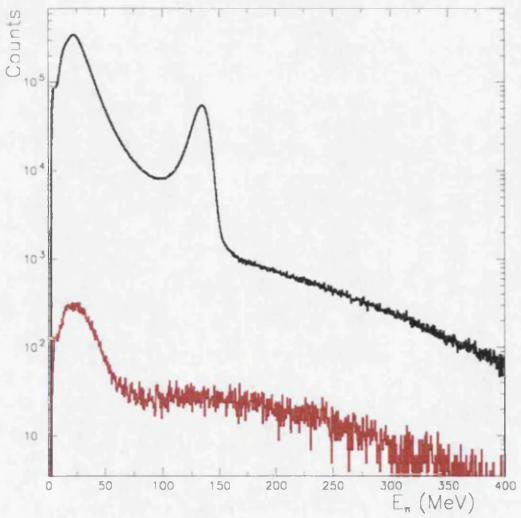

Figure 4.25: **Comparison reconstructed pion mass spectra from ^{208}Pb (black) and from the empty support structure (red) data:** There is no pion peak at 135 MeV in the empty target data.

Table 4.5: **Some of the non-coherent processes contributing to neutral pion photoproduction:** The extra energy required above that for the coherent reaction is shown (only the two lowest excitation states for both nuclei are listed).

Process	Extra Energy Required [MeV]	
	^{16}O	^{208}Pb
Nuclear excitation	6.05, 6.13, ...	2.61, 3.20, ...
Proton knock-out	12.1	8.0
Neutron knock-out	15.7	7.4
Double π^0 production	134.98	134.98

from the tabulated value. This was confirmed by examining the spectrum of the reconstructed pion mass with the veto condition applied. This produced a reduction in the bump at 25 MeV but the counts in the 120-150 MeV acceptance region were not significantly affected [72].

However, even a small reduction could turn out to have a fractionally much larger effect in the kinematic regions where the coherent (γ, π^0) process has a very low cross section, for example at backward pion angles. Hence, the effect of the veto condition on the pion energy difference spectrum which is used to separate the coherent process (see section 4.7.2) was examined at both forward and backward angles. This showed a very small reduction in the number of events in the spectra when clusters were discarded if the veto of the central element had given a signal. However, the fractional reduction of coherent and other events was similar [72]. Therefore, since using the described veto condition did not improve the rejection of non-coherent events but did slightly reduce the number of pions detected ($\sim 5\,\%$ of counts were lost from the coherent peak region when the veto condition was used), and as the efficiencies of the veto detectors were not well known and varied considerably, the veto detector information was not used in the analysis.

4.7.2 Selection of Coherent Events

As discussed in section 1.2.2, several different processes contribute to neutral pion photoproduction. The coherent reaction leaves the residual nucleus in its ground state. However, pion production may also lead to discrete excited states of the residual nucleus and there will be quasifree processes, where a proton or neutron is knocked out of the nucleus and a π^0 is produced, as well as double pion production. To obtain the coherent yield, the yield from non-coherent processes must be eliminated and this separation relies on the fact that the threshold energies for the non-coherent processes are larger. The extra energy required for each non-coherent process is given in Table 4.5.

The separation of the coherent yield was carried out using an analysis technique

[56, 69] very similar to a standard "missing energy" analysis. This technique makes explicit use of the energy information provided by the tagger. Assuming coherent π^0 photoproduction, the centre of mass energy of the π^0 meson can be calculated via

$$E_{\pi_c}(E_\gamma) = \frac{s + m^2 - M^2}{2\sqrt{s}} \tag{4.28}$$

from the energy E_γ of the primary photon (see Appendix A for further details and definition of the symbols used here). It can also be obtained via a Lorentz transformation of the measured energies E_1 and E_2 and emission angles θ_1 and θ_2 of the decay photons in the laboratory system via

$$E_{\pi_c}(\gamma_1, \gamma_2) = \gamma\left[E_1 + E_2 - \beta\left(E_1 \cos\theta_1 + E_2 \cos\theta_2\right)\right] \tag{4.29}$$

with $\beta = \frac{E_\gamma}{(E_\gamma + M)}$ and $\gamma = \sqrt{1 - \beta^2}$ where M is the mass of the target nucleus. The difference of the two energies

$$\Delta E_\pi = E_{\pi_c}(\gamma_1, \gamma_2) - E_{\pi_c}(E_\gamma) \tag{4.30}$$

is the "pion energy difference" and should be zero when the π^0 is produced coherently. Figure 4.26 shows the resulting pion energy difference distributions for (a) ^{16}O and (b) ^{208}Pb taking all pion events. These curves contain a peak structure around zero that is mainly due to coherent π^0 photoproduction and a tail at the negative energy side that is due to incoherent and quasifree π^0 photoproduction processes.

In order to extract the strength of the coherent peak and also, where possible, the incoherent strength from the pion energy difference spectrum, it had to be fitted with one or more functions representing these components. Since the energy resolution of TAPS varies considerably across the photon energy range studied (see Figure 4.27), these fits were performed after the pion energy difference spectra had been split into a series of incident photon energy and pion lab angle bins and the fitting procedure was adapted to allow for the changing resolution. The fits are discussed later in this section.

For ^{208}Pb the TAPS energy resolution was not good enough to separate the incoherent excitation of the lowest states at 2.6 and 3.2 MeV. For ^{16}O, however, a definite peak in the pion energy difference spectrum was observed for some incident photon energy and pion lab angle combinations corresponding to the excitation of one or more of the lowest group of four states in the 6-7 MeV region. This was used to assist in the identification of the coherent events and will be discussed later in this section.

Quasifree events made no contribution in the coherent peak region of the pion energy difference spectrum for low incident photon energies as the increased energy

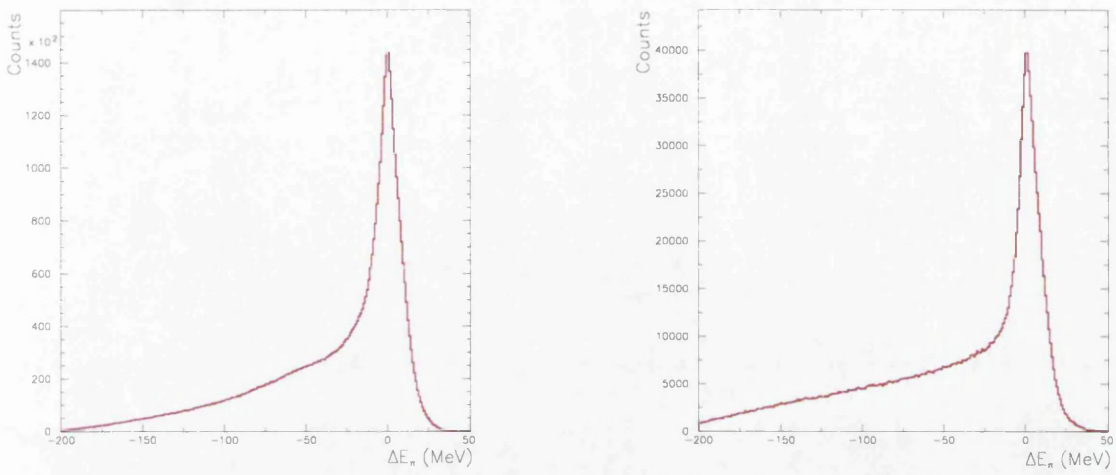

(a) ^{16}O (b) ^{208}Pb

Figure 4.26: **Pion energy difference distributions for all incident photon energies and all pion lab angles:** (a) ^{16}O distribution has FWHM = 18 MeV; (b) ^{208}Pb has FWHM = 16 MeV.

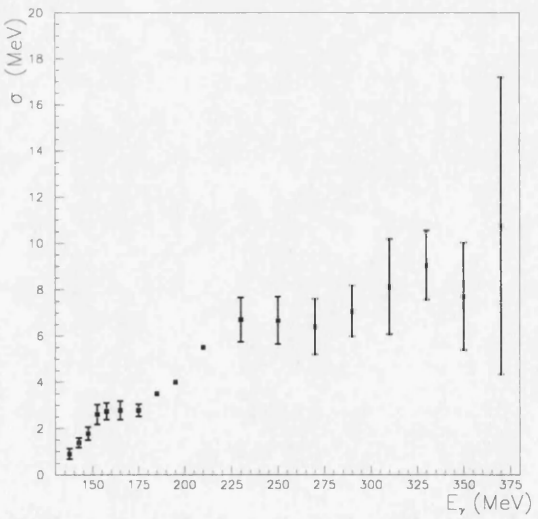

Figure 4.27: **Pion energy difference resolution σ:** Obtained using ^{16}O data and averaged over all pion angles. Statistical errors are shown. Similar values of resolution were obtained for ^{208}Pb.

threshold for such events was considerably greater than the energy resolution. At higher photon energies, an attempt was made to allow for the weak tail of the quasifree energy difference distribution which extends into the coherent region. Double pion production events make no contribution to the observed energy difference distribution at any incident photon energy.

One anticipated and observed difficulty with fitting the pion energy difference spectra occurs because the coherent pion production yield decreases by a large factor with increasing pion angle (θ_π) whereas the yield of the incoherent processes is expected to vary slowly with θ_π [26, 118] (see sections 1.2.2 and 1.3). Therefore, at large θ_π, the ratio of incoherent to coherent events becomes large and the coherent peak becomes difficult to distinguish. This would not be too serious a problem if the energy and angle calibration of TAPS was sufficiently good that the position of the coherent peak in the pion energy difference spectrum remained close to zero at all photon energy (E_γ), θ_π combinations. However, as is shown in Figure 4.28, even at low E_γ the coherent peak position moves around with θ_π. These fluctuations in peak position from one θ_π bin to the next become large shifts with increasing E_γ where there are also increasing contributions from incoherent processes. The largest shifts in the pion energy difference peak position with pion lab angle are seen at incident photon energies of 200-240 MeV. At these energies the minimum opening angle between the two pion decay photons (equation 1.2) is such that they are most likely to be incident on TAPS with one hitting the edge of the forward wall and the other the centre of block C (or D) and vice versa. This combination is known to give problems with the reconstructed photon momenta as was discussed in sections 4.5 and 4.6.2 and so it is not surprising that it also gives problems with the pion energy difference distributions.

At incident photon energies close to the pion production threshold the energy resolution was very good (see Figure 4.29). At threshold there is not enough energy for the incoherent processes to occur and the yield of these processes increases slowly with increasing incident photon energy while the coherent yield initially increases more rapidly [26]. However, the shape of the coherent part of the pion energy difference distribution was found to vary with incident photon energy and pion angle. The methods employed to fit it for ^{16}O and ^{208}Pb are given in the remainder of this section and the regions where the different methods were used are given in Appendix C.

Oxygen-16

At low incident photon energies, the shape of the coherent part of the pion energy difference distributions was generally well fitted with a single Gaussian function and

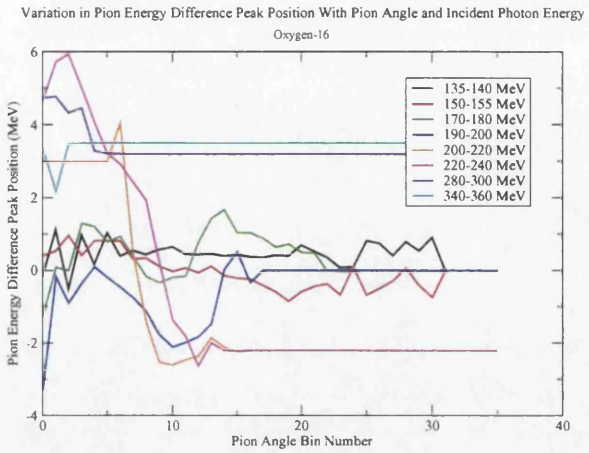

(a) ^{16}O

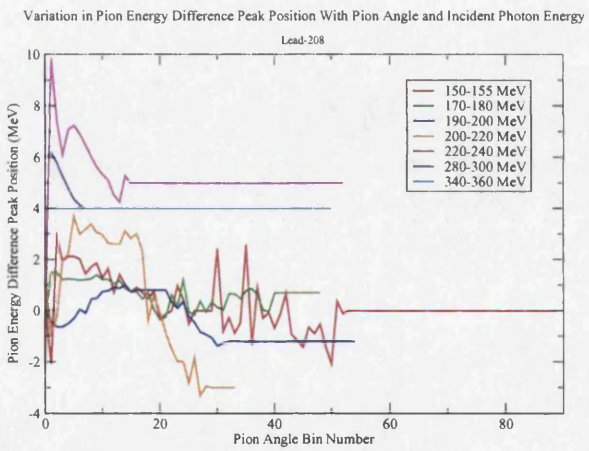

(b) ^{208}Pb

Figure 4.28: **Pion energy difference peak position for the coherent process:** For both targets fluctuations in coherent peak position are seen even at low incident photon energies and pion lab angles. Larger shifts are seen with increasing incident photon energy where there are also increasing contributions from the incoherent processes. (For ^{16}O, pion angle bins of 5° were used so bin number, b, covers the range $5b° < \theta_\pi < (5b+5)°$; For ^{208}Pb, pion angle bins of 2° were used so bin number, b, covers the range $2b° < \theta_\pi < (2b+2)°$.)

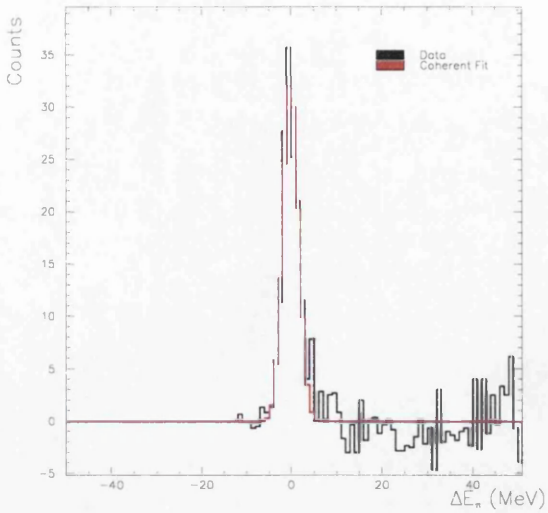

Figure 4.29: **Pion energy difference spectrum for ^{16}O:** for $20° < \theta_\pi < 25°$ and $145 < E_\gamma < 150$ MeV, fitted with method 1.

an example is shown in Figure 4.29. However, some incident photon energy and pion angle combinations gave pion energy difference distributions that were not well described by a Gaussian function. This was probably due to a change in the position of the coherent peak over the incident photon energy range contributing to the data: Figure 4.30 gives an example of such a wider peak, which is probably the sum of many Gaussian distributions, each with a slightly different peak position. It was found that distributions of this shape could be fitted with two Gaussian functions with the same centroid but different widths. A Fermi function was also used if necessary to represent the fall-off of the distribution from the quasifree processes below its average threshold E_{av} (the use of the Fermi function is seen in Figure 4.32).

The function used to fit the data was:

$$F = \frac{A_1}{\sqrt{2\pi}\sigma_1}\exp\left(\frac{-(x-x_c)^2}{2\sigma_1^2}\right) + \frac{A_2}{\sqrt{2\pi}\sigma_2}\exp\left(\frac{-(x-x_c)^2}{2\sigma_2^2}\right) + \frac{A_Q\sigma_F\sqrt{2\pi}}{1+\exp\left(2.4\frac{x-x_c+E_{av}}{\sigma_F\sqrt{2}}\right)} \tag{4.31}$$

where A_1 and A_2 are the areas, σ_1 and σ_2 the widths, x_c the common centre of the Gaussian functions, A_Q the height of the Fermi function, x the pion energy difference, E_{av} the average energy required for the quasifree process and

$$\sigma_F = \sqrt{\frac{A_1\sigma_1^2 + A_2\sigma_2^2}{A_1 + A_2}} \tag{4.32}$$

The width of the Fermi function (σ_F) is obtained from the Gaussian widths,

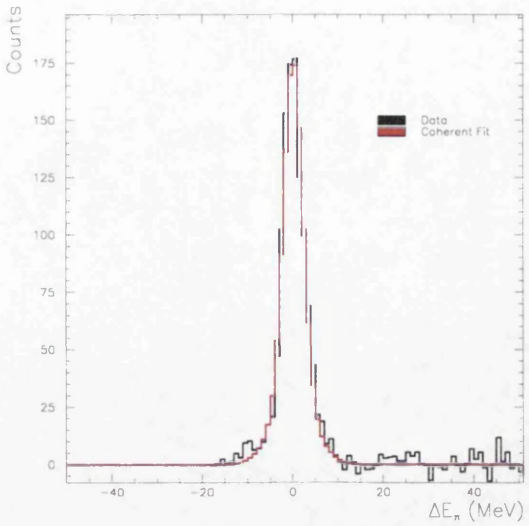

Figure 4.30: **Pion energy difference spectrum for ^{16}O:** for $65° < \theta_\pi < 70°$ and $150 < E_\gamma < 155$ MeV, fitted with method 2.

weighted with the Gaussian areas such that the Gaussian with the largest area determined most of the width to ensure that the resolutions of the distributions describing the coherent and quasifree processes were consistent. For fit method 1, $A_2 = 0$. In both methods 1 and 2, the distance between the centre of the Gaussian function and the centre of the fall-off of the Fermi function was determined by the average extra energy required for the quasifree process.

A different fitting procedure was required at high E_γ's and high θ_π's, where as noted above no clear coherent peak is visible in the pion energy difference distribution. When this was the case, a procedure, method 3, was used in which a single Gaussian was fitted at a fixed peak position using only the data to the right hand side of that peak. This minimises the effect of the incoherent processes on the fit but of course does not completely eliminate it. The fixed peak position was based on that obtained for the coherent peak when method 1 or 2 was used at slightly smaller θ_π and/or E_γ. Figure 4.31 gives an example of such a fit. The fit function used is described by equation 4.31 with $A_2 = 0$, $A_Q = 0$, and x_c fixed as discussed above.

At some incident photon energy and pion angle combinations, a second peak was observed in the pion energy difference distribution at about 6.5 MeV below the coherent peak. There are four excited states in ^{16}O around this energy (at 6.05, 6.13, 6.92, and 7.12 MeV - see Figure 4.50) so this second peak could result from the incoherent process leaving the nucleus in one or more of these excited states. In this situation a fitting procedure, method 4, was used where a single Gaussian was fitted to the coherent peak and a single Gaussian was fitted to the incoherent with its peak position fixed at 6.5 MeV below the coherent. The width of the incoherent peak was fixed to

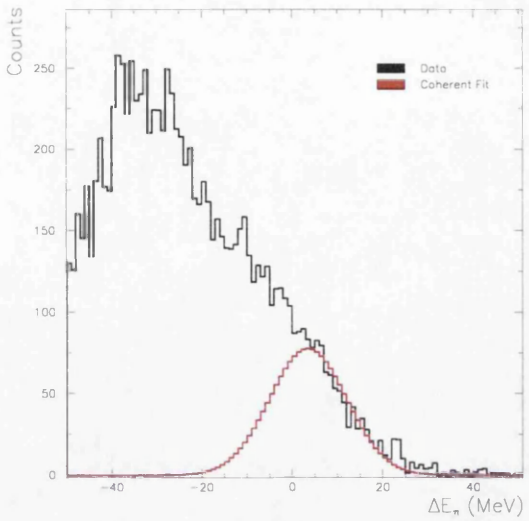

Figure 4.31: **Pion energy difference spectrum for ^{16}O :** for $50° < \theta_\pi < 55°$ and $340 < E_\gamma < 360$ MeV, fitted with method 3.

be the same as the width of the coherent peak. Thus the function used was:

$$F = \frac{A_1}{\sqrt{2\pi}\sigma}\exp\left(\frac{-(x-x_c)^2}{2\sigma^2}\right) + \frac{A_2}{\sqrt{2\pi}\sigma}\exp\left(\frac{-(x-x_c+6.5)^2}{2\sigma^2}\right) + \frac{A_Q\sigma\sqrt{2\pi}}{1+\exp\left(2.4\frac{x-x_c+E_{av}}{\sigma\sqrt{2}}\right)} \quad (4.33)$$

where A_1 and A_2 are the coherent and incoherent areas respectively, σ is the width of both the coherent and the incoherent fits, x_c is the coherent peak position, and E_{av}, x, and A_Q are the same as in equation 4.31. Figure 4.32 gives an example of fit method 4. When the coherent fit is subtracted from the data the incoherent peak gives a good fit to the residual spectrum (Figure 4.32(b)).

This method of fitting the coherent and the incoherent worked well over a wide range of incident photon energies and pion angles (see Appendix C). However, it was sometimes necessary, in order to get a sensible fit, to either fix the width or fix both the width and the coherent peak position (σ and x_c respectively in equation 4.33). Figure 4.33 gives an example of a fit where both the width and position were fixed. The fixed parameter(s) were chosen based on the fitted values for neighbouring bins. The variation of fit parameters with E_γ and θ_π was examined to help decide which fit method to use for each pion energy difference spectrum and cases where the peak width did not vary smoothly or the peak position changed very abruptly were re-examined.

As discussed in section 2.6, the ^{16}O target was in fact a water target. Calculations had been performed to ensure that separation of pions produced from ^{16}O from those

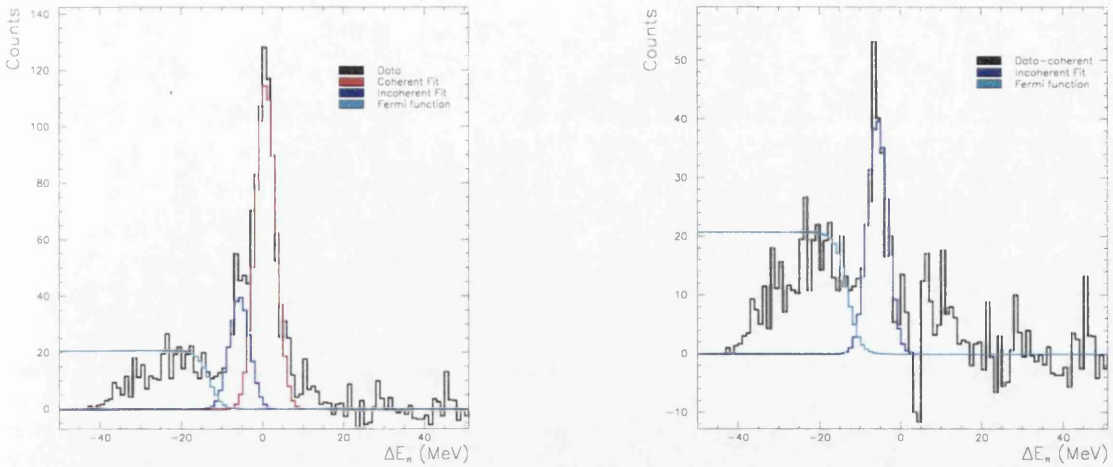

(a) Coherent + Incoherent fit

(b) Data - coherent fit

Figure 4.32: **Pion energy difference spectrum for ^{16}O:** for $95° < \theta_\pi < 100°$ and $170 < E_\gamma < 180$ MeV, fitted with method 4. The coherent plus incoherent fit works well and the incoherent peak gives a good fit to the residual data after the subtraction of the coherent fit, (b).

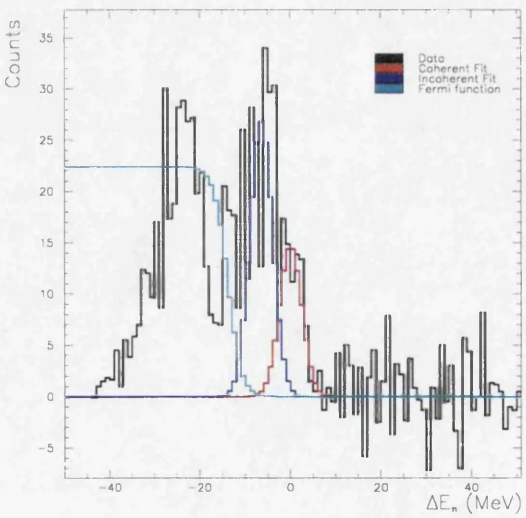

Figure 4.33: **Pion energy difference spectrum for ^{16}O:** for $120° < \theta_\pi < 125°$ and $170 < E_\gamma < 180$ MeV, fitted with method 4 with peak position and width fixed.

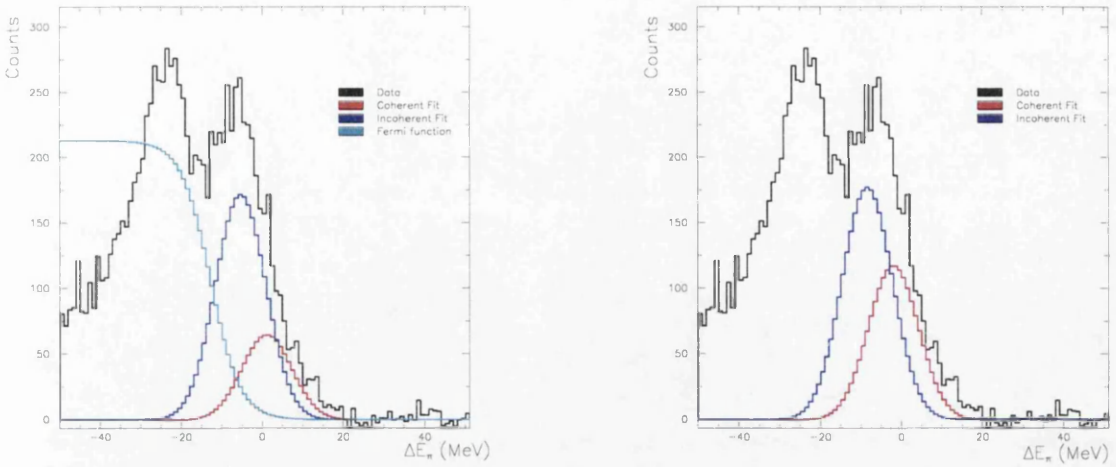

(a) With Fermi function

(b) Without Fermi function

Figure 4.34: **Pion energy difference spectrum for ^{16}O:** for $65° < \theta_\pi < 70°$ and $220 < E_\gamma < 240$ MeV, fitted with method 8 with and without Fermi function: Both have fixed width of 6.6 MeV. (a) peak position at -0.3 MeV: too small a coherent area; (b) peak position at -2.5 MeV: more comparable to peak positions in neighbouring bins.

produced of ^1H could be made (Table 2.3). However, at some incident photon energy and pion angle combinations, a peak in the pion energy difference spectrum could be seen due to pions produced on ^1H (the peak at around $\Delta E_\pi = -25$ MeV in Figure 4.34). In these cases it was found that the Fermi function misrepresented the tail of the distribution due to this process and strongly affected the coherent and incoherent fit in method 4, reducing the fitted coherent area and giving significant shifts in the peak position. Removing the Fermi function improved the fit to the coherent, as is clearly demonstrated in Figure 4.34, although this is probably not completely correct as it may include some contribution from the ^1H peak. It would be better to fit a Gaussian to the ^1H peak too but as the ^{16}O coherent peak position moves with E_γ and θ_π (as shown in Figure 4.28) the ^1H peak probably does too. It was found that removing the Fermi function also improved fits at smaller pion lab angles where the problem was not the contribution from pions from ^1H but from the incoherent process giving the peak 6.5 MeV below the coherent peak. Figure 4.35 gives an example of this.

The pion energy difference distribution for pions produced from ^1H was investigated to determine if the peak position did indeed depend on incident photon and energy and pion angle. If it did it could perhaps be used to help determine the position of the coherent peak for pions produced from ^{16}O since, as discussed in section

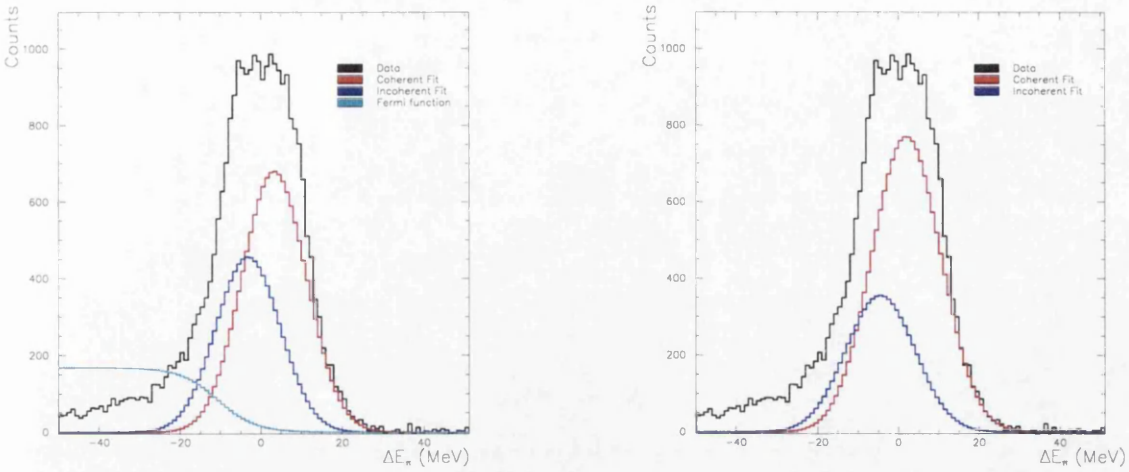

(a) With Fermi function

(b) Without Fermi function

Figure 4.35: **Pion energy difference spectrum for ^{16}O:** for $40° < \theta_\pi < 45°$ and $220 < E_\gamma < 240$ MeV, fitted with method 4 (a) with Fermi function and (b) without Fermi function.

2.6, for any given incident photon energy and pion lab angle the difference in the energy of a pion produced coherently from ^{16}O and the energy of a pion produced from ^{1}H can be calculated. This would be particularly helpful at incident photon energy and pion angle combinations where the ^{1}H peak is the dominant feature in the pion energy difference distributions. Figure 4.36 shows the pion energy difference distributions for (a) pions produced coherently from ^{16}O and (b) pions produced from ^{1}H at $100° < \theta_\pi < 105°$ and $260 < E_\gamma < 280$ MeV. There is no clear coherent peak in the ^{16}O pion energy difference distribution so fit method 3 must be used, requiring a decision to be made about where to put the coherent peak. However, the pion energy difference distribution for ^{1}H has a clear peak just below zero. This peak position was tracked for a number of incident photon energies and its variation with pion lab angle is shown in Figure 4.37. Clearly, the ^{1}H peak shows the same problem of shifting peak position with θ_π as was observed in ^{16}O and again the shifts increase with increasing E_γ. The shift should depend only on E_γ and θ_π and so could in principle predict the position for ^{16}O where data are available for ^{1}H at the same E_γ, θ_π. However, the number of bins where a clear ^{1}H peak was visible was very limited and so it was not used to help determine the position of the ^{16}O peak.

Lead-208

The fit regions and the regions where the different fitting methods were used are not identical for ^{16}O and ^{208}Pb. The coherent differential cross section decreases faster

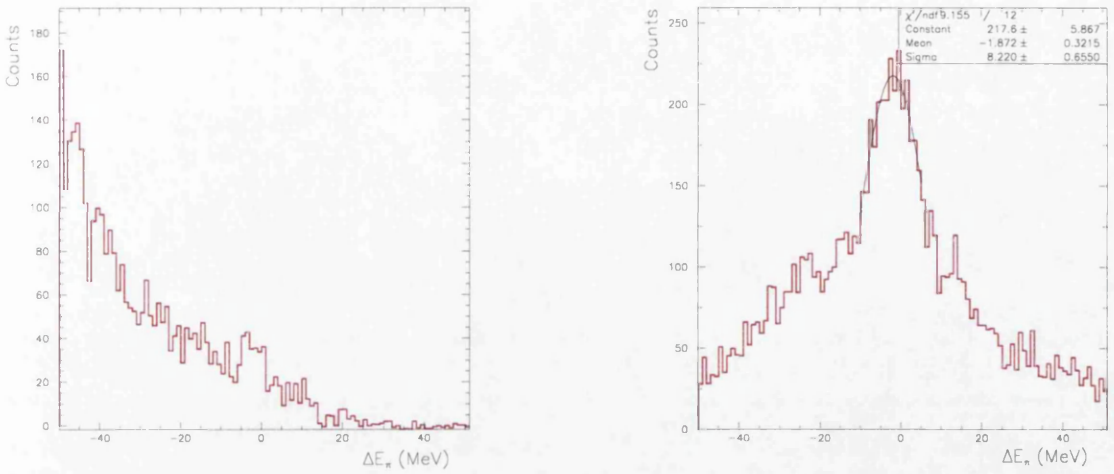

(a) ΔE_π for π^0 produced on ^{16}O

(b) ΔE_π for π^0 produced on ^{1}H

Figure 4.36: **Pion energy difference spectrum:** for $100° < \theta_\pi < 105°$ and $260 < E_\gamma < 280\,\text{MeV}$ for pions produced on (a) ^{16}O and (b) ^{1}H. There is a clear peak for pions from ^{1}H but not for pions produced coherently from ^{16}O.

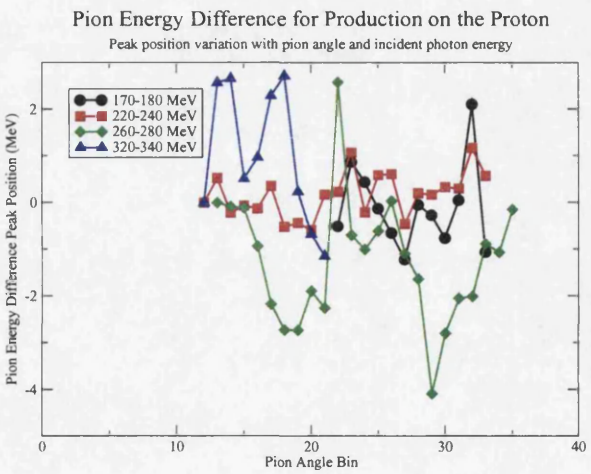

Figure 4.37: **Pion energy difference peak position for the coherent process on ^{1}H:** Fluctuations in the coherent peak position are seen for pions produced from ^{1}H just as they were for pions produced from ^{16}O (see Figure 4.28).

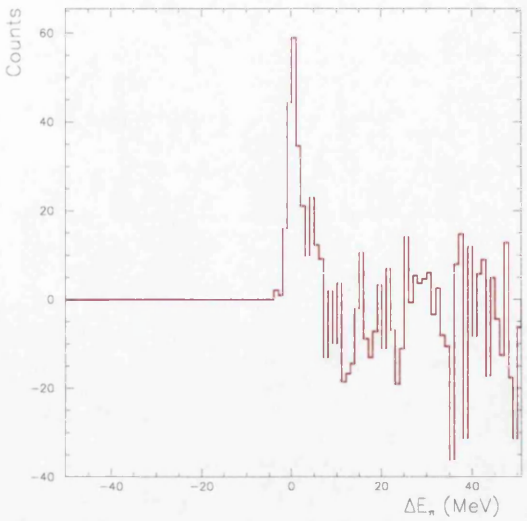

Figure 4.38: **Pion energy difference spectrum for ^{208}Pb:** for $135 < E_\gamma < 140$ MeV and all θ_π.

with pion lab angle for ^{208}Pb than for ^{16}O and therefore the coherent yield could be determined at greater pion lab angles for ^{16}O than for ^{208}Pb. The first nuclear excited state occurs at a lower nuclear excitation energy in ^{208}Pb (at 2.61 MeV, see Figure 4.50). The pion energy difference resolution is much larger than the difference between the ground state and the first nuclear excited state so it was not possible to separate any of them as was done for ^{16}O. Therefore only fit methods 1, 2, and 3 were employed for ^{208}Pb and the use of fit method 3 was necessary at much lower incident photon energies than for ^{16}O ($150 < E_\gamma < 155$ MeV for ^{208}Pb , $340 < E_\gamma < 360$ MeV for ^{16}O).

The differential cross sections for ^{208}Pb have more structure than those for ^{16}O because it is a larger nucleus. Therefore, in order to see this structure pion lab angle bins of 2° were used (5° bins were used for ^{16}O). However, this reduced the number of counts in each bin and at low incident photon energies the statistical errors were large. There were so few pions in the range $135 < E_\gamma < 140$ MeV that it was not possible to obtain a differential cross section. Figure 4.38 shows the pion energy difference distribution for this incident photon energy range for all pion lab angles added together and even this has very poor statistics. Differential cross sections were produced for $140 < E_\gamma < 145$ MeV and $145 < E_\gamma < 150$ MeV in 5° pion lab angle bins. It was possible to use 2° bins for all energies above this.

Figures 4.39 and 4.40 give examples of fit methods 1 and 2 respectively.

There were also very few counts in the pion energy difference spectra in the regions of the minima in the coherent differential cross sections. An example of this is given in Figure 4.41. For ^{16}O, even in the minima regions there were enough counts to use

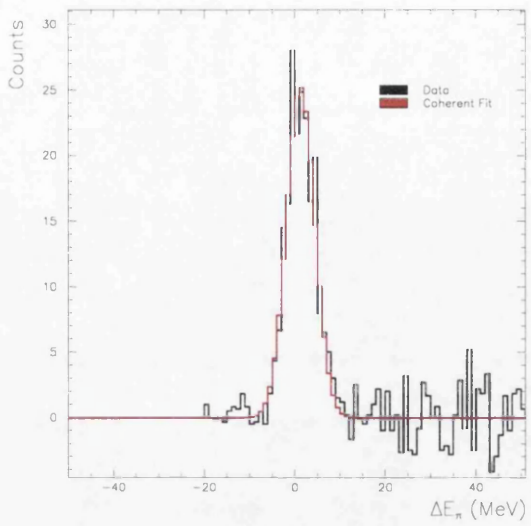

Figure 4.39: **Pion energy difference spectrum for ^{208}Pb:** for $20° < \theta_\pi < 22°$ and $150 < E_\gamma < 155$ MeV, fitted with method 1.

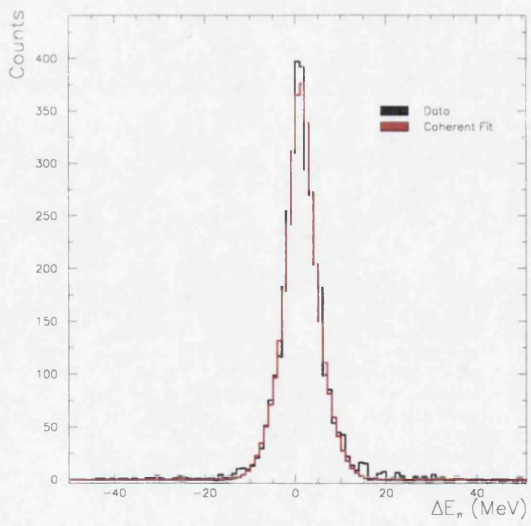

Figure 4.40: **Pion energy difference spectrum for ^{208}Pb:** for $20° < \theta_\pi < 22°$ and $170 < E_\gamma < 180$ MeV, fitted with method 2.

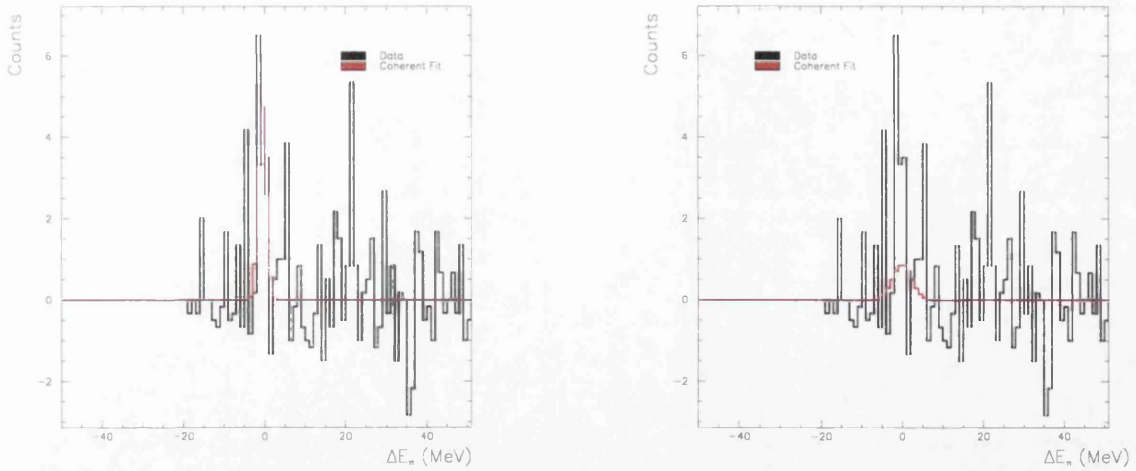

(a) Fit method 1

(b) Fit method 3

Figure 4.41: **Pion energy difference spectrum for ^{208}Pb:** for $54° < \theta_\pi < 56°$ and $150 < E_\gamma < 155$ MeV, (a) fitted with method 1 and (b) fitted with method 3.

either fit method 1 or 2 but for ^{208}Pb these often gave fits with much narrower widths than those obtained away from the minima and peak positions that jumped around significantly from one θ_π bin to the next. Therefore, fit method 3 was employed in these regions with a peak position based on those obtained away from the minimum. The width was also fixed and based on those obtained away from the minimum.

For incident photon energies greater than 300 MeV all the pion energy difference distributions had to be fitted with method 3 and an example is shown in Figure 4.42. The peak position and width were fixed and chosen to reflect those obtained when fit method 1 was used in a nearby bin.

Summary of Pion Energy Difference Fits

Four methods were used to fit the coherent part of the pion energy difference distribution. Methods 1-4 were used for ^{16}O but only methods 1-3 were used for ^{208}Pb. These methods are summarised below.

- **Method 1:** A Gaussian plus a Fermi function were fitted, allowing the fit to determine the height, width, and position of the Gaussian function and the height of the Fermi function. This method was used where the shape of the peak was described well by a single Gaussian function and the peak position was not less than about -4 MeV (see Figures 4.29 and 4.39). The fit function is described by equation 4.31 with $A_2 = 0$.

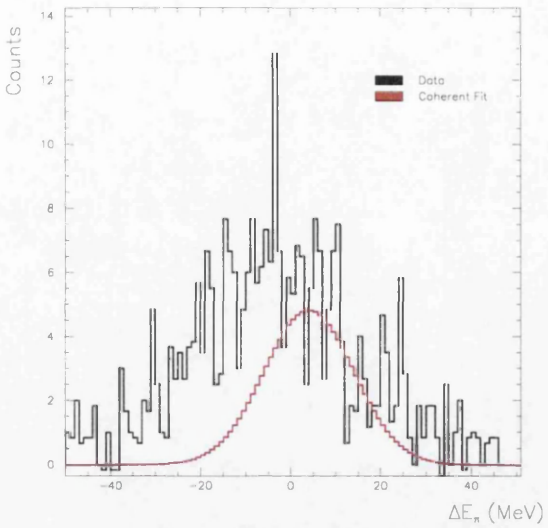

Figure 4.42: **Pion energy difference spectrum for ^{208}Pb:** for $0° < \theta_\pi < 2°$ and $300 < E_\gamma < 320$ MeV, fitted with method 3.

- **Method 2:** Two Gaussians plus a Fermi function were fitted. The two Gaussian functions were centred at the same point. The fit determined the heights, widths, and the position of the Gaussian functions and the height of the Fermi function. This method was used where the shape of the peak was described well by two Gaussian functions, the width of the second was not more than twice that of the first, and the peak position was not less than about -4 MeV (see Figures 4.30 and 4.40). The fit function is described by equation 4.31.

- **Method 3:** The upper half of a single Gaussian was fitted. The centre position of the Gaussian was fixed at a point based on the positions obtained for nearby bins with methods 1 and 2. The fit selected the height and width (optional, can be fixed based on values from previous bins) of the Gaussian. This method was used where incoherent contributions dominated the pion energy difference distribution such that no clear coherent peak could be observed (see Figures 4.31 and 4.42), or the statistics were so poor that methods 1 or 2 could not give sensible fits (see Figure 4.41). The fit function is described in equation 4.31 with $A_2 = 0$, $A_Q = 0$ and x_c fixed.

- **Method 4:** Two Gaussians 6.5 MeV apart and a Fermi function (optional) were fitted, allowing the fit to determine the heights, the common width (optional), the position of the Gaussian function for the coherent part (optional), and the height of the Fermi function. This method was used for ^{16}O only where an incoherent peak was observed or the coherent pion energy difference distribution was broad due to incoherent contributions from excited state(s) (see Figures

4.32-4.35).

4.8 Determination of cross sections

The differential cross section for a particular range of photon energies and pion angles was calculated as follows:

$$\frac{d\sigma}{d\Omega} = \frac{N_{\pi^0}}{\epsilon_{tagg}\,\rho\,N_{TS}\,N_{TC}\,\Omega\,\Gamma_{\gamma\gamma}} \cdot \frac{F_{\gamma\gamma}F_{TT}}{\epsilon_{det}} \tag{4.34}$$

where

N_{π^0} = number of neutral pions detected in TAPS in that E_γ, θ_π range
ϵ_{tagg} = tagging efficiency for that E_γ
ρ = target density $[\frac{\text{nuclei}}{\text{cm}^2}]$
N_{TS} = number of tagger scaler counts
N_{TC} = number of tagger channels in the photon energy bin
Ω = solid angle of the angular bin [sr]
$\Gamma_{\gamma\gamma}$ = branching ratio of the decay $(\pi^0 \rightarrow \gamma + \gamma)$: 98.98 %

Additional corrections were required for TAPS detection efficiency (ϵ_{det}, described in section 3.4) and for events due to neutral pions having been removed by the various cuts described earlier in this chapter - $F_{\gamma\gamma}$ is the correction for the cut on the time difference between the decay photon detection in TAPS and F_{TT} is the correction for the cut on the time difference between TAPS and the tagger.

Separate corrections for the conversion of the π^0 decay photons to e^+e^- pairs in the target and their subsequent rejection by the analysis process were not needed as they were included in the detection efficiency calculations.

The total cross section was obtained by integrating the differential cross section. In practice this was done by summing over the angle bins.

$$\sigma = \int \frac{d\sigma}{d\Omega}(E_\gamma, \theta_\pi)d\Omega \simeq 2\pi \sum_{\theta_\pi} \frac{d\sigma}{d\Omega}(E_\gamma, \theta_\pi) \sin\theta_\pi \cdot \Delta\theta_\pi \tag{4.35}$$

4.8.1 Experimental Uncertainties

Statistical Uncertainties

The main statistical error is in the number of counts in the coherent region and was obtained from the error in the area of the coherent part of the pion energy difference distribution. This was obtained from the fitting procedure.

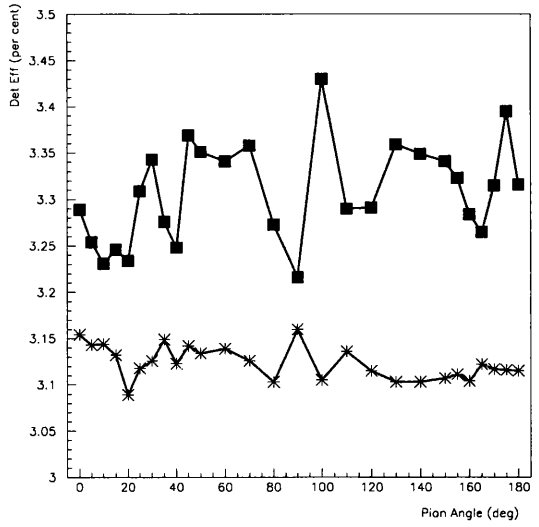

Figure 4.43: **Detection efficiency statistical error** was obtained by looking at the variation at $E_\pi = 135.0\,MeV$ with pion angle. The stars are for the ^{208}Pb target and the filled squares are for ^{16}O. The statistical error for lead is lower than that for ^{16}O as more events were simulated for this target. The effect of the target is visible by a reduction in the overall detection efficiency for ^{208}Pb.

The detection efficiency was determined by a Monte Carlo procedure (see chapter 3) and so also contained a statistical error. The simulation was performed for $E_\pi = 135.0$ MeV and $\theta_\pi = 0-180°$. At this energy decay photons are back-to-back and their direction distribution is isotropic so the detection efficiency should be the same at all values of θ_π; that it is not is a result of the statistical variation and so this can be used to get the statistical error. More events were simulated for ^{208}Pb than for ^{16}O (500,000 compared with 100,000) and so the variation and hence the error is smaller for ^{208}Pb (see Figure 4.43). The mean value of the detection efficiency was $3.307 \pm 0.053\,\%$ for ^{16}O and $3.124 \pm 0.018\,\%$ for ^{208}Pb. These were used to obtain the errors in detection efficiency for each E_γ, θ_π bin: if at some value of E_γ, θ_π, the calculated efficiency is bigger than the mean value at threshold ($E_\gamma = 135$ MeV) by a factor f, then the number of detected pions is bigger by a factor f and so the fractional error is smaller by $\frac{1}{\sqrt{f}}$.

The contributions to the error in the cross section from the fitting and the detection efficiency simulation were combined to produce the statistical errors shown in the cross section plots (Figures 5.2-5.19) and tables (Tables E.1-E.11).

An uncertainty in the tagging efficiency exists from statistical variations in the value found for each tagger channel as discussed in section 4.2. Over the range of photon energies studied in the experiment described here, this uncertainty was $\sim 1\,\%$. Since this is negligible compared with the other statistical errors discussed here it was

not included in the calculation of the error in the cross sections.

Systematic Uncertainties

The main systematic error arose from the the subjective nature of the pion energy difference fitting process. For low E_γ and θ_π the non-coherent yield is small compared with the coherent resulting in energy difference spectra such as those shown in Figures 4.29 and 4.39. Here the coherent peak position is known to a fraction of an MeV so the statistical error dominates with a systematic error of less than 1 %. With increasing E_γ and θ_π the uncertainty in the peak position increases to $\sim$ 2 MeV in the region $200 < E_\gamma < 240$ MeV above which it remains at around this level. The resulting systematic error in the cross sections changes dramatically with incident photon energy and pion angle and depends on the target and on the fit method used. Therefore it was not possible to tabulate it but examples are given below.

As discussed in section 4.7.2, the non-coherent yield increases with incident photon energy and pion angle. At high E_γ and θ_π no clear coherent peak is visible in the pion energy difference distributions. For ^{16}O, a decision had to be made on whether to fit the coherent and the incoherent (fit method 4), or just the right hand side of the coherent at a fixed peak position (fit method 3). Figure 4.44 shows the importance of including the incoherent in the fit where possible. If it is excluded the fit gives a result that is neither coherent only nor coherent+incoherent but somewhere in between and the diffraction structure of the coherent cross section is partially or completely lost. In the first maximum region, fit method 3 results in a cross section 23 % larger than that from fit method 4. This increases with θ_π and in the second maximum region method 3 gives a cross section almost 130 % larger than method 4. The difference between the methods is largest in the minima regions where fit method 3 does not give any clear minima at all: in the first minimum region method 3 gives a cross section $\sim$ 390 % larger than that for method 4, and in the second minimum region this difference has increased to $\sim$ 450 %.

Figure 4.45 is the next incident photon energy bin up from Figure 4.44 and here neither fit produces a believable angular distribution. There is a difference of a factor of 2 between the two fit methods even in the region of the first maximum. The cross section from method 4 (Figure 4.45(a)) has a faster fall-off from the first maximum to the minimum than any of the theoretical predictions or any of the experimental cross sections for lower E_γ bins. Therefore, fit method 3 was used with the understanding that the non-coherent contribution to the resulting cross section was not negligible.

For ^{208}Pb, fit method 3 was used for pion energy difference fits at energies as low as 150 MeV (see section 4.7.2) due to a combination of poor statistics and the inability to separate the coherent yield from the incoherent yield from low-lying nuclear excited

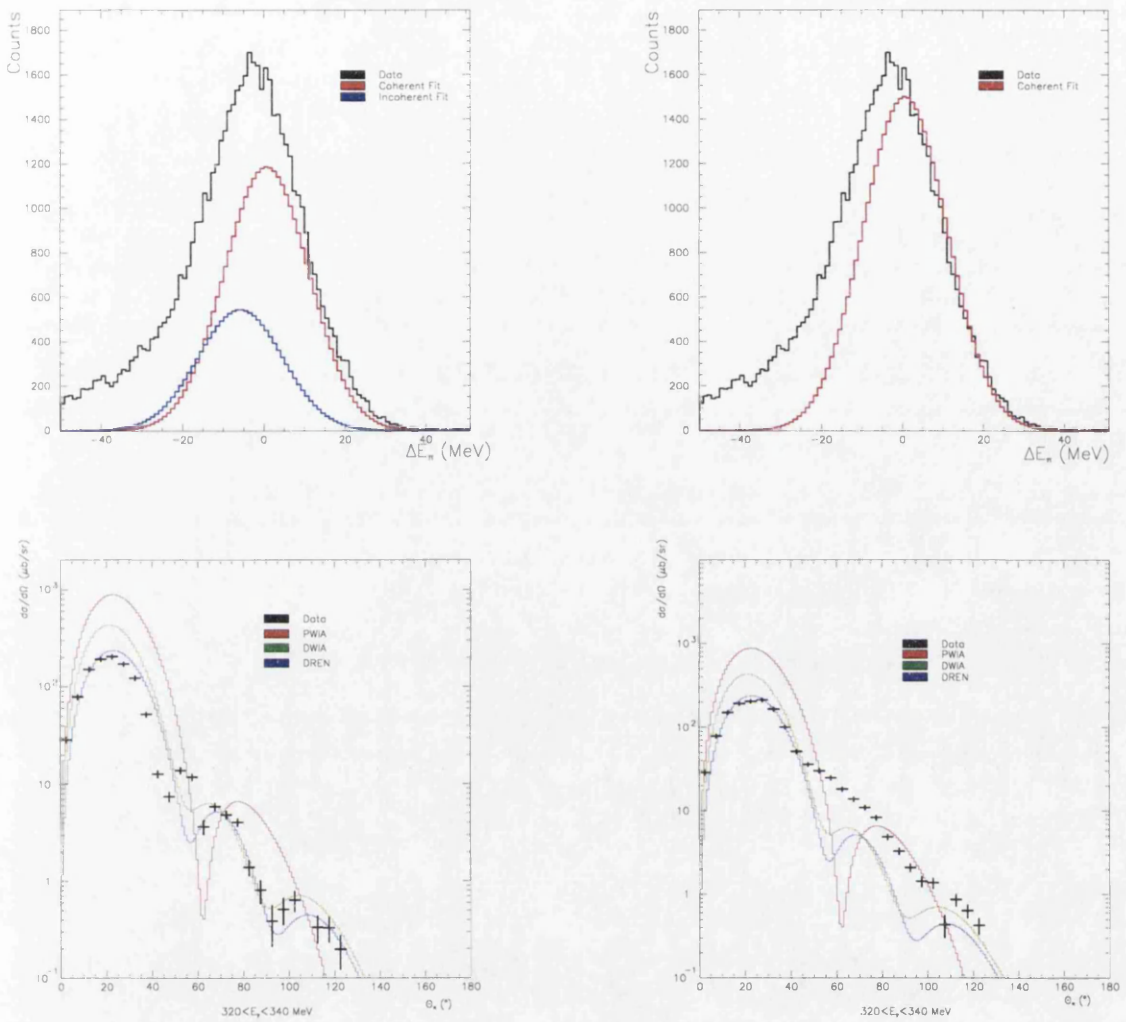

(a) Fit coherent and incoherent

(b) Fit right hand side of coherent only

Figure 4.44: **Effect of pion energy difference fit type on the differential cross section for ^{16}O:** For $320 < E_\gamma < 340$ MeV the coherent peak position was hard to determine. (a) The coherent and the incoherent were fitted for all angles; for $\theta_\pi > 25°$ the coherent peak position and width were fixed. (b) The coherent and incoherent were only fitted for $\theta_\pi < 25°$; for all other angles the coherent peak position was fixed and a Gaussian was fitted to the right hand side only.

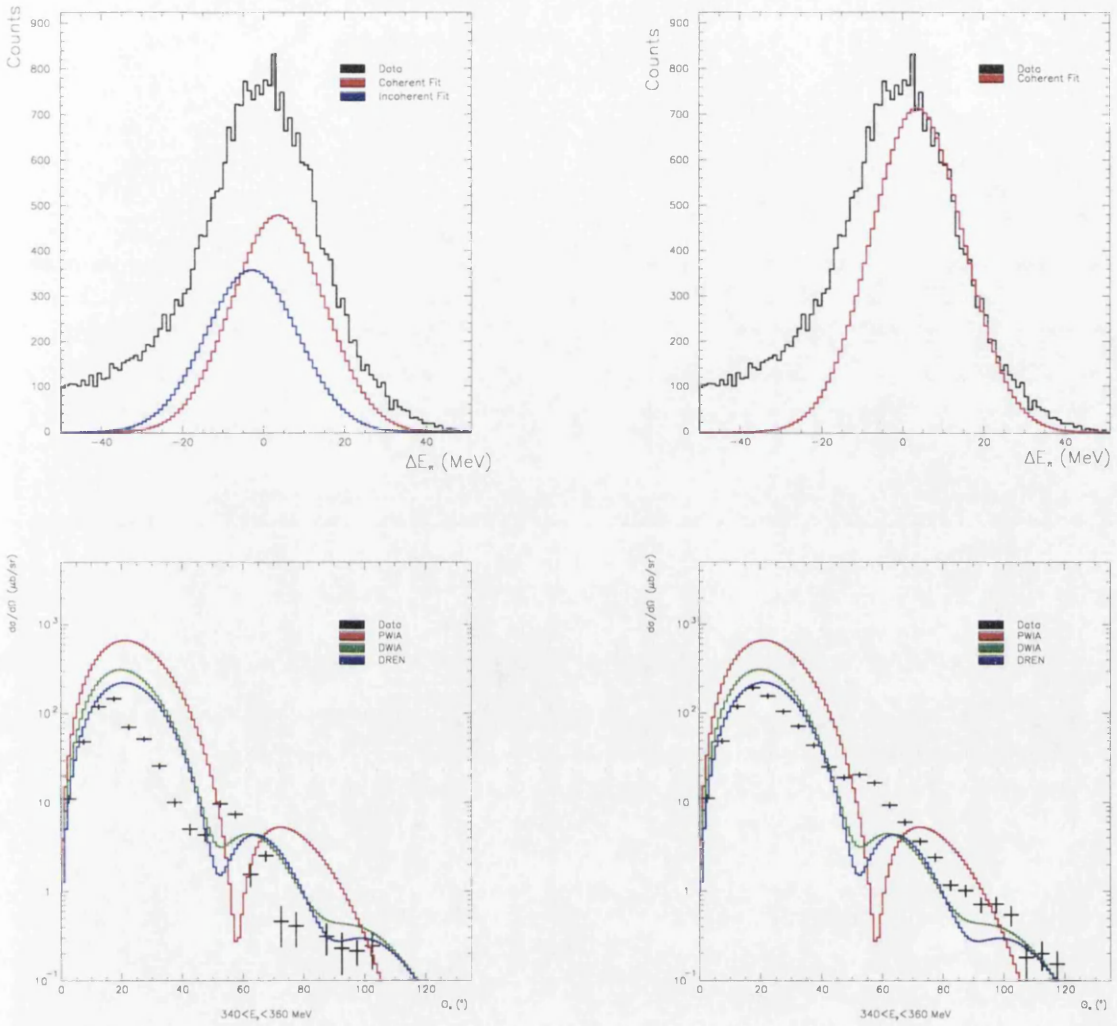

(a) Fit coherent and incoherent

(b) Fit right hand side of coherent only

Figure 4.45: **Effect of pion energy difference fit type on the differential cross section for ^{16}O:** For $340 < E_\gamma < 360$ MeV the coherent peak position was hard to determine. (a) The coherent and the incoherent were fitted for all angles; for $\theta_\pi > 15°$ the coherent peak position and width were fixed. (b) The coherent and incoherent were only fitted for $\theta_\pi < 15°$; for all other angles the coherent peak position was fixed and a Gaussian was fitted to the right hand side only.

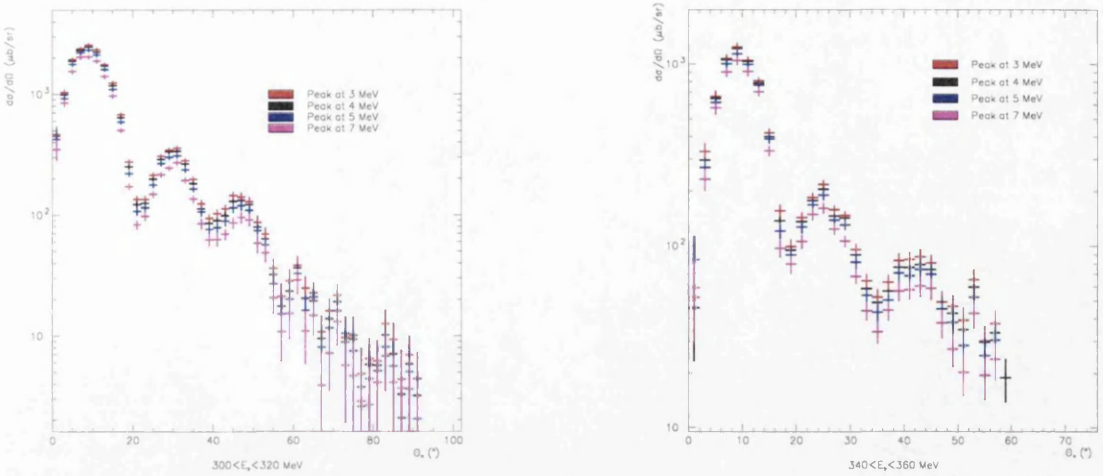

(a) $300 < E_\gamma < 320$ MeV

(b) $340 < E_\gamma < 360$ MeV

Figure 4.46: **Effect of the pion energy difference peak position for fit method 3 on the differential cross section for ^{208}Pb:** (a) for $300 < E_\gamma < 320$ MeV and (b) for $340 < E_\gamma < 360$ MeV. The peak position of 4 MeV (black) was chosen based on the peak positions obtained when fit method 1 was used in nearby bins.

states. For ^{16}O, fit method 3 was only used for $E_\gamma > 340$ MeV (see Figures 4.31 and 4.42). The area of the fitted coherent peak is strongly dependent on the selected coherent peak position, particularly when the coherent region constitutes a small fraction of the total yield. Figure 4.46 shows the effect on the differential cross section for ^{208}Pb of selecting peak positions of 3, 4, 5 and 7 MeV. The shape of the cross section is not much affected, i.e. the maxima and minima are at the same values of θ_π, but the magnitude of the cross section is reduced with increasing coherent peak position. The value used for the fits was 4 MeV based on the positions obtained in neighbouring bins with clear coherent peaks. Decreasing the peak position to 3 MeV increases the cross section by 4 % at the first maximum, by 11 % at the first minimum and by 8 % at the third maximum for $E_\gamma = 300 - 320$ MeV. Increasing the peak position to 5 MeV decreased the cross section by roughly the same amount. At higher incident photon energies, the effect of the peak position on the differential cross section magnitude was generally smaller - a peak position of 3 MeV increases the cross section by 2 % at the first maximum, by 5 % at the first minimum but by 11 % at the third maximum for $E_\gamma = 340 - 360$ MeV.

Another source of systematic error is from the determination of the physical position of the detector system. It is important to know the position of the detectors as any uncertainty leads to an error in the measured momenta of the decay photons and hence the reconstructed momentum of the pion. This will also affect the calculation

Table 4.6: **Fraction of pions inside the cut:**

	^{16}O		^{208}Pb	
	Data	**GEANT**	**Data**	**GEANT**
Fraction	0.7598	0.7557	0.4116	0.5188

of detection efficiency since the detectors in the simulation need to be positioned in the same places as the real detector system. However, since the reconstructed pion mass peak positions for the different block combinations are comparable for the experimental and simulated data (see section 4.6.2 and Table 4.4), this effect is negligible. More significant is the effect of the reconstructed photon energies and positions. As described in sections 4.5 and 4.6.2, the reconstructed pion mass peak position was significantly lower for photons incident in neighbouring TAPS blocks. Corrections as detailed in these sections were applied to the data to reduce these differences but it is estimated that there remains a systematic error of $\sim 2\,\%$ in the pion mass. This will result in errors in the pion energy difference that vary with pion energy and the decay photon opening angle but these are already included in the discussion above.

Comparison of the simulated data with the experimental data identified another systematic error. Ideally the whole reaction process should be simulated and matched to the experimental data. However, as the simulations were only used to obtain detection efficiencies this was not necessary but it was still important to check that agreement is obtained between simulated and experimental data. Therefore, a simulation was performed for pions produced isotropically with energies chosen randomly in the range 135-400 MeV. Since the spectrum for the experimental data includes events from atomic processes that are not included in the simulation, and high energy atomic processes are mainly produced in the forward direction, the reconstructed pion mass spectra for events detected in the TAPS blocks only (i.e. excluding the forward wall) were compared. The simulated data spectrum was scaled for comparison with the experimental data (see Figure 4.47).

In the analysis, an event was classed as a pion only if its reconstructed pion mass was between 120 MeV and 150 MeV and in this region there is quite a good agreement between experimental data and simulation (Figures 4.47(b) and (c)) with the simulated data peak only slightly narrower than that of the experimental data. The fraction of pions inside the cut (i.e. $\frac{\text{No. of } \pi^0 \text{ inside cut}}{\text{Total no. of } \pi^0}$) for the experimental and the simulated data were compared and are given in Table 4.6. This indicates that for ^{16}O the detection efficiencies are $\sim 0.5\,\%$ too small but for ^{208}Pb the indication is that they are $\sim 26\,\%$ too big. However, the ^{208}Pb experimental data contains a much greater proportion of background events than the ^{16}O data due to its greater nuclear size. Even away from forward angles there is clearly still a lot of atomic background (see Figure 4.47(b)). Therefore, the true data-simulation comparison

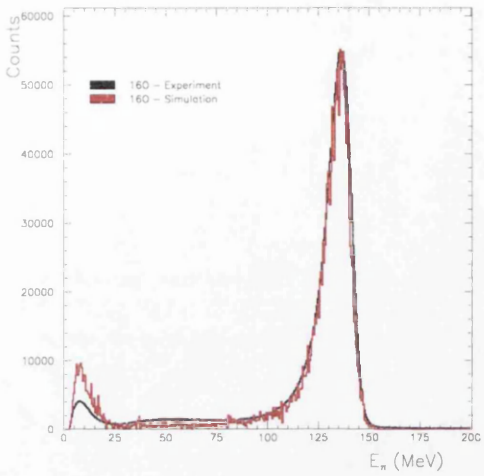

(a) ^{16}O

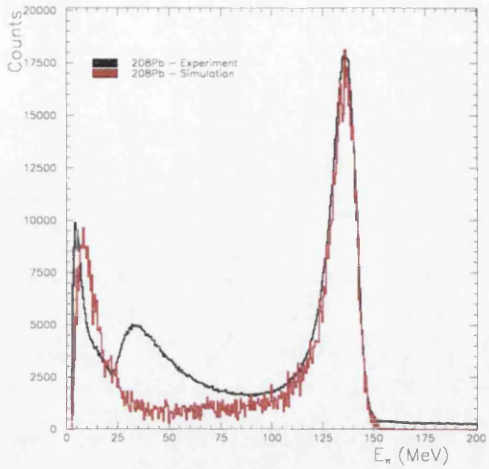

(b) ^{208}Pb

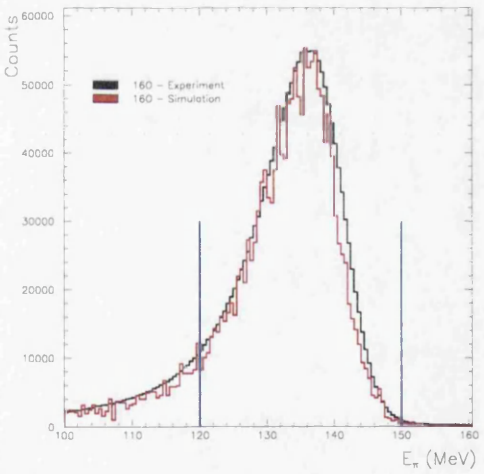

(c) ^{16}O

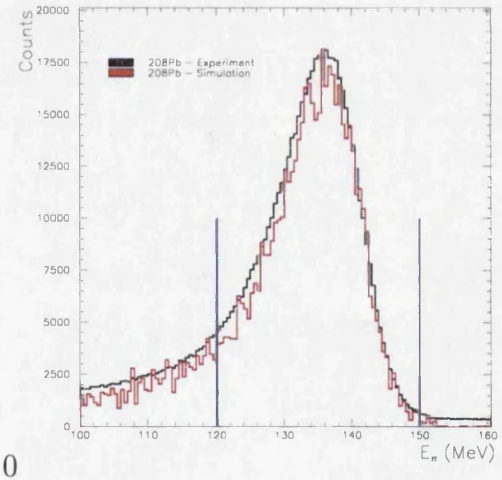

0

(d) ^{208}Pb

Figure 4.47: **Comparison of simulation with data:** Reconstructed pion mass spectra for experimental data (black) and simulation (red). There is a reasonable matching between data and simulation in the cut region (denoted by the blue lines) with the simulation (FWHM: ^{16}O = 12.0 MeV; ^{208}Pb = 14.0 MeV) slightly narrower than the data (FWHM: ^{16}O = 14.0 MeV; ^{208}Pb = 14.5 MeV).

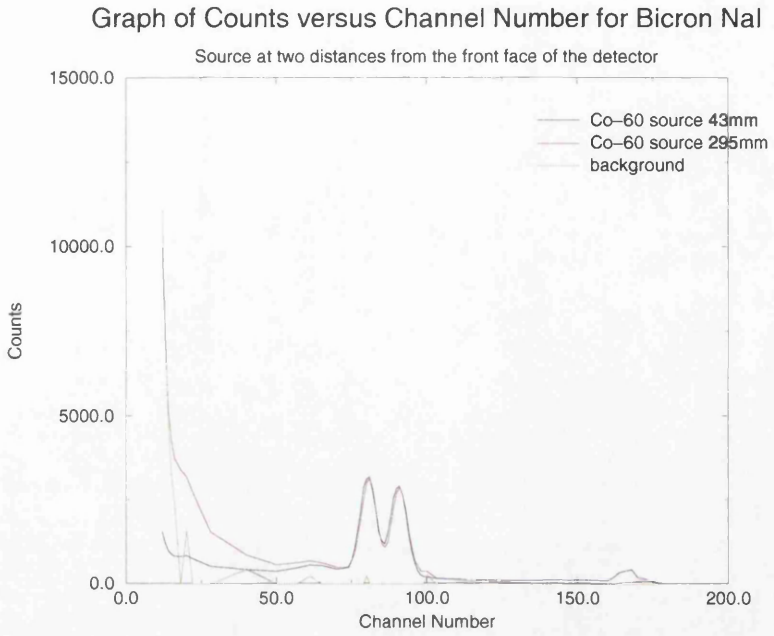

Figure 4.48: **NaI spectrum from ^{60}Co calibration:** The peaks from the two gamma decays of this source are clearly distinguishable.

with atomic processes removed would probably be more like that found for ^{16}O since there is no reason to expect the simulation to be less successful for ^{208}Pb than for ^{16}O; both targets were of similar thicknesses in terms of radiation lengths. This error is negligible compared with the other errors discussed.

A systematic error exists in weighing the target and measuring its surface area together with the determination of the target position with respect to the TAPS detector array and the target angle with respect to the beam. The ^{16}O target was designed such that it would fit into the beam-pipe at 90° and the ^{208}Pb target holder was built to hold it at 45° to the beam. Combining these three contributions gives an uncertainty for the target density of less than 1 % for the oxygen target and nearer to the 2 % level for lead.

4.9 Sodium Iodide Detectors

The sodium iodide (NaI) detectors were calibrated with a ^{60}Co source. The ^{60}Co nucleus is an unstable isotope that β-decays into ^{60}Ni. The resulting ^{60}Ni nucleus is usually in an excited state and quickly decays into a stable state by emitting a 1.173 MeV γ-ray followed by a 1.332 MeV γ-ray. The NaI resolution is good enough to give two distinguishable peaks and a sum peak as can be seen in Figure 4.48. The background is greater for the measurement made at a source to NaI distance of 295 mm than that made at 43 mm due to the increase in the number of decay photons

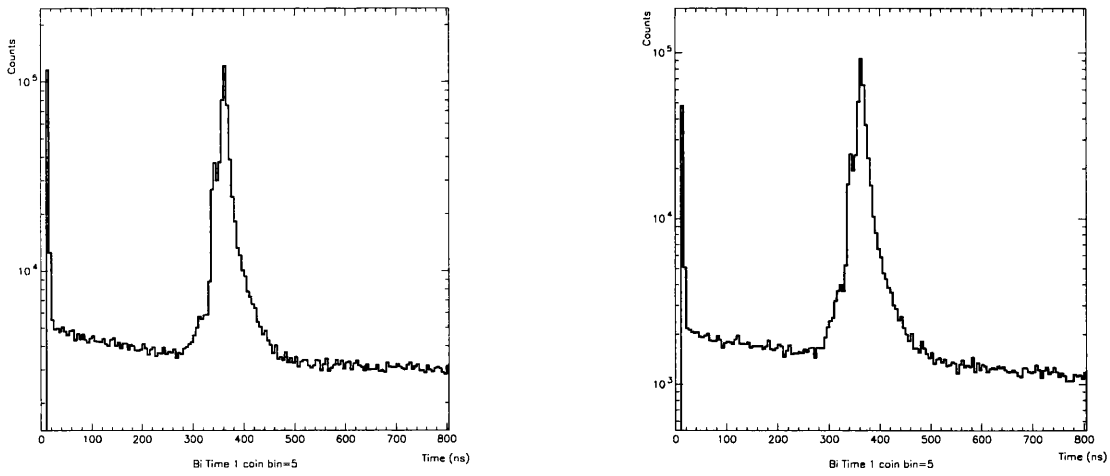

(a) ^{16}O (b) ^{208}Pb

Figure 4.49: **Bicron NaI Time Spectrum.**

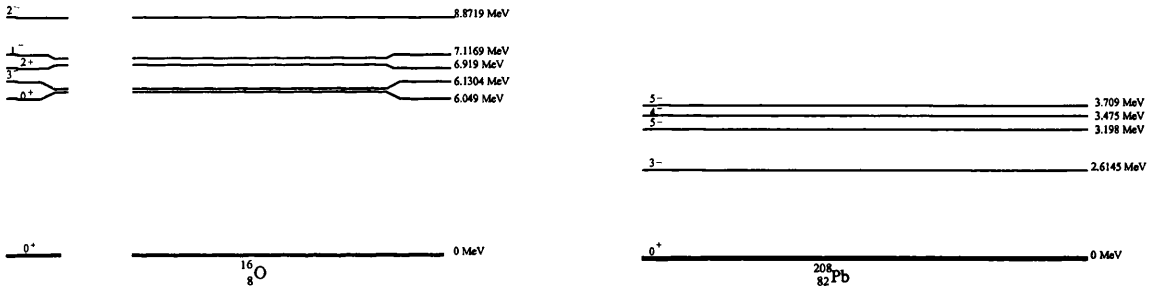

(a) ^{16}O (b) ^{208}Pb

Figure 4.50: **The first few excited nuclear states for ^{16}O and ^{208}Pb.**

that only clip the corners of the NaI crystal and as a result only deposit a fraction of their energy. From this calibration the energy resolution for the NaI detectors was calculated to be 5 %(FWHM) for the Bicron and 6 %(FWHM) for the Harshaw detector.

The time spectra from the Bicron NaI from the ^{16}O and the ^{208}Pb data are shown in Figure 4.49. A peak containing events coincident with the TAPS trigger is clearly visible for both targets.

The first few excited states of ^{16}O and ^{208}Pb are shown in Figure 4.50(a) and (b) respectively. The first excited state of ^{16}O is at 6.049 MeV but the decay from this state is via e^+e^- production and so will not be detected by the NaI detectors. The first excited state in ^{208}Pb is only 2.6 MeV above the ground state. There are many states close together in this nucleus due to its much greater number of protons and

neutrons.

The energy spectra from the NaI detectors for both targets are shown in Figure 4.51(a) and (b) respectively. The events in these spectra were detected in coincidence with the TAPS trigger and are associated with a pion energy difference in the region -40 to +20 MeV. The spectra from both NaI detectors are similar. Both targets give spectra with considerable low energy background above which it is difficult to discern peaks indicating population of low lying states. For ^{16}O a peak in the range 6-7 MeV would be expected from decay photons from the incoherent process and there is some evidence of a yield above the background at around 6.5 MeV. The first excited state of ^{16}O, the 6.05 MeV (0^+) state, will not be seen in the NaI spectra since it decays to e^+e^-. Therefore, this 'peak' at 6.5 MeV could be from any of the next three states. For ^{208}Pb a peak in the range 2.5-4 MeV would be expected and there is maybe a hint of something at about 3 MeV in the Bicron NaI. Again it is not possible to separate individual states as they are too close together. Both targets give very few counts above 8 MeV which suggests that the cross section for excitation to any of the higher energy excited states such as the 8.8719 MeV state in ^{16}O is small. The number of counts in the observed peaks are so small compared to the background that no estimate of the incoherent cross section to any gamma decaying states was made based on these spectra.

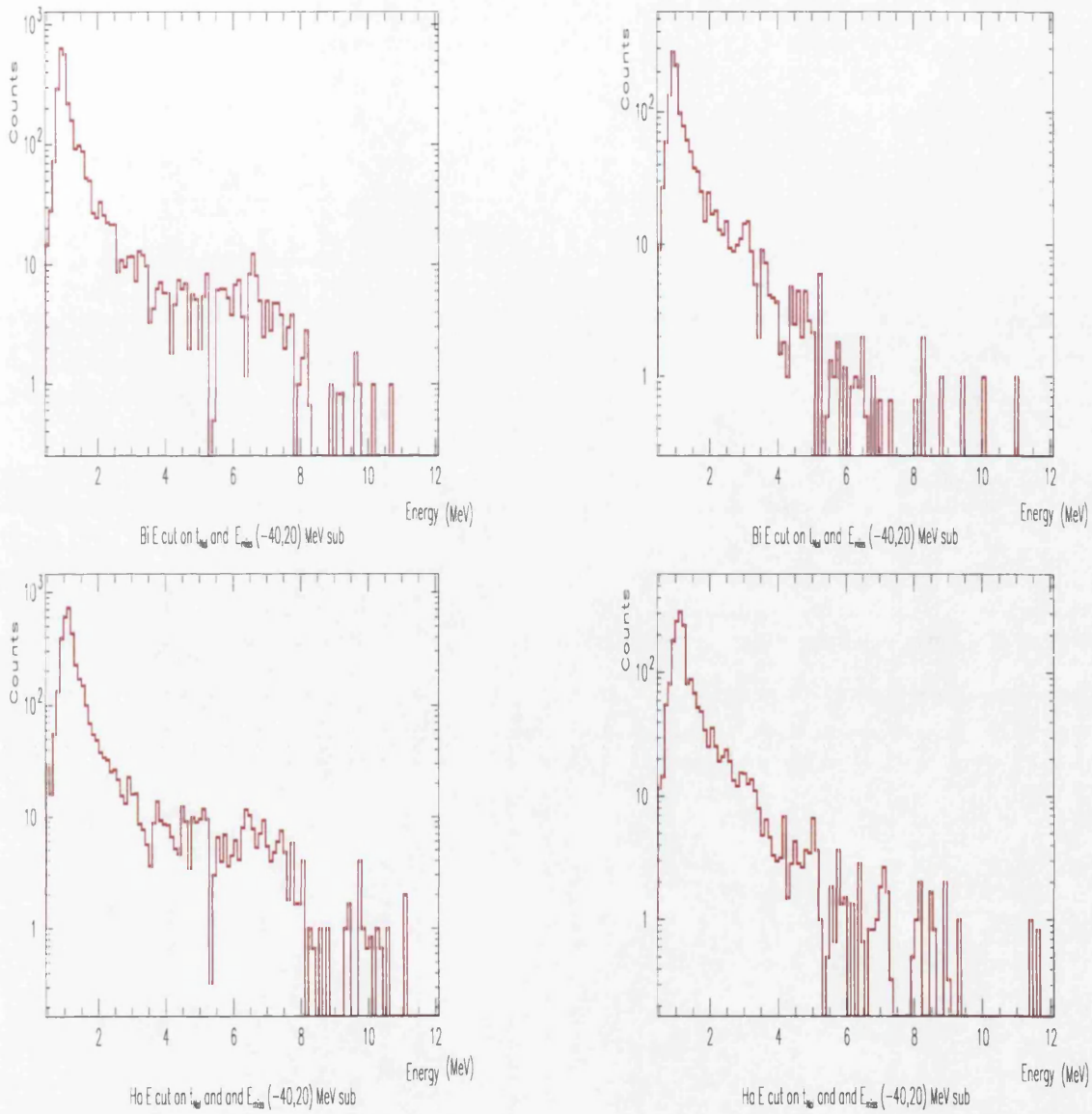

(a) ^{16}O (b) ^{208}Pb

Figure 4.51: **NaI Energy Spectra:** (a) There is maybe a bump around 6 MeV that would indicate the low lying states in ^{16}O but it is not possible to separate these states; (b) There is maybe a bump around 3 MeV that would indicate the low lying states in ^{208}Pb, again it is not possible to separate these states. (The upper spectrum is from the Bicron NaI detector and the lower is from the Harshaw.)

Chapter 5

Results and Discussion

5.1 Oxygen-16

5.1.1 Comparison with Previous Measurements

Only one previous measurement on ^{16}O has been found in the literature [59] and that was performed at pion angles below 10° using a bremsstrahlung beam, producing only four data points of the differential cross section at incident photon energies in the Δ resonance region. The pion decay photons were detected in a π^0 spectrometer, consisting of two Pb-glass detectors with lead collimators and scintillation veto counters, with its acceptance limited to small pion angles so that only the coherent π^0 production would contribute. Figure 5.1 shows the comparison between these results and the present experiment. The statistical accuracy and pion energy resolution is much better in the present work and the data points are significantly below those of Bellinghausen et al.. The difference between the two measurements increases with E_γ indicating that the earlier experiment may contain contributions from incoherent processes. Although incoherent contamination has been mainly discussed as a problem at backward angles where the coherent cross section is small, it could also be a problem at very forward angles for the same reason.

Neither set of measurements is well described by the theoretical predictions. No interpretation of this is offered since in this small θ_π region, we do not have even a qualitative indication of the sensitivity of the theoretical predictions to the input parameters of the models. The two data points for the present experiment for $340 < E_\gamma < 380$ MeV are significantly below the measurements at lower E_γ. This is also observed in the total cross section and is discussed in the next section.

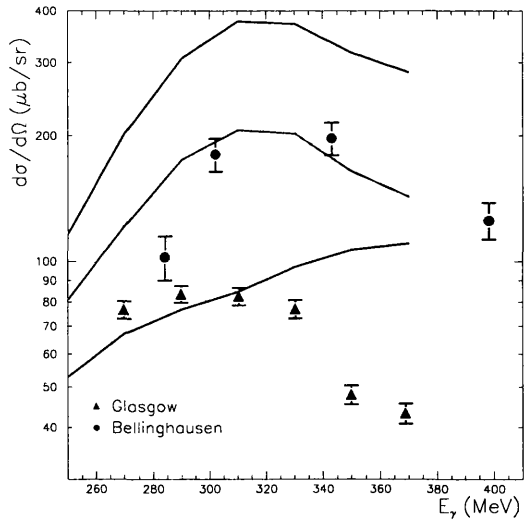

Figure 5.1: **Differential cross section for ^{16}O at $\theta_{\pi_c} = 10°$:** Black-present experiment; magenta-data from Bellinghausen et al. [59]; red-PWIA; green-DWIA; blue-DREN. All theoretical predictions from [79].

5.1.2 Comparison with Theoretical Predictions

Figure 5.2 shows the total cross section for ^{16}O and Figures 5.3-5.7 show the differential cross sections for ^{16}O. The errors bars shown are statistical. The present experimental results are compared with the theoretical model predictions using the PWIA, DWIA, and DREN calculations of Kamalov [79] (see section 1.3).

The theoretical model predictions were made for discrete values of incident photon energy E_γ, with E_γ in 10 MeV steps between 140 MeV and 380 MeV. These predictions were averaged to correspond to the E_γ bins used in the experiment for all E_γ bins except $135 < E_\gamma < 140$ MeV. No theoretical calculations were available in this region so the theoretical values were extrapolated to threshold assuming that the shape of the angular distribution is more or less constant at $E_\gamma \leq 140$ MeV.

The differential and total cross sections for ^{16}O show the expected characteristics. The total cross section (Figure 5.2) increases with E_γ from zero at the neutral pion photoproduction threshold to a maximum value at about $E_\gamma = 210$ MeV, around 80 MeV below the Δ resonance, and then decreases with increasing E_γ.

The differential cross sections (Figures 5.3-5.7) have a diffraction-like shape with one or more maxima separated by minima. A first minimum and a second maximum appear for $E_\gamma > 190$ MeV and a second minimum and third maximum appear at $E_\gamma > 300$ MeV. The positions of the maxima and minima in the differential cross sections for the experimental data and the theoretical predictions are given in Tables 5.1-5.3. The magnitudes of the maxima decrease with increasing pion angle. The magnitude of the first maximum increases with E_γ up to a value of $\sim 2000\,\mu b/sr$ and

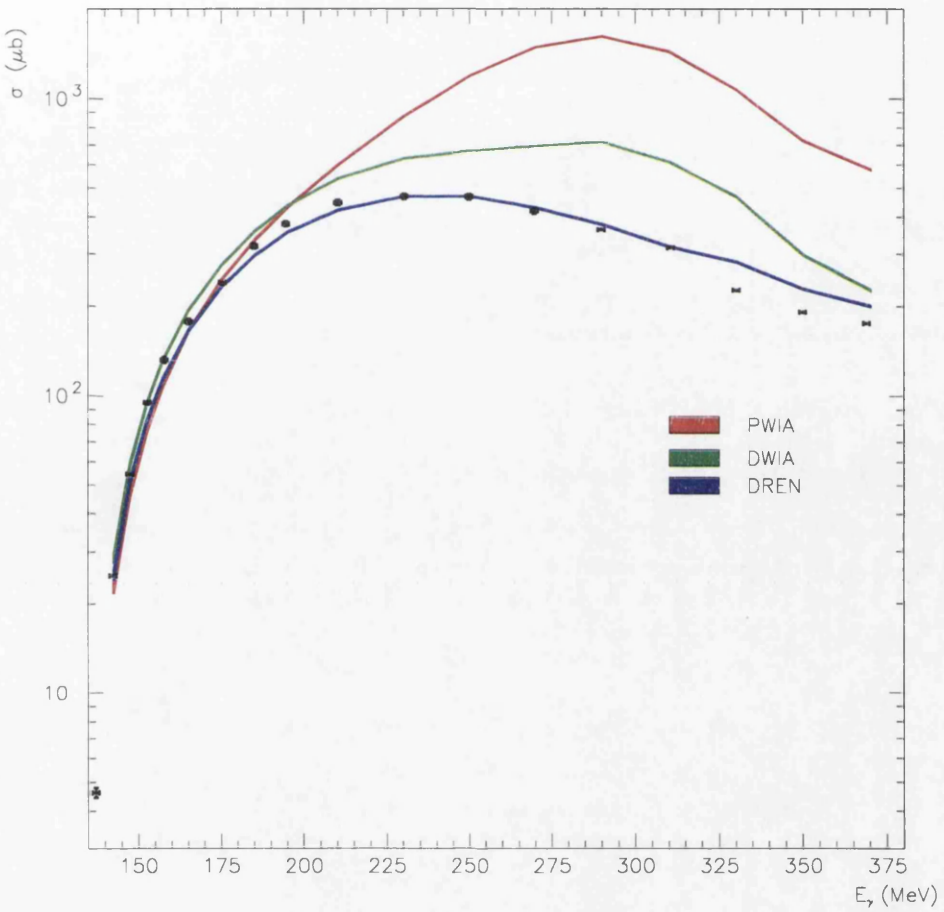

Figure 5.2: **Integrated cross section for** ^{16}O**:** Black - present experiment; red-PWIA; green-DWIA; blue-DREN. All theoretical predictions from [79].

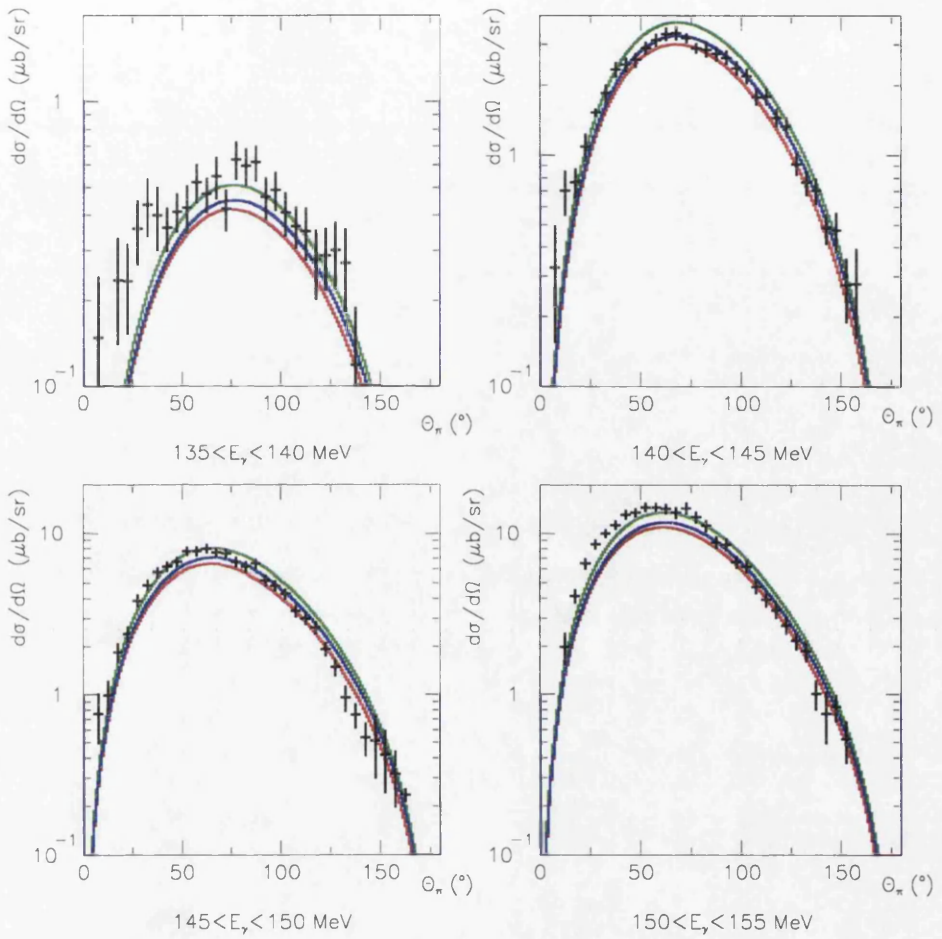

Figure 5.3: **Differential cross sections for ^{16}O:** Black - present experiment; red-PWIA; green-DWIA; blue-DREN. The theoretical prediction for $135 < E_\gamma < 140$ MeV is the adjusted calculation for $E_\gamma = 140$ MeV as described in the text. All theoretical results from [79].

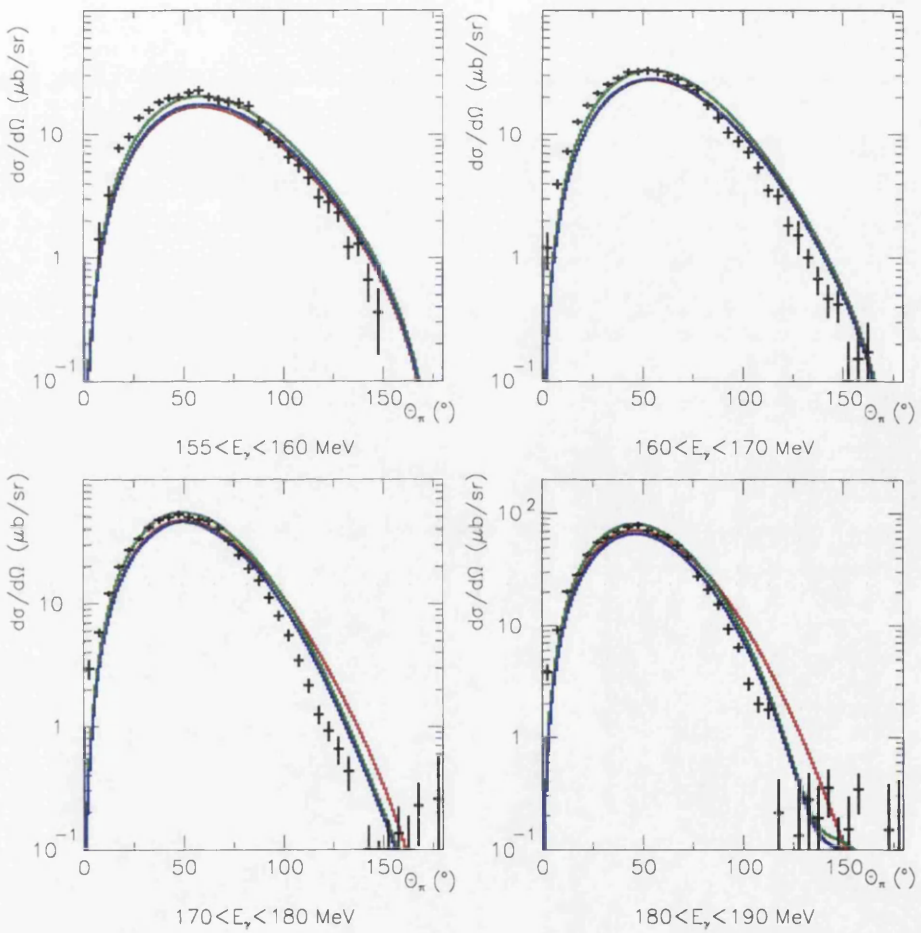

Figure 5.4: **Differential cross sections for ^{16}O:** Black - present experiment; red-PWIA; green-DWIA; blue-DREN. All theoretical predictions from [79].

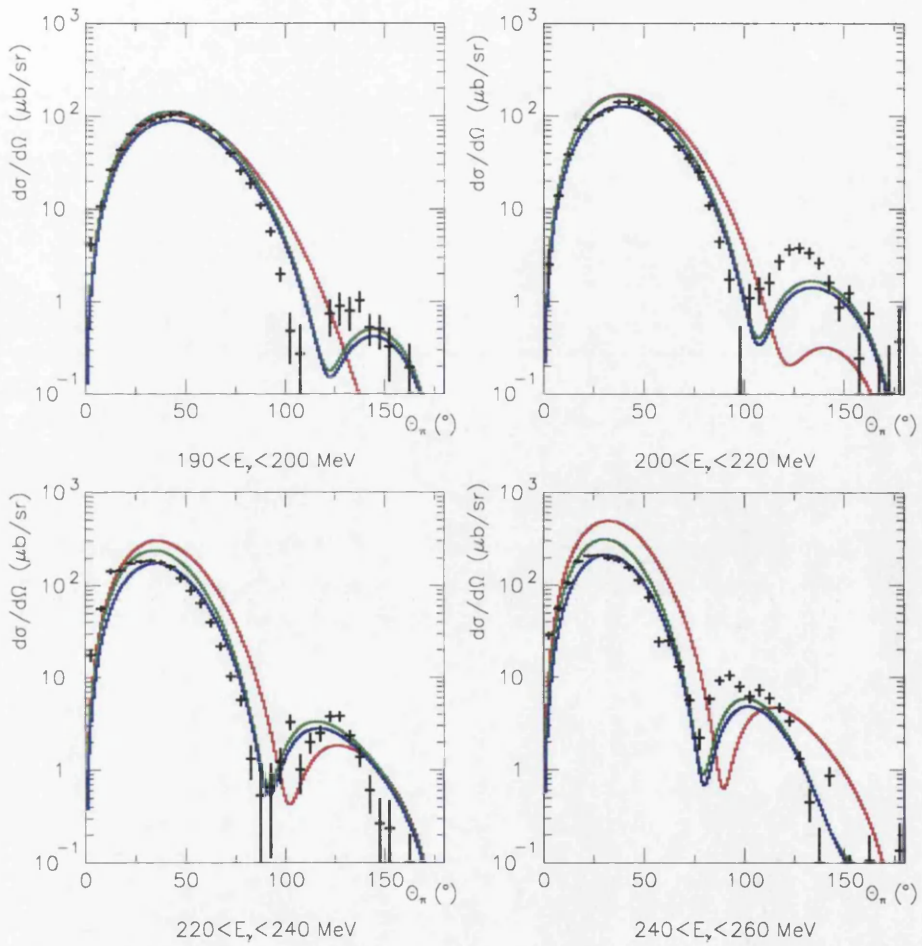

Figure 5.5: **Differential cross sections for ^{16}O:** Black - present experiment; red-PWIA; green-DWIA; blue-DREN. All theoretical predictions from [79].

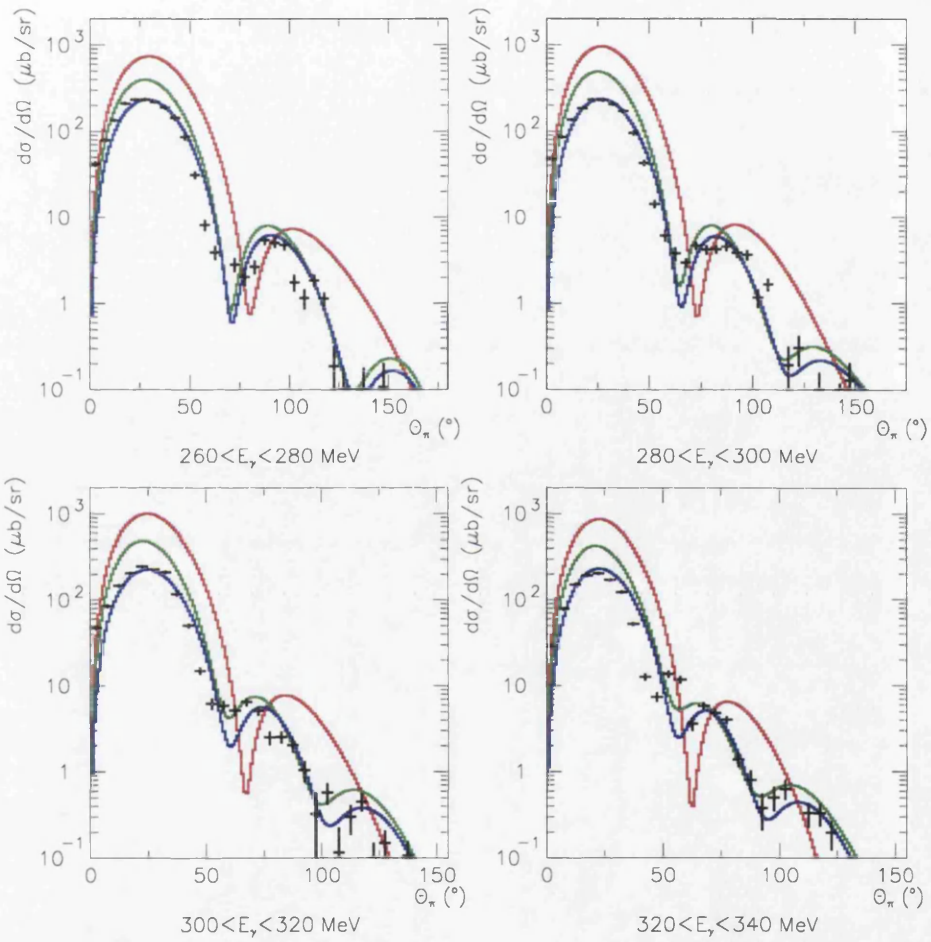

Figure 5.6: **Differential cross sections for ^{16}O:** Black - present experiment; red-PWIA; green-DWIA; blue-DREN. All theoretical predictions from [79].

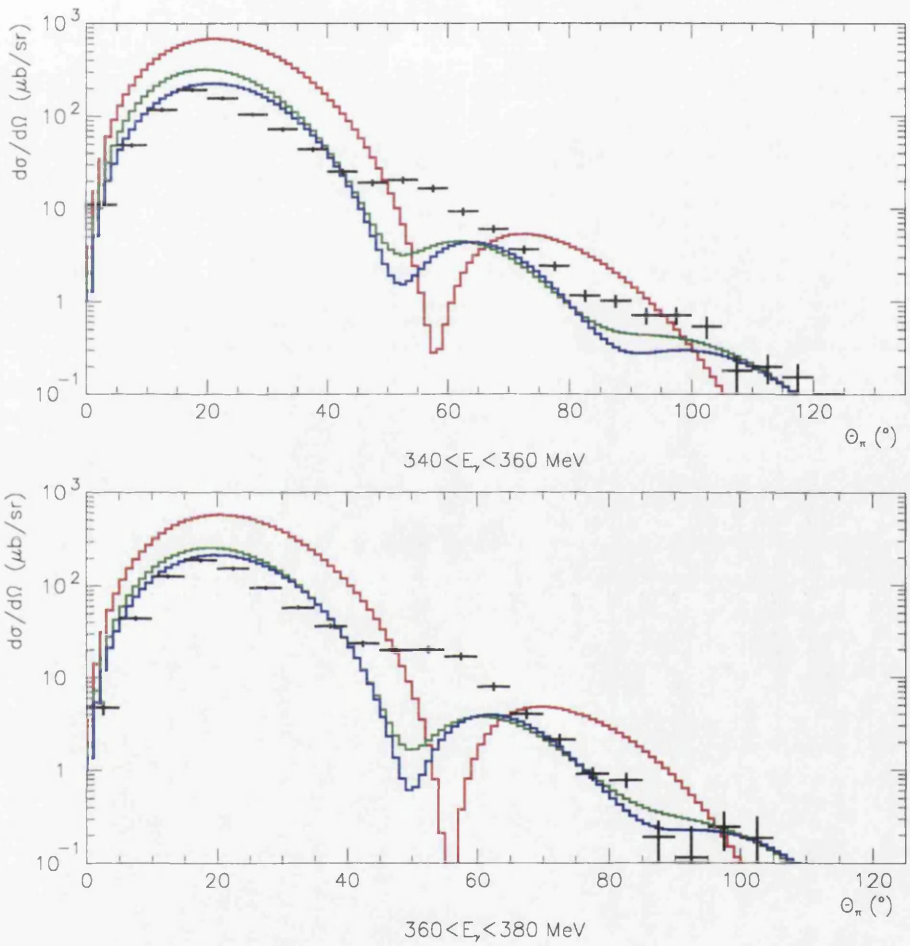

Figure 5.7: **Differential cross sections for ^{16}O:** Black - present experiment; red-PWIA; green-DWIA; blue-DREN. All theoretical predictions from [79].

Table 5.1: **Positions of the first maximum and first minimum in the differential cross section for ^{16}O.**

E_γ	θ_π (°)							
	First max				First min			
[MeV]	Experiment	PWIA	DWIA	DREN	Experiment	PWIA	DWIA	DREN
135-140	78±2	76.5	76.5	77				
140-145	68±2	68	68	69				
145-150	68±2	65	66	66				
150-155	63±2	61	61.5	62				
155-160	58±2	58	59	59				
160-170	53±2	55	54	55	155±5			
170-180	48±2	53	50	50	140±10			
180-190	48±2	50	46	46	130±10			
190-200	45±2	44	43	43	115±2	-	123	123
200-220	40±2	40	39	39	103±2	123	107	108
220-240	33±2	36	34.5	35	88±2	103	92	92
240-260	30±2	33	31	31	78±2	90	80	80
260-280	30±2	30	28	29	68±2	81	71	72
280-300	25±2	27	25	27	68±2	73	65	66
300-320	23±2	25	23	25	58±2	68	60	61
320-340	23±2	23	22	23	58±2	63	57	57
340-360	20±2	22	20	21	48±2	58	54	53
360-380	18±2	21	19	20	48±2	56	50	50

remains at around that value for $E_\gamma > 220$ MeV.

The PWIA does not provide a good description of the experimental data. The total cross section for the PWIA is a factor of ~ 0.8 smaller than the experimental data close to threshold. At $E_\gamma \approx 175$ MeV the PWIA total cross section becomes larger than the experimental data, and with increasing E_γ the difference between the two increases to a factor of ~ 4 in the Δ region (around 300 MeV). In the differential cross sections, the positions of the minima appear at systematically lower angles in the experimental data than in the PWIA calculation.

The DWIA gives a better description of the experimental data than the PWIA, demonstrating the importance of including the final state interaction (FSI) in the description of the pion production process. As discussed in section 1.3, the DWIA approach increases the predicted cross section in the threshold region (due to the attractive p-wave pion-nucleus interaction). A strong imaginary potential is introduced in the Δ region which describes the absorption of the pion in the nucleus and brings the predicted total cross section closer to the experimental data. The FSI shifts the diffraction minima in the differential cross sections to lower angles than those obtained for the PWIA and closer to those in the experimental data. The attractive nature of the FSI also enhances the cross section at backward angles and results in a second

Table 5.2: **Positions of the second maximum and second minimum in the differential cross section for ^{16}O.**

E_γ	θ_π (°)							
	Second max				Second min			
[MeV]	Experiment	PWIA	DWIA	DREN	Experiment	PWIA	DWIA	DREN
190-200	138±2	-	144	145				
200-220	128±2	140	134	134				
220-240	115±2	127	116	117				
240-260	93±2	114	101	102				
260-280	93±2	102	90	91			133	135
280-300	80±2	92	80	82	-	-	116	119
300-320	68±2	84	71	74	103±10	-	101	104
320-340	68±2	78	65	69	93±2	-	92	95
340-360	53±2	73	62	64	88±10	-	-	92
360-380	53±2	70	61	62	93±5	-	-	-

Table 5.3: **Positions of the third maximum in the differential cross section for ^{16}O.**

E_γ	θ_π (°)			
	Third max			
[MeV]	Experiment	PWIA	DWIA	DREN
260-280	-	-	151	152
280-300	-	-	130	133
300-320	118±10	-	114	118
320-340	103±2	-	105	109
340-360	95±5	-	-	99

minimum and a third maximum not predicted in the PWIA. There is some evidence of these in the experimental data.

The DWIA model gives the best description of the experimental data in the threshold region up to $E_\gamma \approx 170$ MeV above which the DREN model gives the best description, particularly in the Δ resonance region. The DREN model takes account of the medium modifications of the Δ resulting in a shift in the maximum of the total cross section from 300 MeV to 250 MeV. The present measurement indicates a shift to ~240 MeV and thus indicates that the Δ mass used in this model perhaps needs some modification. The agreement with the DREN is very good up to $E_\gamma < 320$ MeV. The E_γ bins above this correspond to the region where the pion energy difference fits were particularly difficult (see section 4.8.1) and so may reflect a problem with the experimental data rather than the model. The total cross section for $E_\gamma > 320$ MeV for the experimental data is almost 20 % lower than the DREN prediction. If the experimental total cross section is too low it must be because the experimental data in the regions between the first maximum and first minimum is too low (see Figure 5.7). However, the angular distribution shape varies smoothly with pion angle which hints that the maxima are systematically at smaller values of θ_π than the DWIA and the DREN theories predict. Increasing the experimental cross section in the region between the first maximum and minimum would result in an "odd" shape for the differential cross section which is hard to justify based on the shape of the cross sections at lower incident photon energies.

The position of the first maximum in the differential cross sections (see Table 5.1) is in reasonable agreement with those predicted by the DWIA and DREN models (there is little difference in the positions for these two models). There is a definite indication in the experimental data that the first minimum in the cross section appears at a lower E_γ than any of the theoretical predictions would suggest; there is evidence of this minimum for $E_\gamma > 160$ MeV in the experimental data but the DWIA does not predict it until $E_\gamma > 190$ MeV (see Figure 5.4). The shift in the position of the first minimum to a smaller pion angle for the DWIA compared with the PWIA is largest in the lowest incident photon energy bins where it first appears; for example, for $200 < E_\gamma < 220$ MeV the difference in position is almost 20° but by $320 < E_\gamma < 340$ MeV the difference is down to only 6° (see Table 5.1). The shift in position in the experimental data is even larger; for $200 < E_\gamma < 220$ MeV it is shifted a further 10° compared with the DWIA. This suggests that the π^0-nuclear potential is more attractive than assumed by the theory, i.e. the real part of the optical potential is too weak.

The position of the second maximum is generally at a lower pion angle than predicted by the DWIA and DREN. The second and third minima were harder to identify

and thus there is only one accurate measurement for each but this indicates agreement with the theories.

The magnitude of the second maximum is quite well described by the DREN except in the incident photon energy regions $200 < E_\gamma < 260$ MeV where the DREN is too small by a factor of up to 2.5 (see Figure 5.5). In this region the pion energy difference spectra were fitted with method 4 with a fixed peak position and width as the coherent peak was not easily identified (see section 4.7.2 and Appendix C). It is possible that a different choice of these parameters would have reduced this difference. However, they were chosen based on the values obtained from fits where the coherent peak was easily identified and although a number of different fits were tried the ones chosen gave the most sensible (cross section has the correct shape) and consistent (no sudden shifts in peak position or width) results. The difference between theory and experiment suggests that the real part of the optical potential is too weak since this corresponds to the region where the sensitivity to the π^0-nuclear interaction is greatest (i.e. the difference between the PWIA and the DWIA).

The minima in the differential cross sections for $E_\gamma > 340$ MeV are not as deep as those predicted by the theoretical models. In this energy region the best fitting method that could be applied to the pion energy difference spectra was fit method 3 (see section 4.7.2 and Appendix C) and clearly this includes yield from non-coherent processes that "fill-in" the minima. However, as discussed in section 4.8.1, this was the best that could be done with the available experimental data. The example shown in Figure 4.45 clearly shows that none of the fitting methods described earlier could give a reasonable looking cross section, there is simply not a good enough separation of the coherent process. For $155 < E_\gamma < 340$ MeV, the incoherent yield from the nuclear excitation process(es) around 6.5 MeV was fitted along with the coherent yield (see section 4.7.2) and this has produced coherent differential cross section minima almost as sharp as the theoretical predictions. The incoherent yield is discussed in more detail in the next section.

5.1.3 Incoherent π^0 Photoproduction

The nuclear excited state pion photoproduction process is expected to contribute to the total pion photoproduction yield but, as shown in Figure 4.51(a), the NaI spectra failed to identify nuclear decay photons from any particular nuclear excited state. However, as described in section 4.7.2, a peak attributed to an excited nuclear state(s) was identified in the pion energy difference spectra. Fits were made to the pion energy difference spectra for the coherent and the incoherent yield where possible. Differential cross sections were obtained for both and are given in Figures 5.8-5.10 which clearly demonstrate that the incoherent yield would "fill-in" in the minima in the coherent

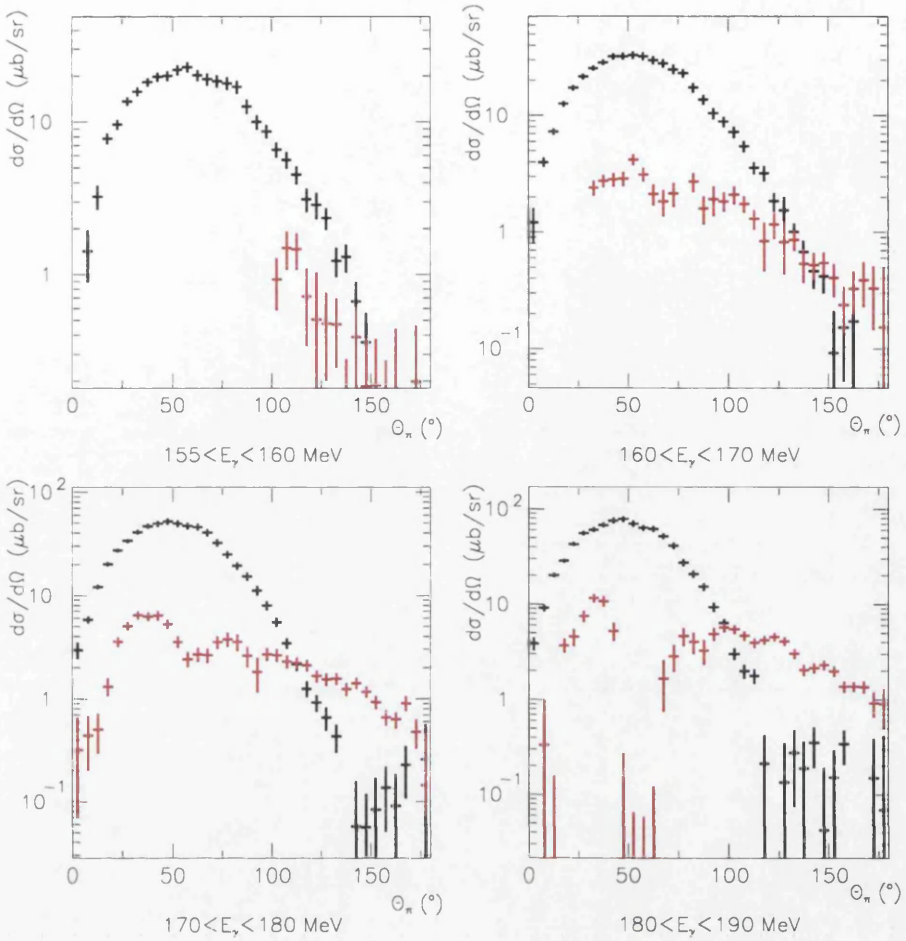

Figure 5.8: **Differential cross section for ^{16}O:** Comparison of coherent (black) and incoherent (red).

differential cross sections if it was not successfully separated.

There are no theoretical calculations for incoherent neutral pion photoproduction on ^{16}O in the literature but an indication of the trends to be expected can be obtained from the calculations for ^{12}C for which some measurements of the non-coherent cross sections are available. Arends et al. measured the non-coherent yield from ^{12}C but only for events that resulted in the break-up of the nucleus [6]. However, this gave differential cross sections that were almost independent of angle with a slight decrease at forward angles. Takaki et al. performed theoretical calculations for incoherent π^0 photoproduction on ^{12}C using the Δ-hole approach [26]. They were surprised to find that the incoherent cross sections were not negligible compared with the coherent cross sections. For example, in pion-nucleus scattering the peak values of the elastic and inelastic 2^+ (4.4 MeV) differential cross sections differ by two orders of magnitude. However, in their π^0 photoproduction calculation, the coherent cross section was only

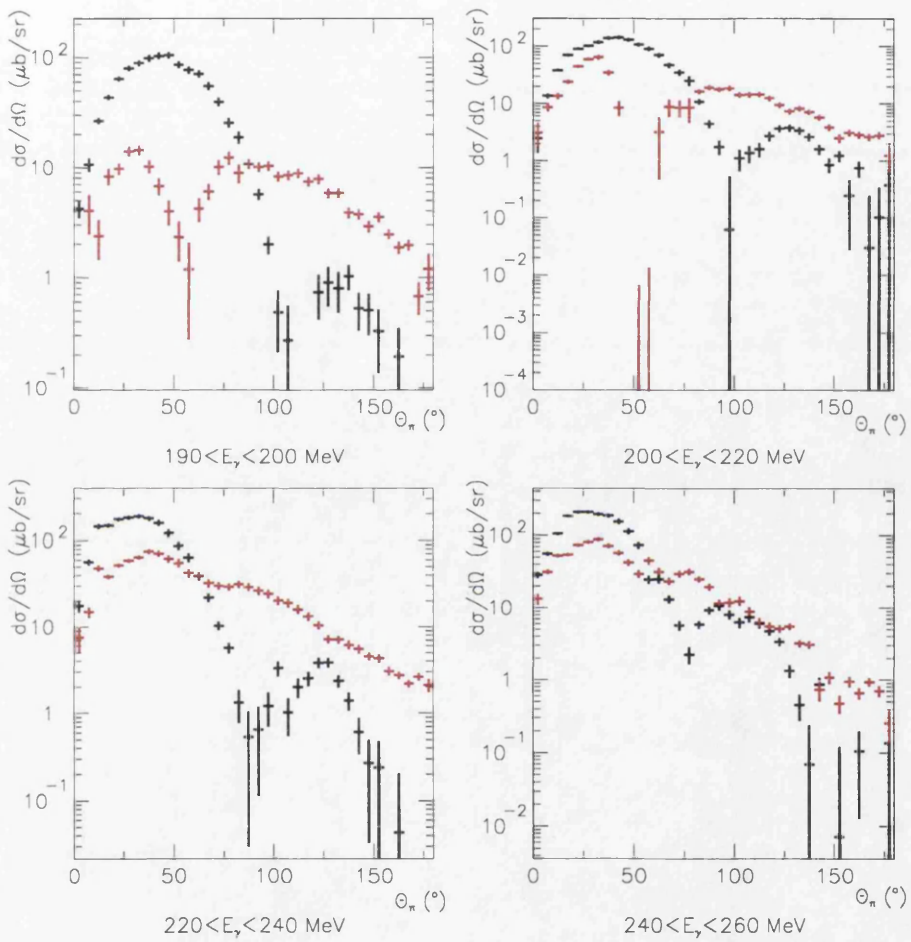

Figure 5.9: **Differential cross section for ^{16}O:** Comparison of coherent (black) and incoherent (red).

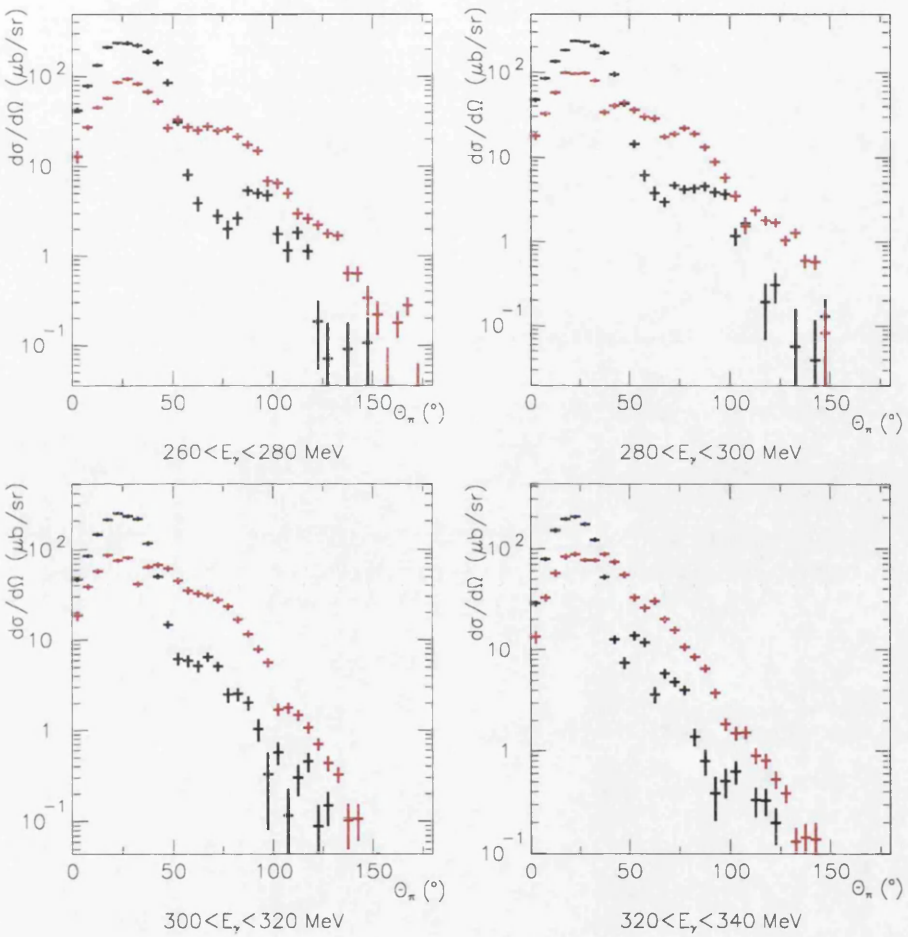

Figure 5.10: **Differential cross section for ^{16}O:** Comparison of coherent (black) and incoherent (red).

six times larger than the incoherent cross section to the 2^+ state in the region of the main coherent peak and fell below it when the region of the first minimum was reached. This different behaviour was shown to be due to the interplay of the nuclear form factors and the elementary pion and photon amplitudes.

The shapes of the coherent and incoherent angular distributions are largely determined by their proportionality to the appropriate form factors and to $\sin^2\theta^*_\pi$ (see section 1.3.1). The coherent form factor has its maximum at zero momentum transfer but the transition form factor, describing the incoherent process, rises from zero at $q = 0$. As a result the maxima and minima should appear at somewhat larger values of θ_π in the incoherent process, and the $\sin^2\theta^*_\pi$ factor therefore increases its relative strength. These general trends are seen in the experimental data presented here. The incoherent cross section is significant even in the region of the first maximum in the coherent cross section and dominates at large pion angles. However, unexpected structure is observed in the incoherent cross sections, in particular a deep minimum in the cross section at $\theta_\pi \sim 50°$ for photon energies of 170-220 MeV with weaker angular variations at other photon energies. This minimum can not be attributed to the transition form factor to any of the four excited states in the 6-7 MeV region (0^+, 1^-, 2^+ and 3^-); these form factors have been measured by Buti et al. [119] and in all cases the first minimum occurs at the same or higher momentum transfer than observed for the elastic form factor, $q = 1.60$ fm^{-1} (see Figure 1.2).

It is thought that the incoherent cross sections (Figures 5.8-5.10) are affected by significant systematic errors caused by the variation in position and shape of the coherent peak in the pion energy difference spectrum as the pion angle and photon energy are varied. This makes it difficult to extract the incoherent strength especially when it is small compared to that of the coherent process. In particular, it is thought that (i) the minimum in the incoherent cross section at $\theta_\pi \sim 50°$ is spurious, (ii) the incoherent cross section at somewhat smaller angles, $\theta_\pi \sim 30°$, is too high and (iii) the "ripples" in the cross section above 50° are also suspect. These comments are based on a more detailed inspection of the pion energy difference fits reported in Appendix D.

The effect of the problems with fitting the incoherent peak on the cross section for the coherent process was estimated to be $\sim 10\,\%$ in a small number of cases but generally much less. This is a major improvement compared to almost all previous measurements in which an indeterminate fraction of the measured "coherent" cross section is due to the unresolved incoherent yield.

5.2 Lead-208

The cross sections at all incident photon energies for ^{208}Pb are larger and show more, well defined minima than those for ^{16}O as a consequence of its larger nuclear size. Since the energy difference resolution was not good enough to separate incoherent, contributions from low-lying nuclear excited states, the fitting process was carried out using only a coherent peak. The "coherent" differential cross sections produced in this way will therefore contain some contribution from the incoherent yield, when it is significant.

5.2.1 Comparison with Previous Measurements

Figures 5.11-5.13 show the differential cross sections for the preliminary data from Krusche et al. [69] compared with the present result for $E_\gamma = 200$ MeV (a weighted average of the results for $190 < E_\gamma < 200$ MeV and $200 < E_\gamma < 220$ MeV was used to obtain this distribution), $280 < E_\gamma < 300$ MeV, and $340 < E_\gamma < 360$ MeV and with theoretical predictions from [79]. The diffraction-like structure is better defined in the present experimental data. The statistical accuracy and pion energy resolution is better in the present work and whereas the differential cross sections in the Krusche et al. data were obtained down to $\sim 10\mu b$, they are obtained down to $\sim 1\mu b$ in the present experimental data at the two lower photon energies. At backward pion lab angles, the differential cross sections from the present experimental data were generally smaller and the minima are sharper than those from reference [69]. At $E_\gamma = 290$ MeV there is a clear third maximum in the present experimental data that is not present in the reference [69] data. Likewise at $E_\gamma = 350$ MeV, the second maximum and minimum are better defined and there is even a hint of the third maximum. These changes result from the improved resolution which reduces the unwanted incoherent contribution to the coherent cross section. As a result, the overall shape of the differential cross sections from the present measurement also agrees better with the theoretical predictions than those from reference [69].

The angles of the maxima and minima in the two sets of data are in reasonable agreement as is shown in Table 5.4. However, a closer examination suggests that there are statistically significant differences in the shape of the cross section rising from $\sim 10\,\%$ at $E_\gamma = 200$ MeV to $\sim 35\,\%$ at 350 MeV. These differences at small pion angles can not be attributed to the incoherent contribution and are more likely to be the combined result of systematic errors in the π^0 detection efficiencies used in both experiments. It is probably relevant that the layout of the TAPS blocks was very different in the present work and the earlier experiment [69], with the block positions at forward angles in the present work corresponding to the spaces between blocks in

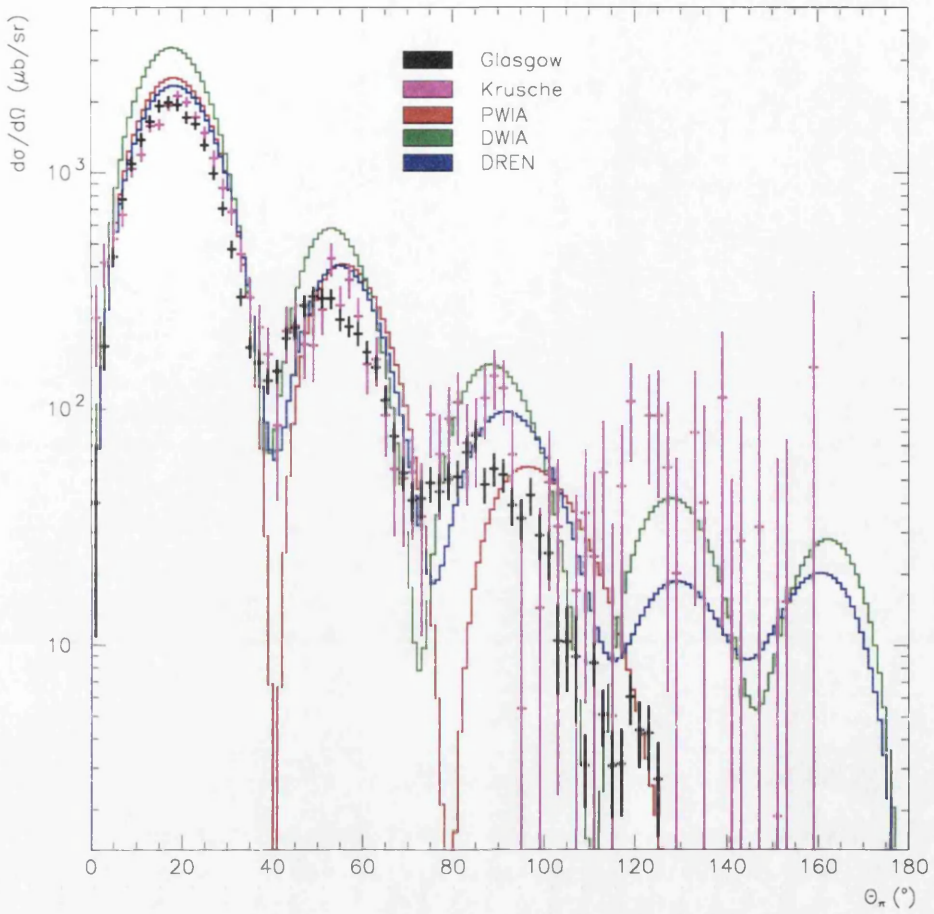

Figure 5.11: **Differential cross section for ^{208}Pb at $E_\gamma = 200$ MeV:** Black-present experiment; magenta - data from [69]; red-PWIA; green-DWIA; blue-DREN. All theoretical results from [79].

Table 5.4: **Comparison of the angles of the maxima and minima in the differential cross sections of the present experiment and the preliminary data of reference [69].**

	θ_π [°]					
	$E_\gamma = 200$ MeV		$E_\gamma = 290$ MeV		$E_\gamma = 350$ MeV	
	Glasgow	**Ref [69]**	**Glasgow**	**Ref [69]**	**Glasgow**	**Ref [69]**
First maximum	17±2	19±2	10±2	11±2	9±2	11±2
First minimum	39±2	41±2	23±2	27±2	19±2	21±2
Second maximum	51±2	53±2	32±2	35±2	25±2	-
Second minimum	70±2	-	43±2	43±2	35±2	-
Third maximum	-	-	49±2	-	42±2	-

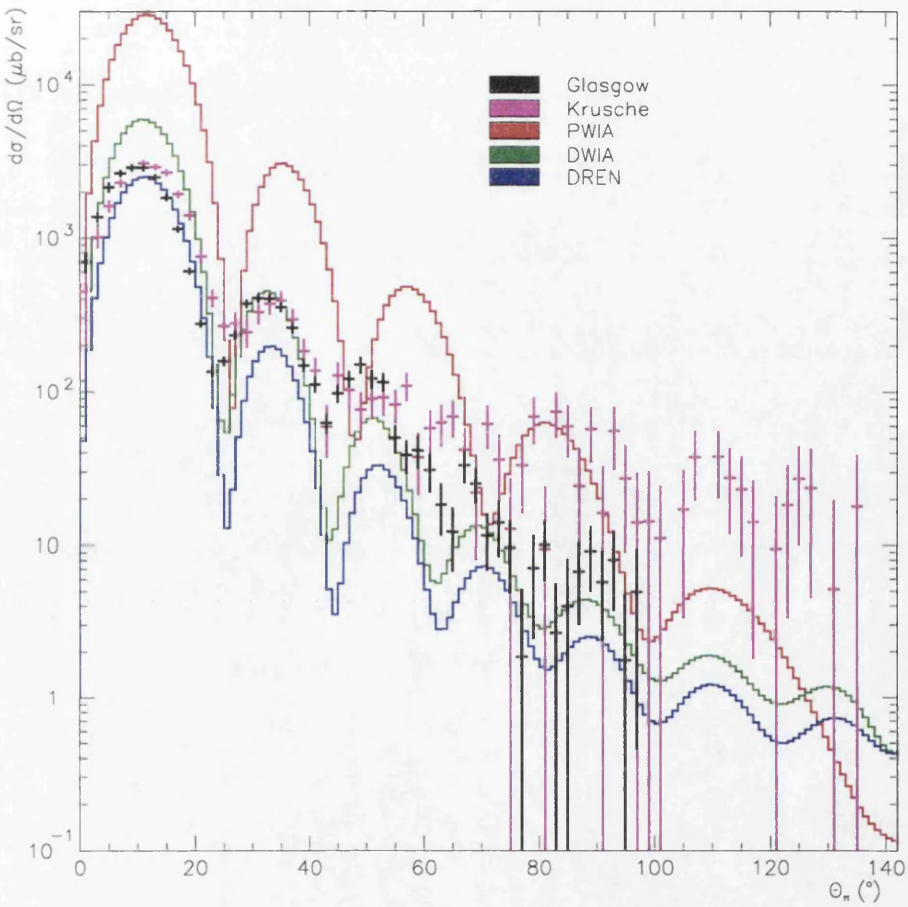

Figure 5.12: **Differential cross section for ^{208}Pb at $E_\gamma = 290$ MeV:** Black-present experiment; magenta - data from [69]; red-PWIA; green-DWIA; blue-DREN. All theoretical results from [79].

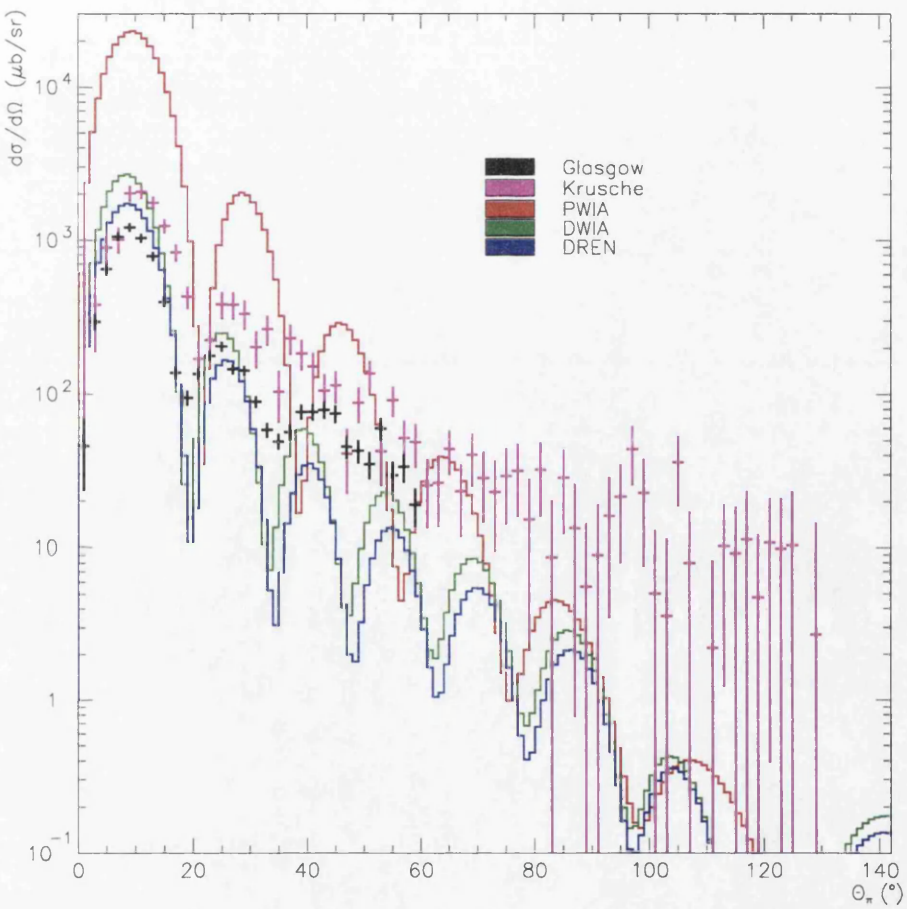

Figure 5.13: **Differential cross section for ^{208}Pb at $E_\gamma = 350$ MeV:** Black-present experiment; magenta - data from [69]; red-PWIA; green-DWIA; blue-DREN. All theoretical results from [79].

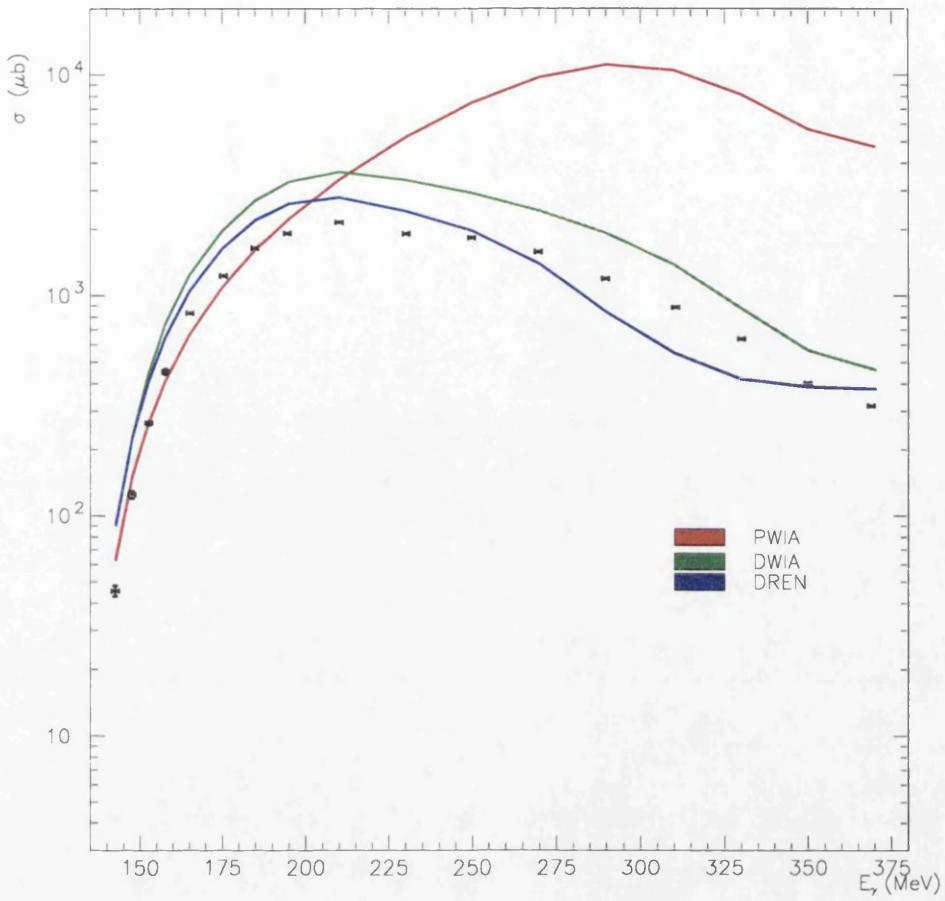

Figure 5.14: **Integrated cross-section for ^{208}Pb:** Black - present experiment; red - DWIA; green - DWIA; blue: DREN. All theoretical results from [79]. (For $140 < E_\gamma < 150$ MeV the DWIA and DREN predictions are identical.)

the earlier work.

5.2.2 Comparison with Theoretical Predictions

Figure 5.14 shows the total cross section for ^{208}Pb and Figures 5.15-5.19 show the differential cross sections. The errors bars shown are statistical. The data are compared with the theoretical model predictions using the PWIA, DWIA, and DREN calculations of Kamalov [79] (see section 1.3).

The theoretical model predictions were made for discrete values of incident photon energy E_γ, with E_γ in 10 MeV steps between 140 MeV and 380 MeV. These predictions were averaged to correspond to the E_γ bins used in the experiment for all E_γ bins.

The total and differential cross sections for ^{208}Pb show the expected general characteristics. The total cross section (Figure 5.14) increases with E_γ to a maximum

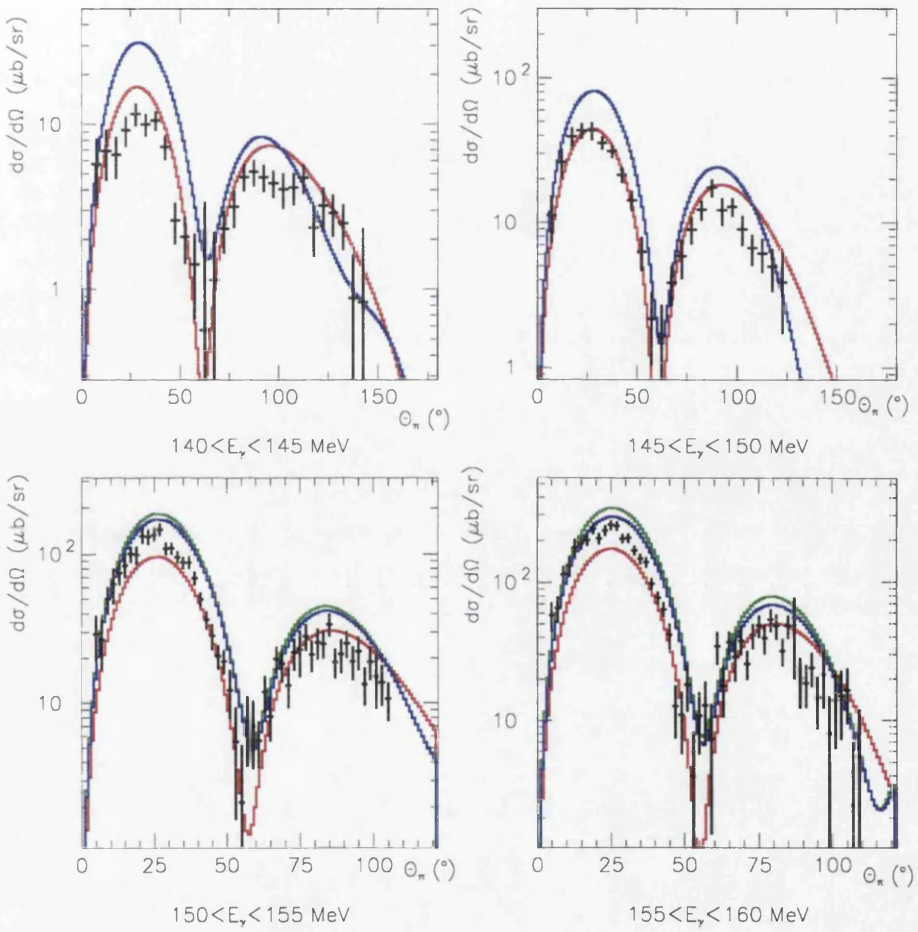

Figure 5.15: **Differential cross-sections for ^{208}Pb:** Black - present experiment; red - DWIA; green - DWIA; blue: DREN. All theoretical results from [79].

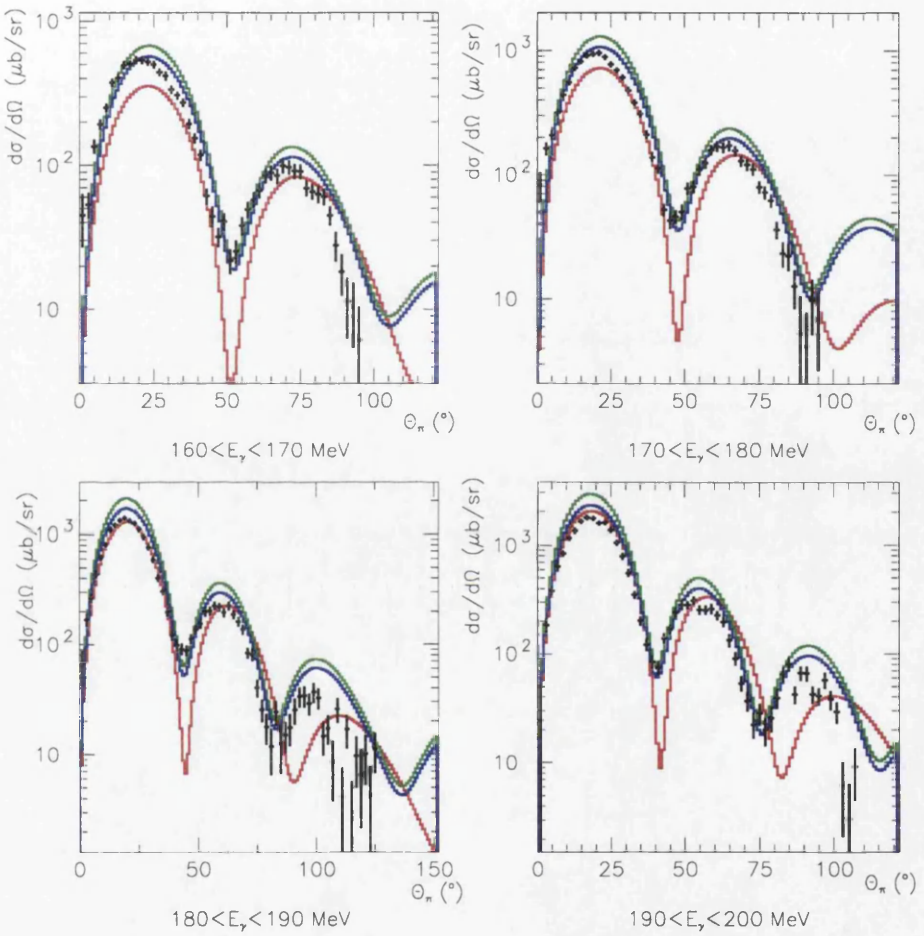

Figure 5.16: **Differential cross-sections for ^{208}Pb:** Black - present experiment; red - DWIA; green - DWIA; blue: DREN. All theoretical results from [79].

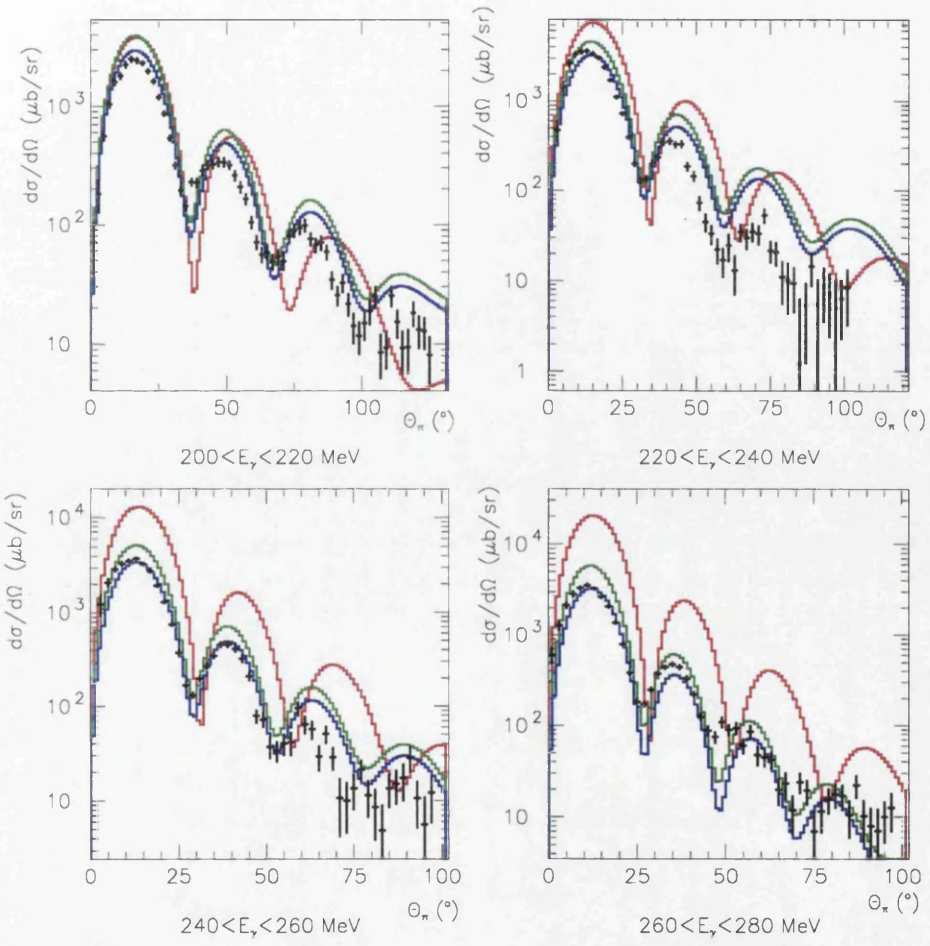

Figure 5.17: **Differential cross-sections for ^{208}Pb:** Black - present experiment; red - DWIA; green - DWIA; blue: DREN. All theoretical results from [79].

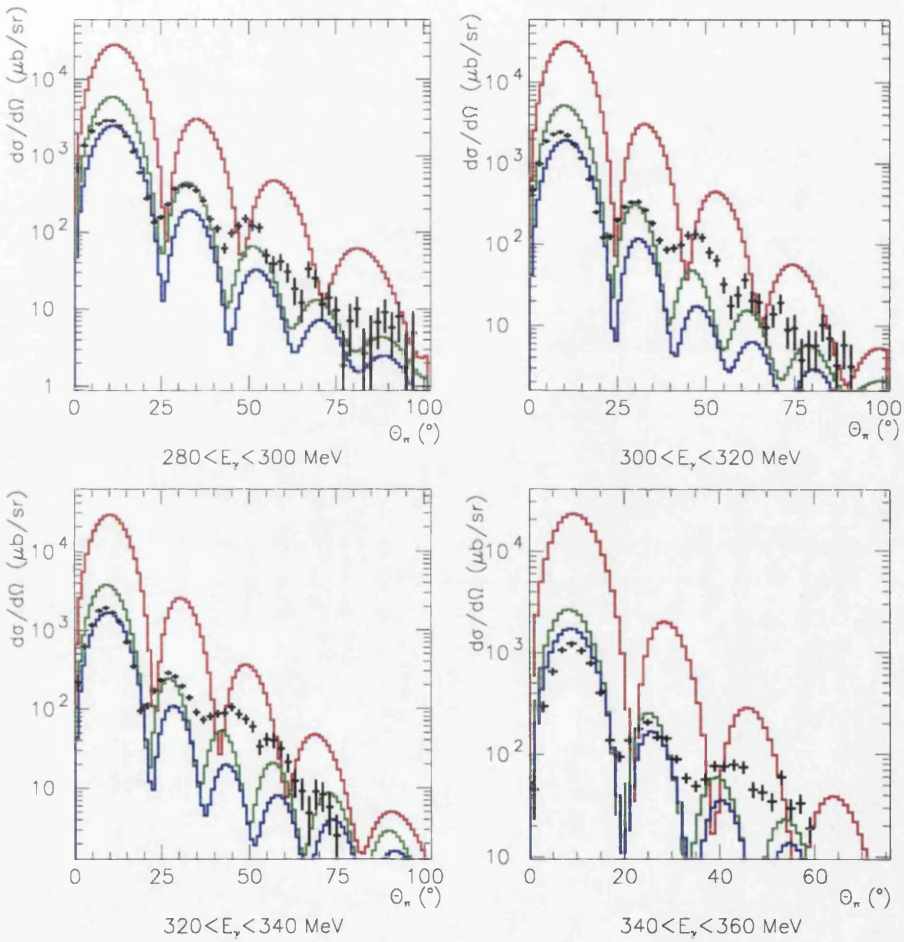

Figure 5.18: **Differential cross-sections for ^{208}Pb:** Black - present experiment; red - DWIA; green - DWIA; blue: DREN. All theoretical results from [79].

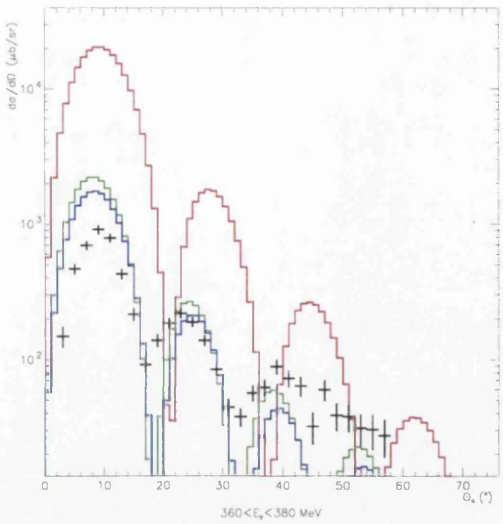

Figure 5.19: **Differential cross-sections for ^{208}Pb:** Black - present experiment; red - DWIA; green - DWIA; blue: DREN. All theoretical results from [79].

value at about 220 MeV, around 70 MeV below the Δ resonance, and then decreases with increasing E_γ.

The differential cross sections (Figures 5.15-5.19) have a diffraction-like shape with two or more maxima separated by minima. The magnitudes of the maxima decrease with increasing pion angle. A second minimum and third maximum appear for $E_\gamma >$ 180 MeV and a there are hints of a third minimum and fourth maximum for $E_\gamma >$ 240 MeV. The positions of the maxima and minima in the differential cross sections are given in Tables 5.5-5.7.

The Differential Cross Sections

The effect of the FSI on the shape of the angular distributions for $^{208}Pb(\gamma, \pi^0)$ is as expected. The minima and maxima in the DWIA and DREN predictions are in general shifted to smaller pion angle compared with the PWIA by an amount varying from 1-2° up to a maximum of $\sim 10°$. The measured angular positions agree with the DWIA and DREN calculations even for the large angle features such as the third minimum which can be identified at some photon energies (see Table 5.7). At the lowest photon energies, $E_\gamma < 170$ MeV, the calculated angular shift in the first minimum is in the opposite direction to that at higher E_γ, an effect not seen in ^{16}O because the cross section minimum never occurs at such a low momentum transfer; in this case the measured positions are not accurate enough to distinguish the PWIA and the DWIA predictions.

Overall, the magnitude of the measured cross sections also supports the DWIA prediction of an order of magnitude reduction in the PWIA cross section due to pion

Table 5.5: **Positions of the first maximum and first minimum in the differential cross section for ^{208}Pb.**

E_γ	θ_π (°)							
	First max				First min			
[MeV]	Experiment	PWIA	DWIA	DREN	Experiment	PWIA	DWIA	DREN
140-145	28±5	29	29	29	63±5	62	64	64
145-150	28±5	28	29	29	63±5	61	63	63
150-155	23±5	26	27	27	54±5	58	59	59
155-160	25±5	25	26	26	56±5	55	57	57
160-170	21±2	24	24	24	51±2	52	53	53
170-180	21±2	22	22	22	46±2	48	48	48
180-190	21±2	20	20	20	45±2	45	44	44
190-200	18±2	19	19	19	43±2	42	41	41
200-220	17±2	17	17	17	35±2	38	37	37
220-240	16±2	16	15	15	33±2	35	33	33
240-260	13±2	14	13	13	29±2	32	30	30
260-280	11±2	13	12	12	27±2	29	27	28
280-300	10±2	12	11	12	23±2	27	26	26
300-320	9±2	11	10	11	20±2	25	24	25
320-340	9±2	10	10	10	19±2	24	22	23
340-360	9±2	10	9	9	19±2	22	20	20
360-380	9±2	10	9	9	17±2	22	19	19

Table 5.6: **Positions of the second maximum and second minimum in the differential cross section for ^{208}Pb.**

E_γ	θ_π (°)							
	Second max				Second min			
[MeV]	Experiment	PWIA	DWIA	DREN	Experiment	PWIA	DWIA	DREN
140-145	88±5	96	92	92				
145-150	88±5	93	90	90				
150-155	77±5	86	84	84.5				
155-160	79±5	81	80	80	-	-	116	117
160-170	69±2	74	72	73	-	-	106	106
170-180	65±2	68	65.5	66	-	102	93	93
180-190	60±5	62	60	60	82±5	91	83	83
190-200	53±5	58	55	55	74±5	83	76	76
200-220	48±2	52	50	50	68±5	74	68	68
220-240	41±2	47	44	44	59±5	65	60	60
240-260	38±2	42	39	39	52±2	58	53	53
260-280	35±2	39	36	36	47±2	53	48	49
280-300	32±2	36	33	34	43±2	49	44	45
300-320	30±2	33	30	31	39±2	45	40	42
320-340	27±2	31	28	29	37±2	42	36	38
340-360	25±2	29	26	26	35±2	39	34	35
360-380	23±2	28	25	25	33±2	38	33	34

Table 5.7: **Positions of the third maximum and third minimum in the differential cross section for ^{208}Pb.**

E_γ	θ_π (°)							
	Third max				Third min			
[MeV]	Experiment	PWIA	DWIA	DREN	Experiment	PWIA	DWIA	DREN
170-180	-	122	113	113				
180-190	99±5	110	100	101	-	-	137	137
190-200	-	100	92	92		-	116	116
200-220	79±2	88	81	81	98±5	-	102	102
220-240	69±5	78	71	71	87±5	101	90	89
240-260	-	69	63	63	-	88	79	79
260-280	-	63	57	57	-	79	70	70
280-300	49±2	58	52	52	-	72	63	63
300-320	46±2	53	46	48	57±2	66	55	57
320-340	45±2	49	42	44	-	61	50	52
340-360	42±5	46	40	41		57	48	49

absorption when the photon energy rises into the Δ resonance region. The only exception occurs for low photon energies, $E_\gamma < 150$ MeV, where the DWIA (and the DREN) predictions lie a factor of two above the PWIA but the measured cross section is close to the PWIA result (see Figure 5.15). For ^{16}O no equivalent effect is seen; the DWIA prediction is only $\sim 20\,\%$ greater than the PWIA at these energies (see Figure 5.3) and the DWIA result gives the best description of the experimental data.

The predicted effect of the Δ-nucleus interaction is a reduction in the DWIA cross section by a factor that rises to ~ 2.5 at $E_\gamma = 300$ MeV, but there is very little difference in the angular variation of the DREN and the DWIA predictions. The measured cross sections tend to lie below the DREN prediction up to $E_\gamma \sim 250$ MeV, and then between it and the DWIA prediction for $E_\gamma = 250$-350 MeV. The shape of the measured angular distribution is reasonably well represented by the calculations except for the photon energy regions $E_\gamma = 200$-260 MeV and $E_\gamma > 280$ MeV.

The Region $E_\gamma = 200$-260 MeV

The magnitude of the differential cross sections for $200 < E_\gamma < 260$ MeV decreases more rapidly with pion angle than the theoretical predictions (see Figure 5.17). This corresponds to the regions where the biggest shifts in the peak position of the pion energy difference spectra are observed (see Figure 4.28). Figure 5.20 gives examples of pion energy difference spectra with the fits used for $200 < E_\gamma < 220$ MeV.

Figure 5.20(a) shows a spectrum from the region of the second maximum in the differential cross section. The magnitude of this maximum is significantly lower in the experimental data than in the theoretical predictions. The pion energy difference

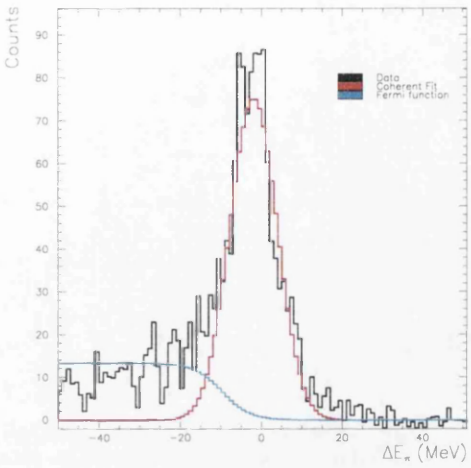

(a) $\theta_\pi = 48 - 50°$

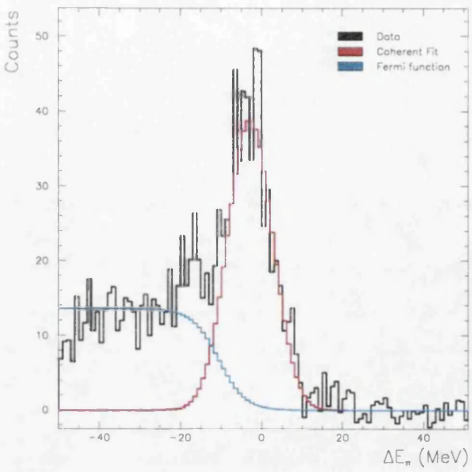

(b) $\theta_\pi = 56 - 58°$

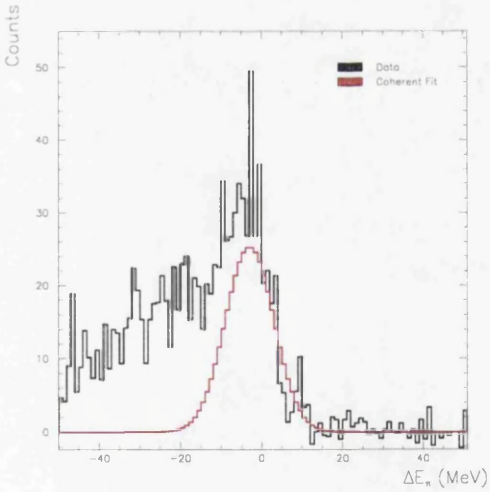

(c) $\theta_\pi = 58 - 60°$

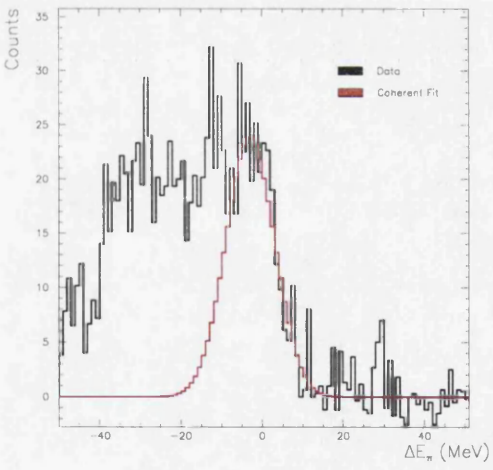

(d) $\theta_\pi = 78 - 80°$

Figure 5.20: **Pion energy difference spectra for $E_\gamma = 200 - 220$ MeV.**

spectrum has a broad base suggesting that the the coherent peak position is shifting over the energy range contributing to the experimental data. However, a single Gaussian with a Fermi function (fit method 1) gives a reasonable fit to the experimental data. Increasing the fitted area would bring the experimental data closer to the theoretical magnitudes but would clearly include even more non-coherent events than it does already (there is a significant tail to the left of the peak) and would therefore certainly not be a measure of the coherent cross section.

Figure 5.20(b) shows a spectrum about half-way down the second maximum towards the second minimum of the differential cross section. This was the largest θ_π bin that could be fitted with method 1 for this energy region (see section 4.7.2 and Appendix C). Again the fit looks reasonable even though the non-coherent tail to the left of the peak has a magnitude of almost half the coherent peak. In the next θ_π bin, the non-coherent tail has a magnitude more than half that of the coherent peak so fit method 3 was employed and this is shown in Figure 5.20(c). The peak position and width of the coherent fit were fixed based on those in the nearby bins. A better fit would have been obtained if the peak position had been allowed to go more negative but we can not be certain that this shift is really a shift of the coherent peak and not caused by the increasing yield from the non-coherent contributions.

Figure 5.20(d) is the pion energy difference spectrum in the third maximum region of the differential cross section. Again, fit method 3 was employed with the same fixed peak position and width as was used in Figure 5.20(c). Here the fit looks a good one even though the non-coherent contribution has the same magnitude as the coherent.

The situation is similar for $E_\gamma = 220 - 240$ MeV: increasing the fitted area would increase the magnitude of the differential cross section but non-coherent contributions would be included. Therefore, we conclude that the angular distribution really is different from the theory in this region and that the cross section is smaller than the DREN prediction. This indicates that some modification of both the pion-nucleus interaction and the in-medium Δ properties is required in this region.

The Region $E_\gamma > 280$ MeV

For $280 < E_\gamma < 360$ MeV, the measured differential cross sections are larger than those of the DREN above the first maximum region and larger than both the DREN and the DWIA in the region above the second maximum (see Figure 5.18). At these incident photon energies fit method 3 was used for nearly all θ_π bins. In fact this method was used for all pion energy difference spectra for $\theta_\pi > 14°$ in the $280 < E_\gamma < 300$ MeV bin and for all incident photon energy bins above this (see Appendix C).

Figure 5.21 gives an example of a pion missing energy spectrum in the second maximum region of the differential cross section for $320 < E_\gamma < 340$ MeV. Clearly, the

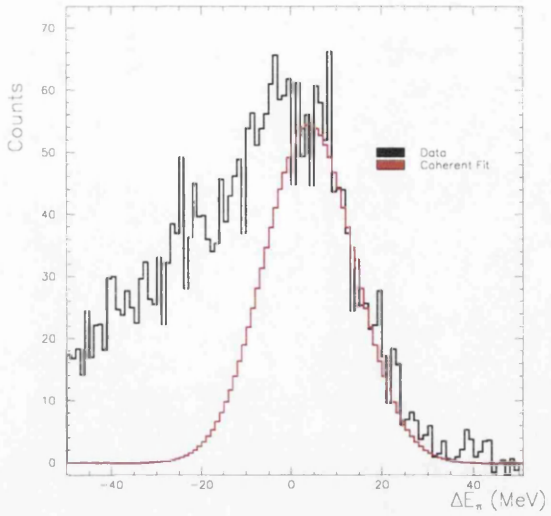

Figure 5.21: **Pion energy difference spectrum for ^{208}Pb:** for $320 < E_\gamma < 340$ MeV and $26 < \theta_\pi < 28°$.

non-coherent yield now dominates and a significant portion of it is probably included in the "coherent" peak. The coherent peak position is known to shift with E_γ and θ_π (see section 4.7.2) even when the non-coherent yield is negligible. Therefore, it will probably continue to shift even when the non-coherent yield is significant, making separation of the coherent process doubly difficult.

Therefore the large cross section magnitudes obtained in the angular ranges 25-75° may be due to non-coherent contributions. This would also explain why the cross section minima are not as deep in the experimental data as those predicted by the theoretical calculations (the theoretical calculations are for the coherent process only). The true coherent cross section could still agree with the DREN.

The Total Cross Section

For ^{208}Pb, the peak positions of the total cross sections for the DWIA and DREN are the same because it is the FSI that shifts the maximum from 300 MeV to $\sim$ 210 MeV rather than the medium modification of the Δ (see section 1.3.5). This peak position is in agreement with that of the experimental data.

The total cross section agrees much better with the DREN than the DWIA. It is slightly smaller than the DREN prediction up to 250 MeV. It is probably close to the DREN prediction for E_γ = 250-350 MeV after allowance for the incoherent contribution. For example, at $300 < E_\gamma < 320$ MeV only 60 % of the total cross section (σ) comes from the first maximum in the angular distribution (see Figure 5.18) so the high values of the differential cross section in the second and third maxima (probably due to incoherent contributions as discussed above) will certainly give a bigger value

Table 5.8: **Comparison of α values obtained for assessment of A dependence**

	α	
E_γ (MeV)	**Present Experiment**	**Boffi Calculation [75]**
155-160	0.61 ± 0.01	—
180-190	0.64 ± 0.01	0.89
240-260	0.46 ± 0.01	0.44
320-340	0.33 ± 0.01	0.33
360-380	0.25 ± 0.01	0.33

of σ (it is probably $\sim 60\,\%$ too big). Finally, the experimental data is maybe a little smaller than the DREN at the highest incident photon energy, $E_\gamma \geq 350$ MeV.

Incoherent π^0 Photoproduction

As discussed in section 4.9, no nuclear decay photons from any particular excited state could be identified in the NaI spectra. It was shown earlier that the contribution of the incoherent process in ^{16}O was significant so it is probable that it is also significant in ^{208}Pb. However, the pion energy difference resolution was not good enough to separate the incoherent excitation of the lowest states.

5.3 The A-dependence of the Coherent (γ, π^0) Total Cross Section

The experiment performed at Mainz in 1999 measured coherent π^0 photoproduction on ^{12}C, ^{16}O, ^{40}Ca, and ^{208}Pb. The first results from ^{12}C and ^{40}Ca were reported in a recent thesis [72] and a more complete analysis of the results for ^{16}O and ^{208}Pb has been reported here. The basic experimental data now exist for a range of nuclei, allowing the A-dependence of the coherent process to be assessed and the more complete analysis was therefore performed on the ^{12}C and ^{40}Ca data. Figure 5.22(a) shows the total (γ, π^0) cross sections for all four nuclei as a function of E_γ and Figure 5.22(b) shows a log-log plot of the cross section versus the mass number, A, at a selection of incident photon energies. Clearly, a straight line dependence is not obtained so that a power law dependence, $\sigma_{\rm coh}\,(A) = \sigma_0 A^\alpha$, gives only an approximate description of the experimental data. The values of α obtained by fitting the experimental data with this relation are given in Table 5.8. Boffi et al. produced a similar plot using the results of their DWIA calculations on ^{16}O, ^{40}Ca, ^{90}Zr, and ^{208}Pb [75], and derived α from the ^{16}O and ^{208}Pb data at incident photon energies of 180, 255, 320, and 360 MeV. Both sets of α values are below 1. This was initially interpreted incorrectly by Boffi et al. as support of "the claim that the coherent production process does not take place

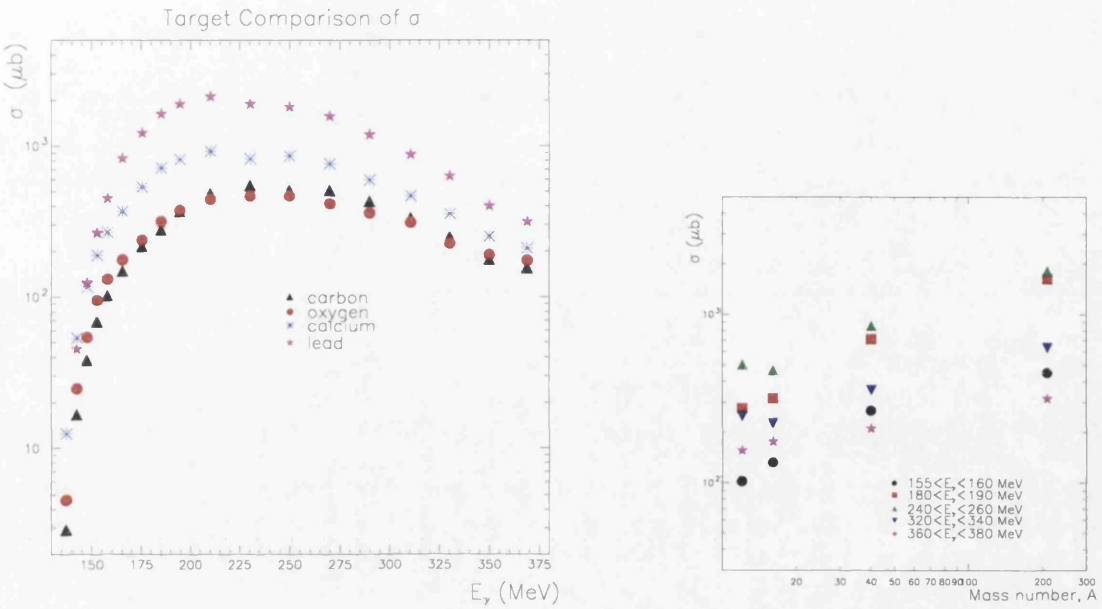

(a) (b)

Figure 5.22: **Assessment of the *A*-dependence of the total cross section:** (a) Comparison of the integrated cross sections for a range of nuclei: ^{12}C (black triangles) and ^{40}Ca (blue stars) are from a more sophisticated analysis of the data in [72]; ^{16}O (red circles) and ^{208}Pb (purple stars) are from this work; (b) Integrated cross section versus mass number, A, for a selection of energies.

Table 5.9: **Position of the total cross section maximum**

Target	σ Peak Position [MeV]
^{12}C	250±20
^{16}O	240±10
^{40}Ca	230±20
^{208}Pb	220±10

on the bulk of the nucleus, which would give rise to an A dependence going approximately as A^2, but is rather a surface effect" [75] but this was later corrected [120]. It is, of course, the coherence of all the A nucleon amplitudes that gives rise to the A^2 dependence seen in the PWIA formula for the cross section (equation 1.4). However, the nuclear form factor, which also appears in equation 1.4, has a sharper momentum transfer dependence as A increases (see Figure 1.2) and very roughly this produces an $A^{-0.5}$ dependence in the angular width of the main peak in the differential cross section, which is integrated to obtain the total cross section. The absorption of the outgoing pion also increases rapidly with nuclear size and with photon energy so that values of α less than 1 are expected. This was also pointed out by Carrasco et al. when they did a similar comparison for their Δ-hole calculations for ^{12}C, ^{40}Ca, and ^{208}Pb [27]. Carrasco et al. quote a value of 0.45 for α at $E_\gamma = 300$ MeV and 0.40 at $E_\gamma = 350$ MeV.

The decrease in the value of α with increasing photon energy observed here and by Boffi et al. [75] is also expected since the pion absorption grows rapidly as E_γ increases up to the Δ region.

The position of the maximum of the total cross section gives an indication of any modification of the properties of the Δ in the nucleus. If there is no modification, the peak would be expected at 300 MeV. Table 5.9 gives the positions of the maximum for the four nuclei studied. Clearly there is the indication of modification of the Δ in the nuclear medium and that this modification probably has an A-dependence. An important point to note, however, is that ^{16}O does have a slightly different shape to the other three targets. The total cross section of ^{16}O is expected to be greater than that for ^{12}C but here it is smaller at incident photon energies greater than 200 MeV. The incoherent peak in the pion energy difference spectra for ^{16}O resulted in a better separation of the coherent process than was possible for ^{12}C where no such peak was observed. Therefore, the ^{12}C experimental data are probably contaminated with some incoherent yield resulting in a total cross section greater than that expected for a purely coherent yield. This will also apply to ^{40}Ca and to ^{208}Pb for which the non-coherent contamination will be even worse than for the lighter two targets since the thresholds for non-coherent processes are smaller.

Chapter 6

Conclusion

The total and differential cross sections for the coherent photoproduction of neutral pions have been obtained for ^{16}O and ^{208}Pb in the incident photon energy range $135 < E_\gamma < 380$ MeV using the π^0 spectrometer TAPS and demonstrate the expected characteristics. The present measurements cover a wider angular range and have smaller statistical errors than previous measurements. The ^{208}Pb data are in reasonable over-all agreement with the previous measurement of ^{nat}Pb [69] but there are discrepancies that are probably the combined result of systematic errors in the π^0 detection efficiencies used in both experiments.

The introduction of two large NaI detectors to attempt to detect the additional decay photons resulting from incoherent pion photoproduction did not aid the separation of the coherent process. However, the "pion energy difference" method employed to separate the coherent and incoherent processes did identify an incoherent yield for ^{16}O from the nuclear excitation process(es) around 6.5 MeV and this was used to obtain a better separation of the coherent than was possible for ^{208}Pb. This also gave an indication of the incoherent differential cross section for ^{16}O at incident photon energies of 155-340 MeV which again demonstrated the expected general characteristics. These incoherent cross sections are thought to be affected by systematic errors but an initial investigation, presented in Appendix D, indicates that these may be reduced by revisiting the pion energy difference fits. However, since the effect on the coherent cross sections is small, this is beyond the scope of this thesis.

As discussed in chapter 1.1, neutral pion photoproduction in nuclei has particular potential as a source of information on the matter distribution in nuclei, but it also has important contributions to make in determining the amplitudes for the (γ, π^0) reaction on nucleons and extending our knowledge of the pion-nucleus interaction and the medium modifications of the pion production process.

The diffraction-like structure due to the nuclear form factor is clearly demonstrated in the differential cross sections for the present experiment. In order to obtain infor-

mation on the matter versus charge distribution an accuracy of the order of a few per cent is required. At present TAPS can not achieve this. The π^0 detection efficiency has large angular variations and the efficiency calculation is probably affected by systematic errors. Also the π^0 energy resolution was not good enough to separate the coherent and incoherent contributions.

Using $^{12}C(\gamma,\pi^0)$ data, Bergstrom et al. [65] extracted information on the P-wave amplitudes and it is probably possible to do the same using the ^{16}O data near threshold ($E_\gamma < 180$ MeV). Above this the systematic uncertainties in the cross section are too large.

The DWIA (and DREN) theoretical predictions show that distortion from the π^0-nucleus interaction shifts the position of the differential cross section minima and changes the cross section magnitude. The present measurements agree with the predictions to a large extent but discrepancies still remain which will allow the optical potential parameters to be "tuned", mostly using the lower E_γ data where good separation of the coherent process was achieved.

The present experimental data is best accounted for by the DREN theoretical prediction which treats the Δ-nucleus interaction via a parameterisation of the Δ self-energy determined from the $^4He(\gamma,\pi^0)$ data of Rambo et al. [56,57]. However, there are signs that the parameterisation could be improved, which is perhaps not surprising considering that it has now been applied to $A = 208$. Care must be taken when using the present data to do this as it is known that there may be systematic problems both with the π^0 detection efficiency, which is noticeable mainly at pion angles up to the first minimum, and with incoherent contamination of the cross section at larger angles. The A-dependence of the total cross section was assessed using the results presented here and those from reference [72]. The position of the maxima in the total cross sections clearly indicates that there is modification of the Δ properties in the nucleus and that this modification probably has an A-dependence.

The difficulties encountered in separating the coherent and non-coherent cross sections at some pion energies and angles suggest that it would be desirable to carry out further calibrations of TAPS to understand properly the cluster energy and position reconstruction. If the systematic errors in the energy and position reconstruction could be eliminated, the shifts in the position of the coherent peak in the pion energy difference spectra may be better understood, allowing the separation of the coherent and non-coherent events to be carried out with a reduced systematic error.

The crystal ball, an array of NaI elements assembled to provide almost 4π solid angle coverage around the target, will be assembled in Mainz in the next 12 months. This detector assembly would be well suited for π^0 production experiments since the angular variation of the detection efficiency would be considerably smaller than that

of TAPS in the present setup. Also, since the energy resolution of NaI is significantly better than that of BaF_2, it may also allow the detection of nuclear decay photons from incoherent processes resulting in a better separation of the coherent and non-coherent processes than has been obtained before.

Appendix A

Kinematics of Coherent Pion Photoproduction and Pion Decay

A.1 Pion Production

In pion photoproduction, a photon, γ, strikes a nucleus, A, of mass M knocking out a pion of mass m. Figure A.1 illustrates this process with E and p representing the energy and momentum of the particle (subscript γ refers to the incident photon, A to the nucleus, and π to the pion. The additional subscript c refers to quantities in the centre of mass frame). Using the standard definition of

$$\beta_i = \frac{p_i}{E_i} \tag{A.1}$$

$$\gamma_i = \frac{E_i}{m_i}$$

where p_i , E_i and m_i are the momentum, energy and mass of particle i, the total

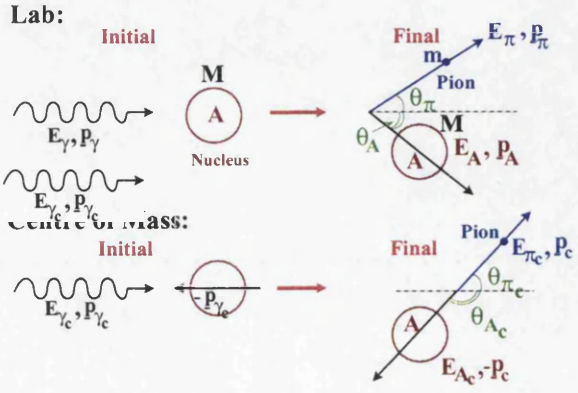

Figure A.1: **Pion Photoproduction.**

energy in the centre of mass (CM) frame, $\sqrt{s}$, is (from the invariance of $(E^2 - p^2)$):

$$\begin{aligned} s &= (E_{\pi_c} + E_{A_c})^2 - 0^2 \quad Final \\ &= (E_\gamma + M)^2 - p_\gamma^2 \quad Initial \\ &= 2E_\gamma M + M^2 \end{aligned} \tag{A.2}$$

The CM energies of the pion, E_{π_c}, and the nucleus, E_{A_c}can be calculated from:

$$\begin{aligned} M^2 - m^2 &= (E_{A_c}^2 - p_c^2) - (E_{\pi_c}^2 - p_c^2) \\ &= E_{A_c}^2 - E_{\pi_c}^2 \\ &= (E_{A_c} + E_{\pi_c})(E_{A_c} - E_{\pi_c}) \end{aligned} \tag{A.3}$$

Hence:

$$E_{A_c} - E_{\pi_c} = \frac{M^2 - m^2}{\sqrt{s}} \tag{A.4}$$

since

$$E_{A_c} + E_{\pi_c} = \sqrt{s} \tag{A.5}$$

Adding and subtracting A.4 and A.5 gives the centre of mass energy of the recoil nucleus

$$E_{A_c} = \frac{s + M^2 - m^2}{2\sqrt{s}} \tag{A.6}$$

and the centre of mass energy of the pion

$$E_{\pi_c} = \frac{s + m^2 - M^2}{2\sqrt{s}} \tag{A.7}$$

A.2 Pion Decay

The neutral π-meson (π^0) has a rest mass of approximately 264 electron masses and decays into two photons in 98.8 % of decays [77]. This is represented schematically in Figure A.2 where E_π is the energy of the moving π^0 and $\underline{P_\pi}$ is its momentum; E_1 $\left(\underline{P_1}\right)$ and E_2 $\left(\underline{P_2}\right)$ are the energies (momenta) of the two decay photons, and θ_1 and θ_2 are the photon directions relative to the direction of motion of the pion. From the conservation of energy and momentum

$$\begin{aligned} E_\pi &= E_1 + E_2 \\ \vec{P_\pi} &= \vec{P_1} + \vec{P_2} \end{aligned} \tag{A.8}$$

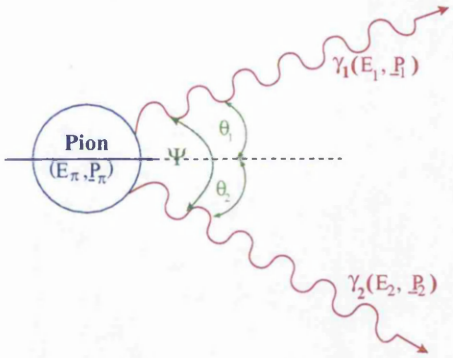

Figure A.2: **Pion decay:** The π^0 meson decays into two photons.

A.2.1 Pion Mass Reconstruction

For photons $P = E$, so if m is the rest-mass of the pion, then

$$\begin{aligned} m^2 &= E_\pi^2 - P_\pi^2 \\ &= (E_1^2 + E_2^2 + 2E_1E_2) - \left(P_1^2 + P_2^2 + 2\vec{P_1} \cdot \vec{P_2}\right) \\ &= 2E_1E_2\,(1 - \cos\psi) \\ &= 4E_1E_2 \sin^2 \tfrac{\psi}{2} \end{aligned} \tag{A.9}$$

where $\psi = \theta_1 + \theta_2 =$ opening angle between the pion decay photons.

A.2.2 Decay Photon Opening Angle

Defining X as

$$X = \frac{E_1 - E_2}{E_1 + E_2} = \frac{E_1 - E_2}{E_\pi} \tag{A.10}$$

or equivalently

$$\begin{aligned} E_1 &= \tfrac{E_\pi}{2}\,(1 + X) \\ E_2 &= \tfrac{E_\pi}{2}\,(1 - X) \end{aligned} \tag{A.11}$$

then

$$E_1E_2 = \tfrac{E_\pi^2}{4}\,(1 - X^2) \tag{A.12}$$

From equation A.12 it is clear that the maximum value of E_1E_2 occurs when $X = 0$, i.e. when the energies of the two photons are equal and each have the value $\frac{E_\pi}{2}$. So

$$(E_1E_2)_{max} = \frac{E_\pi^2}{4} \tag{A.13}$$

Using the fourth equation of A.9, it follows that the minimum value of the opening angle ψ, which occurs when E_1E_2 has its maximum value, is given by

$$\sin\left(\frac{\psi_{min}}{2}\right) = \frac{m}{E_\pi} \tag{A.14}$$

A.3 The X-formula

Combining equations A.9 and A.12 one obtains

$$E_\pi^2 = \frac{4E_1E_2}{1-X^2} = \frac{4}{1-X^2} \cdot \frac{m^2}{2\left(1-\cos\psi\right)} \tag{A.15}$$

so that

$$E_\pi = \sqrt{\frac{2m^2}{\left(1-X^2\right)\left(1-\cos\psi\right)}} \tag{A.16}$$

and this relation is used to obtain the pion energy from the directions and energies of the two decay photons.

A.4 Calculating Incident Photon Energy from Pion Energy and Angle

GEANT3 simulations were performed for a range of discrete pion energy and pion angle combinations (section 3.4) but experimental cross sections were produced for incident photon energy and pion angle combinations (section 4.8). Therefore, it was necessary to calculate the photon energy that would have produced a pion of that energy assuming it was produced coherently.

Working in the lab frame (see Figure A.1), conservation of energy and momentum gives

$$E_\gamma + M = E_A + E_\pi \tag{A.17}$$

$$\overrightarrow{P_A} = \overrightarrow{P_\gamma} - \overrightarrow{P_\pi} \tag{A.18}$$

so that

$$\begin{aligned} P_A^2 &= P_\gamma^2 + P_\pi^2 - 2\overrightarrow{P_\gamma} \cdot \overrightarrow{P_\pi} \\ &= E_\gamma^2 + P_\pi^2 - 2E_\gamma P_\pi \cos\theta_\pi \end{aligned} \tag{A.19}$$

Combining equation A.17 and A.19 gives

$$M^2 = E_A^2 - P_A^2 = \left(E_\gamma + M - E_\pi\right)^2 - \left(E_\gamma^2 + P_\pi^2 - 2E_\gamma P_\pi \cos\theta_\pi\right) \tag{A.20}$$

from which

$$E_\gamma = \frac{ME_\pi - \frac{1}{2}m^2}{M - E_\pi + \sqrt{E_\pi^2 - m^2}\cos\theta_\pi} \tag{A.21}$$

Appendix B

Calculation of Light Path for Implementation of Light Collection in GEANT3

The position of each barium fluoride in TAPS is defined by three angles, two offset distances, and the distance from the centre of the coordinate axes. The distance offsets and the rotation around the central axis of the TAPS block do not affect the equation of its planar front face (or the plane of the photomultiplier tube photocathodes) so we need only consider θ, ϕ.

In Figure B.1 the coordinates of P, $(x_p,\ y_p,\ z_p)$, are $(R\cos\phi\sin\theta,\ R\sin\phi,\ R\cos\phi\cos\theta)$. So, the direction cosines of $\overrightarrow{OP}$ are $(\cos\phi\sin\theta,\ \sin\phi,\ \cos\phi\cos\theta)$.

The equation of the front plane of a block (through P) is [121]

$$x\cos\phi\sin\theta + y\sin\phi + z\cos\phi\cos\theta = R \tag{B.1}$$

where R is the perpendicular distance from the target to the geometrical centre of the front face of the TAPS block.

Similarly, the equation of the photomultiplier photocathode plane is

$$x\cos\phi\sin\theta + y\sin\phi + z\cos\phi\cos\theta = R + L \tag{B.2}$$

where L is the distance from the front surface to the photocathode.

Using the standard formula for the distance from a point to a plane [121], the perpendicular distance from a point $(x,\ y,\ z)$ inside the barium fluorides to the photocathode plane is

$$d = |x\cos\phi\sin\theta + y\sin\phi + z\cos\phi\cos\theta - (L - R)| \tag{B.3}$$

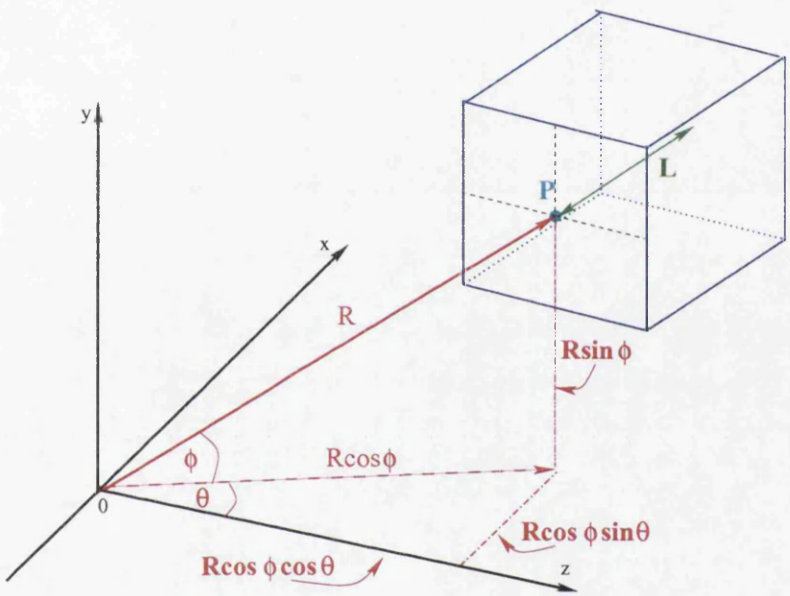

Figure B.1: **TAPS Geometry** for GEANT.

Appendix C

Pion Energy Difference Fits

The methods used to fit the pion energy difference distributions for ^{16}O and ^{208}Pb are given in the following table. Fit methods 1-4 are described in section 4.7.2. Numbers in brackets are (peak position; width of Gaussian) where v means that the fit was allowed to determine the value. NF means that no Fermi function was fitted (fit method 3 never used a Fermi function).

E_γ Range	^{16}O		^{208}Pb	
[MeV]	θ_π Range [°]	Fit Type	θ_π Range [°]	Fit Type
135-140	5-155	1		
140-145	5-20	1	5-145	1
	20-30	2		
	30-160	1		
145-150	5-165	1	5-125	1
150-155	10-65	1	4-44	1
	65-75	2	44-46	3 (0.0; 2.0)
	75-155	1	46-52	1
			52-62	3 (0.0; 2.4)
			64-106	1
			106-108	3 (0.0; 2.0)
155-160	5-100	1	4-10	1
	100-125	4	10-14	2
	125-150	1	14-44	1
			44-64	3 (0.0; 2.7)
			64-94	1
			94-108	3 (0.0; 3.3)
160-170	0-30	1	2-10	1
	30-75	4	10-30	2
	75-80	1	30-34	1
	80-135	4	34-38	2
	135-165	4 (0.0; 2.5)	38-86	1
			86-96	3 (0.0; 3.0)
170-180	0-75	4 (1.0; 3.0)	0-16	1
	75-110	4	16-26	2
	110-180	4 (0.0; 2.5)	26-82	1
			82-96	3 (0.7; 3.6)
180-190	0-75	4 (v; 3.5)	0-12	1
	75-95	4	12-30	2
	95-180	4 (0.3; 3.5)	30-74	1
			74-126	3(-0.5; 4.0)
190-200	0-70	4 (v; 4.0)	0-2	3 (-0.5; 4.0)
	70-85	4	2-14	1
	85-180	4 (0.0; 4.0)	14-22	2
			22-32	1

E_γ Range	^{16}O		^{208}Pb	
[MeV]	θ_π Range [°]	Fit Type	θ_π Range [°]	Fit Type
			32-44	3 (0.8; 5.3)
			44-68	1
			68-108	3 (-1.2; 4.0)
200-220	0-30	4 (3.0;5.5)	0-58	1
	30-45	4 (v; 5.5)	58-128	3 (-3.0;6.0)
	45-80	4		
	80-180	4 (-2.2; 5.5)		
220-240	0-60	4 (NF)	2-30	1
	60-65	4 (v; 8.0; NF)	30-104	3 (5.0; 6.2)
	65-70	4 (v; 6.2; NF)		
	70-180	4 (-2.2; 6.2; NF)		
240-260	0-55	4 (NF)	2-26	1
	55-65	4 (v; 9.5; NF)	26-98	3 (5.0; 7.0)
	65-180	4 (-0.7; 6.2; NF)		
260-280	0-45	4 (NF)	0-24	1
	45-60	4 (4.0; 8.0; NF)	24-96	3 (4.0; 8.0)
	60-150	4 (4.0; 5.4; NF)		
280-300	0-35	4 (NF)	0-14	1
	35-60	4 (3.2; 8.3; NF)	14-98	3 (4.0; 10.0)
	60-150	4 (3.2; 6.2; NF)		
300-320	0-30	4 (NF)	0-92	3 (4.0; 10.0)
	30-60	4 (1.2; 9.8; NF)		
	60-100	4 (1.2; 8.3; NF)		
	100-140	4 (1.2; 4.9; NF)		
320-340	0-25	4 (NF)	0-76	3 (4.0; 10.0)
	25-40	4 (0.6; 10.4; NF)		
	40-65	4 (0.6; 9.8; NF)		
	65-125	4 (0.6; 7.6; NF)		
340-360	0-15	4 (NF)	0-60	3 (4.0; 10.0)
	15-125	3 (3.5; v)		
360-380	0-105	3 (3.5; v)	0-58	3 (4.0; 10.0)

Appendix D

Inspection of the Pion Energy Difference Fits for the Incoherent Contribution from ^{16}O

As discussed in section 5.1.3, unexpected structure is observed in the incoherent cross sections, in particular a deep minimum in the cross section at $\theta_\pi \sim 50°$ for photon energies of 170-220 MeV with weaker angular variations at other photon energies. No real physics explanation for this minimum could be found. We concluded that this "structure" is a feature of our equipment and/or analysis.

The detection efficiencies used for the incoherent cross sections are those calculated for the coherent, i.e. pion energy was converted to incident photon energy assuming coherent pion production. Therefore for the incoherent events a pion energy ~6 MeV too large was used. However, the detection efficiency shows no sharp changes with energy that would explain the observed incoherent shape, see Figure 3.9.

Plots of the incoherent area with the coherent peak position from the pion energy difference fits show that the minima in the incoherent cross sections are usually correlated with shifts in the coherent peak position (see Figure D.1). The coherent peak is known to change shape with incident photon energy and pion angle and different types of fit were used for different incident photon energy, pion angle combinations, see section 4.7.2. The regions where large changes in incoherent area are seen in Figures D.1(a)-(c) correspond to regions where the coherent peak shape has a tail on its right-hand side that is comparable in size to the tail at the left-hand side. Fitting a pion energy difference spectrum with one of the coherent+incoherent fits where if we did not expect the incoherent peak at around 6.5 MeV to contribute we would have fitted the coherent with two Gaussians, would result in a small reduction in the fitted coherent area since the additional area from the second, wider Gaussian is at most 10 % of the main Gaussian area. However, the effect on the incoherent area (which is

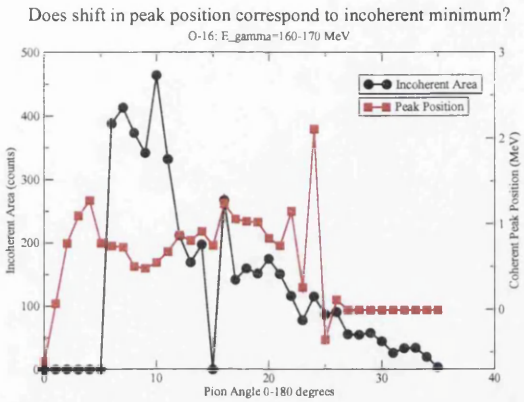

(a) $E_\gamma = 160 - 170MeV$

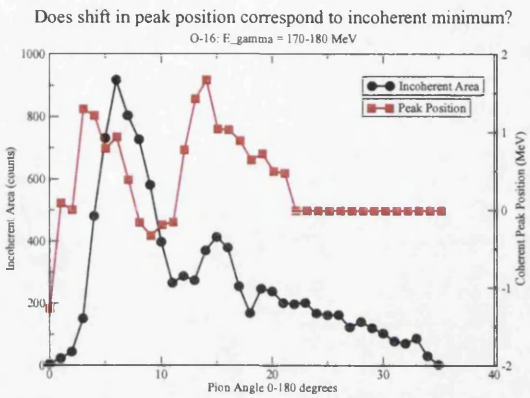

(b) $E_\gamma = 170 - 180MeV$

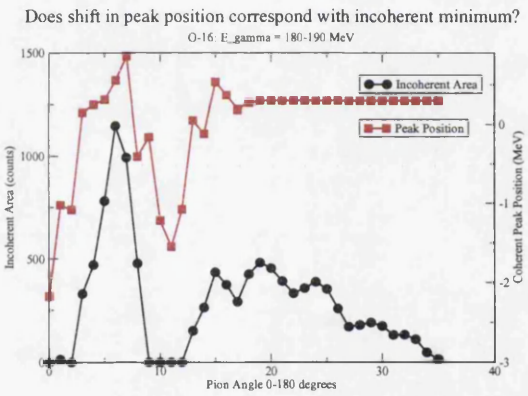

(c) $E_\gamma = 180 - 190MeV$

Figure D.1: **Effect of the coherent peak position on the incoherent cross section:** A systematic variation is seen both in the incoherent fitted area and the coherent fitted peak position with pion lab angle. However, the relationship between the two is not straightforward and is probably the result of a number of effects.

small) would be significant and would probably include coherent events. An example of such a case is shown in Figure D.2(a) where the peak has a broad base with the tail to the right of the peak. Figure D.2 gives examples of pion energy difference spectra for $E_\gamma = 170 - 180\,\text{MeV}$ in the three regions of interest in the differential cross section for this E_γ bin (see Figure 5.8): (a) corresponds to the incoherent cross section maximum region, (b) to the incoherent cross section minimum region, and (c) and (d) to where the incoherent cross section looks as expected. The pion energy difference peak is close to zero for all three cases so it is safe to attribute this to coherent pion photoproduction. The coherent peak in Figure D.2(a) has a slow fall-off on both sides of the peak and, if the incoherent peak 6.5 MeV below the coherent peak had not been seen to contribute, a two Gaussian fit would have been accepted as a good representation of the coherent events. However, a coherent+incoherent fit was used with the peak width fixed and thus results in an incoherent fit that includes coherent events and hence an incoherent cross section greater than the true one. Figure D.2(b) has a sharper coherent peak than (a). Again the fit with fixed width was used but this time the width chosen was possibly too wide resulting in too small an incoherent area and thus too small an incoherent cross section. Figure D.2(c) has a clear incoherent contribution and a fit where both the coherent peak position and width were allowed to vary gave a sensible incoherent cross section. The incoherent contribution dominates in Figure D.2(d) but the fit is still sensible and gives a sensible coherent and incoherent differential cross section.

The incoherent differential cross sections demonstrate the expected general trends and those at high pion angles are largely what would be expected. However, even here where the incoherent process dominates there are some "ripples" in the cross section that do not necessarily have a "real" physics basis. The cross sections at low pion angles are not reliable and probably include some coherent contribution. Therefore, in the region of the first maximum of the coherent differential cross section, the incoherent peak is probably larger than its true value and thus the corresponding coherent peak is slightly smaller than it should be.

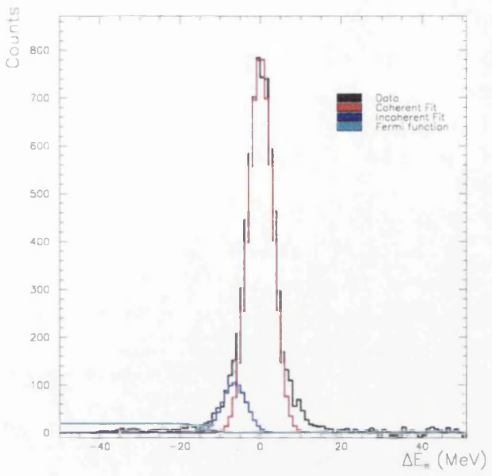

(a) $\theta_\pi = 35 - 40°$

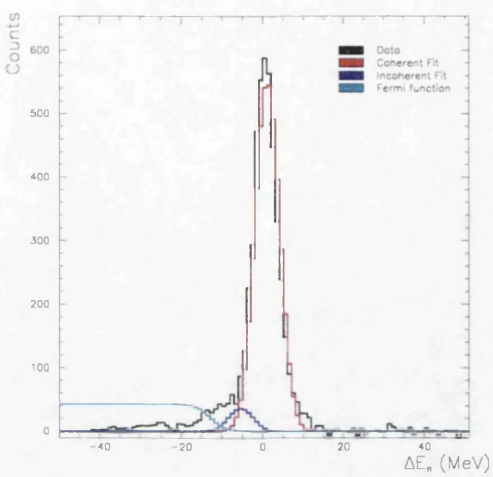

(b) $\theta_\pi = 65 - 70°$

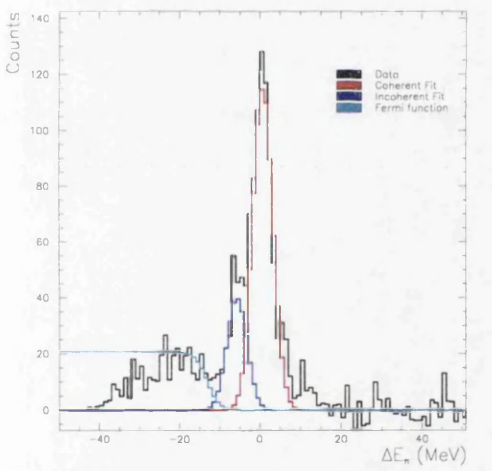

(c) $\theta_\pi = 95 - 100°$

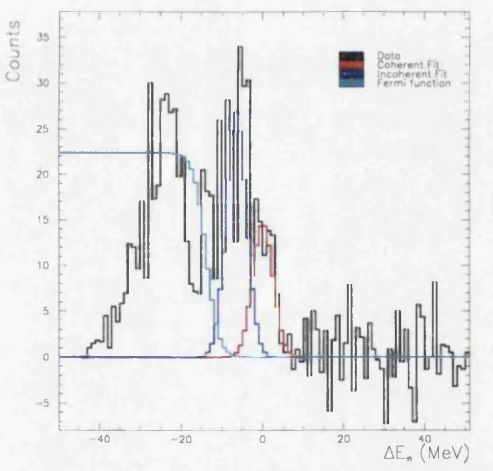

(d) $\theta_\pi = 120 - 125°$

Figure D.2: **Pion energy difference spectra for $E_\gamma = 170 - 180$ MeV:** (a) This spectrum has a broad base with the tail to the right of the peak comparable to the tail to the left and would be better fitted with two Gaussians; (b) This spectrum has a slightly sharper peak than the previous bin again the tail to the right of the peak is comparable to that to the left; (c) This spectrum has a clear incoherent peak ~ 6.5 MeV below the coherent peak; (d) the incoherent now dominates the coherent but the fit is still a good one.

Appendix E

Tables of cross sections

Table E.1 contains the total cross sections for the present ^{12}C, ^{16}O, ^{40}Ca, and ^{208}Pb experimental data. The differential cross sections are contained in Tables E.2-E.17.

Table E.1: **Total Cross Sections for ^{12}C, ^{16}O, ^{40}Ca and ^{208}Pb:**

E_γ [MeV]	σ [μb/sr] ^{12}C	^{16}O	^{40}Ca	^{208}Pb
135-140	2.92 ± 0.13	4.62 ± 0.18	12.50 ± 0.56	
140-145	16.85 ± 0.22	24.90 ± 0.39	54.01 ± 3.09	45.50 ± 2.57
145-150	38.19 ± 0.44	54.38 ± 0.97	117.33 ± 1.95	125.18 ± 4.85
150-155	68.30 ± 0.72	95.33 ± 1.81	188.99 ± 2.49	265.67 ± 6.84
155-160	102.36 ± 1.07	132.23 ± 2.80	269.28 ± 3.66	452.16 ± 12.53
160-170	148.79 ± 1.25	177.57 ± 3.53	369.92 ± 3.96	834.35 ± 12.28
170-180	216.50 ± 1.76	239.99 ± 4.56	538.09 ± 5.45	1229.27 ± 15.95
180-190	277.78 ± 2.29	318.55 ± 6.19	718.77 ± 6.93	1638.33 ± 21.73
190-200	370.43 ± 3.34	378.46 ± 7.85	821.11 ± 8.47	1915.75 ± 27.24
200-220	486.16 ± 3.96	447.49 ± 10.40	928.41 ± 9.32	2143.48 ± 30.83
220-240	547.02 ± 4.82	468.61 ± 10.60	825.58 ± 17.37	1906.11 ± 32.06
240-260	506.75 ± 4.92	467.86 ± 10.05	860.87 ± 9.95	1825.63 ± 28.52
260-280	507.34 ± 4.98	417.73 ± 8.50	764.69 ± 8.62	1580.23 ± 24.36
280-300	429.43 ± 4.31	361.91 ± 6.60	600.27 ± 6.90	1196.69 ± 17.14
300-320	333.52 ± 3.47	314.91 ± 5.45	470.53 ± 5.76	886.96 ± 13.71
320-340	250.68 ± 2.71	226.80 ± 3.81	356.68 ± 4.92	638.34 ± 11.02
340-360	176.75 ± 2.04	191.66 ± 3.21	252.26 ± 3.97	402.70 ± 7.90
360-380	155.64 ± 1.78	175.80 ± 3.17	210.98 ± 3.65	317.06 ± 7.49

E.1 Oxygen-16

Tables E.2-E.4 contain the differential cross sections for ^{16}O for the present experimental data.

Table E.2: **Differential Cross Sections for ^{16}O:**

θ_π [°]	$d\sigma/d\Omega$ [μb/sr] E_γ [MeV]					
	135 - 140	**140 - 145**	**145 - 150**	**150 - 155**	**155 - 160**	**160 - 170**
0 - 5						1.21 ± 0.41
5 - 10	0.15 ± 0.10	0.33 ± 0.17	0.75 ± 0.27		1.42 ± 0.53	3.97 ± 0.36
10 - 15	0.01 ± 0.01	0.70 ± 0.16	0.98 ± 0.23	1.97 ± 0.46	3.24 ± 0.59	7.28 ± 0.47
15 - 20	0.24 ± 0.10	0.76 ± 0.11	1.84 ± 0.26	4.12 ± 0.42	7.76 ± 0.64	12.66 ± 0.70
20 - 25	0.23 ± 0.08	1.09 ± 0.15	2.39 ± 0.27	6.51 ± 0.53	9.58 ± 0.72	17.23 ± 1.03
25 - 30	0.36 ± 0.09	1.53 ± 0.07	3.88 ± 0.36	8.57 ± 0.62	13.65 ± 0.85	21.61 ± 1.21
30 - 35	0.44 ± 0.10	1.85 ± 0.17	4.85 ± 0.39	10.01 ± 0.66	15.76 ± 1.05	25.43 ± 1.35
35 - 40	0.40 ± 0.10	2.34 ± 0.18	5.75 ± 0.43	11.32 ± 0.75	18.22 ± 1.18	28.60 ± 1.63
40 - 45	0.36 ± 0.07	2.45 ± 0.18	6.23 ± 0.44	13.15 ± 0.87	19.69 ± 1.37	32.07 ± 2.03
45 - 50	0.41 ± 0.07	2.57 ± 0.19	6.64 ± 0.47	13.53 ± 0.91	20.03 ± 1.51	32.17 ± 2.24
50 - 55	0.43 ± 0.08	2.90 ± 0.20	7.74 ± 0.55	14.61 ± 1.00	21.85 ± 1.72	32.89 ± 2.44
55 - 60	0.52 ± 0.08	3.14 ± 0.21	7.76 ± 0.55	14.62 ± 1.04	22.78 ± 1.77	32.23 ± 2.52
60 - 65	0.48 ± 0.07	3.32 ± 0.22	8.04 ± 0.57	14.27 ± 1.05	20.19 ± 1.67	29.63 ± 2.46
65 - 70	0.55 ± 0.09	3.36 ± 0.23	7.57 ± 0.56	13.52 ± 1.18	19.04 ± 1.71	28.11 ± 2.48
70 - 75	0.42 ± 0.07	3.20 ± 0.16	7.52 ± 0.57	14.41 ± 1.27	18.43 ± 1.72	24.91 ± 2.26
75 - 80	0.63 ± 0.10	2.90 ± 0.15	6.66 ± 0.53	12.68 ± 1.08	17.89 ± 1.72	23.07 ± 2.01
80 - 85	0.60 ± 0.09	2.85 ± 0.21	6.20 ± 0.50	11.21 ± 0.99	16.91 ± 1.69	17.35 ± 1.60
85 - 90	0.61 ± 0.09	2.73 ± 0.20	6.47 ± 0.51	8.82 ± 0.83	12.61 ± 1.35	13.67 ± 1.35
90 - 95	0.46 ± 0.08	2.64 ± 0.19	5.15 ± 0.43	8.55 ± 0.79	9.96 ± 1.08	10.43 ± 1.15
95 - 100	0.49 ± 0.08	2.38 ± 0.18	4.79 ± 0.40	6.65 ± 0.61	8.67 ± 0.91	8.86 ± 0.93
100 - 105	0.41 ± 0.07	2.19 ± 0.17	4.26 ± 0.35	6.26 ± 0.57	6.57 ± 0.75	7.20 ± 0.78
105 - 110	0.37 ± 0.06	1.78 ± 0.14	3.33 ± 0.29	4.69 ± 0.43	5.65 ± 0.70	5.44 ± 0.58
110 - 115	0.35 ± 0.07	1.79 ± 0.15	2.98 ± 0.28	3.91 ± 0.40	4.49 ± 0.61	3.55 ± 0.42
115 - 120	0.28 ± 0.08	1.45 ± 0.13	2.62 ± 0.26	3.36 ± 0.38	3.10 ± 0.54	3.21 ± 0.47
120 - 125	0.29 ± 0.07	1.33 ± 0.12	1.92 ± 0.20	2.69 ± 0.33	2.86 ± 0.57	1.84 ± 0.34
125 - 130	0.30 ± 0.08	0.92 ± 0.10	1.48 ± 0.19	2.17 ± 0.29	2.34 ± 0.38	1.54 ± 0.46
130 - 135	0.27 ± 0.09	0.76 ± 0.10	0.95 ± 0.18	1.86 ± 0.27	1.23 ± 0.27	1.01 ± 0.18
135 - 140	0.12 ± 0.07	0.71 ± 0.09	0.74 ± 0.14	1.01 ± 0.21	1.30 ± 0.27	0.68 ± 0.17
140 - 145	0.09 ± 0.01	0.48 ± 0.07	0.54 ± 0.13	0.75 ± 0.27	0.66 ± 0.23	0.47 ± 0.14
145 - 150	0.07 ± 0.01	0.47 ± 0.10	0.51 ± 0.22	0.83 ± 0.16	0.36 ± 0.20	0.42 ± 0.12
150 - 155		0.27 ± 0.09	0.42 ± 0.18	0.52 ± 0.16		0.09 ± 0.12
155 - 160		0.28 ± 0.12	0.32 ± 0.12			0.15 ± 0.10
160 - 165			0.24 ± 0.02			0.17 ± 0.13
165 - 170						
170 - 175						
175 - 180						

Table E.3: **Differential Cross Sections for ^{16}O:**

θ_π [o]	$d\sigma/d\Omega$ [μb/sr] E_γ [MeV]					
	170 - 180	**180 - 190**	**190-200**	**200-220**	**220-240**	**240-260**
0 - 5	2.96 ± 0.53	3.86 ± 0.61	4.21 ± 0.73	2.53 ± 1.15	17.64 ± 2.85	28.56 ± 2.91
5 - 10	5.84 ± 0.46	9.18 ± 0.76	10.75 ± 1.50	13.75 ± 1.43	56.40 ± 4.34	55.74 ± 3.36
10 - 15	12.12 ± 0.64	20.28 ± 1.05	26.61 ± 1.66	38.47 ± 2.57	143.77 ± 10.16	105.11 ± 5.03
15 - 20	20.04 ± 0.96	28.65 ± 1.46	43.55 ± 2.53	70.70 ± 3.92	146.62 ± 7.40	182.73 ± 7.99
20 - 25	27.35 ± 1.32	43.20 ± 2.19	64.18 ± 3.37	90.43 ± 4.73	174.15 ± 8.43	209.48 ± 9.28
25 - 30	33.85 ± 1.69	55.86 ± 2.98	80.19 ± 4.52	102.31 ± 5.66	182.52 ± 9.09	210.05 ± 10.06
30 - 35	41.02 ± 2.17	61.18 ± 3.57	89.16 ± 5.54	117.44 ± 8.75	187.20 ± 10.33	196.51 ± 10.77
35 - 40	46.91 ± 2.74	68.40 ± 4.34	98.57 ± 6.50	140.96 ± 9.74	178.12 ± 11.47	187.00 ± 12.34
40 - 45	49.55 ± 3.23	76.43 ± 5.11	104.01 ± 7.13	142.17 ± 10.36	158.31 ± 12.33	155.40 ± 12.49
45 - 50	52.05 ± 3.58	79.20 ± 5.42	105.31 ± 7.51	130.29 ± 10.06	120.51 ± 11.46	113.49 ± 10.97
50 - 55	49.54 ± 3.50	70.84 ± 5.04	86.63 ± 6.45	107.42 ± 8.79	87.79 ± 9.45	73.52 ± 8.17
55 - 60	47.42 ± 3.49	63.92 ± 4.71	77.07 ± 6.01	90.87 ± 7.73	63.67 ± 7.00	24.40 ± 3.19
60 - 65	46.08 ± 3.52	62.24 ± 4.72	71.00 ± 5.69	70.33 ± 6.63	39.65 ± 4.35	24.95 ± 3.20
65 - 70	40.41 ± 3.20	52.18 ± 4.06	55.18 ± 4.46	46.90 ± 4.97	21.90 ± 2.35	13.07 ± 1.57
70 - 75	32.28 ± 2.61	41.62 ± 3.30	39.88 ± 3.52	35.17 ± 4.13	10.27 ± 1.19	5.67 ± 0.84
75 - 80	24.81 ± 2.03	27.60 ± 2.32	25.72 ± 2.59	25.10 ± 4.67	5.68 ± 0.78	2.23 ± 0.58
80 - 85	19.26 ± 1.66	20.98 ± 1.88	18.90 ± 2.44	10.87 ± 1.15	1.32 ± 0.54	5.81 ± 0.72
85 - 90	15.30 ± 1.42	15.35 ± 1.50	10.94 ± 1.04	4.45 ± 0.67	0.53 ± 0.50	9.21 ± 1.09
90 - 95	11.16 ± 1.17	9.40 ± 1.07	5.73 ± 0.65	1.75 ± 0.49	0.65 ± 0.54	10.53 ± 1.29
95 - 100	7.96 ± 0.79	6.44 ± 0.64	2.00 ± 0.37	0.06 ± 0.49	1.22 ± 0.51	8.04 ± 1.11
100 - 105	5.53 ± 0.59	3.04 ± 0.43	0.49 ± 0.27	1.11 ± 0.45	3.30 ± 0.63	6.23 ± 0.98
105 - 110	3.44 ± 0.41	2.00 ± 0.33	0.27 ± 0.29	1.38 ± 0.46	1.01 ± 0.46	7.35 ± 1.09
110 - 115	2.16 ± 0.29	1.79 ± 0.31	0.00±0.00	1.61 ± 0.45	1.99 ± 0.51	5.99 ± 0.85
115 - 120	1.25 ± 0.22	0.21 ± 0.21	0.00±0.00	2.74 ± 0.54	2.50 ± 0.47	4.72 ± 0.60
120 - 125	0.92 ± 0.17	0.00±0.00	0.74 ± 0.32	3.67 ± 0.53	3.80 ± 0.52	3.37 ± 0.43
125 - 130	0.66 ± 0.17	0.14 ± 0.21	0.90 ± 0.35	3.81 ± 0.52	3.82 ± 0.48	1.33 ± 0.27
130 - 135	0.43 ± 0.13	0.28 ± 0.20	0.80 ± 0.32	3.38 ± 0.48	2.34 ± 0.37	0.45 ± 0.18
135 - 140	0.00±0.00	0.19 ± 0.18	1.03 ± 0.26	2.63 ± 0.39	1.39 ± 0.32	0.07 ± 0.17
140 - 145	0.06 ± 0.10	0.36 ± 0.16	0.53 ± 0.20	1.61 ± 0.33	0.61 ± 0.27	0.86 ± 0.20
145 - 150	0.06 ± 0.06	0.04 ± 0.15	0.50 ± 0.20	0.87 ± 0.25	0.27 ± 0.23	0.00±0.00
150 - 155	0.08 ± 0.09	0.15 ± 0.15	0.33 ± 0.19	1.24 ± 0.28	0.24 ± 0.24	0.01 ± 0.11
155 - 160	0.14 ± 0.09	0.34 ± 0.14	0.00±0.00	0.25 ± 0.22	0.00±0.00	0.00±0.00
160 - 165	0.09 ± 0.10	0.00±0.00	0.19 ± 0.16	0.76 ± 0.24	0.04 ± 0.16	0.11 ± 0.09
165 - 170	0.23 ± 0.12	0.00±0.00		0.03 ± 0.21		0.00±0.00
170 - 175	0.00±0.00	0.15 ± 0.24		0.10 ± 0.24		0.00±0.00
175 - 180	0.26 ± 0.32	0.07 ± 0.35		0.37 ± 0.48		0.14 ± 0.13

Table E.4: **Differential Cross Sections for ^{16}O:**

θ_π [°]	$d\sigma/d\Omega$ [μb/sr] E_γ [MeV] 260-280	280-300	300-320	320-340	340-360	360-380
0 - 5	42.32 ± 2.92	47.73 ± 2.78	46.90 ± 2.66	28.77 ± 1.85	11.06 ± 1.00	4.75 ± 0.84
5 - 10	78.85 ± 3.81	85.73 ± 3.88	85.04 ± 4.03	78.60 ± 3.93	48.85 ± 2.52	44.15 ± 2.47
10 - 15	134.14 ± 5.57	136.55 ± 5.56	148.14 ± 6.46	150.85 ± 7.26	118.38 ± 6.06	126.27 ± 6.63
15 - 20	211.41 ± 8.31	184.12 ± 7.09	206.74 ± 8.35	192.70 ± 8.46	192.90 ± 9.24	188.25 ± 9.32
20 - 25	235.95 ± 9.67	236.71 ± 9.30	248.34 ± 9.76	204.43 ± 8.46	155.82 ± 6.92	153.35 ± 7.10
25 - 30	235.43 ± 10.92	230.68 ± 10.29	229.27 ± 9.79	171.60 ± 7.28	104.72 ± 4.60	94.09 ± 4.30
30 - 35	221.15 ± 12.03	208.90 ± 10.82	212.94 ± 10.31	122.81 ± 5.72	72.02 ± 3.38	57.59 ± 2.79
35 - 40	189.86 ± 12.19	171.51 ± 10.10	117.35 ± 6.51	52.10 ± 2.95	43.94 ± 2.53	35.93 ± 2.17
40 - 45	143.41 ± 10.90	96.23 ± 6.65	50.32 ± 3.33	12.62 ± 1.20	25.19 ± 1.76	23.27 ± 1.76
45 - 50	85.80 ± 7.63	43.36 ± 3.62	14.81 ± 1.46	7.41 ± 0.97	19.04 ± 1.56	19.82 ± 1.72
50 - 55	31.29 ± 3.27	14.44 ± 1.56	6.20 ± 0.96	13.70 ± 1.33	20.52 ± 1.77	20.08 ± 1.83
55 - 60	8.15 ± 1.20	6.17 ± 0.97	5.88 ± 0.89	11.78 ± 1.19	16.59 ± 1.53	16.90 ± 1.66
60 - 65	3.90 ± 0.75	3.81 ± 0.70	5.16 ± 0.76	3.62 ± 0.65	9.30 ± 0.90	7.97 ± 0.87
65 - 70	0.00±0.00	2.98 ± 0.39	6.52 ± 0.75	5.83 ± 0.61	6.00 ± 0.58	4.03 ± 0.47
70 - 75	2.84 ± 0.52	4.70 ± 0.50	5.10 ± 0.63	4.81 ± 0.51	3.64 ± 0.37	2.16 ± 0.28
75 - 80	2.02 ± 0.47	4.22 ± 0.53	2.49 ± 0.46	4.02 ± 0.43	2.41 ± 0.26	0.92 ± 0.15
80 - 85	2.65 ± 0.48	4.31 ± 0.52	2.54 ± 0.41	1.39 ± 0.27	1.17 ± 0.17	0.78 ± 0.14
85 - 90	5.41 ± 0.66	4.59 ± 0.54	2.02 ± 0.35	0.80 ± 0.23	1.02 ± 0.16	0.19 ± 0.09
90 - 95	5.07 ± 0.69	3.90 ± 0.50	1.03 ± 0.28	0.38 ± 0.18	0.71 ± 0.14	0.12 ± 0.13
95 - 100	4.79 ± 0.69	3.70 ± 0.52	0.33 ± 0.25	0.51 ± 0.16	0.72 ± 0.15	0.25 ± 0.11
100 - 105	1.76 ± 0.39	1.18 ± 0.28	0.57 ± 0.16	0.63 ± 0.16	0.55 ± 0.15	0.19 ± 0.13
105 - 110	1.15 ± 0.30	1.67 ± 0.28	0.11 ± 0.11	0.00±0.00	0.18 ± 0.08	
110 - 115	1.84 ± 0.31	0.00±0.00	0.30 ± 0.11	0.33 ± 0.11	0.20 ± 0.07	
115 - 120	1.13 ± 0.21	0.19 ± 0.12	0.45 ± 0.11	0.33 ± 0.10	0.15 ± 0.06	
120 - 125	0.19 ± 0.13	0.31 ± 0.12	0.09 ± 0.06	0.20 ± 0.08	0.04 ± 0.04	
125 - 130	0.07 ± 0.11	0.00±0.00	0.15 ± 0.06			
130 - 135	0.00±0.00	0.06 ± 0.10	0.00±0.00			
135 - 140	0.09 ± 0.09	0.00±0.00	0.11 ± 0.05			
140 - 145	0.00±0.00	0.04 ± 0.08				
145 - 150	0.11 ± 0.09	0.13 ± 0.08				
150 - 155						
155 - 160						
160 - 165						
165 - 170						
170 - 175						
175 - 180						

E.2 Lead-208

Tables E.5-E.11 contain the differential cross sections for ^{208}Pb for the present experimental data.

Table E.5: **Differential Cross Sections for ^{208}Pb: E_γ =140-150 MeV**

θ_π [°]	$d\sigma/d\Omega$ μb/sr E_γ [MeV] 140-145	145-150
0 - 5		
5 - 10	5.75 ± 2.51	11.25 ± 3.97
10 - 15	6.94 ± 2.38	26.32 ± 5.87
15 - 20	6.56 ± 1.87	39.45 ± 6.15
20 - 25	9.25 ± 1.93	43.65 ± 5.49
25 - 30	11.61 ± 1.82	43.43 ± 6.23
30 - 35	10.02 ± 1.58	35.70 ± 3.76
35 - 40	10.58 ± 1.42	31.14 ± 3.14
40 - 45	7.32 ± 1.23	21.48 ± 2.73
45 - 50	2.61 ± 0.74	14.26 ± 2.29
50 - 55	2.08 ± 0.66	6.27 ± 1.67
55 - 60	1.42 ± 0.76	2.17 ± 1.13
60 - 65	0.57 ± 2.83	1.65 ± 1.06
65 - 70	1.14 ± 1.08	3.84 ± 1.18
70 - 75	2.33 ± 0.68	5.85 ± 1.80
75 - 80	3.17 ± 0.81	8.98 ± 1.92
80 - 85	4.82 ± 0.90	12.29 ± 1.92
85 - 90	5.15 ± 0.94	17.49 ± 2.50
90 - 95	4.80 ± 0.90	12.21 ± 2.68
95 - 100	4.41 ± 0.83	12.93 ± 1.93
100 - 105	4.06 ± 0.99	9.04 ± 2.16
105 - 110	4.15 ± 0.91	6.68 ± 1.63
110 - 115	4.74 ± 0.96	6.12 ± 1.61
115 - 120	2.36 ± 0.79	4.95 ± 1.64
120 - 125	3.22 ± 0.93	3.88 ± 2.16
125 - 130	2.90 ± 0.83	
130 - 135	2.50 ± 0.78	
135 - 140	0.88 ± 0.74	
140 - 145	0.83 ± 1.52	
145 - 150		
150 - 155		
155 - 160		
160 - 165		
165 - 170		
170 - 175		
175 - 180		

Table E.6: **Differential Cross Sections for ^{208}Pb: E_γ = 150-190 MeV**

θ_π [°]	$d\sigma/d\Omega$ [μb/sr] E_γ [MeV] 150-155	155-160	160-170	170-180	180-190
0 - 2			45.10 ± 18.09	82.71 ± 22.01	64.79 ± 22.84
2 - 4			53.38 ± 11.04	162.88 ± 18.83	167.06 ± 22.35
4 - 6	28.87 ± 9.83	57.82 ± 14.11	135.69 ± 15.50	208.87 ± 18.42	262.98 ± 24.30
6 - 8	26.52 ± 9.78	64.87 ± 13.71	192.61 ± 16.28	316.86 ± 21.58	431.65 ± 30.09
8 - 10	49.94 ± 10.43	114.10 ± 16.91	252.03 ± 17.92	441.58 ± 25.96	613.30 ± 37.35
10 - 12	63.41 ± 17.21	131.62 ± 22.57	376.69 ± 24.86	555.92 ± 30.41	800.55 ± 44.99
12 - 14	75.44 ± 13.11	179.42 ± 27.13	402.83 ± 25.50	728.29 ± 38.16	1091.08 ± 61.10
14 - 16	83.92 ± 14.90	191.46 ± 19.80	494.35 ± 31.69	816.79 ± 42.31	1191.03 ± 63.01
16 - 18	100.10 ± 12.59	200.41 ± 19.14	505.02 ± 29.64	911.61 ± 47.77	1319.56 ± 71.92
18 - 20	98.80 ± 13.64	242.69 ± 22.45	537.41 ± 33.21	938.45 ± 49.08	1377.12 ± 77.81
20 - 22	131.53 ± 13.93	205.99 ± 19.67	536.92 ± 32.00	959.57 ± 50.47	1303.63 ± 72.35
22 - 24	130.76 ± 14.34	235.50 ± 19.55	522.61 ± 31.30	889.55 ± 49.10	1243.07 ± 69.86
24 - 26	135.60 ± 12.98	255.70 ± 20.12	499.38 ± 29.56	778.10 ± 42.80	1104.78 ± 63.19
26 - 28	144.97 ± 12.99	251.87 ± 19.27	443.08 ± 27.21	697.44 ± 38.99	951.91 ± 58.64
28 - 30	108.57 ± 10.47	205.57 ± 16.20	417.85 ± 31.34	609.27 ± 35.34	761.88 ± 49.37
30 - 32	109.38 ± 10.38	207.52 ± 16.06	337.13 ± 22.28	479.75 ± 29.07	592.79 ± 39.12
32 - 34	95.83 ± 9.05	169.08 ± 14.17	306.62 ± 19.23	381.20 ± 24.40	400.66 ± 28.33
34 - 36	88.17 ± 8.53	147.13 ± 12.52	273.22 ± 18.31	308.57 ± 21.51	305.62 ± 23.72
36 - 38	88.08 ± 8.82	138.93 ± 12.68	193.88 ± 15.49	212.10 ± 16.23	195.09 ± 16.72
38 - 40	69.02 ± 7.38	96.99 ± 9.81	154.69 ± 12.10	139.15 ± 12.16	119.21 ± 12.08
40 - 42	49.64 ± 5.81	76.88 ± 8.67	118.36 ± 10.66	112.28 ± 10.46	98.12 ± 12.66
42 - 44	36.23 ± 4.99	63.73 ± 8.07	61.02 ± 8.01	52.26 ± 6.27	90.71 ± 10.82
44 - 46	28.33 ± 5.76	41.43 ± 8.79	44.26 ± 7.43	42.68 ± 5.93	88.32 ± 10.16
46 - 48	20.76 ± 3.88	12.68 ± 5.25	31.84 ± 4.86	45.96 ± 5.85	112.69 ± 11.75
48 - 50	19.06 ± 3.52	10.97 ± 5.27	40.47 ± 5.71	50.41 ± 7.29	135.77 ± 13.32
50 - 52	12.17 ± 4.43	18.15 ± 6.56	21.91 ± 4.31	77.71 ± 9.02	152.90 ± 14.72
52 - 54	5.47 ± 3.82	3.92 ± 4.30	25.50 ± 4.63	80.06 ± 8.89	197.60 ± 18.16
54 - 56	2.16 ± 3.05	10.82 ± 5.16	38.07 ± 5.69	109.58 ± 10.84	201.23 ± 18.47
56 - 58	7.45 ± 3.70	12.84 ± 6.25	49.17 ± 6.44	124.71 ± 12.33	224.59 ± 20.73
58 - 60	7.01 ± 3.42	7.32 ± 5.80	57.59 ± 7.20	159.82 ± 15.02	219.17 ± 20.40
60 - 62	5.56 ± 1.94	34.51 ± 9.12	66.57 ± 7.86	170.72 ± 16.15	196.08 ± 18.49
62 - 64	11.82 ± 3.35	17.61 ± 7.05	85.02 ± 10.11	167.23 ± 16.07	224.44 ± 20.99
64 - 66	8.09 ± 2.61	36.79 ± 7.19	89.18 ± 10.60	172.50 ± 16.56	186.44 ± 17.80
66 - 68	19.78 ± 4.15	28.75 ± 9.57	84.76 ± 10.28	156.72 ± 15.41	160.66 ± 15.97
68 - 70	18.43 ± 4.47	37.59 ± 7.88	99.44 ± 11.83	130.02 ± 13.25	136.84 ± 14.19
70 - 72	13.07 ± 3.88	25.71 ± 6.05	97.21 ± 11.38	120.69 ± 12.71	83.38 ± 9.56
72 - 74	21.67 ± 5.26	41.29 ± 8.45	91.38 ± 11.15	110.96 ± 12.01	80.19 ± 10.23

Table E.7: **Differential Cross Sections for ^{208}Pb: E_γ = 150-190 MeV cont.**

θ_π [°]	$d\sigma/d\Omega$ [μb/sr] E_γ [MeV] 150-155	155-160	160 - 170	170 - 180	180 - 190
74 - 76	22.73 ± 7.91	48.57 ± 9.00	91.18 ± 10.64	79.84 ± 9.40	40.29 ± 7.48
76 - 78	28.01 ± 5.72	39.55 ± 9.39	69.50 ± 8.90	72.15 ± 8.86	25.43 ± 5.80
78 - 80	21.16 ± 5.07	53.78 ± 10.00	65.68 ± 8.31	62.13 ± 7.83	17.71 ± 5.47
80 - 82	25.48 ± 6.01	48.26 ± 9.91	62.95 ± 8.50	36.15 ± 5.74	11.74 ± 5.25
82 - 84	24.83 ± 5.08	31.86 ± 7.25	60.51 ± 8.10	23.38 ± 5.39	24.30 ± 6.23
84 - 86	33.63 ± 6.05	48.28 ± 9.36	44.90 ± 6.74	22.42 ± 5.51	12.56 ± 5.94
86 - 88	18.82 ± 4.25	48.80 ± 28.98	27.94 ± 6.54	12.70 ± 4.37	14.97 ± 4.75
88 - 90	21.31 ± 5.50	20.22 ± 8.10	18.25 ± 5.85	5.33 ± 5.33	17.52 ± 5.67
90 - 92	25.24 ± 5.17	18.78 ± 6.47	11.40 ± 5.13	4.21 ± 3.69	25.27 ± 6.67
92 - 94	19.04 ± 4.89	24.14 ± 6.73	10.35 ± 4.97	9.76 ± 4.56	33.36 ± 6.88
94 - 96	22.15 ± 5.59	14.67 ± 6.03	6.15 ± 4.30	6.97 ± 4.30	33.91 ± 7.43
96 - 98	13.34 ± 3.82	21.64 ± 9.48			28.97 ± 6.55
98 - 100	18.88 ± 4.67	8.08 ± 6.88			36.94 ± 7.80
100 - 102	15.01 ± 5.91	14.02 ± 7.78			32.50 ± 7.05
102 - 104	13.73 ± 4.17	15.13 ± 7.87			14.59 ± 4.83
104 - 106	10.60 ± 3.09	16.59 ± 7.23			17.29 ± 5.11
106 - 108		2.45 ± 4.56			8.47 ± 4.76
108 - 110		5.50 ± 6.57			25.66 ± 6.44
110 - 112					4.17 ± 3.40
112 - 114					16.86 ± 5.65
114 - 116					2.61 ± 3.07
116 - 118					9.72 ± 4.72
118 - 120					6.54 ± 4.41
120 - 122					10.06 ± 4.83
122 - 124					4.28 ± 3.47
124 - 126					11.13 ± 4.45

Table E.8: **Differential Cross Sections for ^{208}Pb: E_γ = 190-280 MeV**

θ_π [°]	$d\sigma/d\Omega$ [μb/sr] E_γ [MeV] 190-200	200-220	220-240	240-260	260-280
0 - 2	24.51 ± 27.21	71.18 ± 33.40			599.01 ± 128.13
2 - 4	184.86 ± 28.67	183.18 ± 58.75	475.47 ± 126.95	1219.64 ± 324.91	1281.11 ± 182.17
4 - 6	381.32 ± 34.05	560.67 ± 53.04	1427.69 ± 187.31	2077.16 ± 220.59	2123.60 ± 188.79
6 - 8	639.93 ± 68.02	1041.35 ± 81.75	2639.94 ± 275.35	2884.85 ± 197.04	2826.62 ± 267.96
8 - 10	837.10 ± 57.42	1598.09 ± 114.42	3289.86 ± 258.91	3322.46 ± 254.17	3320.78 ± 206.22
10 - 12	1168.66 ± 70.12	1806.67 ± 140.92	3520.11 ± 246.06	3571.73 ± 208.95	3544.99 ± 215.18
12 - 14	1350.99 ± 78.36	2238.97 ± 153.37	3618.89 ± 231.25	3771.70 ± 208.95	3254.44 ± 153.28
14 - 16	1629.83 ± 93.39	2500.54 ± 161.29	3389.12 ± 202.33	3257.62 ± 170.05	2639.90 ± 147.83
16 - 18	1767.88 ± 101.12	2438.07 ± 148.72	3036.76 ± 173.70	2749.31 ± 140.49	2050.35 ± 104.57
18 - 20	1752.22 ± 99.18	2314.50 ± 135.17	2378.94 ± 132.74	1947.09 ± 99.69	1368.16 ± 76.62
20 - 22	1583.53 ± 93.11	1976.24 ± 115.21	1710.18 ± 95.43	1306.51 ± 69.38	789.75 ± 38.07
22 - 24	1602.29 ± 91.33	1626.37 ± 94.98	1108.25 ± 62.62	742.57 ± 43.07	382.58 ± 31.91
24 - 26	1369.74 ± 79.99	1195.95 ± 70.68	728.74 ± 43.21	371.00 ± 24.78	183.91 ± 13.15
26 - 28	1058.14 ± 69.84	867.76 ± 53.89	395.63 ± 26.63	168.29 ± 12.64	171.24 ± 12.91
28 - 30	788.68 ± 56.63	541.02 ± 36.09	199.71 ± 15.04	132.17 ± 11.05	250.35 ± 17.75
30 - 32	552.64 ± 47.80	318.13 ± 24.81	125.85 ± 10.82	196.62 ± 15.34	374.54 ± 25.54
32 - 34	349.42 ± 29.70	195.23 ± 16.36	136.51 ± 12.38	264.11 ± 20.23	441.52 ± 31.13
34 - 36	201.96 ± 20.07	142.78 ± 14.29	201.38 ± 17.16	347.23 ± 26.95	475.97 ± 34.84
36 - 38	120.57 ± 14.81	229.98 ± 19.73	236.46 ± 20.93	454.93 ± 35.85	441.67 ± 34.05
38 - 40	83.76 ± 11.79	226.83 ± 24.16	346.50 ± 29.87	455.44 ± 38.48	330.07 ± 27.92
40 - 42	73.68 ± 10.82	286.58 ± 29.12	357.37 ± 32.52	409.96 ± 37.35	221.31 ± 21.18
42 - 44	138.80 ± 15.93	320.64 ± 33.19	327.98 ± 32.50	319.31 ± 31.93	123.64 ± 14.70
44 - 46	167.22 ± 17.07	325.86 ± 33.04	331.88 ± 35.18	208.52 ± 24.33	87.34 ± 12.33
46 - 48	241.39 ± 25.23	338.77 ± 33.47	187.14 ± 23.37	78.74 ± 13.17	75.10 ± 11.93
48 - 50	281.99 ± 29.13	337.07 ± 33.57	145.91 ± 20.54	72.25 ± 13.29	109.50 ± 15.97
50 - 52	281.29 ± 25.51	318.17 ± 30.35	73.35 ± 13.85	36.94 ± 9.45	90.13 ± 13.91
52 - 54	309.30 ± 28.12	260.16 ± 28.44	45.24 ± 10.65	33.79 ± 8.71	93.84 ± 14.92
54 - 56	253.66 ± 24.88	208.77 ± 25.55	33.28 ± 8.33	40.04 ± 10.50	60.32 ± 11.66
56 - 58	252.54 ± 25.05	165.67 ± 19.42	22.35 ± 7.02	41.39 ± 11.95	85.60 ± 16.79
58 - 60	259.93 ± 28.85	104.72 ± 13.26	17.09 ± 6.31	94.90 ± 17.59	47.46 ± 11.95
60 - 62	225.57 ± 22.71	71.08 ± 10.01	24.63 ± 8.55	63.68 ± 14.23	45.05 ± 10.34
62 - 64	196.43 ± 20.59	55.98 ± 8.67	13.07 ± 6.15	56.77 ± 13.04	41.97 ± 9.46
64 - 66	133.75 ± 19.05	58.31 ± 9.08	34.79 ± 8.25	29.09 ± 8.95	19.85 ± 6.66
66 - 68	90.54 ± 12.46	48.82 ± 7.77	29.83 ± 7.92	50.67 ± 11.01	23.09 ± 7.75
68 - 70	53.47 ± 8.75	53.63 ± 8.32	35.36 ± 8.62	28.50 ± 8.00	11.82 ± 5.49
70 - 72	36.65 ± 7.22	49.47 ± 8.56	33.19 ± 8.68	10.67 ± 6.57	23.99 ± 6.14
72 - 74	22.36 ± 5.92	80.14 ± 11.24	53.21 ± 10.35	10.03 ± 5.56	19.40 ± 5.95

Table E.9: **Differential Cross Sections for ^{208}Pb: E_γ = 190-280 MeV cont.**

θ_π [°]	$d\sigma/d\Omega$ [μb/sr] E_γ [MeV] 190-200	200-220	220-240	240-260	260-280
74 - 76	28.24 ± 6.55	89.05 ± 11.99	21.65 ± 6.09	13.39 ± 5.48	6.97 ± 4.41
76 - 78	19.90 ± 5.75	93.89 ± 12.80	20.68 ± 6.20	21.05 ± 5.86	11.43 ± 4.82
78 - 80	25.52 ± 6.67	98.94 ± 13.38	11.02 ± 5.59	11.38 ± 4.83	15.58 ± 5.00
80 - 82	39.08 ± 7.99	75.99 ± 10.54	10.05 ± 5.86	8.54 ± 4.78	17.59 ± 5.37
82 - 84	64.55 ± 10.21	67.35 ± 9.86	9.36 ± 4.97	4.86 ± 4.21	17.05 ± 5.39
84 - 86	80.22 ± 11.95	70.19 ± 10.25	1.22 ± 5.20	13.48 ± 5.15	10.54 ± 4.73
86 - 88	42.23 ± 7.72	58.82 ± 8.90	5.37 ± 4.17	14.95 ± 5.98	22.25 ± 6.27
88 - 90	66.32 ± 10.14	34.46 ± 6.16	14.48 ± 5.97	17.09 ± 7.28	10.30 ± 5.10
90 - 92	66.22 ± 10.19	25.56 ± 5.02	5.48 ± 5.00	28.12 ± 8.75	8.01 ± 4.60
92 - 94	42.39 ± 7.78	32.38 ± 5.90	8.72 ± 5.32	10.63 ± 5.53	7.04 ± 5.39
94 - 96	40.91 ± 7.50	21.58 ± 4.90	7.19 ± 4.84	5.66 ± 5.50	10.03 ± 4.88
96 - 98	57.58 ± 9.65	14.06 ± 4.09	4.97 ± 5.01	12.04 ± 6.27	12.62 ± 5.80
98 - 100	37.89 ± 7.70	11.71 ± 3.65	6.29 ± 4.07		
100 - 102	29.30 ± 6.48	14.89 ± 4.27	8.35 ± 5.21		
102 - 104	6.20 ± 4.10	18.95 ± 4.61			
104 - 106	3.05 ± 3.43	25.00 ± 5.26			
106 - 108	9.14 ± 4.64	8.56 ± 3.50			
108 - 110		9.29 ± 3.20			
110 - 112		25.29 ± 5.21			
112 - 114		15.27 ± 4.17			
114 - 116		9.26 ± 3.70			
116 - 118		9.47 ± 3.85			
118 - 120		18.18 ± 4.39			
120 - 122		13.17 ± 4.10			
122 - 124		12.77 ± 3.86			
124 - 126		8.15 ± 3.53			

Table E.10: **Differential Cross Sections for ^{208}Pb: E_γ = 280-380 MeV**

θ_π [°]	$d\sigma/d\Omega$ [μb/sr] E_γ [MeV] 280-300	300-320	320-340	340-360	360-380
0 - 2	697.72 ± 106.75	463.02 ± 77.74	217.18 ± 49.97	45.78 ± 22.62	
2 - 4	1378.55 ± 99.39	989.24 ± 77.46	624.05 ± 60.85	296.44 ± 36.25	149.19 ± 26.44
4 - 6	2151.21 ± 157.04	1895.98 ± 112.43	1170.82 ± 81.25	648.35 ± 53.81	466.14 ± 40.55
6 - 8	2663.68 ± 140.38	2314.95 ± 134.27	1779.50 ± 109.26	1058.38 ± 70.81	696.40 ± 52.30
8 - 10	2921.10 ± 148.39	2467.89 ± 141.90	1947.45 ± 118.21	1222.36 ± 82.51	914.88 ± 68.98
10 - 12	2891.68 ± 144.01	2241.98 ± 127.34	1687.59 ± 109.19	1036.57 ± 71.94	789.72 ± 59.23
12 - 14	2504.09 ± 119.19	1719.12 ± 95.41	1284.90 ± 79.02	785.03 ± 54.48	427.60 ± 37.37
14 - 16	1844.71 ± 89.28	1177.43 ± 63.70	707.09 ± 44.90	399.26 ± 29.27	215.96 ± 23.17
16 - 18	1148.24 ± 56.84	638.02 ± 34.64	344.94 ± 23.77	137.66 ± 13.56	92.11 ± 11.98
18 - 20	608.82 ± 31.54	250.71 ± 16.02	95.06 ± 9.39	94.71 ± 10.45	138.89 ± 14.89
20 - 22	278.32 ± 16.62	121.73 ± 9.51	110.25 ± 10.20	136.05 ± 11.66	185.25 ± 16.65
22 - 24	135.27 ± 10.17	124.86 ± 10.09	169.46 ± 13.68	177.82 ± 13.64	219.46 ± 18.17
24 - 26	158.54 ± 11.53	198.61 ± 13.51	228.81 ± 15.92	204.95 ± 14.78	189.53 ± 15.33
26 - 28	233.43 ± 15.71	288.73 ± 17.96	285.49 ± 18.01	146.18 ± 11.08	138.79 ± 12.39
28 - 30	372.47 ± 24.25	333.76 ± 20.96	259.07 ± 16.94	142.47 ± 10.74	84.76 ± 8.75
30 - 32	406.81 ± 26.73	337.67 ± 22.12	195.36 ± 13.73	89.52 ± 8.00	44.53 ± 6.27
32 - 34	404.55 ± 27.23	264.80 ± 18.35	138.81 ± 11.19	58.48 ± 6.37	37.77 ± 5.84
34 - 36	354.92 ± 26.05	181.95 ± 14.23	90.75 ± 8.89	49.07 ± 5.92	56.84 ± 7.75
36 - 38	260.08 ± 20.88	112.27 ± 11.07	73.05 ± 8.42	56.74 ± 6.86	62.22 ± 8.62
38 - 40	148.57 ± 14.47	85.43 ± 9.04	81.04 ± 9.00	76.59 ± 8.82	88.63 ± 10.85
40 - 42	112.00 ± 12.96	90.14 ± 10.40	86.66 ± 9.52	76.29 ± 9.42	72.40 ± 10.39
42 - 44	62.73 ± 9.46	98.62 ± 10.60	88.39 ± 10.37	79.10 ± 10.29	63.76 ± 10.46
44 - 46	97.62 ± 12.47	129.86 ± 13.93	105.35 ± 12.25	74.53 ± 9.95	31.98 ± 8.49
46 - 48	120.76 ± 15.30	132.25 ± 15.13	86.15 ± 11.03	45.38 ± 7.85	59.87 ± 10.49
48 - 50	149.99 ± 18.75	121.69 ± 15.04	74.33 ± 10.49	42.77 ± 7.48	38.52 ± 8.96
50 - 52	121.59 ± 17.09	79.38 ± 13.11	59.57 ± 9.89	34.77 ± 7.14	37.76 ± 8.62
52 - 54	115.55 ± 16.26	63.50 ± 10.24	33.29 ± 7.11	59.66 ± 9.92	31.13 ± 8.31
54 - 56	50.19 ± 10.59	32.08 ± 7.26	41.29 ± 7.84	29.65 ± 6.68	30.41 ± 9.00
56 - 58	38.72 ± 9.77	17.64 ± 5.73	40.04 ± 8.68	33.47 ± 7.14	27.36 ± 8.59
58 - 60	41.72 ± 10.28	23.55 ± 7.06	31.13 ± 7.29	18.92 ± 5.40	
60 - 62	30.91 ± 8.81	36.56 ± 8.16	20.97 ± 5.40		
62 - 64	18.39 ± 6.95	20.51 ± 6.31	12.13 ± 4.58		
64 - 66	12.18 ± 5.51	19.41 ± 5.38	9.08 ± 3.88		
66 - 68	33.33 ± 8.10	9.50 ± 3.86	4.85 ± 3.01		
68 - 70	25.19 ± 6.57	13.84 ± 4.20	8.98 ± 3.67		
70 - 72	11.47 ± 4.66	19.20 ± 5.08	8.24 ± 3.30		
72 - 74	13.96 ± 5.66	8.88 ± 3.70	5.67 ± 3.16		

Table E.11: **Differential Cross Sections for ^{208}Pb: E_γ = 280-380 MeV cont.**

θ_π [°]	$d\sigma/d\Omega$ μb/sr E_γ [MeV]				
	280 - 300	**300 - 320**	**320 - 340**	**340 - 360**	**360 - 380**
74 - 76	9.60 ± 4.82	9.37 ± 4.35	2.51 ± 2.05		
76 - 78	1.85 ± 3.28	3.77 ± 3.15			
78 - 80	7.05 ± 4.63	5.77 ± 3.10			
80 - 82	10.07 ± 4.30	5.68 ± 3.00			
82 - 84	2.65 ± 2.98	10.15 ± 3.74			
84 - 86	3.97 ± 4.20	7.05 ± 3.34			
86 - 88	6.72 ± 3.72	3.27 ± 3.12			
88 - 90	9.12 ± 4.19	5.85 ± 2.91			
90 - 92	5.74 ± 3.38	3.19 ± 2.74			
92 - 94	7.99 ± 4.30				
94 - 96	1.75 ± 3.01				
96 - 98	4.91 ± 4.46				

E.3 Carbon-12

Tables E.12-E.14 contain the differential cross sections for ^{12}C for the present experimental data.

Table E.12: **Differential Cross Sections for ^{12}C:**

θ_π [°]	$d\sigma/d\Omega$ [μb/sr] E_γ [MeV]					
	135 - 140	**140 - 145**	**145 - 150**	**150 - 155**	**155 - 160**	**160 - 170**
0 - 5		0.20 ± 0.13	0.24 ± 0.06	0.25 ± 0.19	0.19 ± 0.17	0.80 ± 0.18
5 - 10	0.14 ± 0.05	0.09 ± 0.07	0.42 ± 0.19	0.39 ± 0.17	1.18 ± 0.26	2.21 ± 0.18
10 - 15	0.14 ± 0.17	0.19 ± 0.07	0.66 ± 0.14	1.11 ± 0.18	2.63 ± 0.28	4.21 ± 0.22
15 - 20	0.10 ± 0.07	0.47 ± 0.07	1.00 ± 0.14	2.73 ± 0.26	3.78 ± 0.28	7.18 ± 0.30
20 - 25	0.18 ± 0.08	0.50 ± 0.08	1.64 ± 0.05	3.24 ± 0.24	6.00 ± 0.34	10.16 ± 0.39
25 - 30	0.14 ± 0.06	0.87 ± 0.10	2.20 ± 0.18	4.38 ± 0.27	8.10 ± 0.37	13.75 ± 0.48
30 - 35	0.21 ± 0.06	1.12 ± 0.09	2.67 ± 0.19	6.31 ± 0.32	9.54 ± 0.40	16.51 ± 0.56
35 - 40	0.22 ± 0.05	1.35 ± 0.09	3.28 ± 0.18	7.14 ± 0.33	10.82 ± 0.45	19.01 ± 0.65
40 - 45	0.27 ± 0.05	1.70 ± 0.10	4.20 ± 0.22	8.43 ± 0.36	13.08 ± 0.52	20.76 ± 0.71
45 - 50	0.24 ± 0.05	1.71 ± 0.10	4.57 ± 0.22	8.62 ± 0.37	13.28 ± 0.53	22.56 ± 0.77
50 - 55	0.27 ± 0.05	2.00 ± 0.11	4.54 ± 0.22	9.39 ± 0.39	14.98 ± 0.60	23.65 ± 0.80
55 - 60	0.38 ± 0.06	2.00 ± 0.11	5.11 ± 0.24	10.14 ± 0.42	15.03 ± 0.59	23.60 ± 0.80
60 - 65	0.34 ± 0.05	1.98 ± 0.11	4.66 ± 0.22	9.46 ± 0.40	14.71 ± 0.60	22.46 ± 0.76
65 - 70	0.47 ± 0.07	2.20 ± 0.12	5.57 ± 0.25	9.15 ± 0.39	14.33 ± 0.60	20.55 ± 0.72
70 - 75	0.36 ± 0.06	2.03 ± 0.11	5.09 ± 0.24	8.89 ± 0.39	12.80 ± 0.58	20.76 ± 0.73
75 - 80	0.40 ± 0.06	2.10 ± 0.11	4.47 ± 0.23	8.62 ± 0.39	12.94 ± 0.57	19.13 ± 0.67
80 - 85	0.27 ± 0.06	2.13 ± 0.11	4.34 ± 0.22	7.82 ± 0.37	12.72 ± 0.59	16.10 ± 0.60
85 - 90	0.31 ± 0.05	1.91 ± 0.11	4.36 ± 0.21	7.01 ± 0.34	10.92 ± 0.54	14.22 ± 0.54
90 - 95	0.32 ± 0.06	1.93 ± 0.10	3.77 ± 0.20	6.13 ± 0.31	9.49 ± 0.50	11.66 ± 0.48
95 - 100	0.25 ± 0.05	1.57 ± 0.09	3.53 ± 0.18	5.98 ± 0.30	8.15 ± 0.46	10.38 ± 0.44
100 - 105	0.33 ± 0.06	1.50 ± 0.09	3.18 ± 0.16	4.96 ± 0.26	7.93 ± 0.40	9.49 ± 0.40
105 - 110	0.21 ± 0.04	1.23 ± 0.08	2.58 ± 0.16	4.57 ± 0.26	6.41 ± 0.38	8.30 ± 0.37
110 - 115	0.18 ± 0.05	1.20 ± 0.08	2.71 ± 0.17	3.55 ± 0.23	4.71 ± 0.29	5.89 ± 0.29
115 - 120	0.18 ± 0.04	1.00 ± 0.07	2.30 ± 0.14	3.16 ± 0.21	4.12 ± 0.30	4.97 ± 0.27
120 - 125	0.16 ± 0.03	0.79 ± 0.07	1.82 ± 0.13	2.94 ± 0.22	3.53 ± 0.25	4.63 ± 0.25
125 - 130	0.14 ± 0.07	0.94 ± 0.07	1.50 ± 0.12	2.53 ± 0.20	3.06 ± 0.27	3.10 ± 0.19
130 - 135	0.17 ± 0.08	0.62 ± 0.06	1.16 ± 0.13	2.01 ± 0.17	1.93 ± 0.19	2.66 ± 0.20
135 - 140	0.11 ± 0.06	0.54 ± 0.06	1.10 ± 0.10	1.30 ± 0.14	1.48 ± 0.16	1.78 ± 0.16
140 - 145	0.08 ± 0.05	0.41 ± 0.06	0.81 ± 0.08	1.16 ± 0.14	1.62 ± 0.18	1.49 ± 0.14
145 - 150	0.05 ± 0.02	0.36 ± 0.05	0.56 ± 0.08	0.85 ± 0.11	0.69 ± 0.12	0.95 ± 0.15
150 - 155	0.01 ± 0.01	0.27 ± 0.04	0.25 ± 0.05	0.53 ± 0.10	0.78 ± 0.13	0.69 ± 0.58
155 - 160		0.21 ± 0.05	0.24 ± 0.06	0.50 ± 0.14	0.34 ± 0.17	0.48 ± 0.15
160 - 165		0.13 ± 0.05	0.20 ± 0.05	0.25 ± 0.12	0.20 ± 0.31	
165 - 170			0.11 ± 0.07	0.11 ± 0.01	0.32 ± 0.48	
170 - 175				0.15 ± 0.15	-0.01 ± -0.02	
175 - 180						

Table E.13: **Differential Cross Sections for ^{12}C:**

θ_π [MeV]	$d\sigma/d\Omega$ [μb/sr] E_γ [MeV] 170-180	180-190	190-200	200-220	220-240	240-260
0 - 5	1.14 ± 0.25	2.11 ± 0.30	1.88 ± 0.28			
5 - 10	3.25 ± 0.21	5.01 ± 0.32	7.14 ± 0.49	12.23 ± 0.62	32.80 ± 1.34	52.41 ± 1.89
10 - 15	7.38 ± 0.32	11.01 ± 0.83	15.68 ± 1.08	32.28 ± 1.13	64.19 ± 2.12	91.04 ± 2.91
15 - 20	12.58 ± 0.47	18.54 ± 0.69	29.31 ± 1.49	61.24 ± 1.96	106.94 ± 3.32	139.85 ± 4.34
20 - 25	18.20 ± 0.66	28.26 ± 0.96	44.87 ± 1.62	85.27 ± 2.64	131.59 ± 4.08	170.12 ± 5.27
25 - 30	23.38 ± 0.77	37.31 ± 1.23	60.06 ± 2.16	104.06 ± 3.23	150.03 ± 4.50	175.95 ± 5.45
30 - 35	29.11 ± 0.96	42.71 ± 1.41	64.14 ± 2.12	119.20 ± 3.70	170.18 ± 5.11	183.42 ± 5.69
35 - 40	31.96 ± 1.05	49.04 ± 1.57	72.55 ± 2.39	124.00 ± 3.84	178.84 ± 5.37	198.30 ± 6.15
40 - 45	35.10 ± 1.16	51.45 ± 1.65	75.68 ± 2.42	116.16 ± 3.60	179.41 ± 5.56	195.95 ± 6.07
45 - 50	36.86 ± 1.22	54.71 ± 1.75	81.63 ± 2.61	108.00 ± 3.35	169.05 ± 5.24	160.51 ± 5.14
50 - 55	36.63 ± 1.17	52.57 ± 1.68	75.47 ± 2.41	98.70 ± 3.06	106.28 ± 3.51	91.24 ± 3.28
55 - 60	38.53 ± 1.27	48.99 ± 1.57	67.46 ± 2.09	89.79 ± 2.87	78.98 ± 2.69	49.96 ± 1.90
60 - 65	37.29 ± 1.23	48.63 ± 1.56	67.16 ± 2.15	77.83 ± 2.41	53.89 ± 1.89	40.07 ± 1.52
65 - 70	34.25 ± 1.13	44.73 ± 1.43	56.60 ± 3.11	59.14 ± 1.89	42.13 ± 1.47	24.36 ± 0.97
70 - 75	28.93 ± 0.95	41.02 ± 1.31	51.42 ± 1.65	53.30 ± 1.76	33.95 ± 1.22	13.86 ± 0.61
75 - 80	25.60 ± 0.87	33.97 ± 1.12	40.96 ± 1.31	43.95 ± 1.45	27.94 ± 1.03	8.21 ± 0.42
80 - 85	21.82 ± 0.74	26.83 ± 0.91	34.17 ± 1.13	32.60 ± 1.11	19.80 ± 0.79	5.86 ± 0.32
85 - 90	18.78 ± 0.68	20.96 ± 0.73	24.41 ± 0.83	21.51 ± 0.77	12.42 ± 0.56	6.21 ± 0.38
90 - 95	16.32 ± 0.60	18.11 ± 0.67	16.57 ± 0.65	14.90 ± 0.58	8.37 ± 0.44	6.12 ± 0.41
95 - 100	13.82 ± 0.54	11.59 ± 0.53	11.17 ± 0.48	9.51 ± 0.42	6.77 ± 0.39	5.83 ± 0.41
100 - 105	10.29 ± 0.42	7.52 ± 0.40	6.83 ± 0.33	7.10 ± 0.35	7.24 ± 0.42	4.62 ± 0.39
105 - 110	8.47 ± 0.37	6.51 ± 0.36	4.70 ± 0.27	5.02 ± 0.28	5.31 ± 0.37	3.12 ± 0.30
110 - 115	7.20 ± 0.35	4.50 ± 0.30	4.23 ± 0.29	4.39 ± 0.26	4.75 ± 0.35	3.96 ± 0.32
115 - 120	4.14 ± 0.21	2.72 ± 0.24	2.83 ± 0.20	3.71 ± 0.23	3.97 ± 0.50	4.06 ± 0.30
120 - 125	3.17 ± 0.26	2.27 ± 0.21	1.80 ± 0.17	3.59 ± 0.24	4.61 ± 0.31	2.74 ± 0.22
125 - 130	2.49 ± 0.21	1.27 ± 0.15	2.00 ± 0.23	3.64 ± 0.24	4.36 ± 0.28	2.56 ± 0.20
130 - 135	1.53 ± 0.19	1.06 ± 0.15	1.74 ± 0.18	3.00 ± 0.22	3.51 ± 0.25	1.38 ± 0.14
135 - 140	1.38 ± 0.16	0.81 ± 0.13	0.86 ± 0.10	2.31 ± 0.18	3.71 ± 0.32	0.81 ± 0.11
140 - 145	0.78 ± 0.11	0.63 ± 0.11	0.97 ± 0.11	1.99 ± 0.16	2.90 ± 0.26	0.63 ± 0.11
145 - 150	0.37 ± 0.09	0.18 ± 0.11	0.51 ± 0.08	1.70 ± 0.16	2.21 ± 0.22	0.89 ± 0.16
150 - 155	0.20 ± 0.07	0.26 ± 0.10	0.73 ± 0.15	1.33 ± 0.13	1.79 ± 0.20	
155 - 160	0.17 ± 0.08	0.21 ± 0.08	0.38 ± 0.07	0.65 ± 0.09	0.98 ± 0.17	
160 - 165		0.04 ± 0.09	0.25 ± 0.07		0.96 ± 0.13	
165 - 170					0.49 ± 0.10	
170 - 175					0.40 ± 0.10	
175 - 180						

Table E.14: **Differential Cross Sections for ^{12}C:**

θ_π [°]	$d\sigma/d\Omega$ [μb/sr] E_γ [MeV] 260-280	280-300	300-320	320-340	340-360	360-380
0 - 5		21.85 ± 1.38	17.10 ± 1.15	9.03 ± 0.82	4.99 ± 0.56	1.98 ± 0.18
5 - 10	59.12 ± 2.07	58.87 ± 2.18	55.50 ± 2.22	45.85 ± 1.88	29.79 ± 1.37	21.91 ± 1.05
10 - 15	105.83 ± 3.39	106.02 ± 3.60	104.12 ± 3.64	105.10 ± 4.20	84.22 ± 3.62	73.00 ± 3.21
15 - 20	164.14 ± 5.09	156.94 ± 5.02	152.44 ± 5.18	144.23 ± 5.19	119.77 ± 4.67	118.10 ± 4.61
20 - 25	190.99 ± 5.92	178.34 ± 5.53	160.19 ± 5.29	138.08 ± 4.83	112.39 ± 4.05	109.95 ± 4.07
25 - 30	207.23 ± 6.42	200.57 ± 6.22	169.50 ± 5.42	129.74 ± 4.28	91.92 ± 3.13	83.33 ± 2.83
30 - 35	220.85 ± 6.85	208.42 ± 6.46	171.27 ± 5.48	124.27 ± 4.10	79.32 ± 2.70	60.66 ± 2.00
35 - 40	214.98 ± 6.66	181.81 ± 5.82	133.10 ± 4.39	94.38 ± 3.21	58.90 ± 2.18	48.43 ± 1.70
40 - 45	183.82 ± 5.70	142.49 ± 4.56	94.62 ± 3.22	61.82 ± 2.16	39.41 ± 1.50	34.86 ± 1.25
45 - 50	137.65 ± 4.54	99.79 ± 3.39	63.88 ± 2.30	39.00 ± 1.48	27.22 ± 1.12	23.84 ± 0.88
50 - 55	77.72 ± 2.80	56.53 ± 2.15	37.54 ± 1.50	26.92 ± 1.08	20.57 ± 0.93	19.64 ± 0.75
55 - 60	40.41 ± 1.54	29.38 ± 1.18	22.63 ± 0.95	18.24 ± 0.82	14.04 ± 0.67	13.31 ± 0.52
60 - 65	29.38 ± 1.20	18.64 ± 0.78	12.89 ± 0.58	9.42 ± 0.46	7.02 ± 0.39	6.31 ± 0.26
65 - 70	16.04 ± 0.71	12.35 ± 0.57	8.60 ± 0.42	7.23 ± 0.36	5.36 ± 0.30	4.21 ± 0.17
70 - 75	9.89 ± 0.49	8.17 ± 0.41	7.19 ± 0.35	5.55 ± 0.29	3.62 ± 0.22	2.85 ± 0.12
75 - 80	6.19 ± 0.34	6.40 ± 0.33	6.75 ± 0.34	4.38 ± 0.25	3.12 ± 0.20	2.12 ± 0.09
80 - 85	6.83 ± 0.37	6.98 ± 0.36	6.11 ± 0.32	3.83 ± 0.23	1.67 ± 0.14	1.11 ± 0.05
85 - 90	7.33 ± 0.39	6.83 ± 0.36	5.43 ± 0.30	3.18 ± 0.20	1.57 ± 0.14	1.08 ± 0.06
90 - 95	8.25 ± 0.44	6.58 ± 0.36	4.15 ± 0.27	2.21 ± 0.18	1.34 ± 0.13	0.87 ± 0.06
95 - 100	6.25 ± 0.42	5.66 ± 0.36	3.20 ± 0.25	2.02 ± 0.18	0.66 ± 0.10	0.80 ± 0.07
100 - 105	5.15 ± 0.38	3.73 ± 0.30	2.68 ± 0.23	1.68 ± 0.18	1.11 ± 0.14	0.48 ± 0.04
105 - 110	4.50 ± 0.36	2.99 ± 0.27	2.04 ± 0.20	1.18 ± 0.15	0.76 ± 0.12	0.16 ± 0.02
110 - 115	4.47 ± 0.31	3.01 ± 0.24	1.31 ± 0.14	0.83 ± 0.11	0.11 ± 0.04	0.22 ± 0.03
115 - 120	2.77 ± 0.22	1.80 ± 0.17	1.10 ± 0.12	0.61 ± 0.09	0.31 ± 0.06	0.10 ± 0.01
120 - 125	2.16 ± 0.19	1.04 ± 0.12	0.56 ± 0.08	0.35 ± 0.06	0.18 ± 0.05	
125 - 130	1.25 ± 0.13	0.84 ± 0.11	0.36 ± 0.07	0.17 ± 0.05		
130 - 135	1.20 ± 0.13	0.76 ± 0.11	0.32 ± 0.06	0.14 ± 0.04		
135 - 140	0.79 ± 0.11	0.19 ± 0.06		0.09 ± 0.04		
140 - 145	0.84 ± 0.13	0.26 ± 0.07				
145 - 150		0.20 ± 0.07				
150 - 155		0.23 ± 0.08				
155 - 160		0.06 ± 0.04				
160 - 165						
165 - 170						
170 - 175						
175 - 180						

E.4 Calcium-40

Tables E.15-E.17 contain the differential cross sections for ^{40}Ca for the present experimental data.

Table E.15: **Differential Cross Sections for ^{40}Ca:**

θ_π [°]	$d\sigma/d\Omega$ [μb/sr] E_γ [MeV]					
	135 - 140	**140 - 145**	**145 - 150**	**150 - 155**	**155 - 160**	**160 - 170**
0 - 5			1.11 ± 0.59	2.26 ± 1.09	2.78 ± 1.47	5.47 ± 1.17
5 - 10	-0.09 ± -0.14	0.85 ± 0.53	2.40 ± 0.87	3.74 ± 0.83	9.01 ± 1.38	16.32 ± 1.16
10 - 15	0.08 ± 0.07	2.07 ± 0.99	4.34 ± 0.76	11.97 ± 1.39	18.24 ± 1.50	34.20 ± 1.61
15 - 20	0.30 ± 0.31	1.97 ± 0.86	7.60 ± 1.10	18.38 ± 1.36	30.22 ± 1.75	61.99 ± 2.36
20 - 25	0.87 ± 0.55	4.09 ± 1.31	11.49 ± 1.02	26.11 ± 1.67	41.98 ± 2.01	86.19 ± 3.10
25 - 30	1.14 ± 0.32	5.05 ± 1.46	15.18 ± 1.26	32.25 ± 1.64	55.16 ± 2.37	101.93 ± 3.57
30 - 35	0.83 ± 0.23	6.71 ± 1.75	19.69 ± 1.24	36.96 ± 1.70	60.83 ± 2.43	109.70 ± 3.62
35 - 40	1.10 ± 0.23	7.21 ± 1.82	21.25 ± 1.53	42.24 ± 1.86	70.56 ± 2.75	114.56 ± 3.90
40 - 45	1.59 ± 0.35	8.37 ± 2.05	22.37 ± 1.36	38.56 ± 1.70	65.67 ± 2.63	89.18 ± 3.12
45 - 50	1.55 ± 0.26	8.39 ± 1.93	23.80 ± 1.29	42.67 ± 1.83	62.85 ± 2.58	102.82 ± 3.70
50 - 55	2.11 ± 0.26	8.55 ± 1.89	21.94 ± 1.08	40.47 ± 1.74	62.47 ± 2.56	66.93 ± 2.61
55 - 60	1.22 ± 0.25	8.31 ± 1.89	20.58 ± 1.11	34.51 ± 1.55	58.50 ± 2.46	76.20 ± 3.12
60 - 65	1.87 ± 0.25	8.60 ± 1.94	19.33 ± 1.60	33.91 ± 1.53	45.41 ± 2.09	58.29 ± 2.22
65 - 70	2.11 ± 0.30	7.87 ± 1.79	18.67 ± 0.99	27.44 ± 1.37	33.41 ± 1.77	41.41 ± 1.78
70 - 75	1.62 ± 0.22	7.72 ± 1.79	15.81 ± 0.92	21.00 ± 1.20	28.69 ± 1.66	31.90 ± 1.47
75 - 80	1.65 ± 0.25	6.79 ± 1.64	13.58 ± 1.06	19.48 ± 1.19	22.67 ± 1.50	22.38 ± 1.16
80 - 85	1.42 ± 0.23	5.40 ± 1.40	11.29 ± 0.79	14.95 ± 1.05	18.11 ± 1.36	16.31 ± 1.03
85 - 90	1.34 ± 0.25	5.62 ± 1.43	8.31 ± 0.61	9.86 ± 0.86	9.65 ± 1.09	5.32 ± 0.79
90 - 95	1.26 ± 0.28	4.66 ± 1.22	6.00 ± 0.49	8.66 ± 0.78	8.08 ± 1.41	3.66 ± 0.76
95 - 100	1.07 ± 0.22	3.52 ± 1.00	5.36 ± 0.53	5.60 ± 0.69	5.01 ± 1.10	2.31 ± 0.58
100 - 105	0.91 ± 0.23	2.78 ± 0.82	4.32 ± 0.42	4.81 ± 0.68	4.12 ± 0.90	1.92 ± 0.55
105 - 110	0.85 ± 0.22	2.47 ± 0.79	3.61 ± 0.43	3.45 ± 0.56	3.28 ± 2.24	1.28 ± 0.75
110 - 115	0.54 ± 0.20	2.24 ± 0.74	2.00 ± 0.34	3.22 ± 0.67	1.69 ± 0.55	0.79 ± 0.78
115 - 120	0.65 ± 0.17	1.71 ± 0.62	1.94 ± 0.38	2.77 ± 0.65		1.36 ± 0.57
120 - 125	0.80 ± 0.37	1.30 ± 0.51	1.58 ± 0.32			1.38 ± 0.52
125 - 130	0.31 ± 0.17	0.71 ± 0.37	0.95 ± 0.28			1.97 ± 0.52
130 - 135	0.40 ± 0.16	0.63 ± 0.31	0.64 ± 0.63			2.50 ± 0.59
135 - 140		0.33 ± 0.36	0.47 ± 0.32			2.17 ± 0.55
140 - 145		0.58 ± 0.32	0.26 ± 0.77			2.54 ± 0.53
145 - 150		0.43 ± 0.31	0.21 ± 0.26			2.11 ± 0.52
150 - 155		0.37 ± 0.28	0.34 ± 0.26			0.84 ± 0.47
155 - 160		0.15 ± 0.14				0.30 ± 0.54
160 - 165						0.41 ± 0.61
165 - 170						
170 - 175						
175 - 180						

Table E.16: **Differential Cross Sections for ^{40}Ca:**

θ_π [MeV]	$d\sigma/d\Omega$ [μb/sr] E_γ [MeV] 170-180	180-190	190-200	200-220	220-240	240-260
0 - 5	12.60 ± 1.58	7.83 ± 1.39	14.02 ± 2.00	26.33 ± 2.82	63.96 ± 8.06	112.97 ± 8.02
5 - 10	28.06 ± 1.71	50.30 ± 2.41	57.68 ± 3.00	102.33 ± 5.32	260.68 ± 10.69	314.83 ± 11.33
10 - 15	61.51 ± 1.85	93.48 ± 3.46	138.71 ± 5.13	257.42 ± 8.75	460.43 ± 27.63	537.47 ± 17.20
15 - 20	100.51 ± 3.52	151.85 ± 5.16	227.30 ± 7.73	406.65 ± 12.61	601.91 ± 43.34	678.70 ± 23.75
20 - 25	128.65 ± 9.91	219.16 ± 7.01	317.50 ± 10.48	505.23 ± 15.66	589.64 ± 65.45	667.08 ± 22.01
25 - 30	156.09 ± 4.99	255.15 ± 8.16	366.33 ± 13.19	515.70 ± 15.99	504.26 ± 15.63	550.85 ± 19.83
30 - 35	163.83 ± 5.24	252.27 ± 8.07	341.20 ± 11.60	474.08 ± 14.70	395.33 ± 12.26	380.82 ± 12.19
35 - 40	165.30 ± 5.29	244.13 ± 7.81	312.24 ± 10.30	388.27 ± 12.04	285.85 ± 9.15	243.31 ± 8.03
40 - 45	159.77 ± 5.27	224.25 ± 7.40	257.16 ± 8.49	264.92 ± 8.21	177.78 ± 6.22	125.31 ± 4.76
45 - 50	139.82 ± 4.61	188.63 ± 6.22	208.78 ± 6.89	130.52 ± 4.57	81.68 ± 3.68	57.11 ± 2.97
50 - 55	113.01 ± 3.84	144.46 ± 4.91	143.09 ± 4.58	71.76 ± 2.87	30.19 ± 2.20	29.74 ± 2.08
55 - 60	88.99 ± 3.11	100.36 ± 3.51	74.50 ± 3.20	40.44 ± 1.86	12.51 ± 1.33	29.98 ± 2.25
60 - 65	70.86 ± 2.55	72.23 ± 2.96	47.58 ± 2.38	18.29 ± 1.06	12.65 ± 1.21	38.38 ± 2.46
65 - 70	50.52 ± 1.97	52.62 ± 2.37	28.78 ± 1.70	17.29 ± 1.09	18.17 ± 1.42	36.51 ± 2.19
70 - 75	33.62 ± 1.48	26.05 ± 1.49	15.86 ± 1.22	19.18 ± 1.11	18.22 ± 1.26	27.34 ± 1.72
75 - 80	20.37 ± 1.10	14.77 ± 1.20	13.78 ± 1.17	26.17 ± 1.41	19.93 ± 1.32	15.16 ± 1.15
80 - 85	12.60 ± 1.03	8.17 ± 0.83	15.26 ± 1.24	29.55 ± 1.57	18.66 ± 1.31	12.10 ± 0.97
85 - 90	6.26 ± 0.82	9.08 ± 0.90	14.43 ± 1.13	25.72 ± 1.36	13.40 ± 1.13	9.80 ± 0.98
90 - 95	5.08 ± 0.76	10.63 ± 0.97	20.37 ± 1.45	23.66 ± 1.30	7.42 ± 0.88	5.15 ± 0.80
95 - 100	3.79 ± 0.68	11.21 ± 0.94	15.02 ± 1.19	18.80 ± 1.13	2.96 ± 0.62	4.41 ± 0.90
100 - 105	5.27 ± 0.80	11.61 ± 1.03	13.06 ± 1.14	15.46 ± 0.99	4.77 ± 0.69	6.18 ± 0.90
105 - 110	7.14 ± 0.86	14.07 ± 1.10	12.10 ± 1.09	9.91 ± 0.83	3.41 ± 0.65	5.39 ± 1.01
110 - 115	8.78 ± 0.93	11.50 ± 1.02	13.80 ± 1.16	6.02 ± 0.63	2.97 ± 0.97	4.12 ± 0.83
115 - 120	9.63 ± 0.92	13.25 ± 1.10	10.11 ± 1.01	3.19 ± 0.46	1.83 ± 0.45	6.91 ± 0.84
120 - 125	10.08 ± 1.03	9.01 ± 0.89	8.39 ± 0.94	2.10 ± 0.44	3.03 ± 0.55	3.28 ± 0.51
125 - 130	6.83 ± 0.73	7.23 ± 0.82	4.69 ± 0.74	2.47 ± 0.41	2.75 ± 0.55	2.17 ± 0.43
130 - 135	7.59 ± 0.77	5.75 ± 0.73	3.47 ± 0.63	2.60 ± 0.40	1.04 ± 0.50	
135 - 140	7.42 ± 0.96	5.25 ± 0.68	2.06 ± 0.62		2.82 ± 0.59	
140 - 145	4.47 ± 0.64	2.05 ± 0.44			1.25 ± 0.40	
145 - 150	3.11 ± 0.50	1.12 ± 0.33			1.72 ± 0.42	
150 - 155	1.95 ± 0.39	2.07 ± 0.41				
155 - 160	1.05 ± 0.43	0.74 ± 0.25				
160 - 165		0.58 ± 0.28				
165 - 170						
170 - 175						
175 - 180						

Table E.17: **Differential Cross Sections for ^{40}Ca:**

θ_π [°]	$d\sigma/d\Omega$ [μb/sr] E_γ [MeV]					
	260-280	**280-300**	**300-320**	**320-340**	**340-360**	**360-380**
0 - 5	137.86 ± 9.51	127.65 ± 8.04	107.35 ± 6.76	66.45 ± 5.18	32.62 ± 3.59	12.46 ± 2.20
5 - 10	311.20 ± 11.51	355.76 ± 13.16	339.85 ± 13.25	278.10 ± 12.24	170.28 ± 8.00	126.82 ± 6.85
10 - 15	553.73 ± 19.93	546.52 ± 18.58	513.97 ± 18.50	486.88 ± 19.48	373.38 ± 15.68	318.57 ± 14.02
15 - 20	731.94 ± 23.42	622.80 ± 19.93	552.14 ± 19.32	476.35 ± 17.62	365.44 ± 14.98	313.95 ± 13.50
20 - 25	643.95 ± 19.96	491.07 ± 15.71	369.71 ± 12.20	269.11 ± 9.42	181.38 ± 7.07	146.70 ± 6.01
25 - 30	486.77 ± 15.09	347.93 ± 11.13	221.80 ± 7.32	121.20 ± 4.36	70.13 ± 2.81	50.43 ± 2.32
30 - 35	300.29 ± 9.61	191.41 ± 6.51	104.34 ± 3.76	56.22 ± 2.30	31.97 ± 1.47	25.58 ± 1.38
35 - 40	152.42 ± 5.33	78.18 ± 3.05	49.35 ± 2.12	34.84 ± 1.60	30.61 ± 1.56	34.87 ± 1.95
40 - 45	65.95 ± 2.90	38.85 ± 1.90	41.35 ± 1.98	44.07 ± 2.03	41.10 ± 2.06	38.52 ± 2.23
45 - 50	43.40 ± 2.30	58.03 ± 2.79	62.79 ± 2.83	52.33 ± 2.51	36.15 ± 2.17	31.70 ± 2.19
50 - 55	45.49 ± 2.64	63.04 ± 3.34	57.02 ± 2.91	44.42 ± 2.40	31.40 ± 1.92	24.73 ± 1.90
55 - 60	45.80 ± 2.93	44.50 ± 2.45	34.88 ± 2.16	21.96 ± 1.49	13.96 ± 1.21	14.35 ± 1.41
60 - 65	50.46 ± 2.83	30.34 ± 1.91	15.15 ± 1.17	8.98 ± 0.90	7.97 ± 0.83	5.82 ± 0.83
65 - 70	31.84 ± 1.91	14.96 ± 1.15	8.82 ± 0.82	7.01 ± 0.72	4.74 ± 0.57	3.95 ± 0.60
70 - 75	15.47 ± 1.19	6.39 ± 0.86	8.51 ± 0.79	5.38 ± 0.56	3.83 ± 0.48	
75 - 80	7.05 ± 0.76	4.88 ± 0.65	4.88 ± 0.55	3.33 ± 0.43	1.94 ± 0.33	
80 - 85	5.15 ± 0.61	3.84 ± 0.53	5.74 ± 0.61	3.28 ± 0.44		
85 - 90	6.79 ± 0.77	8.16 ± 0.80	5.38 ± 0.59	2.11 ± 0.38		
90 - 95	5.43 ± 0.73	6.42 ± 0.71	3.37 ± 0.46	1.03 ± 0.28		
95 - 100	5.65 ± 0.87	6.17 ± 0.78	2.35 ± 0.50	1.02 ± 0.28		
100 - 105	4.85 ± 0.81	2.43 ± 0.58	0.84 ± 0.34			
105 - 110	5.73 ± 0.84	2.22 ± 0.53	0.90 ± 0.36			
110 - 115	2.69 ± 0.54	1.11 ± 0.36				
115 - 120						
120 - 125						
125 - 130						
130 - 135						
135 - 140						
140 - 145						
145 - 150						
150 - 155						
155 - 160						
160 - 165						
165 - 170						
170 - 175						
175 - 180						

Bibliography

[1] E.H. Bellamy. *Prog. Nucl. Phys.*, 8:237, 1960.

[2] J.E. Leiss and R.A. Schrack. *Phys. Rev.*, 30:456, 1958.

[3] G. Davidson. PhD thesis, Massachussetts Institute of Technology, 1959.

[4] R.A Schrack et al. *Phys. Rev.*, 127:1772, 1962.

[5] R.A Schrack. *Phys. Rev.*, 140:B 897, 1965.

[6] J. Arends et al. *Z. Phys*, A 311:367, 1983.

[7] M.I. Adamovich et al. *Sov. J. Nucl. Phys.*, 9:848, 1969.

[8] H. Überall et al. *Phys. Lett.*, B 44:324, 1973.

[9] I. Endo et al. *Phys. Lett.*, B 47:469, 1973.

[10] T. Fujii et al. *Nucl. Phys.*, B 120:395, 1977.

[11] D. Rowley et al. *Phys. Rev.*, C25:2652, 1982.

[12] J. Arends et al. *Z. Phys.*, A 305:205, 1982.

[13] S. Maleki. *Nucl. Phys.*, A 403:607, 1983.

[14] H. de Vries et al. *At. Data Nucl. Data Tables*, 36:495, 1987.

[15] E. Mazzucato et al. *Phys. Rev. Lett.*, 57:3144, 1986.

[16] S. Nozawa. *Phys. Rev.*, C41:1306, 1990.

[17] R. Beck et al. *Phys. Rev. Lett.*, 65:1841, 1990.

[18] J. Bergstrom. *Phys. Rev.*, C44:1768, 1991.

[19] D. Dreschel and L. Tiator. *J. Phys. G: Nucl. Part. Phys.*, 18:449, 1992.

[20] M. Harita et al. *Ann. Phys.*, 108:116, 1977.

[21] Y. Horikawa et al. *Nucl. Phys.*, A 345:386, 1980.

[22] E. Oset and W. Weise. *Nucl. Phys.*, A 368:375, 1981.

[23] J.H. Koch and E.J. Moniz. *Phys. Rev.*, C20:235, 1979.

[24] J.H. Koch and E.J. Moniz. *Phys. Rev.*, C27:751, 1983.

[25] A.N. Saharia and R.M. Woloshyn. *Phys. Rev.*, C23:351, 1981.

[26] T. Takaki et al. *Nucl. Phys.*, A 443:570, 1985.

[27] R.C. Carrasco et al. *Nucl. Phys.*, A 565:797, 1993.

[28] D. Branford. *AIP Conference Proceedings*, 603:335, 2001.

[29] C. Sterner. Deeply bound pionic states in ^{208}Pb(d,^{3}He). http://www.nscl.msu.edu/undergrad/reu/199/reports/sterner/sterner.pdf, 1999.

[30] A. Nagl, V. Devanathan, and H. Überall. *Photoproduction of pions.* Springer-Verlag, 1991.

[31] G. Koch et al. *Phys. Rev. Lett.*, 63:498, 1989.

[32] I. Anthony. *Nucl. Instr. Meth.*, A 301:230, 1991.

[33] S.J. Hall et al. *Nucl. Instr. Meth.*, A 368:698, 1996.

[34] M.J. LeVine. *IEEE Transactions on Nuclear Science*, NS-32:1360, 1985.

[35] J. Steinberger et al. *Phys. Rev.*, 78:802, 1950.

[36] W.K.H. Panofsky et al. *Phys. Rev.*, 86:180, 1952.

[37] Y. Goldshmidt-Clermont et al. *Phys. Rev.*, 89:329, 1953.

[38] A. Silverman and M. Stearns. *Phys. Rev.*, 88:1225, 1952.

[39] G. Cocconi and A. Silverman. *Phys. Rev.*, 88:1230, 1952.

[40] J.W. DeWire et al. *Phys. Rev.*, 92:520, 1953.

[41] E.L. Goldwasser et al. *Phys. Rev.*, 95:1692, 1954.

[42] G. deSaussure and L.S. Osborne. *Phys. Rev.*, 99:843, 1955.

[43] L.M. Saunders. *Nucl. Phys.*, B7:293, 1968.

[44] P. Argan et al. *Phys. Rev.*, C21:1416, 1980.

[45] P. Argan et al. *Phys. Rev.*, C24:300, 1981.

[46] P. Argan et al. *Phys. Lett. B.*, 206:4, 1988.

[47] G.W. Dodson et al. *Phys. Rev.*, 26:2548, 1982.

[48] L. Jammes et al. *Phys. Letts. B.*, 227:21, 1989.

[49] G. Tamas. *Nucl. Phys.*, A 446:327c, 1985.

[50] E. Mazzucato. *Phys. Letts.*, B 185:25, 1987.

[51] I.V. Glavanakov et al. *Phys. Lett.*, B 178:155, 1986.

[52] J. LeFrançois et al. *Il Nuovo Cimento*, 65:333, 1970.

[53] D.R. Tieger et al. *Phys. Rev. Lett.*, 53:755, 1984.

[54] P.S. Anan'in et al. *Sov. J. Nucl. Phys.*, 41:883, 1985.

[55] V. Bellini et al. *Nucl. Phys.*, A 646:55, 1999.

[56] F. Rambo et al. *Nucl. Phys.*, A 660:69, 1999of the.

[57] D. Dreschel et al. *Nucl. Phys.*, A 660:423, 1999.

[58] B. Bellinghausen et al. *Nucl. Phys.*, A 358:373c, 1981.

[59] B. Bellinghausen et al. *Z. Phys.*, A 309:65, 1982.

[60] G. Koch et al. *Phys. Lett.*, B 218:143, 1989.

[61] R.W. Gothe et al. *Phys. Lett.*, B 355:59, 1995.

[62] S. Boffi and R. Mirando. *Nucl. Phys.*, A 448:637, 1986.

[63] A.A. Chumbalov et al. *Z. Phys.*, A 328:195, 1987.

[64] M. Schmitz. *Experimentelle Untersuchung der Photoproduktion neutraler Pionen an C-12 im Bereich der Delta-Resonans.* PhD thesis, University of Mainz, Germany, 1996.

[65] J.C. Bergstrom et al. *Phys. Rev.*, C55:2923, 1997.

[66] J.C. Bergstrom et al. *Phys. Rev.*, C57:3203, 1998.

[67] J.C. Bergstrom et al. *Phys. Rev.*, C59:2588, 1999.

[68] J.M. Vogt et al. *Nucl. Instr. Meth. Phys. Res.*, A 366:100, 1995.

[69] B. Krusche et al. *Phys. Lett.*, B 526:287, 2002.

[70] A.R. Gabler et al. *Nucl. Instr. and Meth.*, A 346:168, 1994.

[71] A.R. Gabler. *Ansprechverhalten des Detektorsystems TAPS für monochromatische Photonen im Energiebereich E_γ = 50 - 780 MeV.* PhD thesis, University of Giessen, 1993.

[72] L.S. Fog. *Coherent production of neutral pions on ^{12}C and ^{40}Ca.* PhD thesis, University of Glasgow, 2001.

[73] V. Girija et al. *Phys. Rev.*, C27:1169, 1983.

[74] B. Karaoglu and E.J. Moniz. *Phys. Rev.*, C33:974, 1986.

[75] S. Boffi et al. *Il Nouvo Cimento*, 104:843, 1991.

[76] H. Yukawa. *Proc. Phys. Math. Soc. Japan*, 17:48, 1935.

[77] American Institute of Physics. Review of particle properties. *Phys. Rev.*, D50:1173, 1994.

[78] H. Ströher. Neutral pion photoproduction experiments near threshold. Habilitationsschrift, 1990. University of Giessen.

[79] S. Kamalov. Private communication.

[80] D. Dreschel et al. *Nucl. Phys.*, A 645:145, 1999.

[81] W. Peters et al. *Nucl. Phys.*, A 640:89, 1998.

[82] G.F. Chew et al. *Phys. Rev.*, 106:1345, 1957.

[83] F.A. Berends et al. *Nucl. Phys.*, B4:1, 1967.

[84] V. Devanathan and G. Ramachandran. *Nucl. Phys.*, 23:312, 1961.

[85] A. Ramakrishnan et al. *Nucl. Phys.*, 24:163, 1961.

[86] V. Devanathan and G. Ramachandran. *Nucl. Phys.*, 38:654, 1962.

[87] V. Devanathan and G. Ramachandran. *Nucl. Phys.*, 42:256, 1963.

[88] K. Stricker et al. *Phys. Rev.*, C19:929, 1979.

[89] K. Stricker et al. *Phys. Rev.*, C22:2043, 1980.

[90] L.S. Kisslinger. *Phys. Rev.*, 98:761, 1955.

[91] L.J. Abu-Raddad et al. *Phys. Rev.*, C60:054606, 1999.

[92] A.A. Chumbalov and S.S Kamalov. *Phys. Lett.*, B 196:23, 1987.

[93] S.S Kamalov and T.D. Kaipov. *Phys. Lett.*, B 162:260, 1985.

[94] R.M. Woloshyn. *Phys. Rev.*, C18:1056, 1978.

[95] L.S. Kisslinger and W.L. Wang. *Ann. Phys. (N.Y.)*, 99:374, 1976.

[96] J.W. Staples. Master's thesis, University of Illinois, 1969.

[97] H. Herminghaus et al. *Proc. Lin. Accel. Conf.* Albequerque, 1990.

[98] R. Novotny. *IEEE Transactions on Nuclear Science*, 38(2), April 1991.

[99] R. Novotny. *Nucl. Tracks Radiat. Meas.*, 21:23, 1993.

[100] *GEANT - Detector Description and Simulation Tool.* Geneva, CERN Program Library Long Writeup W5013 edition, 1993.

[101] R. Novotny. *Nucl. Phys. B (proc. Suppl.)*, 61B:137, 1998.

[102] M. Laval et al. *Nucl. Instr. and Meth.*, 206:169, 1983.

[103] R. Novotny. *Nucl. Instr. Meth.*, A 262:340, 1987.

[104] T. Matulewicz et al. *Nucl. Instr. and Meth.*, A 289:194, 1990.

[105] J. Clayton et al. *Nucl. Instr. and Meth.*, A 305:116, 1991.

[106] K. Wisshak and F. Käppler. *Nucl. Instr. and Meth.*, 227:91, 1984.

[107] K. Molenaar. Performance of TAPS in the tagged photon beam of MAMI. Master's thesis, University of Groeningen, 1992.

[108] M. Winter. http://www.webelements.com. University of Sheffield, 2001.

[109] M. Pfeiffer. Private communication.

[110] V. Hejny. *Photoproduction von η-mesonen an Helium 4.* PhD thesis, University of Giessen, 1998.

[111] M. Röbig. Eichung des taps-detektorsystems mit höhenstrahlung. Master's thesis, University of Giessen, 1991.

[112] J.B. Birks. *The Theory and Practice of Scintillation Counting.* Pergamon Press, Ltd., 1964.

[113] V.A. Baranov. *Nucl. Instr. Meth.*, A 374:335, 1996.

[114] T.C. Awes et al. *Nucl. Instr. Meth.*, A 311:130, 1996.

[115] F.M. Marques et al. *Nucl. Instr. Meth.*, A 365:392, 1995.

[116] M. Kotulla. PhD thesis, University of Giessen, 2001.

[117] G. Koch. *Photoproduction von neutralen Pionen an Kohlenstoff und Calcium im Bereich der Produktionsschwelle.* PhD thesis, University of Giessen, 1988.

[118] V.A. Tryasuchev and A.V. Kolchin. *Sov. J. Nucl. Phys.*, 53:439, 1991.

[119] T. Buti et al. *Phys. Rev.*, C33:755, 1986.

[120] S. Boffi et al. *Electromagnetic Response of Atomic Nuclei.* Oxford University Press Inc., 1996.

[121] M.L. Boas. *Mathematical Methods in the Physical Sciences.* John Wiley and Sons, Inc., 1983.